Studying divertor relevant plasmas in linear devices

Studying Divertor Relevant Plasmas in Linear Devices

Experiments and transport code modelling

PROEFSCHRIFT

ter verkrijging van de graad van doctor aan de Technische Universiteit Eindhoven, op gezag van de rector magnificus prof.dr.ir. F.P.T. Baaijens, voor een commissie aangewezen door het College voor Promoties, in het openbaar te verdedigen op donderdag 10 januari 2019 om 13:30 uur

door

Karol Ješko

geboren te Košice, Tsjechoslowakije

Dit proefschrift is goedgekeurd door de promotoren en de samenstelling van de promotiecommissie is als volgt:

voorzitter:	prof.dr.ir. G.M.W. Kroesen
1e promotor:	prof.dr.ir. M.C.M. van de Sanden
copromotor(en):	dr. J.P. Gunn (CEA Cadarache)
leden:	prof.dr. G. Cartry (Aix-Marseille Université)
	prof.dr B. Lipschultz (The University of York)
	prof.dr. U.M. Ebert
	Prof.Dr.rer.nat. D. Reiter (University of Düsseldorf)
adviseur(s):	dr. H.J. van der Meiden (DIFFER)

Het onderzoek of ontwerp dat in dit proefschrift wordt beschreven is uitgevoerd in overeenstemming met de TU/e Gedragscode Wetenschapsbeoefening.

Studying Divertor Relevant Plasmas in Linear Devices

Experiments and transport code modelling

Karol Ješko

Eindhoven University of Technology / Aix-Marseille Université
December 2018

This thesis was carried out under the joint supervision of Eindhoven University of Technology and Aix-Marseille université in the framework of the International Doctoral College in Fusion Science and Engineering (Fusion-DC), with an agreement for an international joint supervision (co-tutelle) in place.

This work is part of the research programme of the Foundation for Fundamental Research on Matter (FOM), which is part of the Netherlands organization for Scientific Research (NWO).This work was granted access to the HPC resources of Aix-Marseille University financed by the project Equip@Meso (ANR-10-EQPX-29-01) of the program “Investissements d'Avenir” supervised by the Agence Nationale pour la Recherche. This work has been carried out within the framework of the EUROfusion Consortium and has received funding from the Euratom research and training programme 2014-2018 under grant agreement No 633053. The views and opinions expressed herein do not necessarily reflect those of the European Commision. DIFFER is a partner in the Trilateral Euregio Cluster (TEC).

A catalogue record is available from the Eindhoven University of Technology library.

ISBN: 978-94-638-0203-1

NUR: 924

Printed by: ProefschriftMaken || www.proefschriftmaken.nl

Contents

Part I

Framework & overview of research

Chapter 1

Introduction

1.1 Nuclear Fusion

The global energy challenge will be one of the key problems for humankind to be solved in the 21st century. This is becoming evident especially in view of the Paris climate agreement, which aims to keep the increase of the global average temperature well below 2 °C with respect to pre-industrial levels [1]. This will be a very difficult task, considering that the world population is projected to increase to about 10 billion by 2100 based on conservative estimates [2]. Moreover, most of the world population lives in developing and newly industrialised countries, where energy consumption per capita is still rather low. The increase of the development index in these countries will lead to a further increase in the energy demand. Harnessing nuclear fusion on Earth [1] would provide a clean and safe energy source, with potentially inexhaustible fuel supplies and manageable amounts of nuclear waste products. The fusion reaction that is deemed most feasible in terrestrial conditions is the reaction of hydrogenic isotopes of deuterium ($^2_1$D) and tritium ($^3_1$T) nuclei[2], forming an alpha particle ($^4_2$He) and a neutron (n):

$$^2_1\mathrm{D} + {}^3_1\mathrm{T} \rightarrow \mathrm{n} + {}^4_2\mathrm{He}. \tag{1.1}$$

The energy released per reaction is 17.6 MeV. In terms of fuel, deuterium is abundant, accounting for about 0.0115% of all hydrogen occurring on Earth, the rest being protium, the common, neutron-free isotope. Deuterium can readily be extracted from heavy water (D_2O), which can in turn be separated out from naturally ocurring water at the industrial scale by the Girdler sulfide process [3]. Tritium, on the other hand, does not occur naturally since it is not stable, β-decaying into ^{3}He, an energetic electron and an electron neutrino, with a half-life of about 12 years. However, tritium can be synthetised from the naturally abundant ^{6}Li isotope, which splits into ^{4}He and tritium when bombarded by energetic neutrons. One can notice that the energetic

[1] It should be noted that due to delays in the advancement in fusion research, commercially available fusion is still a distant future and the climate problem has to be solved by other means in the meantime.

[2] It is important to note that this reaction is not the primary source of solar energy; in stars of the size of the Sun, it is the proton-proton reaction chain that dominates. In stars larger than the Sun, theoretical models suggest the carbon-nitrogen-oxygen (CNO) cycle.

neutron from reaction 1.1 can be used in this process, and this is indeed the concept envisaged for a fusion reactor, where the tritium will be created in-situ in a *breeding blanket* in the vicinity of the reactor volume.

In order for the fusion reaction 1.1 to occur, one first has to overcome the repulsive electrostatic forces between the nuclei before the strong interaction takes over that holds the protons and neutrons of the reaction product in place. In other words, the reaction partners must have a sufficient relative kinetic energy to overcome the repulsive force. One option is to heat the reactants to extremely high temperature (the DT reaction rate peaks at about 70 keV or 800 million K). This option, when we rely on the thermal motion of particles is called *thermonuclear fusion*. There is another, different approach: Firing a high-power laser at a pellet made of a mixture of D-T fuel, thereby compressing and heating it to a point where the fusion reaction takes place. This is a pulsed concept and is called *inertial fusion*.

1.1.1 Magnetic confinement fusion

The focus of this thesis is on steady-state, thermonuclear fusion using magetic confinement. Long before fusion-relevant temperatures are reached, the fuel is in the state of a plasma, i.e. the electrons are not bound to the nuclei. This gives the possibility to confine the thermonuclear plasma using magnetic fields, as charged particles spiral around on helical trajectories wrapped around the magnetic field lines. There are several concepts of devices that use different magnetic field geometries to confine the hot, thermonuclear plasma, the most successful and extensively investigated concept being the tokamak invented by I. Tamm and A. Sakharov in the 1950s. In this concept, the magnetic field of a tokamak is defined by two components:

- A strong toroidal magnetic field generated by external currents in toroidal field coils.
- A poloidal magnetic field generated by a toroidal plasma current.

The poloidal field is typically an order of magnitude smaller than the toroidal field. The resulting field is a helical field. Figure 1.1 illustrates the tokamak configuration. A plasma in a purely toroidal field would drift towards the outer wall due to the ∇B drift inherently present in this configuration. This drift may be countered by balancing the outward force with the magnetic pressure from the poloidal field, produced by the plasma current[3]. The poloidal field coils depicted in the Fig. 1.1 stabilize the plasma position and are also used for plasma shaping, for example to create the so-called divertor configuration.

It is insightful to look at the global power balance in a fusion reactor. Let n be the volume averaged density of D-T fuel in the reactor, T be the temperature. The D-T fusion reaction releases 17.6 MeV, however, from momentum conservation, 4/5 of this

[3]Another very promising concept is the stellarator, which is designed without the large plasma current by generating the poloidal field using external coils, thus being inherently less prone to instabilities of the plasma.

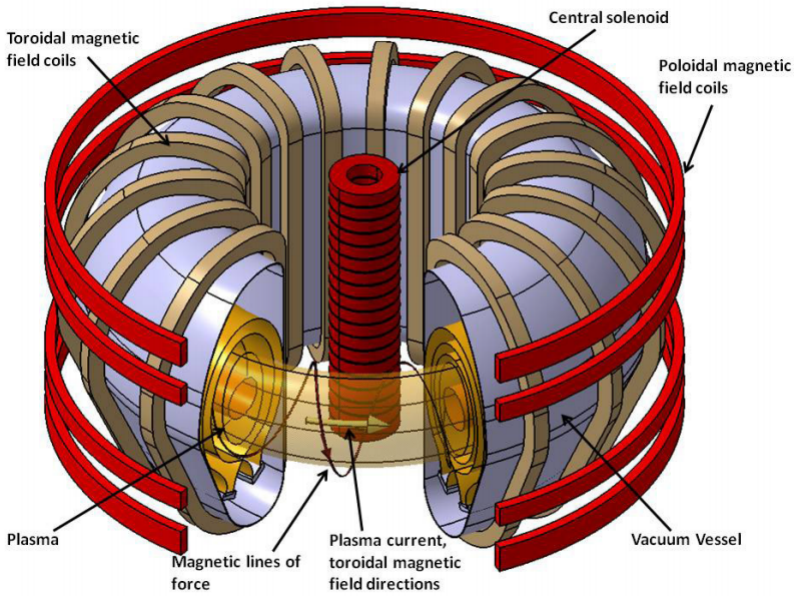

Figure 1.1 – A schematic overview of the tokamak configuration, depicting the main features: a vacuum vessel surrounded by toroidal field coils, plasma current and poloidal field coils. Reproduced from [4] with permission from IAEA.

energy is carried away by the neutron which is not confined by the magnetic field, and only 1/5 by the alpha particle. Therefore, the maximum available heating power due to fusion is in fact the power going to the alpha particles, $P_\alpha = \frac{1}{4}n^2 < \sigma v >_{\mathrm{DT}} E_\alpha$, where $< \sigma v >_{\mathrm{DT}}$ is the D-T reaction (temperature dependent) rate coefficient and $E_\alpha = 3.5$ MeV is the energy released per alpha particle. Then, in order to sustain the fusion reactions, the alpha particle heating power must be higher than the energy loss rate (P_{loss}) due to various processes, e.g. outward particle and energy transport, radiative losses and so forth, i.e. $P_\alpha \geq P_{\mathrm{loss}}$. This energy loss rate from the system is commonly approximated by introducing a global *energy confinement time* τ_E, a very useful engineering parameter that gives a simple relation between the loss rate and the total energy content of the plasma: $P_{\mathrm{loss}} = \frac{W_p}{\tau_E}$, where $W_{\mathrm{p}} = 3nk_BT$ is the total plasma energy content (k_B is the Boltzmann constant). Putting this together, we can derive the following condition

$$n\tau_E \geq \frac{12k_BT}{E_\alpha \langle \sigma v \rangle_{\mathrm{DT}}} \tag{1.2}$$

This is the simplest version of the *Lawson criterion* [5] and it states that in order to sustain the the burning fusion plasma, the product of density and confinement time must be larger than the temperature dependent function on the R.H.S. This function is plotted in Fig. 1.2 for the D-T, D-D and D-^{3}He reactions and has a minimum around T=25 keV in case of D-T, indicating the easiest operating point in terms of the $n\tau_E$ product.

Another interesting insight can be obtained by looking at the dependence of the energy confinement time. Energy confinement in a fusion device is complex and multi-faceted, and there is no generic model that can give predictions based on engineering

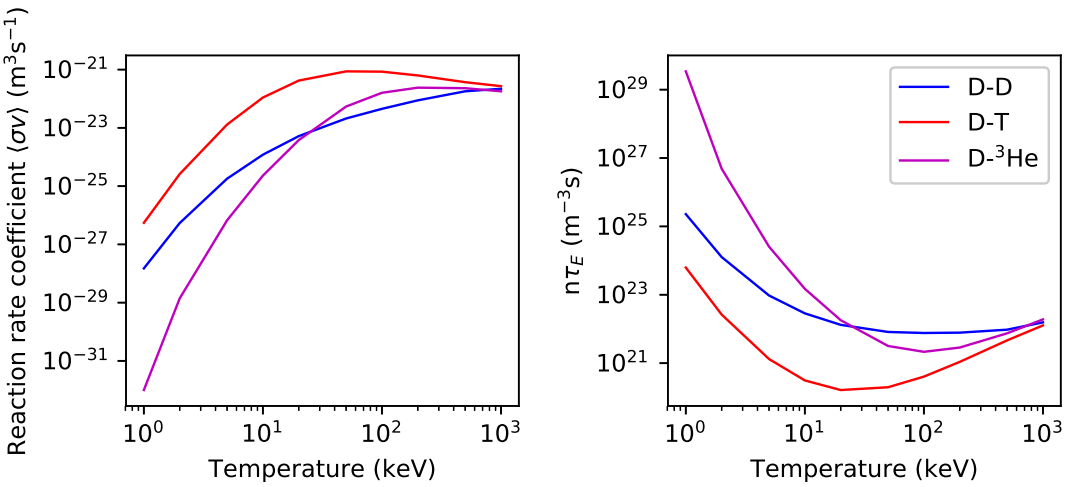

Figure 1.2 – Fusion reaction rates and $n\tau_E$ product as a function of temperature for several relevant reactions. The source of the data is the NRL plasma formulary [6].

inputs. In view of this, the fusion community has resorted to the use of empirical scaling laws. A parametric dependence on a number of engineering parameters was obtained by fitting experimentally inferred τ_E from a number of tokamaks, establishing a multi-machine scaling law. The one pointed out here is the H98 scaling [7], which has the form

$$\tau_{\mathrm{E}}^{\mathrm{H98}} = 5.62 \times 10^{4} I^{0.93} B^{0.15} n^{-0.41} P^{-0.69} R^{1.97} \kappa^{0.78} \epsilon^{0.58} M^{0.19}, \tag{1.3}$$

where I is the plasma current, B is the toroidal magnetic field, n is the density, P is the heating power, R is the major radius, κ is the plasma elongation, ϵ is the inverse aspect ratio (the latter two are geometrical parameters describing the shape of the plasma) and M is the hydrogen isotope mass number. One can immediately see that the confinement time strongly depends on the major radius, which is one of the reasons why new tokamaks are typically larger compared to their predecessors - in other words, a larger tokamak is more efficient.

In practice, to achieve thermonuclear conditions, the plasma must be heated to temperatures of several tens of keV, as we can see from the Lawson criterion. Inherently, the plasma is heated by Ohmic heating due to the plasma current. However, Ohmic heating alone cannot be used to increase the temperature to the required values, as the plasma resistivity drops with increasing electron temperature, $\eta \sim T_e^{-3/2}$. The plasma resitivity was calculated by Spitzer in the 1950s based on electron-ion collisions [8]. The $T_e^{-3/2}$ dependence of the resistivity is a property that is fundamentally different from e.g. solid conductors, for which the resistivity increases with increasing temperature, giving a positive feedback mechanism instead. Therefore, additional heating systems have to be applied in order to drive the temperature higher. One group of methods is microwave heating, where power is deposited by high-frequency electromagnetic waves at characteristic plasma frequencies, with their names based on these frequencies: *Ion Cyclotron Resonance Heating* (ICRH), *Electron Cyclotron Resonance Heating* (ECRH) and *Lower Hybrid* (LH) heating. The other group of heating systems are *Neutral Beam*

Injectors (NBIs). In this case, deuterium ions are accelerated to high energies outside the device. Subsequently, they are neutralized and are guided into the tokamak plasma, where they deposit their energy by collisional relaxation.

In order to make a such a fusion reactor energetically and economically viable, the heating power from the fusion reactions must be significantly higher than power coming from the external heating sources needed to maintain the burning plasma. The ratio of the fusion power P_{fus} and the external heating power P_{h} is called the Q parameter, or *fusion gain*, which is a commonly used engineering parameter that characterises the performance of a fusion reactor. Currently, the largest tokamak in the world, the *Joint European Torus* (JET) has achieved a record Q value of 0.64 in a deuterium-tritium campaign in 1997 [9–11]. ITER, the International Thermonuclear Experimental Reactor will be the largest thermonuclear fusion reactor ever built is aiming for a fusion gain of Q =10. More specifically, the goal is to produce 500 MW of fusion power with 50 MW of external heating power in long pulses of 400 seconds. It should be pointed out that ITER is still an experimental reactor without the capability of suppliyng power into the grid. For instance, the external heating alone will consume about 300 MW of electrical power. Therefore, for efficient electricity generation, an even higher Q is needed.

DEMO, the first fusion reactor to demonstrate feasibility as a power plant, is expected to operate at a fusion gain of Q=25 to achieve engineering breakeven. The limit when no external heating power is needed to sustain the burning plasma is called ignition for which $Q \to \infty$.

1.2 Power exhaust in tokamaks

In a tokamak, the hot, burning plasma in the center of the device, albeit confined by a magnetic field, has to coexist with a containment (i.e. a vacuum vessel) made of solid materials. It is clear that such a coexistence will be troublesome and that it will necessarily lead to steep gradients of the plasma temperature and density. Particles and energy are expelled from the plasma and are transported to the wall, leading to complex plasma-wall interactions (PWIs). For instance, one major concern is the pollution of the plasma with impurities coming from wall sputtering, having a high atomic number and therefore strongly radiating at high temperatures. This can lead to significant cooling and can prevent achievement of reactor-relevant conditions. Since interaction of the plasma and the enclosing solid surfaces is unavoidable, we should strive for a scenario which minimises their impact on plasma performance. Other issues are related to the survival of the plasma-facing components (PFC) themselves, also related to material erosion during plasma exposure, degradation of mechanical and thermal properties of PFCs, and even melting during off-normal and potentially even normal events [12]. In the following, two geometrical configurations of localising the PWI in a tokamak are described.

1.2.1 Limiters vs. divertors

In the limiter configuration, the location of the plasma-wall interaction is defined by inserting a protruding solid object into the tokamak vessel, called a limiter, which can have various forms. The most simple concept is a circular diaphragm perpendicular to the toroidal field. This is called a poloidal limiter. Other geometrical configurations are also possible, e.g. a rail limiter which is toroidally symmetric, which means it can be displayed in a 2-D poloidal cross section of the device, as depicted in Fig. 1.3 (a). By introducing such a structure in the vessel, some magnetic field lines intersect the solid surface, while others remain closed within the plasma. This defines a *last closed flux surface* (LCFS). The region radially inside the LCFS is called the main, or core plasma while the one outside is called the *scrape-off layer* (SOL). Typically, particles entering the SOL from the main plasma terminate on the solid limiter surface. The disadvantage of limiters is that the impurities coming from the wall can easily enter the core region.

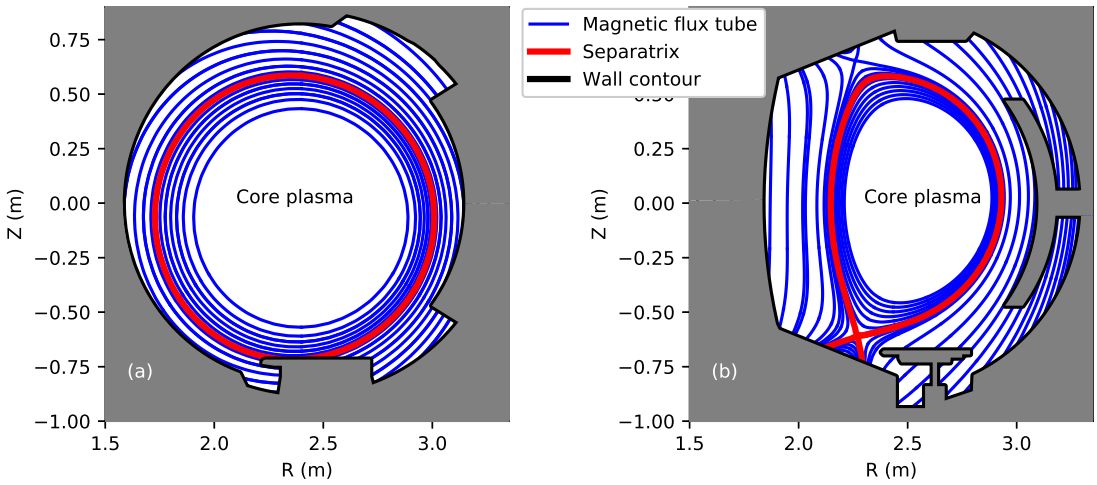

Figure 1.3 – Illustration of a limiter configuration at Tore Supra (a) and a divertor configuration (b) at the WEST tokamak, the successor of Tore Supra. In fact, in (b) a double-null configuration is depicted, with the secondary X-point being at the top of the vessel.

Divertors have the advantage that they keep the plasma surface interaction at a distance from the core plasma, reducing core contamination, as well as they can typically maintain a higher neutral pressure[4], facilitating pumping and thereby the removal of helium ash. In the case of a divertor configuration, an X-point[5] is formed, and in

[4]The neutral population originates from target neutralisation: the plasma particles neutralise on a solid surface, and a large fraction of is subsequently released back into the vessel. Subsequently these neutrals can be ionised in the plasma again. This is called *plasma recycling*.

[5]The magnetic X-point (or poloidal field null) into the poloidal magnetic field is done by driving a current through dedicated poloidal field coils. The simplest and most common case is to have one poloidal field coil placed under the vacuum vessel - this coil is often termed the divertor coil. For an X-point to form, the current in the poloidal field coils must have the same sign (direction) as the plasma current.

this case the LCFS is given by the magnetic separatrix arising from this configuration. The place where the separatrix intersects the solid surface, usually a divertor target plate, is called the *strike point*. In a standard divertor configuration with one X-point, one has two strike points when looking at the poloidal cross section of the tokamak vessel. In Fig. 1.3 (b), a double-null configuration of the WEST tokamak is depicted, however the main separatrix is shown in red. One can also see a second X-point at the top of the device and its corresponding separatrix. As in the limiter case, the area inside the (primary) separatrix, on closed flux surfaces, is the main plasma, while the area situated radialy outward, on "open" field lines is the scrape-off layer.

The divertor configuration is used at most current tokamaks, like JET, DIII-D, Alcator C-mod, WEST, MAST-Upgrade, COMPASS, ASDEX-Upgrade, KSTAR, EAST etc., and will be used also for ITER. It should be noted that the WEST configuration depicted in Fig. 1.3 has a relatively open divertor, with the X-point being close to the divertor targets. The newly designed MAST-upgrade divertor, for instance, called the *Super-X divertor* [13], uses a long-legged, tightly baffled configuration to move the strike points very far from the core plasma. Although it may seem that divertors are the way to go, limiter configurations still maintain a degree of relevance since plasma startup in most devices (and this will be true also for ITER) occurs in a limiter configuration [14], the X-point being formed in later stages of the discharge. For instance, the ITER limiter design was re-shaped recently, based on an improved understanding of the width of the limiter SOL [15].

It is important to note that when plasma particles arrive at a solid target surface, they neutralise - a solid surface acts as a sink for the plasma. The ultimate fate of these neutral particles depends strongly on the species involved and on the properties of the surface, i.e. material, surface roughness etc, but also on the plasma conditions.

1.2.2 Width of the scrape-off layer

A poloidal cross section of the tokamak and the topology of the energy flow in a divertor configuration is depicted in Fig. 1.4. The main power source is located in the main (core) plasma, where it is deposited by auxiliary heating systems or fusion α particles in case of a reactor. This power then flows through the magnetic separatrix (or LCFS) into the SOL and subsequenty to the plasma facing components (i.e. the divertor targets). Therefore, the average, unmitigated heat flux transported to the plasma facing components from the core can be estimated by taking the total power that crosses the separatix, and dividing it by the size of the plasma wetted area.This wetted area depends on width of the SOL, and more specifically the width of the heat flux profile λ_q. Based on a multi-machine scaling law [16] derived from a large database of devices, for H-mode inter-ELM plasmas, this was found to have an unfavourable scaling with machine settings and has the following form:

$$\lambda_q = 0.86 \cdot B_{\mathrm{T}}^{-0.8}(\mathrm{T}) q_{\mathrm{cyl}}^{1.11} P_{\mathrm{SOL}}^{0.11}(\mathrm{MW}) R^{-0.13}(\mathrm{m}). \tag{1.4}$$

where B_{T} is the toroidal magnetic field, q_{cyl} is the cylindrical safety factor which is inversely proportional to the poloidal field B_p, P_{SOL} is the power crossing the separatrix

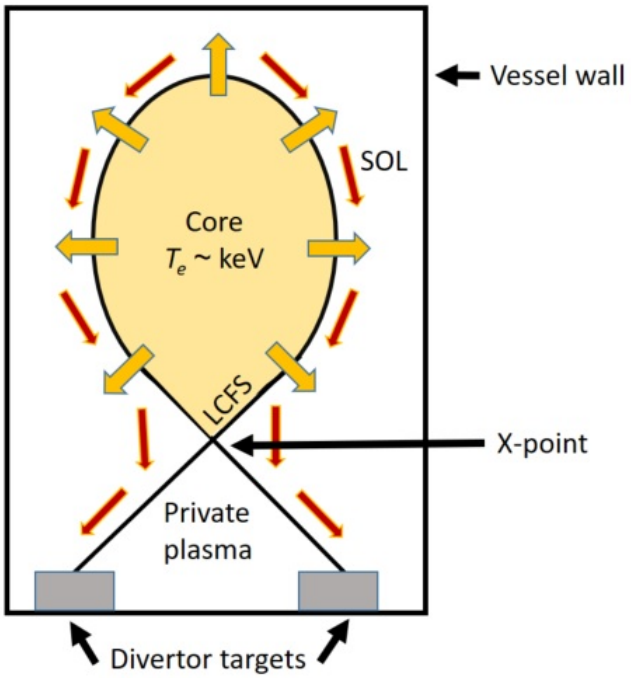

Figure 1.4 – Poloidal cross section of a divertor configuration, depicting the typical power flows from the core through the SOL to the divetor targets.

and R is the major radius. It turns out that the high magnetic fields needed for good confinement (equation 1.3) work against us in terms of power exhaust by decreasing λ_q. The scaling was compared to predictions from the heuristic drift model [17], a recently developed theoretical framework for SOL energy transport, and have found good agreement [18]. What is striking is that there is no, or only negligible dependence on the system size in the scaling. For larger machines, the power crossing the separatrix will be higher, but λ_q will not be affected by the system size. For an ITER Q=10 high confinement scenario, the scaling yields a λ_q value of about 1 mm [16]. The power entering the SOL is expected to be $\sim$ 100 MW, leading to an average heat flux density of $\sim$40 MW/m^2 in case of no mitigation (the quoted heat flux includes geometrical means of mitigation, like the use of inclined targets that minimise the B-field angle of attack, and flux expansion, i.e. spreading out of the field lines in the divertor. Both methods lead to an increased plasma wetted area). However, the technological limit for steady-state power loading of ITER plasma facing components is 10 MW/m^2 [19]. This mismatch of expected and tolerable power fluxes is a major challenge on the way to harnessing fusion energy. The excess power has to be radiated away either by neutral hydrogenic or impurity species, ultimately leading to a state called divertor plasma detachment, a regime in which both particle and power fluxes to divertor targets are strongly reduced. Understanding the key processes at play in divertor detachment is mandatory in order to optimize divertor performance.

1.3 Divertor plasma detachment in tokamaks

In short, plasma detachment can be characterised as a state in which particle and power fluxes to the divertor targets are strongly reduced. This is achieved by a multitude of complicated, interlinked processes in the scrape-off layer and especially the divertor.

The following sections attempt to give a simple introduction to the basics of detachment in tokamaks, focusing mainly on features which will be relavant in later parts of this thesis. For a recent, comprehensive review of detachment in tokamaks, the reader is referred to [20].

1.3.1 Plasma recycling

When charged particles strike a solid surface, most of them tend to recombine on the surface and are subsequently released (or, typically in case of energetic particles, back-scattered, in case of a reflection process) back into the plasma as neutral atoms or even thermal molecules. Some can also be absorbed and trapped in the solid, however, under steady-state conditions (i.e. saturated surfaces), there is no net absorption and all the plasma flux to the solid is compensated by an equal outflux of neutrals (in terms of mass) back into the plasma. These neutrals can then be re-ionised by the plasma, and can be transported to the wall again where the cycle starts all over. This process is called *recycling* and is typical for tokamaks as well as any other laboratory plasma device. In case of an ionisation mean free path comparable to the machine size, this re-ionisation will occur uniformly in the plasma-occupied volume of the device. In case it is short, it will occur in areas localized in the vicinity of the plasma facing surfaces.

1.3.2 The high recycling regime

In tokamaks, at low densities, when the ionisation length is large compared to the characteristic size of the divertor, we are in the *low recycling* or *sheath limited* or *convective* regime, and the bulk of the ionisation source is located in the main plasma. The particles crossing the separatrix flow directly to the divertor target. However, if the density is increased, e.g. via increasing the gas feed rate[6], the ionisation length can become comparable or shorter than the size of the divertor, and a recycling region is formed, amplifying the particle flux to the target. The bulk of the ionisation source is now localised near the divertor targets. This is called a *high recycling* regime and is characterised by large particle fluxes to the divertor plates, and also high density and low temperature in the divertor. First mentions of such a regime can be traced back to [21]. In the high recycling regime, the upstream flow pattern also changes radically: the particle flow here is small and virtually stagnated, and it is the power conducted from upstream regions of the SOL to the divertor that is the driver of the recycling region. It is this ionisation cooling that drives the temperature down, since each ionisation event happens at an energy cost. We should note here that this is a simplified picture, since neutral atoms and molecules can also radiate before being

[6]This scenario is typically referred to as a *density ramp* experiment.

ionised, creating additional energy sinks. Moreover, impurities in the plasma, be they intentional or not, also constitute important energy sinks that affect the energy balance of the recycling region.

1.3.3 The detached regime

The low temperature close to the target plates in high recycling divertors is beneficial since it reduces the physical sputtering yield and it was also considered as a solution to the heat exhaust problem in the past [22]. However, the particle flux to the targets remains high and this is a concern, since each ion deposits up to 13.6 eV of potential energy during surface recombination at the target. This can in principle go even higher when the resulting atoms recombine further into molecules, releasing up to an additional 2.2 eV per incident ion [23]. The energy flux associated with surface recombination can easily exceed the technological limit of 10 MW/m^2 [19] of the ITER divertor plates, provided that the target ion flux is high. Therefore, it is mandatory also to reduce the particle flux arriving at the target.

Further increasing the plasma density in a tokamak has led to the discovery and characterisation of the detached regime in the 1990s, when both the heat flux *and* particle flux to the target is strongly reduced. An overview of these experiments and comparison with high recycling regimes is described in [24].

To give basic insight into the drivers of the reduction of the particle flux to the walls in a tokamak, we use the simple, 0-D particle and power balance model developed in [25]. This model states that the total, integrated ionisation source in the tokamak volume Γ_{ion} (i.e. units s^{-1})) equals the sum of the total particle flux to the wall Γ_w (integrated over the whole surface area of the device, i.e. given simply in s^{-1}) and the total sink due to volume recombination Γ_{rec}, i.e.

$$\Gamma_{\mathrm{ion}} = \Gamma_w + \Gamma_{\mathrm{rec}} \tag{1.5}$$

Next, the global power balance of the SOL is written in the following way (again, all terms are total, volume integrated quantities):

$$Q_{\mathrm{SOL}} = Q_{\mathrm{imp}} + Q_{\mathrm{H}} + Q_{\mathrm{neut}} + \gamma T_w \Gamma_w, \tag{1.6}$$

where Q_{SOL} is the power entering the SOL from the core plasma, Q_{imp} corresponds to impurity radiation, Q_{H} is the power associated with ionisation of neutral hydrogen and Q_{neut} is the power lost to neutrals that is eventually transported to the wall, e.g. by charge-exchange or elastic ion-neutral collisions. The last term is the energy transported to the walls and T_w is an effective temperarature at the wall. Q_{H} and Q_{neut} can be described using effective energy costs, and take the form $Q_{\mathrm{H}} = E_{\mathrm{ion}}\Gamma_{\mathrm{ion}}$ and $Q_{\mathrm{neut}} = E_{\mathrm{neut}}\Gamma_{\mathrm{neut}}$, with typical values of E_{ion}=30 eV and E_{neut}=5 eV, respectively [25]. Combining equations 1.5 and 1.6 gives the following relation:

$$\Gamma_{\mathrm{w}} = \frac{Q_{\mathrm{SOL}} - Q_{\mathrm{imp}} - (E_{\mathrm{ion}} + E_{\mathrm{neut}})\Gamma_{\mathrm{rec}}}{E_{\mathrm{ion}} + E_{\mathrm{neut}} + \gamma T_w}. \tag{1.7}$$

In the temperature range of interest, e.g. $T_w \sim 1$ eV the expression can be further reduced to $\Gamma_{\rm w} = (Q_{\rm SOL} - Q_{\rm imp} - (E_{\rm ion} + E_{\rm neut})\Gamma_{\rm rec})/(E_{\rm ion} + E_{\rm neut})$. As can be seen from this analysis, for a given power crossing the separatrix $Q_{\rm SOL}$, the total plasma particle flux arriving at the targets can be reduced either by increasing radiative impurity losses, or by increasing volume recombination, or, alternatively, by increasing the energy costs $E_{\rm ion}$, $E_{\rm neutr}$, associated with the interaction of the plasma and neutral hydrogenic species.

Recently, there has been increasing theoretical [25, 26] and experimental [27] evidence suggesting that these are the principal mechanisms responsible for the observed rollover and reduction of particle flux during detachment in tokamaks.

1.4 Linear devices as divertor simulators

Linear plasma devices have been used extensively as divertor simulators in the past, as they can generally produce plasmas with similar densities and temperatures as observed in detached or high recycling divertors . A very important aspect of linear devices is that their cost per shot is significantly lower than in standard tokamaks, due to their inherently simpler construction and less demanding staffing requirements. First experiments simulating and demonstrating the feasibility of a gaseous divertor concept were performed at the QED device [28, 29], showing strong reduction of power flux to a solid target in the last chamber of the device by increasing the neutral pressure in the chamber. This reduction was attributed to ions diffusing radially due to elastic collisions with neutral molecules, which were fed into the chamber. In similar experiments at PISCES [30], strong reduction of heat flux to the target was also found with increase of target chamber gas pressure, explained by anomalous radial transport.

Investigations in the 1990s at TU Eindhoven on the physics of expanding argon and hydrogen plasmas generated by cascaded arc sources (i.e. not necessarily fusion-motivated experiments) have led to the very important, fusion relevant discovery of molecular activated recombination (MAR), an alternative recombination process to two- and three-body recombination, published in [31]. Moreover, gas recirculation effects have been observed in the exhaust vessel of the cascaded arc source [32, 33] as well as wall association of atoms into molecules. A number of diagnostic techniques have been developed and validated for determination of plasma and neutral particle parameters [34–39].

A significant body of knowledge originates from the Nagdis linear device. In [40–42], based on spectroscopy and comparison with the CRAMD collisional radiative model [43], (MAR) was shown also in the fusion community as an important process that reduces the particle flux arriving at the target, in H/He mixture plasmas. However, the importance of radial transport is also pointed out in [44] at Nagdis. Additionally, the effect of transients on a detached plasma are assessed in [45]. Other devices with divertor physics research include TPD-I, MAP-2 and GAMMA10/PDX and progress on these is reviewed in [46].

In this work, we study a divertor-relevant plasma in the Pilot-PSI and Magnum-PSI devices. These devices can provide densities of $10^{20} - 10^{21}$ m^{-3}, which is about

one order of magnitude higher than typical plasmas produced by the other devices mentioned before, and more relevant to the regimes expected in ITER. The typical electron temperature (T_e) close to the plasma source (an arc discharge source, in our case) is 3-5 eV in a hydrogen plasma, and densities of 10^{21} m^{-3} can be exceeded, but can be modulated by tuning the input power and B-field strength.

1.4.1 Relevance of linear devices to divertor physics

The relevance of experiments in linear devices to tokamak divertors is often discussed, e.g. in [20]. Indeed, in a tokamak SOL, T_e upstream, e.g. at the midplane separatrix, is ∼100 eV, while T_e at the divertor target can be even below 1 eV under detached conditions. Clearly, Pilot-PSI cannot access the high upstream temperatures. Therefore, Pilot-PSI can only mimic the area adjacent to the targets, where T_e is low. More subtle differences that might not be so evident are related to the physics of particle balance: under high recycling and detached conditions in tokamaks, most of the particle source is concentrated in a "recycling region", poloidally located between X-point and the target plate. The ionization is maintained by power arriving via conduction from further upstream (which is a fraction of the auxiliary heating power). In Pilot-PSI the particle source is maintained by the cascaded arc, and a part of this plasma exhausts into the target chamber. The operation of the cascaded arc is de-coupled from what is happening in the target chamber, as will be seen later. Another difference is that the neutral background pressure P_n in the vessel is set by the inflow of residual gas from the cascaded arc discharge chamber, since only about 10% of the gas fed into the discharge chamber is exhausted to the vessel in the form of plasma. In a tokamak, all neutrals in the divertor originate from plasma recombination, primarily on the solid surface. This is illustrated by the fact that the divertor neutral pressure is strongly coupled to the target particle flux, while in Pilot-PSI it is not the case..

Regarding the differences between divertors and linear plasma machines it is evident that a direct extrapolation of results from one to the other is difficult. However, it is still valuable to apply an edge transport suite to a linear device. Firstly, it can be checked how accurately the code reproduces trends observed experimentally (i.e. code-experiment benchmarking), possibly pointing at additional missing physics in the code. Secondly, the code can give good insights into which atomic/molecular (or other) processes are responsible for the reduction of power and particle fluxes to the target, i.e. do the book-keeping between the various mechanisms that drive flows in the plasma, i.e. ionisation/recombination, parallel and perpendicular transport etc.

Several linear devices have been modelled previously using different code packages. For instance, Pilot-PSI has been simulated using the B2.5-Eunomia code [47], Eunomia being a neutral Monte-Carlo (MC) code specifically developed for the geometry of linear devices. An advantage of the B2.5-Eunomia suite is a built-in collisional-radiative model that can calculate line emission using the local T_e and also the population densities of vibrational states. Next, simulations for Magnum-PSI have been carried out by B2.5-Eirene [48]. However, these simulations were performed before the Magnum-PSI device was launched and therefore without input from experiments. In the simulations,

typically higher temperatures were obtained compared to the actual operational characteristics of Magnum-PSI [49]. Moreover, the geometry of the device assumed in the simulations does not correspond to the final layout. In another instance [50], the PSI-2 linear plasma device was simulated by the B2.5-Eirene package in a non-homogeneous magnetic field. In this work, it was found that inhomogeneities in the magnetic field can drive supersonic transitions in the plasma beam and also that the choice of artificial flux limiters used in the fluid code can significantly influence results in these low temperature cases. In a more recent study [51], a new transport code LINDA for linear devices is introduced and used to assess cooling efficiencies of various noble gases in the end cell of the GAMMA-10/PDX tandem mirror, identifying xenon as the most efficient radiator.

To summarize, linear devices offer a simple physical system, and combined with modelling can help to shed light on features that could otherwise remain hidden or cannot be easily interpreted due to the inherently complex geometry of tokamaks.

1.5 This thesis & Research question

In previous sections, the background related to the topic of this thesis was outlined. In this section, we summarise our motivations and formulate the main goals of this thesis work. After that, a "manual" on how to read this thesis is provided.

As stated in section 1.3.3, plasma detachment is needed to mitigate both power and particle fluxes arriving at the plasma facing components in ITER and next step nuclear fusion devices. The detached, near target plasma state expected in ITER is characterised by relatively low, sub 5 eV electron temperatures and densities of around 10^{20} m^{-3}. The presence of the wall acts as a source of neutral particles which in turn interact with the plasma. Additionally, at very low temperatures, below 1 eV, plasma recombination in the volume is expected to occur. This means that we are no longer dealing with pure plasma physics, but rather a coupled plasma-neutral feedback system. This illustrates that edge and divertor physics is complex and multi-faceted. Currently, the most useful modelling tools that include as much physics as possible without being computationally untractable are edge transport codes. Codes of this type usually involve a fluid plasma solver coupled to a Monte Carlo code that addresses the dynamics of neutrals. Such codes, and the SOLPS package in particular, have been used to interpret experimental observations and also for predictive modelling of ITER and next step devices [52, 53].This thesis contributes to the edge plasma and divertor physics research in the following way. The aim is to take advantage of the good diagnostic access of a linear device and characterise the plasma beam, and its response to control parameters. The subsequent goal is to set up a commonly used edge transport code in the geometry of the linear device, and try to simulate the performed experiments, and interpret the simulation results. Naturally, comparing the experiments and simulations is also part of the thesis. Ultimately, in the case of discrepancies, we strive to discuss possible missing mechanisms that could explain them.

To be more specific, we attempt to answer the following research questions:

- Can main experimental features of Pilot-PSI be reproduced by using an edge transport code?
- What are the main physical mechanisms causing particle, momentum and power dissipation in the plasmas of Pilot- and Magnum-PSI?
- How important is molecule activated recombination (MAR) in Pilot- and Magnum-PSI in terms of particle removal?
- What implications can be drawn for the understanding of divertor plasmas from this work?

1.5.1 How to read this thesis

This thesis is structured as follows. It is divided into parts I and II. Part I contains the introductory chapter which comes to an end by this section. Next, chapter I.2 describes the linear plasma devices used in the frame of this thesis and also the Soledge2D-Eirene edge transport code. Chapter I.3 an overview of results deemed important is provided. Chapter I.4 summarises the mains findings, with respect to the research questions stated, and gives concluding remarks. In part II, work that has been published in the literature, or in preparation for publication, is provided with minimal amendments, and generally offers more detail than the results in the overview chapter I.3. However, I3 also contains material which was not submitted for publication, yet it is still considered important with respect to the topic of the thesis.

Chapter II.5 contains experimental work from the early days of this thesis, namely background pressure scans and measurements with Thomson scattering and a target Langmuir probe. However, the obtained datasets were used throughout a large part of the thesis. Chapter II.6 describes the first stages of modelling work performed in the frame of this thesis, and can be looked at as a sensitivity study to different refinements of the atomic physics model used in the neutral particle code Eirene. Here, the paramount importance of inclusion of the elastic ion-molecule collisions was clearly identified in the simulations. The next chapter II.7 contains a more thorough interpretation of the simulations results, with detailed breakdown of various particle, momentum and energy loss processes at play, as well as comparison to the experimental data from chapter II.5. The last chapter is about experiments at Magnum-PSI, mainly focused on determination of the sheath heat transmission factor. Moreover, preliminary comparisons between the radiated power from the code and the newly commissioned resistive bolometer diagnostic are shown.

Chapter 2

Experimental setups and modelling tools

2.1 Pilot-PSI

Pilot-PSI [54, 55] was a linear plasma device located at the Dutch Institute of Fundamental Energy Research (DIFFER). A schematic of the device is in Fig. 2.1. It operated until October 2015 and it was the forerunner of the larger Magnum-PSI facility, the flagship linear device for testing materials under ITER-like plasma conditions. However, already Pilot-PSI was extensively used as a plasma irradiation facility as it delivered the required particle and heat fluxes to the target.

Pilot-PSI uses a *cascaded arc source* to generate the plasma [56–60]. This is a wall-stabilised thermal electric arc disharge, a schematic drawing of the source is provided in Fig. 2.2. Under steady state discharge conditions, the source is fed by a constant gas flow rate typically in the range of 1.5 to 10.0 standard liters per minute (slm), resulting in a discharge channel pressure in the range 10^3 -10^4 Pa. Due to the pressure gradient between the source discharge channel and the vessel, the plasma exhausts into the vessel at sonic speeds at the nozzle. The magnetic field is provided by a set of five oil-cooled copper coils, providing a magnetic field of up to 1.6 T. The Ohmic heating of the coils limits the pulse duration to about 10 s when operating at 1.6 T. At a field setting of 0.2 T, the oil cooling of the coils allows for continuous, steady state operation. This property was heavily exploited, for instance during ITER material testing under ultra-high fluences [61].

Ionization fractions close to the source exit are typically 10% [57], i.e. most of the feeding gas is exhausted as neutrals. The power supply is current-regulated and typical discharge currents are 100 - 220 A. Voltages range between 50 and 200 V, depending on the desired current setting, gas flow and working gas type. Available gas species were argon, hydrogen, deuterium, helium and neon. The pressure in the vessel is determined by the pumping and the inflow of the residual neutrals from the source and is typically of the order of several Pa. The plasma beam is terminated at a distance of 56 cm from the nozzle by a solid, actively cooled target, of a diamter of 9 cm. Typical beam width in Pilot-PSI are 1-3 cm, depending on the machine settings (especially the B-field) and

the gas species used.

For completeness, it should be mentioned here that Pilot-PSI also had a capacitor bank, which could be used to sequentially discharge the energy of the capacitors in order to mimick edge localized modes [62–65], a transient event that is present in tokamaks during H-mode operation and is a major concern for the survival and lifetime of plasma facing components [12].

Diagnostics at Pilot-PSI

The key diagnostic was Thomson scattering (TS) which was performed at two axial locations (at z=4 cm and z=54 cm, referred to as "upstream" and "target" locations, respectively) and is particularly suited to measure low temperature plasmas in the range 0.07 eV to 35 eV [66] with a radial spatial resolution of 0.6 cm. The system uses an Nd:YAG laser operating at the second harmonic, 532 nm. The scattered light detection is performed with an image intensifier and an ICCD camera. The system is capable of measuring electron density and temperature profiles of a plasma column of 30 mm in diameter.

In the frame of the experiments presented at later stages of this thesis, a single Langmuir probe was embedded in the target with a collecting area of circular shape and a diameter of 2 mm. The probe area was perpendicular to the magnetic field lines, minimising effects of the magnetic pre-sheath which tend to increase the effective collection area of the probe, especially at low grazing angles of the magnetic field [67]. Optical emission spectroscopy was performed at the same location as target TS, i.e. at z=54 cm, in the near UV spectral range 370 - 440 nm, using one channel of an Avantes ULS2048 spectrometer. The line of sight was perpendicular to the beam, focused on the central part.

The voltages on the cathode and the floating cascaded plates are monitored at all times during operation, giving information on the source operation. The background neutral pressure in the vessel, which we will denote as P_n in further parts of this thesis, was measured by a capacitance manometer located at a port about 20 cm radially outwards from the axis of symmetry.

The device also had surface temperature diagnostics, in particular a FLIR SC7500MB high speed infrared camera and a FAR FMPI spectro-pyrometer, however these were not used in the frame of this thesis.

2.2 Magnum-PSI

The Magnum-PSI linear plasma device [49, 68, 69] is the successor of Pilot-PSI. It also uses the same type of cascaded arc source, Fig. 2.3, to generate the plasma. However, Magnum-PSI has a number of major advantages with respect to it. Firstly, it uses a superconducting magnet, which enables continuous operation at a magnetic field of up to 2.5 T, as opposed to the pulsed mode in Pilot-PSI. Secondly, it uses a two-stage differential pumping system to minimise the leakage of residual neutrals from the cascaded arc source to the target exposure chamber [70]. Thirdly, it has a

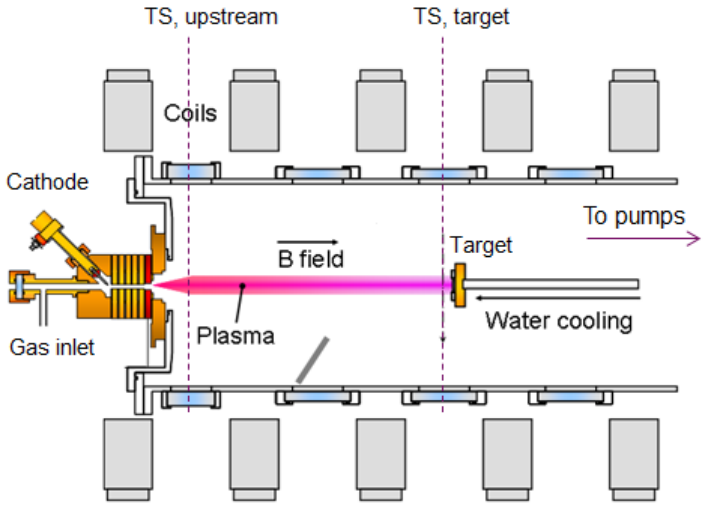

Figure 2.1 – Schematic layout of the Pilot-PSI device, depicting the location of the cascaded arc source, the target, the coils, and the positions of the two beamlines along which Thomson scattering measurements can be performed.

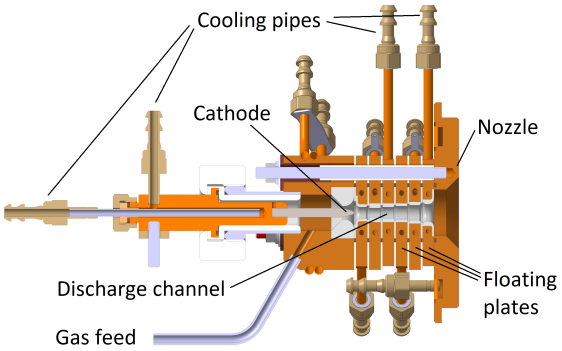

Figure 2.2 – Cross section of the cascaded arc source used in the Pilot-, and Magnum-PSI devices. A negative voltage is supplied to the cathode with respect to the grounded nozzle. This voltage differenece drives the arc discharge. A steady flow of working gas is fed into the source discharge channel, typically between 1 and 10 standard liters per minute.

target analysis chamber (TEAC), where previously exposed targets can be subjected to ion beam analysis techniques without the need to remove them from the vacuum vessel. Finally, the Magnum-PSI target station is designed to be able to move along the machine axis, and also to rotate and tilt, making possible the testing of PFC materials at grazing B-field incidences, as well as exposing up to 5 samples without the need to open the vessel, when the multi-target holder is used. Additionally, the position of the cascaded arc source can also be moved axially. Fig.: 2.3 shows a screenshot from a CAD drawing of Magnum-PSI. The source is located in the left part of the image and generates a plasma which passes through the differentially pumped vacuum chambers separated by skimmers before reaching the target. The first chamber is the source chamber, where a large fraction of the residual neutrals coming from the cascaded arc source is pumped away. The second chamber is also called the heating chamber and

offers potential to install an auxiliary heating system. The third one is the target chamber where the actual exposures take place.

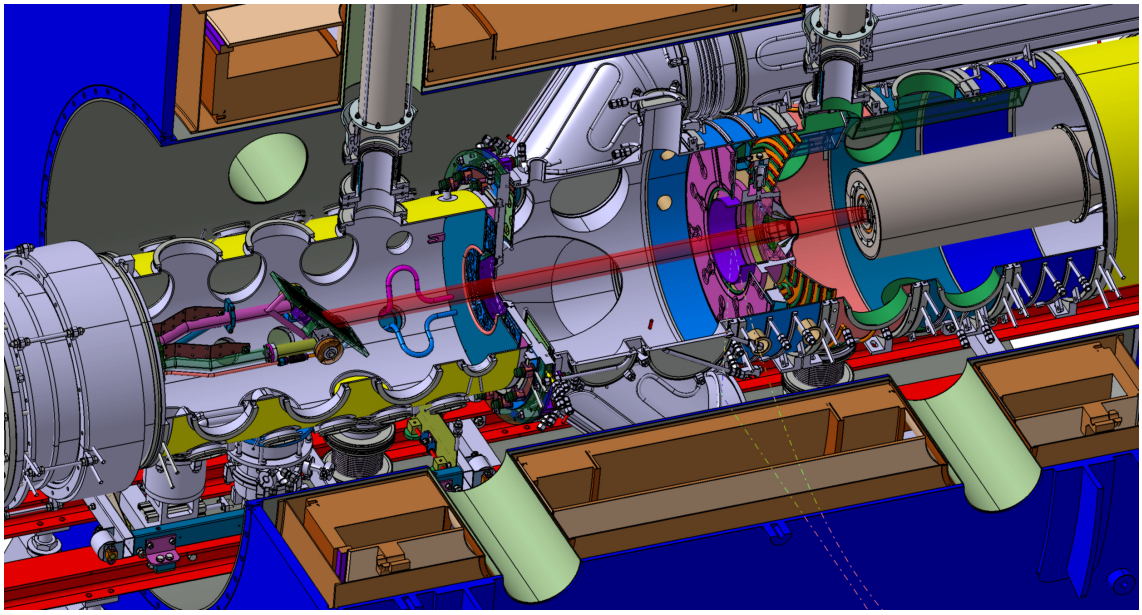

Figure 2.3 – Selection from a CAD drawing of the Magnum-PSI linear plasma device, showing the source chamber (right), heating chamber (middle) and target chamber (left), separated by skimmers.

Due to the fact that the cascaded arc source can be moved in the Z (axial) direction, it cannot be used as a reference point for distance as in the case of Pilot-PSI. Instead, the $Z = 0$ location is defined as the axis of the vacuum port/tube depicted at the top of the target chamber, Fig. 2.3. This tube is the one used for the target chamber Thomson scattering laser beamline. The positive direction is defined as the one going towards the source. The source chamber Thomson tube is, Fig. 2.3, located at Z =1250 mm. The typical position of the source nozzle and target surface is Z =1350 mm and Z =-20 mm, respectively.

Diagnostics at Magnum-PSI

Magnum-PSI has all of the diagnostics which were listed in the previous section for Pilot-PSI. Here, we will focus only on the main differences. As indicated in the previous section, Thomson scattering can also be performed at two locations of the plasma beam, namely in the source chamber and in the target chamber. A calorimetric diagnostic was available, making possible measurements of the total power deposited on the target, from the difference of the incoming and outgoing cooling water temperature and the cooling water flow rate. Additionaly, a new bolometric diagnostic was installed recently [71], based on resistive foils, to measure the radiated power close to the target.

2.3 The SolEdge2D-Eirene transport code

In this thesis, the Soledge2D-Eirene transport code was used to perform the modelling work. Although B2.5-Eunomia [47] is the in-house transport code at the DIFFER institute, the author was stationed at CEA Cadarache at the when this work was to be performed, where the Soledge2D-Eirene [72] code package was developed and maintained. For pragmatic reasons, i.e. accessibility of experts, Soledge2D-Eirene was chosen.

2.3.1 On the role of transport codes

Predictive modelling of divertor operation for ITER and next step devices relies heavily on the use of edge plasma transport codes, which involve a large variety of physics happening on different scales, treated with different levels of refinement. Examples of edge plasma suites are SOLPS, SolEdge2D-Eirene, EDGE2D-Eirene, SOLDOR/NEUT2D, UEDGE. Typically, at the heart of an edge plasma suite lies a fluid code for the plasma (electrons, bulk and impurity ions), coupled to a Monte-Carlo code for neutral particles. On top of this, other physics models, principally treating the details of plasma surface interactions are available in the codes as add-ons. For instance, in the case of Soledge2D-Eirene, there is a model for sputtering based on Bohdansky [73, 74], a sheath model based on results of a PIC code [75]. Next, angular distribution for reflected particles can be taken from tabulated output of the TRIM code [76]. Moreover, a PFC surface temperature model [77] in combination with a model for desorption [78] is under development in order to treat the recycling self-consistently. In view of the shear amount of sub-models involved, each with its unknown parameters ("knobs"), it is clear that a typical edge plasma suite is not a high-fidelity model, but rather a *code experiment*.

The overwhelming complexity of transport codes can evoke a sense of their completeness and an authority of obtained results. This is however misleading given all the uncertainties in the inputs. Despite of this, edge transport codes are still regarded as useful, as they are perfectly suited to do *book keeping* tasks, by which we mean keeping track of where particles, momentum and heat go in a the realistic 2-D geometry (this would be impractical and cumbersome using simple analytical models). To summarise, transport codes themselves cannot reduce their own uncertainties, but they can help us to make use of the limited information that we already have [23].

In view of improving predictive capabilities of edge plasma suites, it is essential to check how well existing experiments can be reproduced. Recently, code-experiment comparisons were performed for several tokamaks and edge plasma suites, e.g. [79–81]. However, as a general feature, the combination of uncertainties in magnetic reconstruction and the steepness of gradients in the tokamak edge plasma render comparison with modelling difficult. Here, we can take advantage of the simple magnetic configuration and cylindrical symmetry of Pilot-PSI, and the diagnostic accessibility.

2.3.2 The Soledge2D fluid code

The SolEdge2D-Eirene fluid code [72] was developed for two main purposes: (a) to provide a testbed for determining the potential of numerical schemes that could be used in the more complete, 3D turbulence code TOKAM3X [82,83] and (b) to provide modelling support to the new WEST tokamak [84,85]. The code essentially solves the same Braginskii-type equations on a 2-D grid aligned with the magnetic flux tube, so as do similar codes like B2 and EDGE2D but relying on a different numerical scheme. An initial condition is evolved in time until a steady states solution is reached. One significant difference lies in the implementation of the boundary conditions at the wall: Soledge2D uses an immersed boundary condition technique called the penalisation technique [86–89]. This makes it possible to simulate the plasma just up to the first wall, which is not necessarily aligned with the simulation grid. Penalisation is a technique in which the equations are solved also in the wall, however within the wall, large sink terms are defined on the right hand side of the equations which mimick the strong sink action due to surface recombination at the wall. This approach naturally recovers the Bohm condition $|M_\parallel| \geq 1$. The code solves equations for conservation of mass, momentum, ion and electron energy. Only two species, singly charged ions and electrons are considered here, i.e. $n_i = n_e = n$. The particular equations used in the code setup in the framework of this thesis will be listed in the following.

(i) Particle conservation:

$$\frac{\partial n}{\partial t} + \vec{\nabla} \cdot (n u_\parallel \vec{b}) = \vec{\nabla} \cdot (D \vec{\nabla}_\perp n) + S_n^{(N)} + S_n^{(\mathrm{ext})} \tag{2.1}$$

(ii) Momentum conservation:

$$\frac{\partial n u_\parallel}{\partial t} + \vec{\nabla} \cdot (n u_\parallel^2 \vec{b}) + \nabla_\parallel \left(n k_B \frac{T_e + T_i}{m_i} \right) = \vec{\nabla} \cdot (\nu \vec{\nabla}_\perp n u_\parallel) + S_G^{(N)} \tag{2.2}$$

(iii) Ion energy conservation:

$$\begin{aligned} &\frac{\partial}{\partial t} \left(\frac{3}{2} k_B n T_i + \frac{1}{2} m_i u_\parallel^2 \right) + \vec{\nabla} \cdot \left(\frac{5}{2} k_B n u_\parallel T_i \vec{b} + \frac{1}{2} m_i n u_\parallel^3 \vec{b} + \kappa_i^0 T_i^{5/2} \nabla_\parallel T_i \vec{b} \right) + u_\parallel \nabla_\parallel (n k_B T_e) = \\ &\vec{\nabla} \cdot \left(\left(\frac{3}{2} k_B T_i + \frac{1}{2} m_i u_\parallel^2 \right) D \vec{\nabla}_\perp n + \frac{3}{2} k_B \chi_\alpha n \vec{\nabla}_\perp T_i + \nu n \vec{\nabla}_\perp \left(\frac{1}{2} m_i u_\parallel^2 \right) \right) + Q_{ei}^{(c)} + S_{E,i}^{(N)} + S_{E,i}^{(\mathrm{ext})} \end{aligned} \tag{2.3}$$

(iv) Electron energy conservation:

$$\begin{aligned} \frac{\partial}{\partial t} \left(\frac{3}{2} k_B n T_e \right) + \vec{\nabla} \cdot \left(\frac{5}{2} k_B n u_\parallel T_e \vec{b} + \kappa_e^0 T_e^{5/2} \nabla_\parallel T_e \vec{b} \right) - u_\parallel \nabla_\parallel (n k_B T_e) = \\ + \frac{3}{2} k_B \vec{\nabla} \cdot \left(T_e D \vec{\nabla}_\perp n + \chi_\alpha n \vec{\nabla}_\perp T_e \right) - Q_{ei}^{(c)} + S_{E,e}^{(N)} + S_{E,e}^{(\mathrm{ext})} \end{aligned} \tag{2.4}$$

where n is the plasma density ($n = n_e = n_i$), T_i and T_e are the ion and electron tempertures, respectively, $u_\parallel$ is the plasma fluid velocity parallel to the magnetic field, $\vec{b}$ is the unit vector in the direction of the magnetic field and the operators are defined in the following way: $\nabla_\parallel = \vec{b}\cdot\vec{\nabla}$ and $\vec{\nabla}_\perp = \vec{\nabla} - \vec{b}\nabla_\parallel$. The term Q^c_{ei} represents the coupling between electrons and ions. The anomalous perpendicular transport coefficients D, ν and χ_α are for density, parallel momentum and temperature, respectively, and are uniform in the whole simulation domain throughout this work. The terms $S^{(N)}_n$, $S^{(N)}_G$ and $S^{(N)}_{E,\alpha}$ are sources of particles, parallel momentum and energy due to neutral particles, respectively. These source terms due to neutrals are calculated by the kinetic Monte-Carlo (MC) code Eirene [90], which will be described in the following section.

2.3.3 The Eirene neutral Monte-Carlo code

Neutral particles are ubiquitous in divertor plasmas as well as linear plasma devices, simply because of the recycling process described in section 1.3.1, which arises from the presence of solid surfaces. However, the neutral mean free path in the plasma is not necessarily shorter than typical gradient lengths of the plasma, i.e. neutral atoms and molecules can "see" changing plasma conditions when passing through the plasma. Therefore, the usual way to approach neutrals in a transport code is by solving the neutral kinetic equation using a Monte-Carlo (MC) approach[1]. This is done in the neutral MC code Eirene [90], a code extensively used in the magnetic fusion community which was coupled to a number of plasma fluid solvers, e.g. B2 (together forming the SOLPS package), EDGE2D, the 3D fluid EMC3 code and of course Soledge2D as well. An attempt to outline the approach used in Eirene is provided in the following. For a more detailed and rigorous introduction, the reader is referred to the Eirene manual, readily accessible at www.eirene.de.

We start from the force-free Boltzmann kinetic equation

$$\frac{\partial f(\mathbf{r},\mathbf{v},t)}{\partial t} + \mathbf{v}\cdot\vec{\nabla} f(\mathbf{r},\mathbf{v},t) = \iiint \sigma(\mathbf{v}',\mathbf{V}';\mathbf{v},\mathbf{V})||\mathbf{v}'-\mathbf{V}'||f(\mathbf{v}')f_b(\mathbf{V}')\mathrm{d}\mathbf{v}'\mathrm{d}\mathbf{V}'\mathrm{d}\mathbf{V} - \iiint \sigma(\mathbf{v},\mathbf{V};\mathbf{v}',\mathbf{V}')||\mathbf{v}-\mathbf{V}||f(\mathbf{v})f_b(\mathbf{V})\mathrm{d}\mathbf{v}'\mathrm{d}\mathbf{V}'\mathrm{d}\mathbf{V} + \mathrm{Q}(\mathbf{r},\mathbf{v},\mathrm{t}), \quad (2.5)$$

where f is the distribution function of the neutral particles of interest (we will refer to them as *test particles* from now) and f_b is the distribution of "background" particles (in our case, this is the plasma), σ is the collisional cross section of a binary collisional process and Q is an external particle source term (in our case, this could correspond to neutrals born from surface plasma recombination). The velocity pairs $\mathbf{v}', \mathbf{V}'$ and $\mathbf{v}, \mathbf{V}$ correspond to test particle and background particle velocities prior (primed variables) and after (unprimed variables) a collision. In principle, each species of interest, i.e. atoms, molecules etc. has such an equation. The first integral describes

[1]Neutral fluid models are also employed frequently, their advantage being reduced demands on computational resources, overall simplicity and absence of statistical noise. For instance, UEDGE [91] uses a fluid neutral model.

the total rate of collisional transitions into the velocity space interval $[\mathbf{v}, \mathbf{v} + \mathrm{d}\mathbf{v}]$ for the test particles. The second integral describes the total collisional loss rate of test particles from the phase space interval $[\mathbf{v}, \mathbf{v} + \mathrm{d}\mathbf{v}]$. If we assume a fixed background plasma and no self-collisions and also no cross-collisions (i.e. collisions between species for which the Boltzmann equation is solved), then the equation can be linearised, which is a major simplification to the problem (in dense divertor plasmas however, neutral-neutral collisions can become important, for instance). Thus, in the second term on the R.H.S. $f(\mathbf{v})$ can be taken out in front of the integral, and we end up having (apart from dependence on individual velocity $\mathbf{v}$ of test particle species) a term that is only dependent on cross sections averaged over velocity distributions of background particles. The latter is usually referred to as a *reaction rate* and in the case of Maxwellian distributions can be characterised as functions of the local temperature.

In practice it is usually not necessary to know the distribution function $f(\mathbf{r}, \mathbf{v}, t)$ itself but it is of interest to calculate some moments of this function, like density, temperature etc. For this one may take advantage of the Monte Carlo method, in which a stochastic process is is constructed in such a way that the solution of equation 2.5 is the expectation value of a random variable. Such a variable is called an unbiased estimator. An MC solver like Eirene simulates a number of particle trajectories, and based on these trajectories, calculates the quantities of interest. Thus, an MC code requires a recipe to sample these trajectories and estimators of the moments of interest of $f(\mathbf{r}, \mathbf{v}, t)$ (for instance, neutral densities and temperatures) that tend to the true values of the quantities of intereset as the number of trajectories is increased.

Atomic physics model

The species considered in Eirene are hydrogen atoms H and molecules H_2 and H_2^+ molecular ions. The atomic physics model used in Eirene in the frame of this thesis[2] is depicted in Tab. 2.1. This model is the same as the model described in [92], which was used extensively in predictive simulations for ITER [93], however, in simulations presented later in this thesis, neutral-neutral collisions and radiation opacity were not included. Including molecular processes is critical for reproduction of basic experimental features in Pilot- and Magnum-PSI. A plot of selected rate coefficients for reactions in Tab. 2.1 is shown in Fig. 2.4 in order to show which processes become dominant in which temperature regions for a given density. We point out here the importance of the ion conversion process (7) that is the dominant contributor to the formation of H_2^+ molecular ions in the T_e range of interest. The molecular ion can then either dissociate into a main ion and an atom, reaction (9), or dissociatively recombine into two atoms. The latter process, including the preceding ion conversion, is termed molecular assisted recombination (MAR). The third possible reaction including H_2^+, dissociative ionisation (8) is comparatively negligible in the T_e range of interest.

[2]It should be noted that also a simpler version of this model was used to as a sensitivity study.

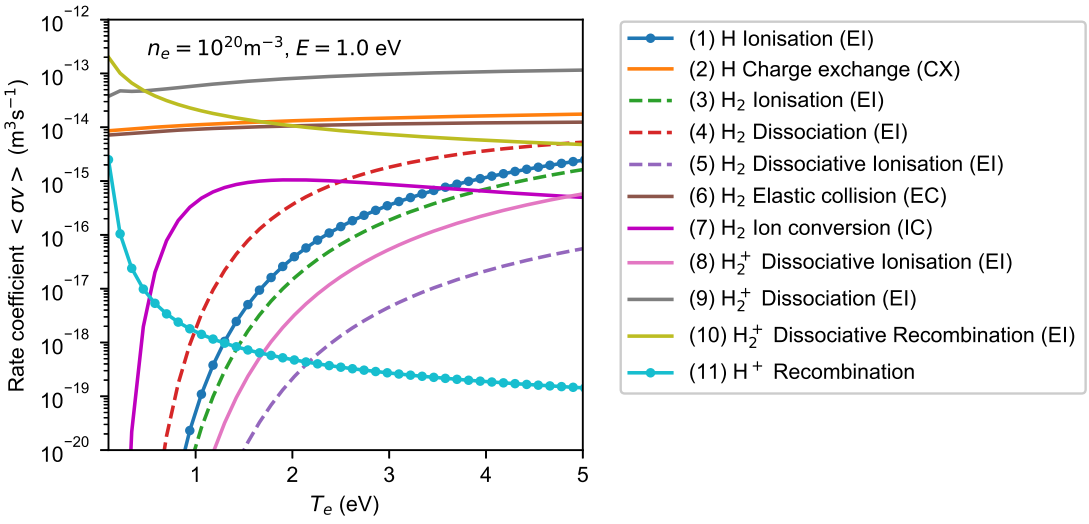

Figure 2.4 – Plots of rate coefficients for different processes used in the atomic physics model in Eirene as a function of T_e and for n_e=10^{20} m^{-3} in case of density dependent rate coefficients (processes (1), (3-5) and (8-11)) and for a relative energy of $E = 1$ eV for reactions (2) and (6)). The reaction numbering in the legend of the figure is the same as in Tab. 2.1. The rate coefficients are taken from the AMJUEL database (available from www.eirene.de) .

2.3.4 Basics of coupling Soledge2D with Eirene

The quantities calculated by Eirene enter the Soledge2D simulations via the source terms due to neutrals, on the R.H.S. of equations 2.1, 2.2, 2.3 and 2.4. After receiving these quantities, the plasma is evolved for a certain number of timesteps (i.e. iterations), usually more than 50. This process is called short-cycling [94]. However, there is a limit up to which the number of short cycles can be increased. This limit is determined by the ratio of the time that the simulation spends short-cycling τ_c (in the sense $\tau_c = k\Delta t$, where k is the number of short-cycles and Δt is the Soledge2D timestep) to the time scale of characteristic evolution of the total particle content in the simulation domain [95]. Then, the newly calculated plasma background is handed over the Eirene again which calculates the neutral particle moments again, and so forth. This procedure is repeated until a steady state is achieved. However, as Eirene is a MC code, the solution provided is only accurate up to the statistical noise. Therefore, one can never reach a true steady state, but rather the solution of the coupled codes tends towards a *statistically stationary state*, SSS[3].

In view of the needs of later parts of this thesis, it is useful to break down the calculation of the source terms due to neutrals as they appear in the Soledge2D equations 2.1, 2.2, 2.3 and 2.4. Provided that we have the moments of neutral species and molecular ions (the densities especially) at our disposal from Eirene, the source terms are the following:

[3]It should be pointed out that oscillatory solutions have been also been found as results of transport code simulations [96, 97] and also predicted theoretically [98].

Table 2.1 – List of atomic and molecular physics processes used in Eirene.

#	Reaction	Event type
(1)	$H + e \rightarrow H^+ + 2e$	Electron impact ionization
(2)	$H + H^+ \rightarrow H^+ + H$	Charge exchange
(3)	$H_2 + e \rightarrow H_2^+ + 2e$	Electron impact ionization
(4)	$H_2 + e \rightarrow 2H + e$	Dissociation
(5)	$H_2 + e \rightarrow H + H^+ + 2e$	Dissociative ionization
(6)	$H_2 + H^+ \rightarrow H_2 + H^+$	Elastic collision
(7)	$H_2 + H^+ \rightarrow H_2^+ + H$	Ion conversion
(8)	$H_2^+ + e \rightarrow H^+ + H^+ + 2e$	Dissociative ionization
(9)	$H_2^+ + e \rightarrow H^+ + H + e$	Dissociation
(10)	$H_2^+ + e \rightarrow 2H$	Dissociative recombination
(11)	$H^+ + e \rightarrow H$	Electron-ion recombination

- Particle source $S_n^{(\mathrm{N})}$

$$\begin{aligned} S_n^{(\mathrm{N})} =& n_e n_{\mathrm{H}} \langle \sigma v \rangle^{(1)} + n_e n_{\mathrm{H}_2} \langle \sigma v \rangle^{(5)} - n_e n_{\mathrm{H}_2} \langle \sigma v \rangle^{(7)} \\ &+ 2 n_e n_{\mathrm{H}_2^+} \langle \sigma v \rangle^{(8)} + n_e n_{\mathrm{H}_2^+} \langle \sigma v \rangle^{(9)} - n_e^2 \langle \sigma v \rangle^{(11)}, \end{aligned} \tag{2.6}$$

- Momentum source $S_{\mathrm{G}}^{(\mathrm{N})}$

$$\begin{aligned} S_{\mathrm{G}}^{(\mathrm{N})} =& m_i n_e n_{\mathrm{H}} \langle \sigma v \rangle^{(1)} v_{\mathrm{H}} + m_i n_e n_{\mathrm{H}} \langle \sigma v \rangle^{(2)} (v_{\mathrm{H}} - u_{\parallel}) + m_i n_e n_{\mathrm{H}_2} \langle \sigma v \rangle^{(5)} \frac{v_{\mathrm{H}_2}}{2} \\ &+ m_i n_e n_{\mathrm{H}_2} \langle \sigma v \rangle^{(6)} (v_{\mathrm{H}_2} - u_{\parallel}) - m_i n_e n_{\mathrm{H}_2} \langle \sigma v \rangle^{(7)} u_{\parallel} + m_i n_e n_{\mathrm{H}_2^+} \langle \sigma v \rangle^{(8)} v_{\mathrm{H}_2^+} \\ &+ m_i n_e n_{\mathrm{H}_2^+} \langle \sigma v \rangle^{(9)} \frac{v_{\mathrm{H}_2^+}}{2} - m_i n_e^2 \langle \sigma v \rangle^{(11)} u_{\parallel} \end{aligned} \tag{2.7}$$

- Ion energy source $S_{\mathrm{E,i}}^{(\mathrm{N})}$

$$\begin{aligned} S_{E,i}^{(N)} =& + n_e n_{\mathrm{H}} \langle \sigma v \rangle^{(1)} E_{\mathrm{H}} + n_e n_{\mathrm{H}} \langle \sigma v \rangle^{(2)} (E_{\mathrm{H}} - E_i) + n_e n_{\mathrm{H}_2} \langle \sigma v \rangle^{(5)} \frac{E_{\mathrm{H}_2}}{2} \\ &+ n_e n_{\mathrm{H}_2} \langle \sigma v \rangle^{(6)} (E_{\mathrm{H}_2} - E_i) + n_e n_{\mathrm{H}_2} \langle \sigma v \rangle^{(7)} E_i + n_e n_{\mathrm{H}_2^+} \langle \sigma v \rangle^{(8)} E_{\mathrm{H}_2^+} \\ &+ n_e n_{\mathrm{H}_2^+} \langle \sigma v \rangle^{(9)} \frac{E_{\mathrm{H}_2^+}}{2} - n_e^2 \langle \sigma v \rangle^{(11)} E_i, \end{aligned} \tag{2.8}$$

- Electron energy source $S_{\mathrm{E,e}}^{(\mathrm{N})}$

$$\begin{aligned} S_{E,e}^{(N)} =& - \chi^{(1)} n_e n_{\mathrm{H}} \langle \sigma v \rangle^{(1)} - \chi^{(4)} n_e n_{\mathrm{H}_2} \langle \sigma v \rangle^{(4)} - \chi^{(5)} n_e n_{\mathrm{H}_2} \langle \sigma v \rangle^{(5)} \\ &- \chi^{(3)} n_e n_{\mathrm{H}_2} \langle \sigma v \rangle^{(3)} - \chi^{(8)} n_e n_{\mathrm{H}_2^+} \langle \sigma v \rangle^{(8)} - \chi^{(9)} n_e n_{\mathrm{H}_2^+} \langle \sigma v \rangle^{(9)} \\ &- n_e^2 \langle E \sigma v \rangle^{(11)} - n_e n_{\mathrm{H}} \Big(\langle E \sigma v \rangle^{(1)} - \chi_{\mathrm{ion}}^{(1)} \langle \sigma v \rangle_{\mathrm{ion}}^{(1)} \Big), \end{aligned} \tag{2.9}$$

Table 2.2 – List of potential energies (in eV) appearing in the electron energy loss terms of equation 2.9. The number in the superscript refers to the label of the reaction in Tab. 2.1 to which the potential is associated

$\chi^{(1)}$	$\chi^{(4)}$	$\chi^{(5)}$	$\chi^{(3)}$	$\chi^{(8)}$	$\chi^{(9)}$
13.6	10.5	28.1	15.4	10.5	25.5

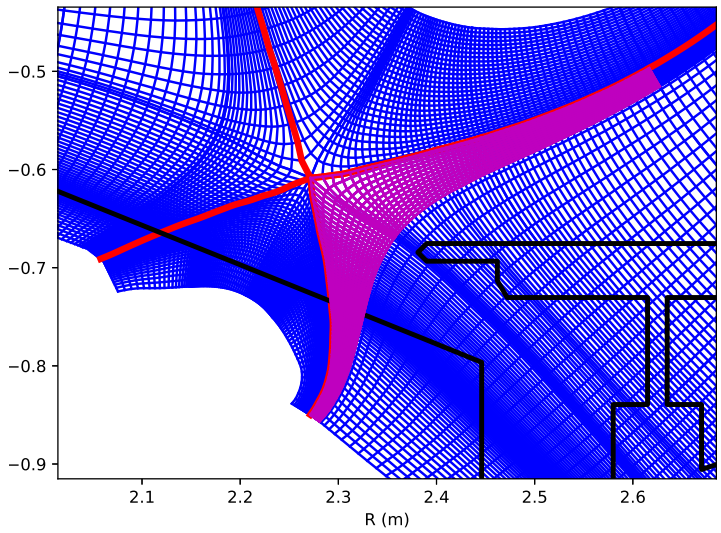

Figure 2.5 – Close-up of a the Soledge2D grid in the divertor region of the WEST tokamak. The grid is indicated in blue, the magnetic separatrix in red and the black line corresponds to the wall contour. The area highlighted in magenta is a selection of the grid which is in fact topologically equivalent with a linear device.

where n_e, n_H and n_{H_2} are the electron, neutral atom and neutral molecule densities, $\langle\sigma v\rangle^{(\mathrm{i})}$ are rate coefficients in $\mathrm{m^3 s^{-1}}$ and the upper index (i) denotes the process they are associated to from Tab. 2.1. The energies denoted $E_i, E_{\mathrm{H}}, E_{\mathrm{H_2}}, E_{\mathrm{H_2^+}}$ are mean kinetic energies in of ions, atoms, molecules and molecular ions in the laboratory frame, which is, for molecules for instance, $E_{\mathrm{H_2}} = \frac{3}{2}k_B T_{\mathrm{H_2}} + \frac{1}{2}m_{\mathrm{H_2}}\mathbf{v}^2_{\mathrm{H_2}}$. The values $\chi^{(\mathrm{i})}$ are the required potential energies associated with processes from Tab. 2.1, e.g. for the H ionisation reaction (1) this energy is equal to the ionisation potential, $\chi^{(1)}$= 13.6 eV. The values of the other potentials are listed in Tab. 2.2. The quantities of the form $\langle E\sigma v\rangle^{(\mathrm{i})}$ are total energy loss rate coefficients associated with a certain process or set of processes. These loss rates are obtained from collisional radiative modelling and are readily available in the AMJUEL database (www.eirene.de). In this case, we have the energy loss rate for electron-ion recombination (penultimate term in equation 2.9), and a term associated with line radiation by atomic hydrogen, which corresponds to the last term $-n_e n_{\mathrm{H}}\Big(\langle E\sigma v\rangle^{(1)} - \chi^{(1)}_{\mathrm{ion}}\langle\sigma v\rangle^{(1)}_{\mathrm{ion}}\Big)$. Since the energy weighted rate coefficient $\langle E\sigma v\rangle^{(1)}$ already includes the losses due to ionisation, we have to subtract them from total energy loss since we have already included net ionisation losses in equation 2.9 (1st term). Therefore, the last term in equation 2.9 represents the net electron energy loss due to hydrogenic radiation.

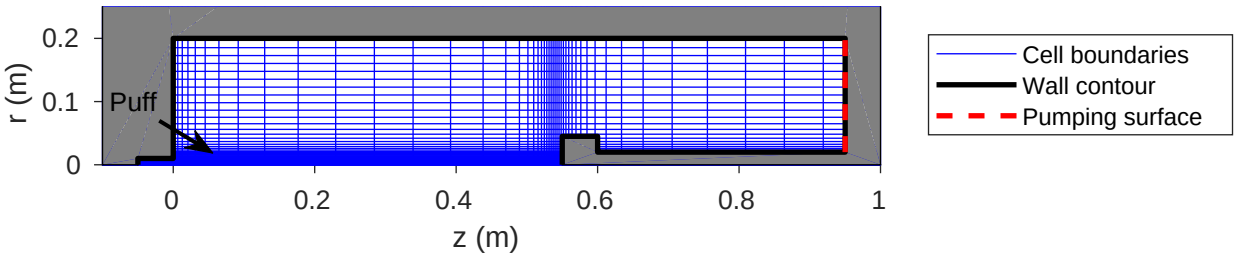

Figure 2.6 – The Pilot-PSI non-uniform grid used in the Soledge2D-Eirene simulations. The source nozzle is located on the left side of the figure, at $z = 0$ m, while the target is on the right, at $z = 0.55$ m..

2.3.5 Application to a linear device

The geometry of the linear plasma device may seem very different from a tokamak, however they have common aspects, which enable to create a field-aligned grid that the code can directly use. In Fig. 2.5 a Soledge2D grid is depicted. The grid for the linear device can be regarded as a subspace of a tokamak grid, and the selection in highlighted in magenta in Fig. 2.5. It is in fact topologically equivalent to a scrape-off layer with no toroidal field, i.e. the plasma is simulated up to the axis of symmetry. In this sense, the axial magnetic field of the linear device corresponds to the poloidal magnetic field of a tokamak.

The grid used in the simulations of Pilot-PSI is depicted in Fig. 2.6. Additionally, a variable grid density is used in order to provide high resolution in the plasma beam and close to the walls, while in areas of less interest the cells are larger, to save computational time.

It is beyond the scope of this thesis to model the cascaded arc discharge self-consistently. This would require inclusion of the electric currents and drifts in the simulations, as well as thermionic emission from the hot cathode. Instead, the principal focus of this work is in the interaction of the plasma beam with the surrounding neutral gas. As a result, the plasma particle and power sources are directly prescribed as external volumetric source terms $S_n^{(ext)}, S_G^{(ext)}, S_{E,i}^{(ext)}, S_{E,e}^{(ext)}$ in the Soledge2D equations 2.1 through 2.4. The shape and magnitude of these is defined to match Thomson scattering profiles measured close to the source. For instance, the external volumetric source terms for the plasma ion/electron source has the form of a Gaussian function in both r and z directions:

$$S_n^{(ext)}(r,z) = \frac{S_n^{(ext,tot)}}{C} \exp\Big(-(r-r_0)^2/\lambda_r^2 \Big) \exp\Big(-(z-z_0)^2/\lambda_z^2 \Big), \tag{2.10}$$

where r_0, z_0 are the positions of the profile maxima, λ_r, λ_z are the profile widths, C is a normalization constant such that the volume integral over the simulation domain be equal to the total number of injected particles, i.e. $\int_V S_n^{(ext)} \mathrm{d}V = S_n^{(ext,tot)}$. A similar external source term is also defined for the energy source on electrons and ions, $S_{Ee}^{(ext)}$ and $S_{Ei}^{(ext)}$, respectively. The position and spatial extent of the external volumetric

source terms was chosen such that it stays well within the small area of the cascaded arc source.

It should be noted that a stagnated plasma is injected, which then accelerates towards the target due to the pressure gradient. Therefore, we do not control the velocity at the cascaded arc nozzle, and this is a result of the code rather than a boundary condition. Plasma sources of this type are characterized by a sonic velocity at the nozzle, i.e. [99]. Our simple approach to model the source does not recover the sonic velocity at the nozzle, and the plasma remains sub-sonic throughout the whole beam, up to sheath edge in front of the target, where the Bohm boundary condition is recovered. However, in [54] it has been shown that in a magnetized cascaded arc plasma, the flow velocity was 3.5 km/s already 4 cm downstream from the nozzle (i.e. at the upstream TS location), i.e. already strongly sub-sonic for thermal plasmas with $T_e \sim 1$ eV. In this work, we are only interested the plasma behaviour downstream from the source.

The interaction of plasma and neutrals is treated by the Eirene code [90]. In Pilot and Magnum-PSI, neutrals enter the system by three channels 1) the residual gas entering the vessel from the cascaded arc source 2) main ion recycling, e.g. at the target and 3) recombination in the volume. The latter two are calculated self-consistently by Eirene, while the constant gas inflow rate is simulated as a constant puff of H_2 at ambient temperature (0.03 eV) at the location depicted in Fig. 2.6 in the case of Pilot-PSI. In the experiment, this is an externally controllable quantity, and the value is chosen such that the sum of the total puff rate and total plasma injection rate (i.e. $S_n^{(ext,tot)}$ from eq. 2.10) equals the gas feed rate to the cascaded arc in the experiment, in a mass-sense. The recycling coefficient at the plasma-wall interface is set to unity throughout all the simulations presented here, except for two locations: The pumping surface is located at the back end of the vessel, Fig. 2.6, where one can specify an absorption probability (albedo) for neutral particles. The absorption probability is set to match measurements of the neutral pressure in the vacuum vessel, typically in the range of several Pa. The second region where the recycling coefficient is not unity is the source region, where it is set to 0, as source behaviour within the cascaded arc is not modelled self-consistently, but rather tuned to match upstream experimental TS profiles.

Chapter 3

Overview of results

In the following sections, the a comprehensive overview of the main results obtained in the course of this thesis work will be presented. In most cases, the results are simplified and for a more detailed analysis the reader is referred to part B of this thesis. On the other hand, supporting material that has not been published or submitted for publication also appears in this overview.

3.1 Plasma rarefaction measurements at Pilot-PSI

In order to investigate the interaction of the ITER-relevant plasma beam of Pilot-PSI and the neutral gas, a background pressure P_n scan was performed by changing the pumping speed. The magnetic field used in these experiments was B=0.2 T. The species used was hydrogen. The schematic layout of the device is depicted in Fig. 2.1. P_n scans were performed by changing the pumping speed for two values of gas flow and discharge current settings. The range of achieved P_n varies from 2.4 Pa to 12.6 Pa. Fig. 3.1 shows the target ion flux measured by a Langmuir probe (LP) and estimated from Thomson scattering (TS) measurements 2 cm in front of the target, for different discharge settings of the cascaded arc source. It can be seen that the ion flux is reduced by more than two orders of magnitude in the course of this P_n variation[1]. Additionally, results of the two diagnostics are in good agreement, which is shown in Fig. 3.1.

Plasma detachment in tokamaks is manifested by breaching of the plasma pressure balance on the open magnetic flux surfaces of the SOL [24]. These pressure gradients appear when the target T_e is low enough for momentum-removal processes to start occurring, typically for $T_e < 10$ eV [101]. In this section, the upstream pressure is compared to the target pressure via the introduction of a pressure loss factor, defined by $f_{\text{loss}} = p_u/p_t$ where p_u and p_t are the upstream and target total plasma pressures (static+dynamic), respectively. Such ratios, or their inverse equivalents, are commonly introduced in two-point models of tokamak SOLs, e.g. [102, 103].

The measurements clearly demonstrate that the f_{loss} is correlated to the P_n in the vessel, indicating the importance of plasma-neutral interaction processes (including

[1]The exact procedure on how the fluxes and associated errorbars are calculated is described in section 5.4.4 or alternatively in [100].

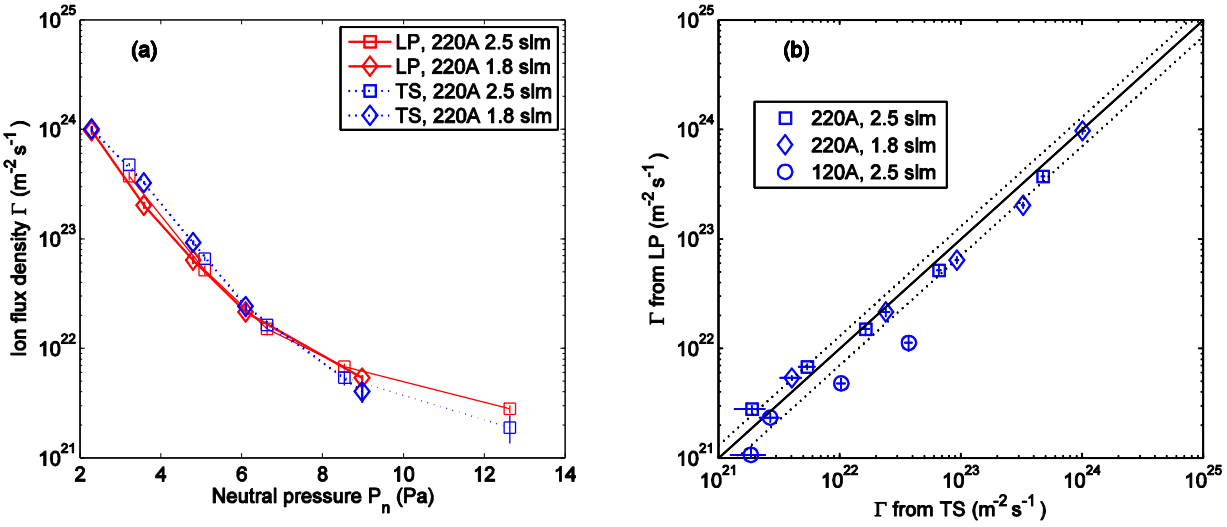

Figure 3.1 – Comparison of the ion fluxes from the LP and TS displayed as a P_n scan (a) and as a direct comparison (b) for different source settings from Table 1. In (a), the 120A case is omitted in order to maintain clarity of the figure, nevertheless showing the same trend. In (b), the solid line indicates equality while the dashed lines represent 30% deviation from equality. In the legend, 'LP' means Langmuir probe, 'TS' means Thomson scattering, and the numbers are either source discharge current (220A, for instance) or source gas flow (2.5 slm, for instance).

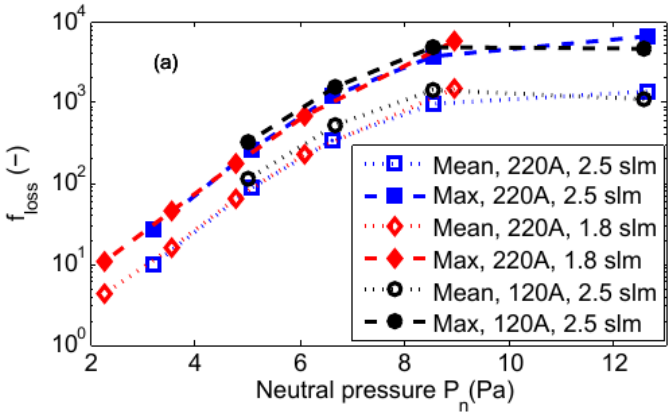

Figure 3.2 – Pressure loss factor calculated from plasma pressure as a function of P_n (a) and the target temperature for the different discharge conditions, source current in amps and gas flow in slm, respectively. 'Mean' denotes the mean value of the profile, 'Max' denotes the value taken at the center of the profile, i.e. at $R = 0$.

interactions with H_2 molecules), as can be seen in figures 3.2 and 3.3. However, it is important to point out again that the build-up of P_n in the vessel is not determined by the recycling and recombining neutrals, as in a tokamak, but by the influx of residual neutrals from the source, meaning that extrapolation to tokamaks has to be done carefully. On the other hand, this enables to decouple P_n from the target flux Γ and it effectively becomes a control parameter, while in tokamaks the two quantities are strongly coupled.

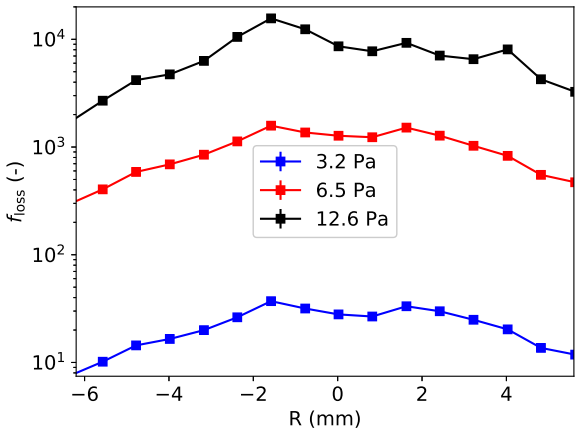

Figure 3.3 – Radial profile of the pressure loss factor calculated from the static plasma pressures based on plasma parameters obtained from Thomson scattering, for three cases of background pressure, listed in the figure legend.

These well controlled experiments motivated us to apply an edge transport code to simulate Pilot-PSI plasmas. Firstly, it can be checked how accurately the code reproduces trends observed experimentally (i.e. code-experiment benchmarking), possibly pointing at additional missing physics in the code. Secondly, the code can possibly indicate which atomic/molecular (or other) processes are responsible for the reduction of power and particle fluxes to the target, i.e. do the *book-keeping* between the various mechanisms that drive flows in the plasma, i.e. ionisation/recombination, parallel and perpendicular transport etc. The following section will focus on modelling of Pilot-PSI using the Soledge2D-Eirene code, interpretation of code results and comparison with the experimental P_n scan presented above.

3.2 Soledge2D-Eirene simulations of Pilot-PSI plasmas

First, we shall provide a typical simulation case where we highlight and interpret the basic features observed.

The reference case is defined by the input parameters in Tab. 3.1, case (a). The absorption coefficient that mimicks the pumping, which we will call the *albedo*[2], was adjusted to match a background pressure of P_n=3.2 Pa. The external source terms were tuned in order to match Thomson scattering measurements close to the source. The resulting upstream ($Z = 4$ cm) radial profiles of n_e and T_e of the reference case simulation are shown in Fig. 3.4 together with the upstream Thomson scattering measurements which were used for the matching. Next, 2-D maps of plasma parameters of the reference case (a) are shown on Fig. 3.5. As a general feature, there is a strong, monotonic axial reduction of all the quantities from upstream towards the target (with

[2]A term borrowed from astrophysics.

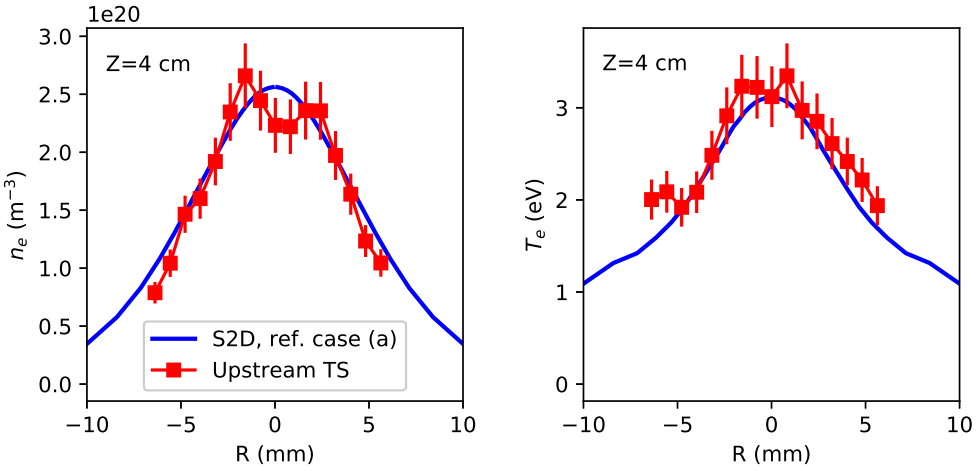

Figure 3.4 – Comparison of upstream n_e, T_e profiles measured by Thomson scattering, 4 cm in front of the cascaded arc source nozzle (red squares) and Soledge2D-Eirene simulation results (blue solid line) for the reference case (a). The match was obtained by adjusting the free parameters of the external volumetric source terms.

the exception of the parallel velocity, which is not monotonic, but decelerates in the usptream region of the beam and then accelerating towards the target again, which is expected from the boundary conditions).The seemingly fast-flowing part of the beam off-axis, occurs an an area where the density is already very low and is therefore not considered of interest. The total plasma pressure is the sum of the static and dynamic components, $P_{\text{tot}} = P_{\text{stat}} + P_{\text{dyn}} = n_i k_B T_i + n_e k_B T_e + n_i c_s^2 M^2$. From the plot of the flux density Γ and total plasma pressure P_{tot}, it may misleadingly seem that the beam is not reaching the target, however, this is just a consequence of the specific geometry and the imposed radial transport. In fact, in the reference case, most of the ion flux from the source plasma is reaching the target. This is shown in Fig. 3.6 (A), where the axial profile of the total, cross-section integrated ion flux density, $\Gamma_{\text{tot}} = \int_0^{2\pi} \int_0^{R_{\text{vess}}} r\Gamma(r) \mathrm{d}r\mathrm{d}\phi$ is plotted (R_{vess} is the radius of the vessel). Γ_{tot} decreases only by about 20%, meaning that there are net sinks of plasma between upstream and target locations, however most of the flux still reaches the target. Instead, the strong reduction in the parallel ion flux density observed in Fig. 3.5 is driven mainly by the radial transport, which is effectively causing broadening of the beam, from about ∼4 mm upstream to ∼ 12 mm at the target.

3.2.1 Sensitivity to radial transport coefficients

Cross field transport is not modelled self-consistently due to its turbulent nature [104], which is observed in tokamaks as well as linear plasma devices [105–108]. Instead, effective, so-called *anomalous* perpendicular transport coefficients are used to account for enhancement due to filamentary/blobby transport are typically used in edge transport code simulations. As these anomalous transport coefficients are free parameters of the model, it is important to check the sensitivity of the results to the choice of

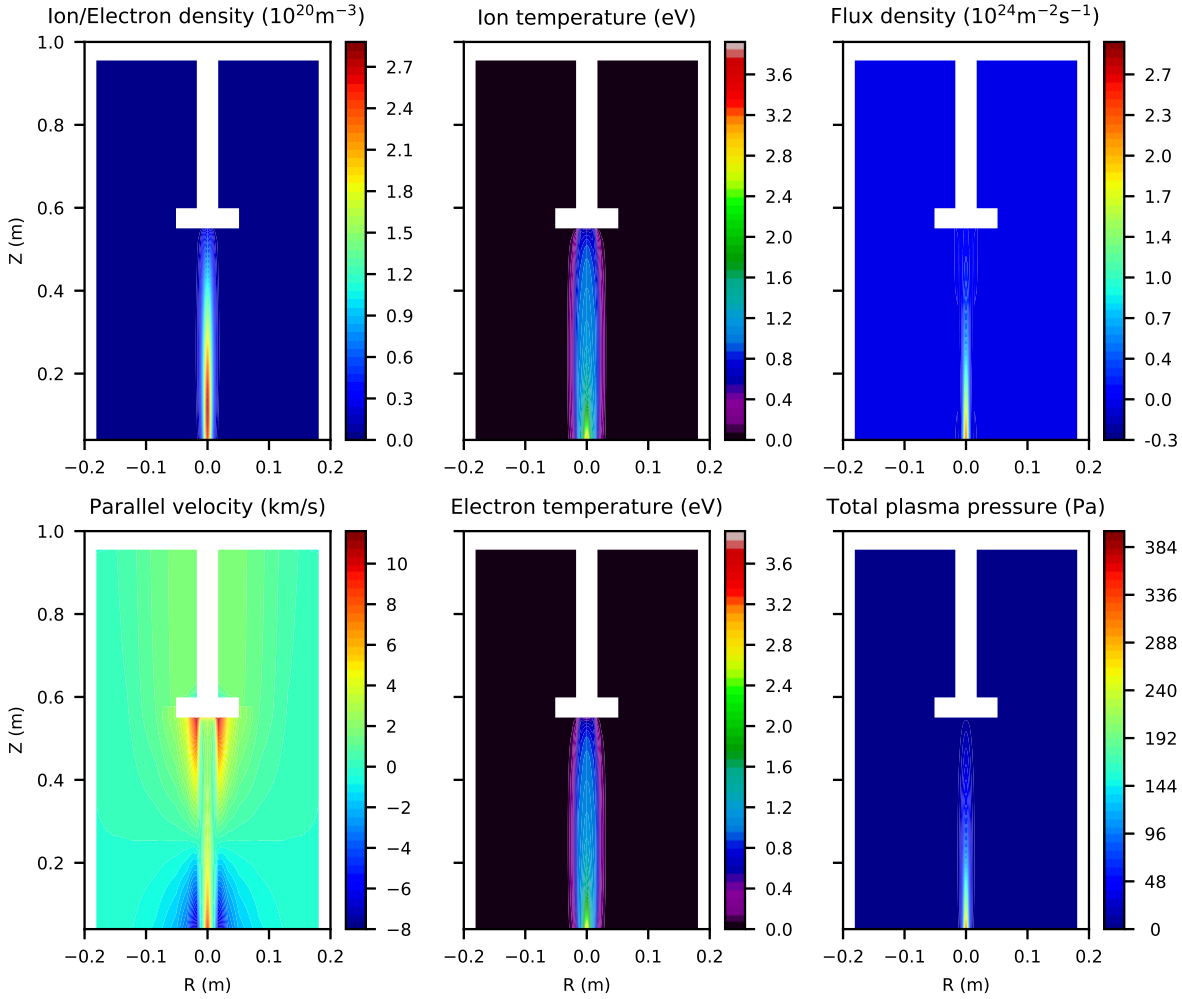

Figure 3.5 – Plots of plasma parameters obtained from the Soledge2D-Eirene simulation for the reference case (a). The blank areas correspond to space taken up by the target and vessel walls.

these coefficients. Four different sets of transport coefficients were tested including the reference case and are listed in Tab. 3.1, cases (a)-(d). All other parameters, including the external volumetric source terms, were kept constant for these cases. From Fig. 3.6 (B), it can be seen that in case (b), where only the energy transport coefficients were changed, there is no significant difference neither in the axial profiles of the total ion flux, beam width and total energy flux. However, when the particle diffusion coefficient D is changed, the beam width increases much faster for case (c), when $D = 1$ m/s^2 and slower when $D = 0.1$ m/s^2. In terms of changes of total ion flux, Fig. 3.6 (A) it decreases roughly by similar amounts, between about 15-25%. However, it should be noted that the total initial ion fluxes (i.e. at the upstream location, Z=4 cm) are not identical. This means that the transport coefficients do have an impact on the simulations ocurring further upstream, where T_e is higher. On the other hand, the behavior of the beam is similar (in terms of the *reduction* of particle flux), regardless of the initial flux.

Table 3.1 – The values of the anomalous transport coefficients (as used in 2.1-2.4) and pumping albedos (absorption coefficients) used in the simulations presented, and the resulting background pressures P_n.

Case	D (m^2/s)	χ_e, χ_i (m^2/s)	albedo ($\times 10^{-2}$)	P_n (Pa)	Remark
(a)	0.3	0.3	5.40	3.3	ref. case
(b)	0.3	1.0	5.40	3.4	
(c)	1.0	1.0	5.40	3.6	
(d)	0.1	0.1	5.40	3.2	
(e)	0.3	0.3	2.00	1.3	
(f)	0.3	0.3	1.20	1.9	
(g)	0.3	0.3	0.80	2.6	
(h)	0.3	0.3	0.40	4.1	
(i)	0.3	0.3	0.25	5.0	
(j)	0.3	0.3	0.17	6.0	
(k)	0.3	0.3	5.40	4.0	el. coll. off

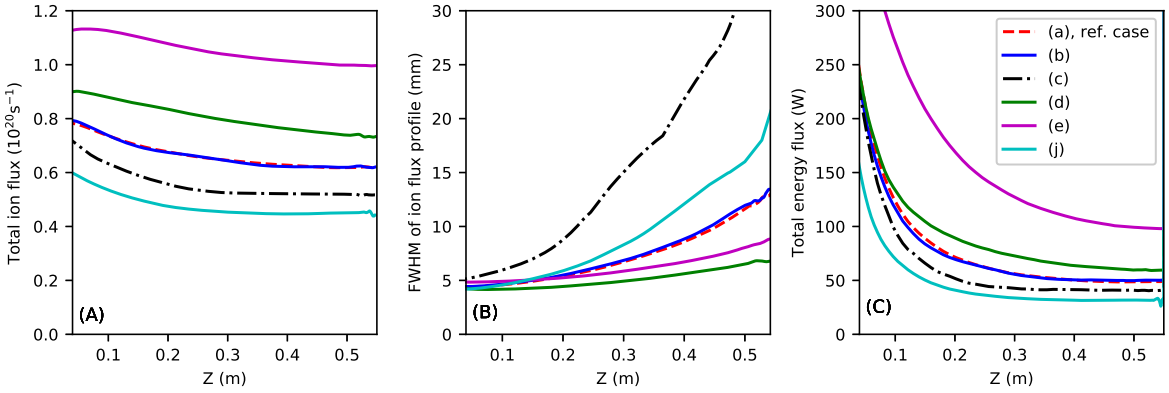

Figure 3.6 – (A) Parallel profiles of the total, section integrated flux density, (B) parallel profile of the beam width (Full width half maximum of the radial flux density $\Gamma(r)$) and (C) parallel profile of the total, section integrated energy flux, listed for a number of different simulation cases. The legend refers to cases described in Tab. 3.1. In the case of profiles of section-integrated quantities, the integration is performed up to the vessel wall at R=20 cm in the radial direction.

Concerning the energy flux, from Fig. 3.6 (C) it can be seen that most energy is reaching the target in the case (d) (excluding case (j) which belongs to a different scan), when the transport coefficients have the lowest values, and is about 60 W. However, the difference between the other cases is not substantial, the amount being 50 W, 49 W, 41 W for cases (a), (b), (c), respectively.

This shows that even though the exact values of the transport coefficients (the main free parameters of the model) are unknown, the overall behavior of the plasma beam between the upstream TS location and the target does not change over a large range of variation of these coefficients. In particular, the decrease in total flux is always aproximately 20 % (integrated particle flux over the device cross section) and 80 %

(energy flux integrated over the device cross section).

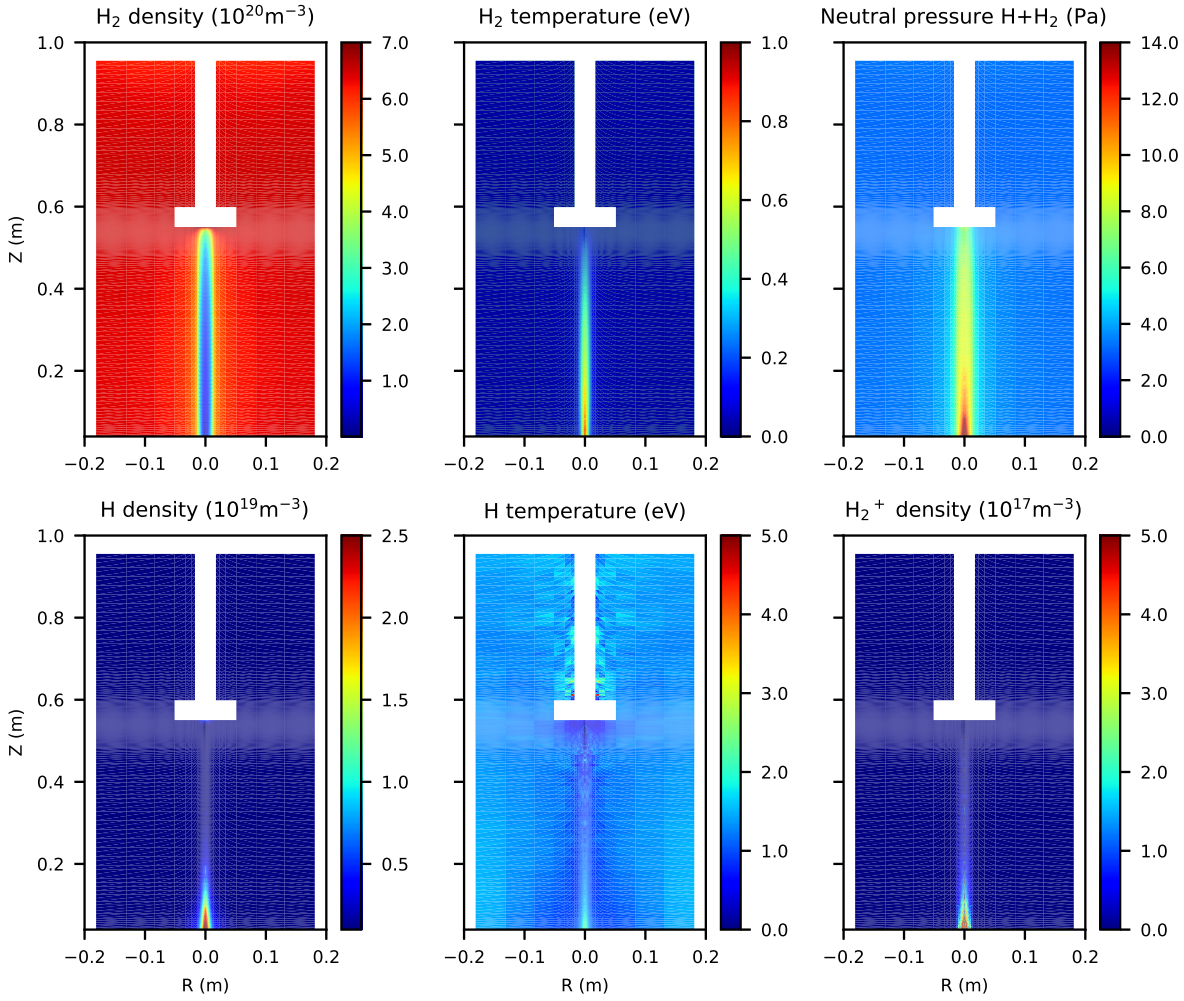

Figure 3.7 – Plots of parameters of species treated by Eirene for the reference case (a). The blank areas correspond to space taken up by the target and vessel walls. The neutral pressure is the combined static pressure of atoms and molecules, $P_n = n_{\mathrm{H}} k T_{\mathrm{H}} + n_{\mathrm{H_2}} k T_{\mathrm{H_2}}$.

3.2.2 Behaviour of H_2 molecules, H atoms and H_2^+ molecular ions

2D maps of various moments of species treated by Eirene are depicted in Fig. 3.7 for the reference case (a). It can be seen that the molecular density profile is hollow, with molecules depleted in the center of the beam. The remaining molecules in the beam are heated by the plasma to typical temperatures up to 1 eV. Hollow molecular profiles and heating of molecules was observed in Pilot-PSI in [109] and this is in line with the modelling. In [110], hollow molecular profiles were also inferred from spectroscopy and could only be explained by an artificial increase of the MAR rate.

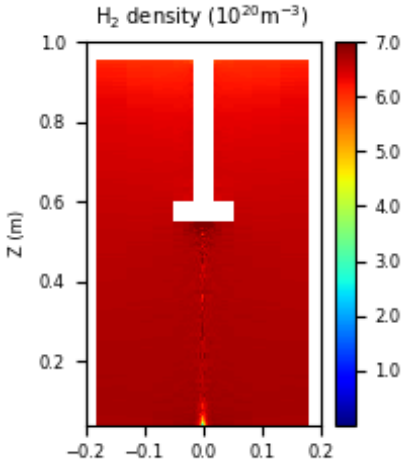

Figure 3.8 – 2D plot of the neutral molecule density for case (k), Tab. 3.1, i.e. where the ion-molecule elastic collisions were turned off in Eirene.

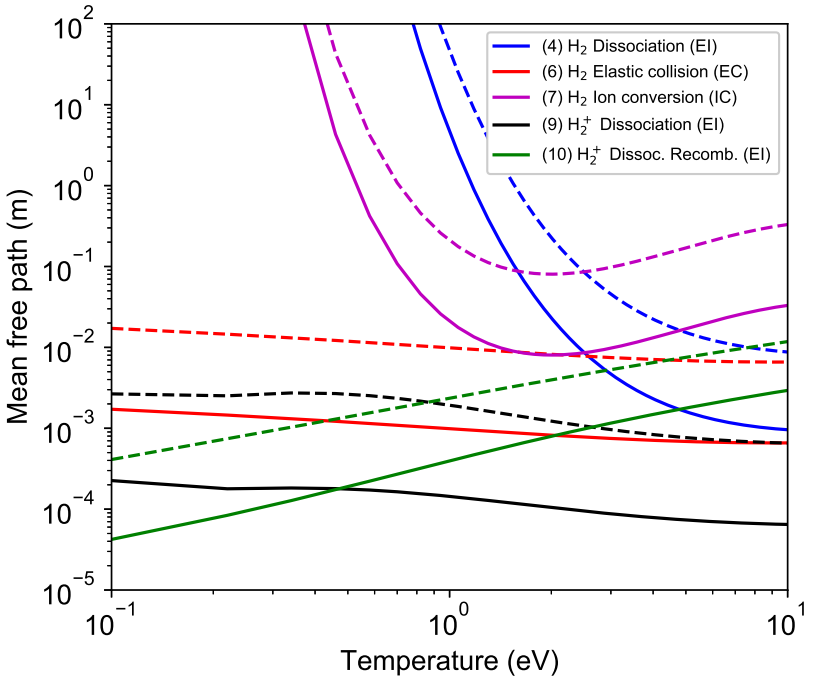

Figure 3.9 – Mean free paths of thermal (i.e. wall temperature) H_2 molecules for several collisional processes for two plasma densities: 10^{19} m^{-3} (dashed lines) 10^{20} m^{-3} (solid lines). The data is from the AMJUEL database.

In our simulated case, the H atoms are mainly present in the upstream area of the plasma, where the plasma is hot enough for dissociation of molecules and molecular ions to be efficient. There is no volumetric process that creates H atoms in the beam region further downstream, i.e. for $Z > 0.15$ m, where also $T_e < 1.2$ eV. Then we are left with the obvious question of what causes the molecular density depletion in

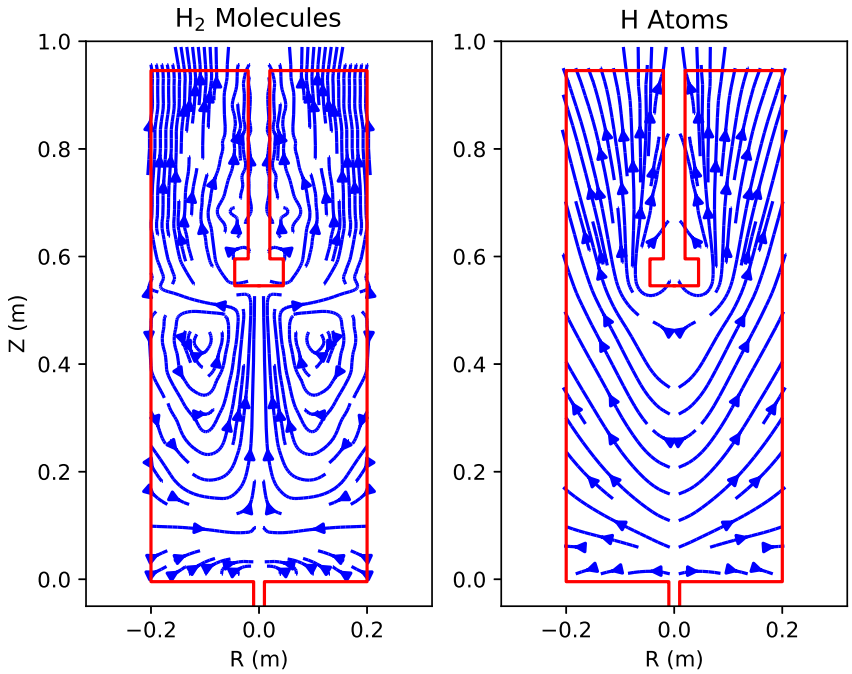

Figure 3.10 – Streamlines of the velocity field for hydrogen molecules (left) and atoms (right) using the full neutral physics model from Tab. 2.1. It should be noted that the density of the streamlines does not give information on the number densities of species.

the center of the beam even in the region further downstream. The answer is *elastic collisions between ions and molecules*, i.e. process (6) from Tab. 2.1, as molecules are accelerated by the plasma in the parallel direction. Further evidence comes from the fact that when the elastic collisions were turned off in the model (case (k), Tab. 3.1), the hollow profile virtually disappeared, as can be seen in Fig. 3.8, with only a small part limited to the upstream, relatively high T_e beam area, where dissociative processes by electron impact are efficient at destroying the molecules. This result could be suspected already from Fig. 2.4, where the elastic collision rate coefficient remains high even where T_e becomes low, i.e. where other processes, like ion conversion (7) or molecular dissociation (4) become low. However, the rate coefficent alone is not a good measure of importance of a given process since it contains no information on transport. To include transport, it is much more illuminating to look at mean free paths or, alternatively, collision times/transit times.

In Fig.: 3.9 the mean free paths (MFPs) of H_2 molecules and H_2^+ molecular ions are plotted as a function of electron or ion temperature, depending on the type of process, for two different plasma densities. For this estimation, the rate coefficients from AMJUEL are used and both species are considered to be thermal, determined by the wall temperature, which was set to 0.03 eV in all simulations presented. It can be seen that the MFP for classical dissociation (4) becomes much larger than typical beam widths (about 1 cm) for T_e <2 eV. Further, the MFP for ion conversion (7) increases sharply when T <1 eV. As the ion coversion is the first step of molecule activated

recombination[3], this already indicates that MAR will not play a significant role in the prevailing, low temperature regions of the beam. What is important to note here is that the mean free path for elastic collisions (6) remains small even for low temperatures, in the order of several mm, depending on the density. This has consequences for both plasma and neutral transport, which will be addressed further.

The density of molecular ions is significantly lower than the typical plasma, molecule and atomic densities, and peak values are of the order $10^{17}\mathrm{m}^{-3}$, concentrated in upstream areas of the beam. The neutral background pressure P_n is uniform outside of the plasma beam and is elevated in the center due to the higher neutral temperatures there. The elevated neutral temperature is also consistent with spectroscopic observations in [109].

We will focus now on the flow pattern of neutral molecules and atoms. In Fig.: 3.10, the streamlines of H_2 molecules and also H atoms are plotted. The plot only contains directional information on the flow pattern.

- In the region of the plasma beam, the flow of molecules is directed towards the target. The molecules are accelerated by the plasma flow via elastic collisions[4] (6). However, close to the walls, the molecules flow in the reverse direction. The resulting velocity shear gives rise to a clearly visible recirculation cell in the area where the molecular flows meet. The pump is located at the back wall of the vessel which is why many flow lines terminate on the corresponding surface. On a part of the remaining surfaces, especially the one that directly "sees" the plasma beam, the origins of many streamlines can be identified, indicating sources of molecules. This corresponds to sources due to surface recombination of atoms hitting the wall.

- For atoms the situation is different. Almost all of the streamlines begin in the plasma beam and terminate on the solid surfaces of the vessel. This is expected, as atoms are mostly created in dissociative processes in the plasma beam. Upon impinging on a material surface, most of them recombine into molecules again. An exception to this behavior is the surface of the target, where atomic streamline origins are visible. This is due to surface recombination of plasma ions into atoms[5] and their subsequent release into the plasma.

Fig. 3.11 shows radial profiles of plasma and neutral densities, T_e and plasma sources and sinks. The latter two are in fact the sums of plasma sources due to processes (1), (5), (8) and (9), and sum of the sinks due to processes (7) and (11), equation 2.6, and Tab. 2.1. This separation of the particle source into positive sources and negative sinks is due to convenience in plotting these quantities which vary many orders of magnitude in the parameter space of the simulations. It can be seen that both the plasma density and the temperature decrease with the axial direction. The

[3]Of the *ion conversion branch*, in particular.

[4]More convincing evidence will be provided in the following section, where a different solution will be retrieved whilst turning the elastic collisions off in the model.

[5]This reflection coefficient is material dependent and is taken from output of the TRIM code [111].

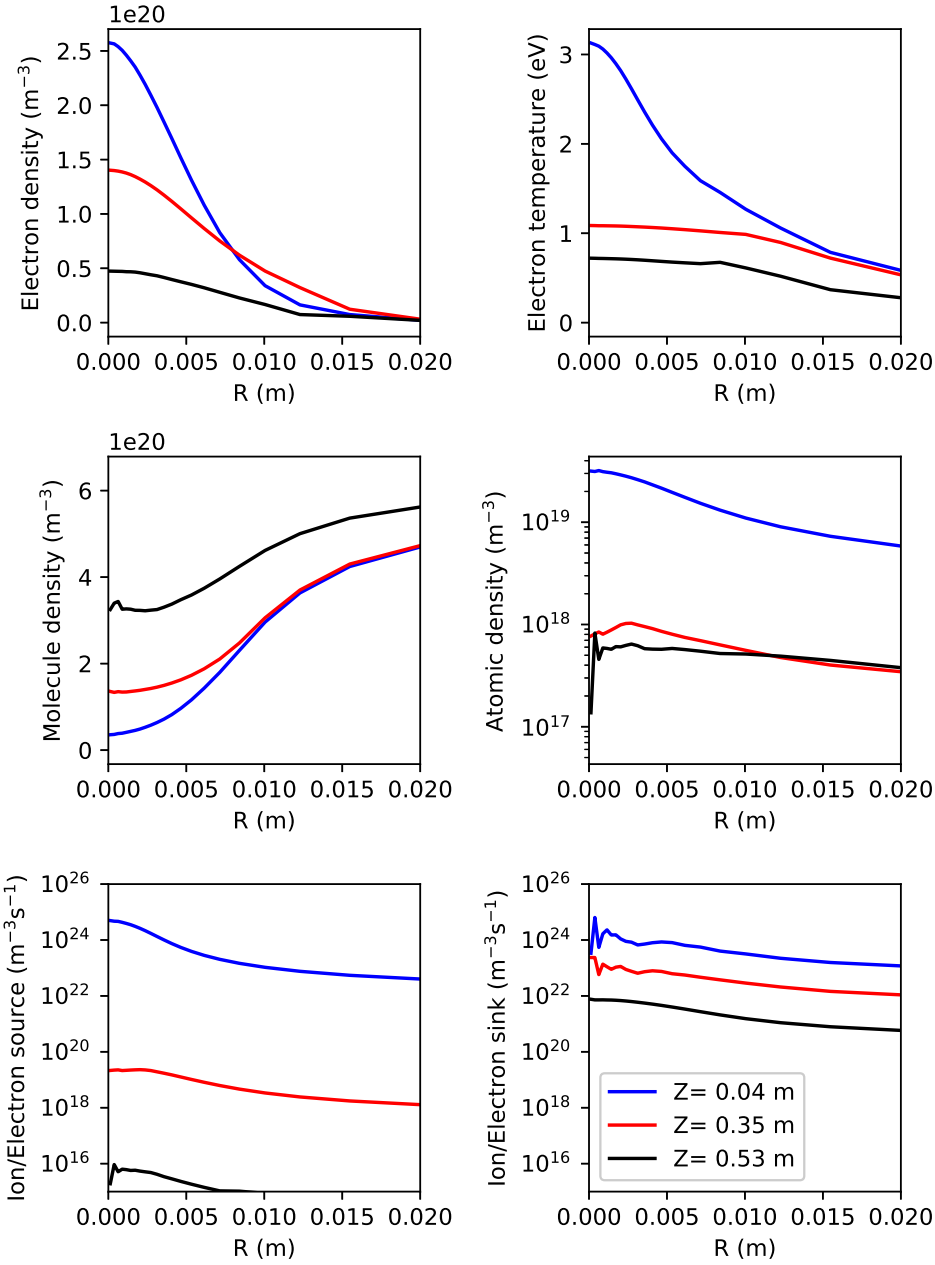

Figure 3.11 – Radial profiles of various quantities for the reference case simulation (a) for three different axial locations given in the legend, while Z=0.04 m and Z=0.53 m correspond to the positions of upstream and target Thomson scattering, respectively. One of the important features is the hollow molecular profile observed in the simulations, attributed to elastic collisions between ions and molecules.

molecular density profile is significantly rarified in the upstream plasma, where T_e is still relatively high. Close to the target this rarification is still visible, however it is less pronounced, with the molecular density dropping by a factor ~ 2. Concering the plasma particle sources and sinks, in the upstream region ($Z = 0.04$ m), sources are

larger than sinks in the region close to the axis, up to about R <5 mm. For R >5 mm, they are comparable but with the sinks being larger in magnitude. In the regions further downstream, the sinks are dominant, albeit they are much lower in absolute values than in the upstream region.

Overall, based on Fig. 3.6 (A), about 20% of the total, section integrated particle flux is removed by recombination. Above 90% of the total sink action is due to ion conversion MAR, i.e. the reaction chain (7) and (10), in the cases studied here. However, it should be pointed out that the modelling underestimates the recombination with respect to the experiments, which will be further discussed in section 3.2.4.

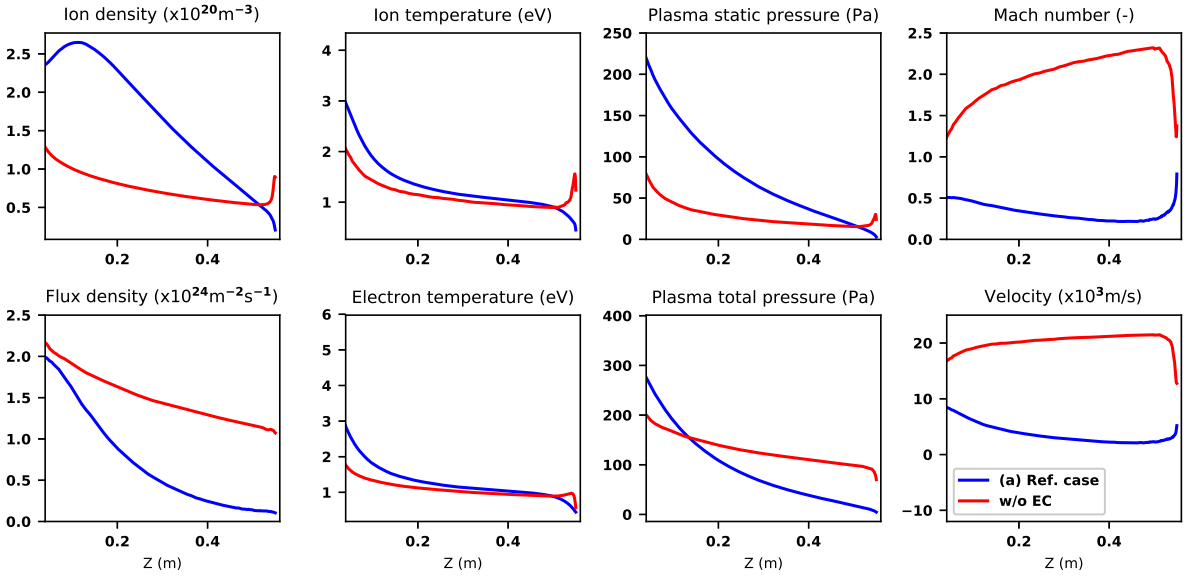

Figure 3.12 – Parallel profiles of various plasma parameters located on field line 1.7 mm radially from the axis of symmetry, obtained by the Soledge2D-Eirene code for the full atomic and molecular physics model and the reduced model without ion-molecule elastic collisions. Blue lines indicate the reference case simulation with elastic collisions on, red lines with elastic collisions off.

3.2.3 Effect of removing elastic ion-molecule collisions on simulation results

It has already been shown that the elastic ion-molecule collisions have a strong impact on the dynamics of neutral molecules. In this section the impact of these elastic collisions (reaction (6), Tab. 2.1) on the plasma solution is addressed. In Fig. 3.12 parallel profiles of a number of plasma parameters for the reference case (a) are shown and also for case (k), which is different in that the elastic collisions (6) were turned off. The parallel profiles are taken at a radius of 1.7 mm from the axis of symmetry, i.e. very close to the axis of symmetry. It can be seen that without the elastic collisions (EC), the plasma enters a supersonic regime very close to the nozzle. However, with EC it is found that the plasma remains subsonic throughout the plasma beam and accelerates to sonic speed in the near vicinity of the target, which is due to the penalization technique

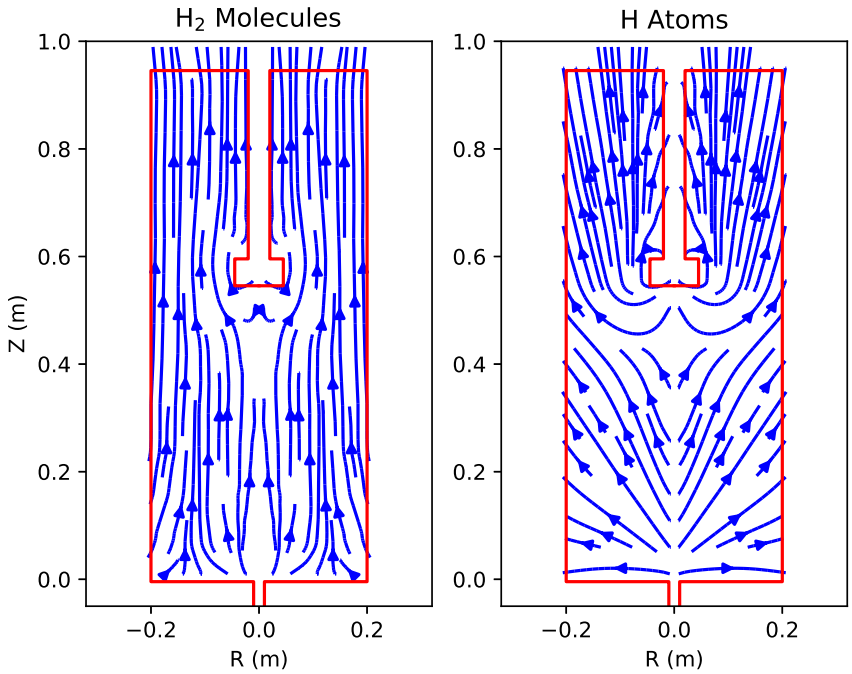

Figure 3.13 – Streamlines of the velocity field for hydrogen molecules (left) and atoms (right), without the inclusion of elastic collisions (6) in the atomic physics model. In contrast with the case where elastic collisions are enabled, a flow pattern without a recirculation cell is now observed for molecules. The topology of the atomic flow is the same regardless of the inclusion of elastic collisions. It should be noted that the density of the streamlines does not give information on the number densities of species.

which is applied there. Moreover, the ion flux and plasma pressure reaching the target are also strongly reduced as opposed to the case without elastic collisions. Although it is known [80, 92] that the elastic collision process is important in detached/low temperature plasmas, this study clearly demonstrates the consequences that omission of this process can have on the simulation results (e.g. by using a more crude atomic physics model).

The streamlines of the velocity fields for hydrogen molecules and atoms are plotted in Fig. 3.13. It can be seen that without the inclusion of elastic collision (6) in the model, there is no longer a recirculation cell, in contrast to Fig. 3.10, indicating that the acceleration of the molecules by the flowing plasma is driving the recirculation cell. The flow pattern for atoms is similar for both cases. It should be restated here that neutral-neutral interactions are not taken into account in this framework.

3.2.4 Comparison of Pilot-PSI simulations and experiments

In order to see whether we can reproduce basic experimental trends, we simulated part of a background pressure scan experiment described in section 3.1. In this experiment, the effect of the background pressure in the vessel P_n on the plasma beam was in-

Table 3.2 – The values of the anomalous transport coefficients (as used in 2.1-2.4) and pumping albedos (absorption coefficients), and the resulting background pressures P_n for the comparison with the experimental scan. This is a selection from Tab. 3.2 for convenience.

Case	D (m^2/s)	χ_e, χ_i (m^2/s)	albedo ($\times 10^{-2}$)	P_n (Pa)	Remark
(a)	0.3	0.3	5.40	3.3	ref. case
(e)	0.3	0.3	2.00	1.3	
(f)	0.3	0.3	1.20	1.9	
(g)	0.3	0.3	0.80	2.6	
(h)	0.3	0.3	0.40	4.1	
(i)	0.3	0.3	0.25	5.0	
(j)	0.3	0.3	0.17	6.0	
(k)	0.3	0.3	5.40	4.0	el. coll. off

vestigated, by changing the pumping speed. In the simulations, P_n was changed by changing the albedo of the pumping surface at the back of the vessel, Fig. 2.6, in order to achieve similar background pressures as in the experiment. The parameters used in the simulations are presented in Tab. 3.2, cases (e-j). In the last column of the table, the background pressure is listed for each case: this is not an input parameter, but a result of the simulation.

Next, we focus on comparing these simulations with the background pressure scan experiment. In Fig. 3.14 (A), Numerical instabilities in the code related to the ion conversion reaction (7) have so far prevented us to converge cases with P_n higher than 6.0 Pa. To be more specific, it was found that by removing reaction (7), higher pressures can be reached. The most striking finding resulting from this comparison is shown in Fig. 3.14 (C). The code is unable to reproduce the low temperatures found in the experiment (using spectroscopy and Thomson scattering), and this is even true for the reference case (the case where $P_n = 3.2$ Pa), i.e. the one used for matching the upstream profiles. The electron temperature in the simulations seems to saturate at a level of ~ 0.7 eV. This happens regardless of the assumed value of the radial transport coefficient D. We think that this affects the particle balance, leading to further discrepancies, which we address in the following.

In Fig. 3.14 (A), the flux density at the target is plotted, measured by a Langmuir probe embedded in the target and recalculated from the Thomson scattering (assuming that the density at the TS target position is equal to the density at the sheath edge). Both from the TS and LP a strong reduction of the flux density with the background pressure is found.

For completeness, the upstream flux density is also plotted, both from the code and recalculated from upstream TS. However, it is important to note that the experimental value is just a rough estimate, assuming an upstream Mach number between 0.2 and 0.7 (these were typical values measured in Pilot-PSI in [54]). These bounds give the associated error bars shown for the upstream flux in Fig. 3.14 (A) and (B). However, even such a large uncertainty cannot prevent from concluding that the flux density is strongly reduced at the target.

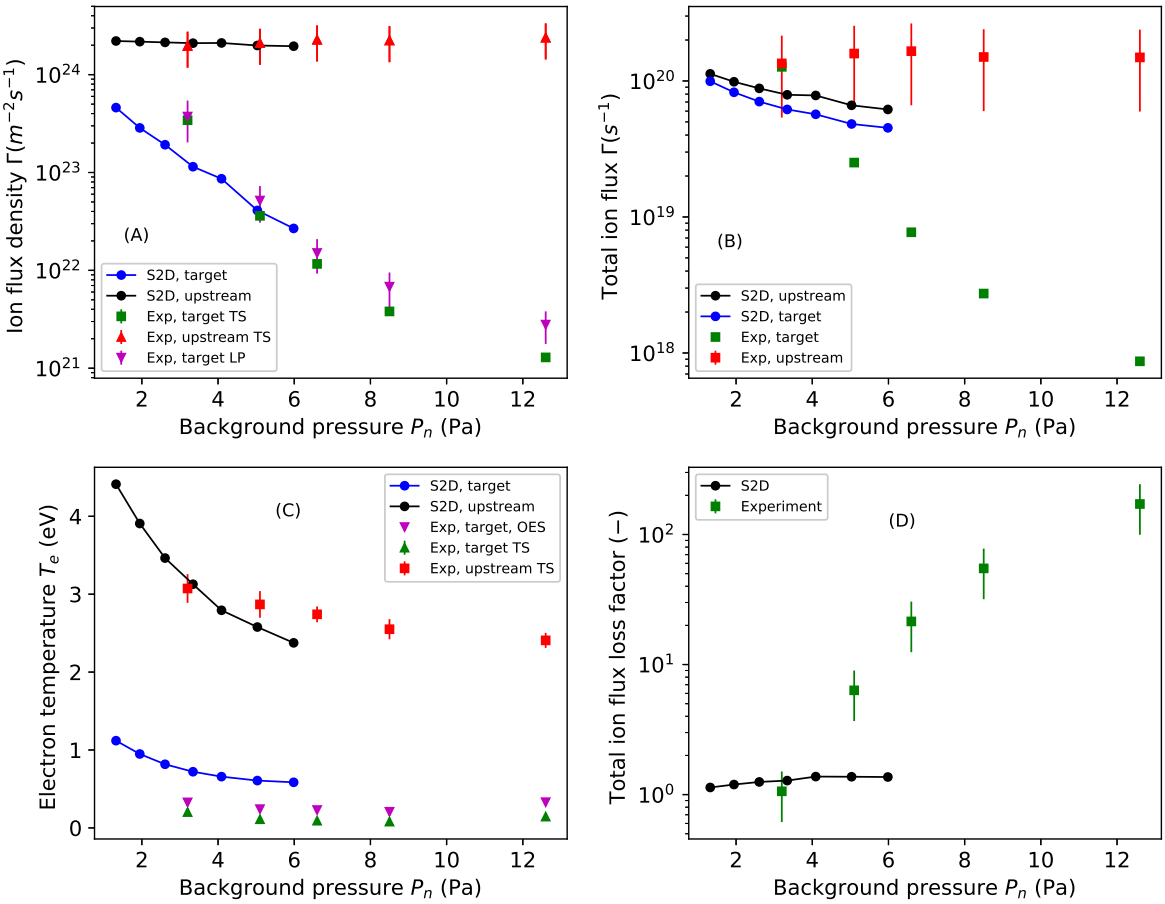

Figure 3.14 – Comparison of flux density for a given field line (A), total ion flux (B), T_e (C) and the total flux loss factor between simulations and estimated from available diagnostics for the P_n scan. The total flux loss factor is calculated simply as the total upstream flux divided by the total target flux. In subfigures (A) and (C) the values are given on-axis (both in modelling and experiement), while figures (B) and (D) depict section-integrated quantities. The Langmuir probe was 2 mm in diameter, centered on the target, i.e. measuring at the position of peak particle flux. The label 'S2D' indicates simulation results, while the label 'Exp.' indicates experimental results, TS indicates the Thomson scattering diagnostic and OES is for optical emmission spectroscopy.

The approach from the previous section, where we compare flux densities, cannot give conclusions on the global particle balance, e.g. on the importance of recombination, as a reduction of flux density can be driven also by radial transport. Therefore, in Fig. 3.14 (B), the section-integrated particle flux is plotted, again as a function of P_n, from the target and upstream TS profiles and from the simulation result. For the calculation of the fluxes from the TS profiles, the same approach as in the previous section was used. Figure 3.14 (D) shows the ratio of the upstream total ion flux to the target total ion flux for both experiment and simulation. Experimentally, the integrated fluxes are strongly reduced for cases where P_n >4.0 Pa, even given the experimental uncertainty on the upstream flux. This indicates that there is strong volume recombination occurring between the upstream and target locations for these cases.

The code, on the other hand, does not show a strong drop in the integrated particle flux at the target. The integrated upstream particle flux is also decreasing in the simulations. The strong local reduction found in Fig. 3.14 (A) and weak reduction of the total particle flux in Fig. 3.14 (B) indicate that the assumed radial transport coefficients chosen might be too high for the cases studied here. However, the sensitivity study performed in section 3.2.1 indicates that beam-width effects arising from changing the radial transport coefficient are not significant, as they tend to impact the density more than T_e, the latter being the important driver for recombination.

As rate coefficients for atomic and molecular processes, e.g. recombination, are a strong functions of T_e, we also compare the T_e from the code and the experiment. For the target location, apart from TS, T_e was also determined using optical emission spectroscopy, using a Boltzmann plot[6] method on high-n Balmer lines. In the experiment, both upstream and target T_e are weak functions of P_n. Upstream, $T_e \sim$ 2.5 -3.0 eV, and at the target, $T_e \sim$ 0.1 - 0.3 eV. In the code, the upstream T_e is more sensitive to increasing P_n, but at the target, T_e appears to decrease only slightly, and is higher by about a factor $\sim$3 than values measured experimentally. Typically (e.g. based on Fig. 2.4), one would expect the plasma to be strongly recombining also at sub 1 eV temperatures predicted by the simulations, but Fig. 3.14 (B) shows that this is not the case. The reason for this can be illustrated by comparing typical recombination time scales. For the electron-ion recombination process (11), Tab. 2.1, a density of 5×10^{19} and T_e=0.7 eV, the recombination time[7] $\tau_{\mathrm{rec}} = 7.8$ ms. The typical particle transit time, between upstream and target, is evaluated as $\tau_{\parallel} = \int_u^t 1/u_{\parallel} \mathrm{d}z$, where $u_{\parallel}$ is the parallel fluid velocity and the integral is performed along the parallel coordiante z. The parallel transit time for the highest P_n case (j) obtained in the simulations is $\sim$0.3 ms, and is lower for the cases with lower P_n. Therefore, the ion electron pairs simply do not get enough time to recombine via channel (11) under these conditions. If T_e were $\sim$0.2 eV, $\tau_{\mathrm{rec}} = 0.2$ ms, indicating that the recombination would become important[8]. This shows that conclusions on the global importance of recombination cannot be based on arguments related to the local T_e or simply on the dominance of certain rate coefficients, but rather the whole transport picture, including the macroscopic flow has to be considered.

To summarize this part, we find that the code does not reproduce the strong T_e reduction observed experimentally by two diagnostics (section 3.2.4, Fig. 3.14). We infer that this is also the reason that electron-ion recombination is not removing a significant amount of particles in the simulations, although experimentally it is apparent

[6]Such a Boltzmann plot is depicted in section 7.5.4, Fig. 7.12, or, alternatively in [112].

[7]The recombination time for a given n_e and T_e was estimated using the tabulated rate coefficients from the AMJUEL database.

[8]In fact, it was also found that one can easily "engineer" synthetic, continuous and monotonic plasma profiles that match the upstream TS measurements and also the low T_e target TS measurements, such that the total amount of particle flux loss due to electron-ion recombination (EIR) is comparable to the total upstream ion flux. It should be noted however that these synthetic profiles were not necessarily self-consistent, i.e. they did not fulfil the steady-state transport equations. Still, we think that this adds to the evidence that EIR is removing a significant fraction of the particle flux in the experiment.

that it does. This indicates that there could be missing energy dissipation channels in the simulations. For instance, the vibrational distribution of neutral hydrogen molecules is described in a simplified way. Individual vibrationally excited species are not followed, but a vibrational distribution as a function of the local T_e is assumed based on [113]. Therefore, the energy costs associated with vibrational excitations are also not accounted for, and it is speculated that these additional energy sinks could contribute to further reduction of T_e.

Concerning the H_2^+ branch of the MAR pathway, the situation is more complicated, since the recombination rate depends on the rate of formation of H_2^+ via ion conversion, which decreases as a function of T_e, and also on the ratio of the rates of the dissociative recombination (10) and of the competing, purely dissociative process (9), which is stronger for $T_e > 1$ eV. In any case, these processes are included in the framework of the code and they are not causing significant recombination in the cases considered.

In this perspective, the B2.5-Eunomia simulations of Pilot-PSI should be mentioned, where good agreement with experiment was achieved. On the other hand, the comparison was performed for a different plasma regime, with a much higher target T_e, of about ~ 3 eV. Moreover, the comparison was performed for one experimental case, rather than a full experimental scan. It should also be mentioned that in the atomic physics model in [47], the purely dissociative branch of H_2^+ (reaction (9), Tab. 2.1) is not included, thereby possibly overestimating the contribution of MAR to recombination.

3.2.5 Two-point analysis of simulation results

In order to analyse the resulting profiles in more detail, we apply a 2-point formatting analysis inspired by similar analyses performed in [114–116].The aim here is to do the "book keeping" between different processes driving the gradients in the profiles of the particle flux density $\Gamma = nv$, total plasma pressure $\Pi = nm_iv_i^2 + n_ikT_i/e + n_ekT_e/e$ and the parallel heat flux density for electrons q_e and ions q_i. To identify which terms contribute the most to the reduction of e.g. the particle flux, we integrate the continuity equation 2.1 between an upstream position, denoted "u" and a position close to the target, denoted "t". Further on, these two positions correspond to upstream and target TS positions, i.e. Z=4 cm and 54 cm, respectively. Next, we formally look at the radial transport term $\vec{\nabla}\cdot(D\vec{\nabla}_\perp n)$ on the R.H.S. of the equation as an additional source term and denote it $S_n^\perp$. Taking into account the simple, orthogonal geometry of the linear device and assuming steady state (time dependent term vanishes, which is the case in a converged simulation), we obtain the following:

$$\Gamma_t - \Gamma_u = \underbrace{\int_u^t S_n^{(\perp)}\mathrm{d}z}_{\text{Radial tranport}} + \underbrace{\int_u^t S_n^{(N)}\mathrm{d}z}_{\text{Neutrals}} \tag{3.1}$$

where Γ is the parallel particle flux density. The external source term $S_n^{(\mathrm{ext})}$ from equation 2.1 vanishes by definition due to the choice of the "u" and "t" positions. The same can be done with the momentum equation 2.2, in which case we multiply the

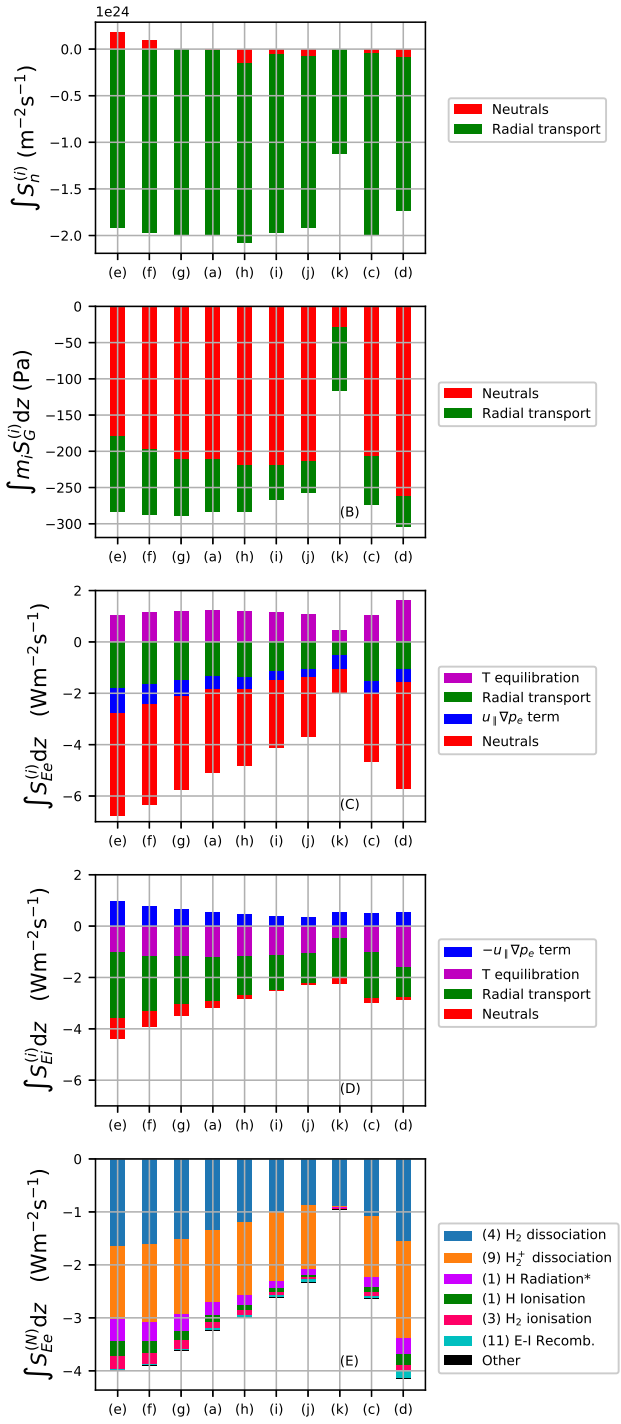

Figure 3.15 – Bar plot of the integrated source terms for particles (A), momentum (B), electron energy (C), ion energy (D) and the energy source term due to interactions with neutrals (E) broken down into its different contributions. The integration is carried out between the target location and the upstream Thomson scattering location, i.e. over the length of about 51 cm. This is for the flux tube located 1.4 mm from the axis of symmetry. Detailed meaning of the plotted terms is described in the text around equations 3.1, 3.1 and 3.3.

equation by the ion mass m_i so that the quantity in the divergence on the L.H.S. is the total plasma pressure Π defined earlier in this section. Again, we formally rename the term associated with radial transport $\vec{\nabla} \cdot (\nu \vec{\nabla}_\perp n u_\parallel)$ as $S_G^{(\perp)}$. After the integration we have:

$$\Pi_t - \Pi_u = \underbrace{\int_u^t m_i S_G^{(\perp)} \mathrm{d}z}_{\text{Radial tranport}} + \underbrace{\int_u^t m_i S_G^{(N)} \mathrm{d}z}_{\text{Neutrals}} \tag{3.2}$$

i.e., the reduction of the total pressure between upstream and target location for a given flux tube is driven by momentum sources (sinks) due to neutrals and radial transport.

For the ion and electron energy equations 2.3 and 2.4, we move the electron pressure gradient term $u_\parallel \nabla_\parallel n k_B T_e$ to the R.H.S. of the equation. Then, we formally rename the perpendicular energy transport term (the 1st term on the R.H.S. of equations 2.3, 2.4) as $S_{E,i}^{(\perp)}$ and $S_{E,e}^{(\perp)}$, respectively. After integration, we obtain the following:

$$q_{t,\alpha} - q_{u,\alpha} = \underbrace{\int_u^t S_{E,\alpha}^{(\perp)} \mathrm{d}z}_{\text{Radial tranport}} + \underbrace{\int_u^t S_{E,\alpha}^{(N)} \mathrm{d}z}_{\text{Neutrals}} \pm \underbrace{\int_u^t Q_\alpha^{(c)} \mathrm{d}z}_{\text{Temp.equilib.}} \mp \underbrace{\int_u^t u_\parallel \frac{\partial (n k_B T_e)}{\partial z} \mathrm{d}z}_{\text{Press.gradient}} \tag{3.3}$$

where q is the total heat flux density and α is a species index, i.e. ions or electron in our case. In case of the double sign ($\pm$) operator, the upper and lower sign corresponds to ion and electrons, respectively. The other symbols were defined in section 2.3. The obtained equation states that the reduction of the total heat flux density between upstream and target location for a given flux tube for a given species is driven by radial transport, sources/sinks due to the interaction with neutrals, sources/sinks due to temperature equilibration and a term associated with the pressure gradient, which is in fact the combined effect of the electric field force and ion-electron friction force. The obtained equation states that the reduction of the total heat flux density between upstream and target location for a given flux tube for a given species is driven by radial transport, sources/sinks due to the interaction with neutrals, sources/sinks due to temperature equilibration and a term associated with the pressure gradient, which is in fact the combined effect of the electric field force and ion-electron friction force.

For the electron energy equation, we can go one step further, and decompose the electron energy source term due to neutrals $S_{E,e}^{(N)}$ into its different contributions, based on equation 2.9, thus we can break down the contributions corresponding to different processes.

In Fig. 3.15 (A), the integrated loss term for particle flux density Γ is plotted in the form of a bar chart and is split into two contributions: radial transport and sources due to neutrals, for cases (e), (f), (g), (a), (h), (i), (j) from Tab. 3.1. The cases are ordered by increasing background pressure. Case (k) uses the same setting as the reference case (a) with the exception that the elastic ion-molecule collision (process (6), Tab. 2.1) is switched off. The charts are for the flux tube located 1.4 mm off-axis. If the bar is positive, the contribution of the given process increases the flux density Γ; if

it is negative, it decreases Γ. The sum of the two contributions is then equal to the difference in target and upstream flux, $\Gamma_t - \Gamma_u$. From the bar chart, it can clearly be seen that most of the reduction of the target flux density is driven by the radial transport, in every plotted case. For cases (e-g), with lower background pressure, the integrated source term due to neutrals is positive, meaning that ionisation dominates recombination. However, as P_n is increased, it can be seen that this contribution is reduced and that the balance flips towards negative contribution for cases (h-j), meaning that in those cases recombination dominates. Still, the source terms related to neutral interactions remain comparatively small with regard to radial transport. Case (k), where the elastic collision was switched off, is qualitatively different from the other cases. Here, the contribution of radial transport is about ~ 2 times smaller and the contribution of neutrals is negligible.

In Fig. 3.15 (B), the integrated loss term for the total pressure Π is plotted, in a similar way as the particle flux density in the previous paragraph. In this case, the reduction of total pressure is driven mostly by interactions with neutrals, and radial transport plays a secondary role. As P_n is increased, there is also a slight increase in the momentum sinks due to neutrals, and a reduction of the momentum sinks due to radial transport. However, in case (k), when the elastic collision (6) is switched off, the momentum sink term is significantly decreased. This indicates that elastic ion-molecule collisions are dominantly responsible for reduction of the total plasma pressure Π.

In Fig. 3.15 (C) and (D) the integrated loss terms for the energy flux density of electrons and ions are plotted, respectively. As pointed out earlier in this section (equation 3.3), the reduction in energy flux density can be driven by sources/sinks due to neutrals, radial transport, electron-ion temperature equilibration and a term related to the pressure gradient. In the case of electrons, most of the energy is dissipated by neutrals, a smaller part of it by radial transport and an even smaller fraction by the pressure gradient term. In case of the electrons, there is also a positive contribution due to the temperature equilibration term. For the reduction of ion energy flux density, the channel due to neutrals is small and energy flux dissipation due to radial transport is dominant. The temperature equilibration term has the same magnitude but opposite sign, by definition. As a general feature, the ions are transfering heat to the electrons. This is consistent with the fact that the combined energy sinks due to other processes are stronger for electrons in the regimes explored here, particularly the sinks due to neutrals. Still, the temperature equilibration term is strong enough to maintain $T_e = T_i$ throughout the axial profile.

It is interesting to further break down the integrated electron energy sink term due to neutrals $S_{E,e}^{(N)}$ following equation 2.9. This is plotted in Fig. 3.15 (E). It can be seen that the strongest energy neutral dissipation channels are dissociation of H_2 molecules (4) and H_2^+ molecular ions (9). Processes related to atomic hydrogen, like ionisation and line radiation, play a secondary role in energy dissipation. Moreover, even the atomic hydrogen results from the presence of molecules, as most of it is formed by dissociation of molecules or molecular ions.

Although this analysis is performed locally (i.e. at a given field line, in this case close to the axis, $r = 1.4$ mm), we should note that the plots are qualitatively similar

also at larger radii[9].

We also point out here that electric currents were not included in the simulations presented here. It is difficult to make statements about their impact without running the simulations with their inclusion. However, currents flowing through a plasma are expected to act as additional heating mechanism via Ohmic heating, especially for low temperature plasmas when the resistivity is high. On the other hand, the low magnetic field (0.2 T) used during the Pilot-PSI experiments means that Ohmic heating effects are reduced, based on interpretations of B-field scan experiments [54]. In any case, additional heating would lead to an even higher T_e at the target, not helping resolve the observed discrepancy.

To summarize this part, the main findings are the following: 1) the local reduction of target ion flux density is caused mainly by radial transport (i.e. recombination only plays a minor role) and this holds regardless of the choice of the anomalous perpendicular transport coefficients (section 3.2.5, Fig. 3.15), 2) the momentum loss is caused mainly by ion-neutral friction, and ion-molecule elastic collisions in particular and 3) The strongest cooling channel is electron impact dissociation of molecules and molecular ions.

3.3 Target gas puff experiments at Magnum-PSI

In the final part of this overview, we turn our focus to divertor-relevant plasmas at the Magnum-PSI device. Magnum-PSI can provide densities of $10^{20} - 10^{21}$ m^{-3}, relevant to the regimes expected in ITER. In the frame of this overview, we focus on the most robust result of the Magnum-PSI experiments, which are centered around the determination of the energy flux to the target.

3.3.1 Reduction of ion flux at the target

The main purpose of the experiment was to investigate the effect of neutral gas on the plasma beam in the target chamber. This was done by performing a scan of the target chamber background pressure by puffing aditional H_2 gas into the target chamber. Fig. 3.16 (A) shows the total ion flux (i.e. integrated over the cross section) as a function of the changing background pressure P_n estimated from Thomson scattering using cylindrical integration:

$$\Gamma_{\mathrm{tot}} = \int_0^{2\pi} \int_0^{R_{\mathrm{vess}}} r\Gamma(r)\mathrm{d}r\mathrm{d}\phi \tag{3.4}$$

where the local ion flux density to the target was estimated using the Bohm criterion, assuming $T_i = T_e$, a polytropic coefficient of unity and assuming a 1/2 drop of density in the pre-sheath, i.e. $\Gamma(r) = \frac{1}{2} n_e^{(\mathrm{TS})} \sqrt{2kT_e^{(\mathrm{TS})}/m_{\mathrm{i}}}$, where $n_e^{(\mathrm{TS})}$ and $T_e^{(\mathrm{TS})}$ are

[9] Additionally, if this analysis is performed in the volume (effectively removing the need to account for radial transport terms, as these only lead to spatial redistribution), the main conclusions about particle, momentum and energy dissipation processes still remain the same.

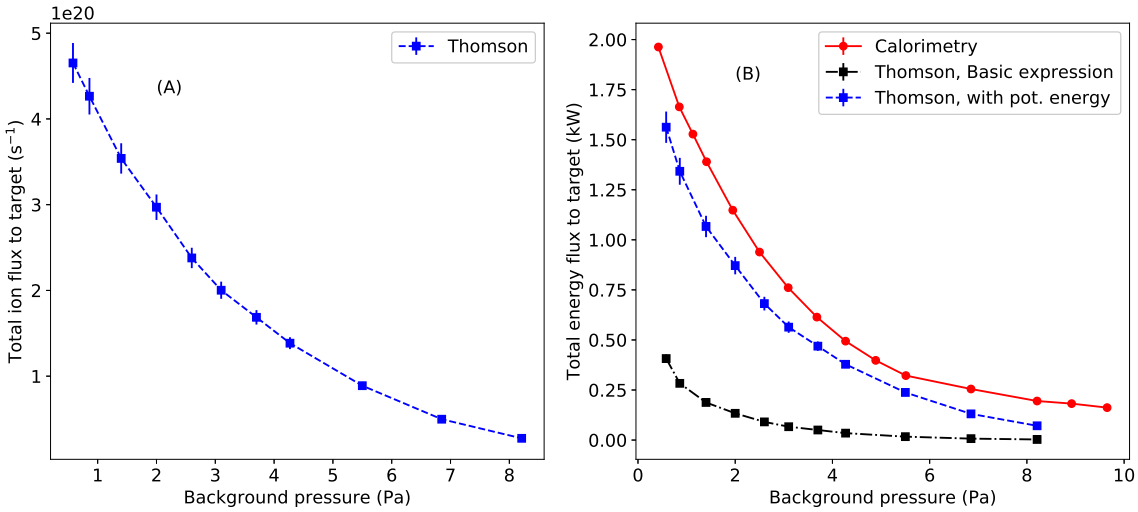

Figure 3.16 – Response of the total ion flux density to the target (A) and the total energy flux to the target (B) to the background pressure, which was varied by puffing neutral gas into the target chamber. In figure (B) the comparison is for the values estimated from Thomson scattering (using two different expression for the target energy flux, with and without the inclusion of potential energy terms) and calorimetry.

the measured electron density and temperature, respectively. The latter assumption (i.e. on the density drop in the pre-sheath) was verified in Pilot-PSI experiments [117]. It can be seen that the total ion flux drops from the value of about 4.6×10^{20} s^{-1} to below 5×10^{19} s^{-1}. However, all the source settings are kept the same. This indicates that the plasma is recombining and the results is consistent with earlier experiments at both Magnum-PSI and Pilot-PSI [100, 112].

3.3.2 Comparing energy flux to target from calorimetry and Thomson scattering

The calorimetric diagnostic gives the total energy flux absorbed by the target station. For comparison, we want to estimate this also from the TS measurements located 2 cm in front of the target. The energy flux impinging on the target is typically calculated from sheath physics and is parametrized for a given sheath edge ion flux density Γ_i and electron temperature T_e by using a dimensionless "sheath heat transmission factor" γ_{sh}, i.e. $q_{\mathrm{t}} = \gamma_{\mathrm{sh}} T_e \Gamma_i$. For $T_e = T_i$, following the analysis in [23], p. 654, the value of the sheath heat transmission factor can be written as

$$\gamma_{\mathrm{sh}} = \underbrace{(2.5 - e\frac{V_{\mathrm{sh}}}{T_e})(1 - R_{\mathrm{i,E}})}_{\text{(i)}} + \underbrace{\frac{2}{1-\delta}(1 - R_{\mathrm{e,E}})}_{\text{(ii)}} + \underbrace{\frac{\chi_i}{T_e}}_{\text{(iii)}} + \underbrace{\frac{\chi_r}{T_e}(1 - R_{\mathrm{i,N}})}_{\text{(iv)}} . \tag{3.5}$$

The first term represents the kinetic energy of the ions entering the sheath (assuming a 1D drifting Maxwellian velocity distribution) and the energy acquired in the

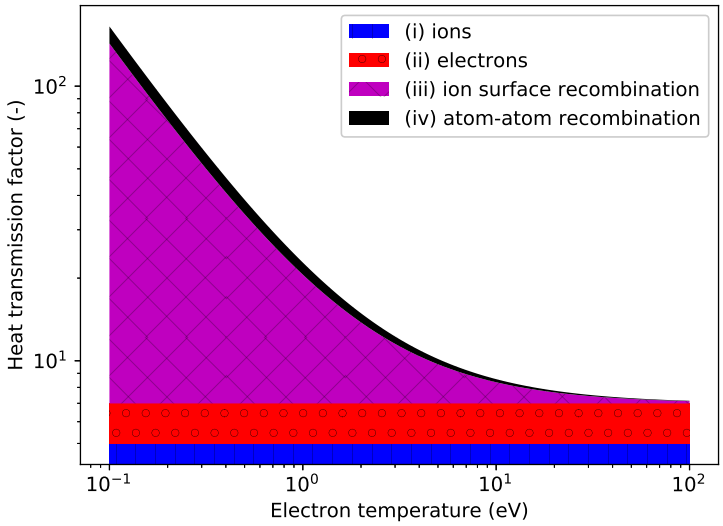

Figure 3.17 – The sheath heat transission factor broken down into its various contributions based on expression 3.5. The meanings of the various terms (i-iv) used in the expression are detailed in the text. It can be seen that for $T_e < 5$ eV, the heat transmission factor is dominated by the surface recombination channel.

Table 3.3 – Values of the individual constants used in the calculation of the sheath heat transmission coefficient, expression 3.5, in order to obtain Fig. 3.17.

χ_i (eV)	χ_r (eV)	$R_{\mathrm{i,E}}$, $R_{\mathrm{e,E}}$, $R_{\mathrm{i,N}}$ (-)	δ (-)
13.6	2.2	0	0

sheath electric field, eV_{sh}. Reflection is allowed for, $R_{\mathrm{e,i}}$ being the ion energy reflection coefficient (accounting for ion backscatter as a neutral atom). The second term represents the energy deposited by electrons, which is increased by secondary electron emission, δ being the secondary electron emission yield, and decreased by reflection, $R_{\mathrm{e,E}}$ being the electron energy reflection coefficient. The third term represents the recombination energy of ions χ_i on the surface. Lastly, the fourth term represents the atom-atom recombination energy into molecules at the surface, with reflection allowed for by the coefficient $R_{\mathrm{i,E}}$. Usually, terms 3 and 4 are neglected (e.g. for reasons detailed in [118]), yielding the typically used value of this coefficient of around 7-8 [23] for a hydrogen plasma and a floating target. However, when T_e is lower than 10 eV, especially term (iii) and also (iv) gain significant importance This can be seen in from Fig. 3.17, where the heat transmission factor was plotted as a function of T_e (=T_i) assuming that the individual quantities in expression 3.5 take the values from Tab. 3.3.

We calculate the total energy flux from the TS measurements by cylindrical integration of the radially resolved energy fluxes for two different cases: (a) without considering terms (iii) and (iv) in expression 3.5, i.e. using the standard value, T_e independet value of $\gamma_{sh} = 7$ and (b) with considering the (T_e dependent) terms (iii) and (iv), and using values from Tab. 3.3. We do this for each case of the background pressure/target puff scan. The comparison of these energy fluxes obtained from TS

with calorimetry is shown in Fig. 3.16. The case without the inclusion of (iii) and (iv) grossly underestimates the energy absorbed by the target. On the other hand, when (iii) and (iv) are included, reasonable agreement between the calorimetry and TS estimations of the energy flux are obtained, the TS estimation being always lower than calorimetry, by roughly 20%. This is not surprising, since the TS estimation inherently only includes the energy flux due to the plasma. However, neutral atoms and molecules are also present in and in the vicinity of the plasma, and undergo collision processes with it. For instance, dissociation products, charge-exchange atoms etc. can also contribute to the heating of the target, as well as photonic radiation due to the decay of excited atomic levels or due to radiative recombination.

This comparison shows that it is crucial to include the terms (iii) and (iv) when estimating the energy flux to the target from TS measurements in typical Magnum-PSI conditions, which are similar to those expected in the ITER divetor during detachment.

Chapter 4

Conclusions and Outlook

In the frame of this thesis, a number of plasma characterisation experiments have been carried out at the Pilot- and Magnum-PSI linear plasma devices, mainly background pressure scans, revealing a strong reduction of both particle and power fluxes to the target plates. These results share similarities with experiments performed in early divertor simulation experiments [28, 29]. The obtained datasets motivated us to use the Soledge2D-Eirene edge transport code to simulate the plasmas produced by these linear devices, in order to check how well the codes can reproduce the observed experimental features and to indentify the main particle and power removal processes at play. We have broken down the work into several main research questions and we attempt to provide answers to them, based on the obtained experimental and simulation results.

Can main experimental features of Pilot-PSI be reproduced by using an edge transport code?

The high density, low temperature plasma present in Pilot-PSI was simulated by the Soledge2D-Eirene edge transport code. Qualitatively, the reduction of both density and temperature is indeed reproduced when background pressure scan experiments are simulated. For Pilot-PSI, it has been found that in the simulations, T_e close to the target is systematically higher in comparison to the measurements using TS and spectroscopy (section 3.2.4, Fig. 3.14). T_e in the simulations appears to saturate at 0.7 eV for a wide range of parameters, while experimentally values of 0.1-0.3 eV are found. This was also tested in response to changes of the perpendicular transport coefficients, which are the main free parameters in the simulations, however the result showed to be robust even with respect to these changes.

A strong experimentally measured reduction of the local particle flux density at the target end of Pilot-PSI was determined through Thomson and target Langmuir probes; the reduction increased exponentially with the chamber pressure. The modeled dependence of the loss of ion flux density on neutral pressure can also be characterized as exponential with similar magnitude (Fig. 3.14 (A)). However, it was found that in the modelling, the reason for the local reduction of flux density was caused by redistribution of plasma flux over a larger area due to radial transport. The reason why

increasing the background neutral pressure increases radial losses is due to an increase of the ion parallel transit time due to ion-molecule friction, effectively giving the plasma more time to diffuse radially. However, from the experiments, by comparing total upstream and target particle fluxes, large fraction of particles (>90%) is conjectured to recombine in the volume, especially for high background neutral pressure.

The simulations do not reproduce this strong volume recombination, despite the lowest recovered electron temperatures being ∼0.7 eV, where electron-ion volume recombination is often said to be important. In fact, by comparing typical ion transit times with the timescales of electron-ion recombination, it is found that the latter happens on a longer timescale in the conditions of the Pilot-PSI simulations. Indeed, the 0.7 eV electron temperatures in the modelling (which are themselves overestimated) are still too high for electron-ion recombination to remove a substantial amount of the particle flux in the Pilot-PSI cases studied here. To summarise this part, it is conjectured that the overestimation of T_e in the simulations is the cause for the underestimation of the volume recombination. This also illustrates the fact that conclusions on the importance a certain processes cannot be based solely on the dominance of rate coefficients, but the whole transport picture has to be considered, i.e. at least by comparing transit times to collision times, or alternatively, mean free path to typical beam dimensions.

The high T_e values indicate that there could be missing energy dissipation channels in the simulations. The intrinsic radiation of molecules themselves (e.g. due to molecular lines/bands) was considered, but initial estimates based on data from AMJUEL showed that the power dissipated by this channel is negligible and is not significant, especially at low T_e. Other possible dissipation mechanisms should be considered to resolve this discrepancy. It is also important to stress here that the vibrational distribution of neutral hydrogen molecules is described in a simplified way. In particular, individual vibrationally excited species are not followed, but a vibrational distribution as a function of the local T_e is assumed based on [113]. Therefore, the energy costs associated with vibrational excitations are also not accounted for, and it is speculated that these additional energy sinks could contribute to further reduction of T_e. Their importance remains to be quantified in future work.

What are the main physical mechanisms causing particle, momentum and power dissipation in the plasmas of Pilot- and Magnum-PSI?

This research question is related to the *book keeping* function of an edge transport code. Based on detailed analysis of the code results using a two-point formatting analysis method, we could identify the dominant terms in the model equations that cause reduction of the particle, total pressure and electron and ion energy flux densities. Such an analysis is performed locally, for a given field line, particularly in section 3.2.5, Fig. 3.15.

For the reduction of the parallel particle flux density, losses due to radial transport are by far the strongest, in comparison to sink action due to various recombination

processes[1]. The exact fractional amount by which the particle flux density is reduced is sensitive to the choice of the perpendicular particle transport coefficient, which is a free parameter in our simulations, but is expected to take values between 0.1 - 0.5 m^2/s, based on values commonly used in tokamaks and also on experimental validation in this work. One could argue that the result is just a consequence of our assumption on the transport coefficient, however, in a sensitivity study we show that the overall result is robust with respect the exact choice of this coefficient in the range considered.

For the reduction of total plasma pressure, elastic ion-molecule collisions have been found to be the dominant mechanism. In fact, without the inclusion of this process, supersonic flows were obtained in the simulations. The molecules provide friction to the plasma via this process, and are themselves accelerated towards the target. This creates a flow pattern for molecules, characterised by a recirculation cell in the 2-D projection of the molecular flow field in the (R, Z) plane. Such a flow pattern was experimentally observed in [36]. Additionally, the elastic collisions are concluded to be the reason why the molecular density profile is hollow in the plasma beam region, even in regions where molecular dissociation is innefective.

For the electron energy flux density, inelastic collisions between electrons and neutral backround particles dissipate most of the heat flux. From these inelastic processes, dissociation of molecules and molecular ions were found to be the strongest contributors. However, these energy sinks are located in the upstream region, where T_e is high enough to efficiently break up molecules and molecular ions; in locations close to the target, the simulations do not predict any mechanism that could dissipate the heat flux and subsequently reduce T_e to values of 0.2 eV found in the experiment, i.e. where volume recombination could remove a significant number of plasma particles.

For the ion energy flux density, the volume sinks are comparatively smaller than in the case of electrons. The strongest mechanisms are in fact energy losses to electrons via Coulomb collisions and perpendicular energy transport. The latter is again influenced by our choice of the corresponding transport coefficient, however, from the performed sensitivity study, the result was consistent for all transport coefficients in the tested range.

How important is molecule activated recombination (MAR) in Pilot- and Magnum-PSI in terms of particle removal?

There is a long standing discussion whether MAR is an important recombination pathway. Evidence that MAR is occurring is indeed ubiquitous from linear plasma devices, usually from detailed analysis of excited state populations. However, the actual number of particles that are removed by this recombination channel is difficult to quantify experimentally. Here, we again task the edge transport simulation to do the book keeping of this process for us. Only the ion conversion branch was considered, which has a higher rate coefficient for hydrogen plasmas.

First of all, it has been concluded that the total, volume integrated recombination

[1]It is important to note that this is with the caveat that the strong recombination inferred from experiment is not reproduced by the model.

sink removes only up to 25% of the particle flux, for all simulation cases. Most of this recombination (usually >90%, but it varies from case to case) is indeed happening as a result of ion conversion MAR. As concluded previously, EIR was not an efficient particle removal mechanism due to the systematically higher simulated near target T_e with respect to experiments.

Ion conversion, even though it has a high rate coefficient, peaking at $T_e \sim 2$ eV, is only efficient to a certain extent in removing particles from the plasma (section 3.2.2), at least in the cases studied in this thesis, for the following reasons. First, the resulting molecular ion is more likely to dissociate into an ion and atom again (based on AMJUEL data), especially at T_e >1 eV, effectively becoming only a purely dissociative energy loss process. Dissociative recombination of the molecular ion becomes the dominant destruction mechanism for about T_e <0.6 eV, which is a temperature at which the ion conversion is not efficient anymore, at the densities studied (this is consistent with the study of the effect of MAR on recombination in the ASDEX-Upgrade divertor [119]). Second, for MAR to be important, a large reservoir of molecules is also needed, which is indeed inherently present in linear devices with a cascaded arc source. However, we have shown that elastic collisions cause rarefaction of the molecular density profile in the beam. In the regions where $T_e \sim$ 2-3 eV, also electron impact dissociation, and even the ion conversion itself, followed by the aforementioned dissociation, contribute to hollowing of the molecule density profile. Due to this, MAR seems only to be strong at the very edge of the beam. These findings lead us to believe that only limited particle losses can be obtained by MAR in the high density, low temperature plasmas studied in this thesis.

What implications can be drawn for the understanding of divertor plasmas from this work?

Implications of results from linear devices for tokamak divertors have to considered carefully due to the differences in geometry and operation. However, we think that the findings presented here can still provide some useful insights. It has been shown that inelastic collisions of the electrons with the surrounding molecules provide a strong heat dissipation channel, accounting for >50% of the reduction of the total heat flux density (Fig. 3.15) for a given flux tube. It is important to point out that in Pilot-PSI a large part of the molecules originate from the cascaded arc source, since only a fraction (typically ∼10%) is ionised. In tokamaks this is not the case, since the neutrals in the divertor are exclusively supplied by the plasma recycling itself, i.e. via target plate neutralisation and volume recombination of ions and electrons and further recombination of the resulting atoms into molecules. In general, the molecule density is typically lower than the atomic density and it is concentrated close to the target plates, especially for open divertor configurations. However, recent modelling efforts of closed divertor geometries at DIII-D [120–122] have shown molecular densities comparable to Pilot-PSI conditions, up to 10^{20} m^{-3} and a near-target T_e ∼1 eV. Such refinements of the divertor geometry have resulted in better performance in terms of power dissipation, both from the edge transport code modelling and experiments. Similar results

have been obtained by modelling of the super-X divertor for MAST-upgrade [123], which has a very closed divertor wall geometry and is expected to operate at high molecular pressures. It is expected that in such divertor conditions, the principle acting mechanisms in terms of atomic and molecular physics, will be the same as in the two linear devices studied in this work. In our setup of the Soledge2D-Eirene transport code, comparisons with modelling and experiments show that T_e close to the target is overestimated by the code under the examined, low T_e, high n_e conditions, leading also to an overestimation of the target particle load and consequently also the heat load.

Outlook

The systematic overestimation of target T_e found in this thesis triggers the need for future investigations related to energy dissipation mechanisms and its completeness in the edge transport code setups similar to the one used in the frame of this thesis. In particular, it is recommended to perform code runs with full vibrational kinetics and investigate their impact on the solution. This has been partially already done using B2.5-Eunomia [47], however, with a less detailed atomic physics model, not including the pure, non-recombinative dissociation of H_2^+ ions (possibly overestimating the MAR effect thereby) and for significantly hotter plasmas of about $\sim$3 eV at the target. In particular, it is recommended to investigate whether energy losses due to electron excitation of vibrational states can play a role in driving a further reduction of T_e, especially at T_e <1 eV and high density, observed in Magnum- and Pilot-PSI plasmas.

Further possibilities to study plasmas relevant to detachment are offered by the Magnum-PSI linear plasma device, with a better diagnostic coverage. Target calorimetry and a newly installed bolometric diagnostic could shed more light on studies of the power balance. This effort was already started in the frame of this thesis. Moreover, a collective Thomson scattering diagnostic, experimentally tested already at Pilot-PSI [124] is under development at Magnum-PSI, with potential to deliver information on ion temperatures and especially the plasma parallel flow velocity.

Part II

Publications

Chapter 5

Plasma pressure and particle loss studies in the Pilot-PSI linear plasma generator

*Published as K. Jesko, H. van der Meiden, J. Gunn, J. Vernimmen, and G. De Temmerman, Plasma pressure and particle loss studies in the Pilot-PSI linear plasma generator, Nuclear Materials and Energy, **12**, pp. 1088-1093, aug 2017*

5.1 Abstract

Plasma detachment in tokamak divertors reduces the particle and power fluxes to the plasma facing components and is essential for successful operation of ITER. The linear plasma generator Pilot-PSI can produce a high density ($\sim 10^{20}\mathrm{m}^{-3}$), low temperature ($\sim$ 1 eV) plasma which is similar to that expected at the ITER divertor strike-points during the partially detached regime [19]. Given the simple geometry of the device, Pilot-PSI allows to diagnose the plasma beam at multiple axial positions. In this study, the incoherent Thomson scattering (TS) diagnostic [66] is exploited to measure the radial plasma T_e and n_e profiles at two locations of the hydrogen plasma beam: near the plasma source (upstream) and 2 cm from the target plate. At the target, the TS measurements are supported by an embedded Langmuir probe. These measurements prove the existence of parallel plasma pressure loss as well as particle loss, confirming that physical processes believed to cause detachment in tokamak divertors also hold in Pilot-PSI (ion-neutral friction, volume recombination). It is found that the fractional reduction of the plasma pressure varies between 4 and 5000, depending strongly on the pressure of the background neutrals. The importance of individual loss channels is discussed.

5.2 Introduction

In ITER, during D-T operation at $Q = 10$, the steady state power crossing the last closed flux surface (LCFS) and entering the scrape-off layer (SOL) is expected to be about ∼100 MW [125]. From multi-machine scaling laws and also theoretical considerations the characteristic power scrape-off length in the inter-ELM phase is expected to be $\lambda_q < 5$ mm . This leads to a total plasma wetted area which, accounting for flux expansion and target inclination, is estimated to be around 2.3 m^2. This would result in a power loading of ~ 40 MW/m^2 of the divertor targets which is above the technological limit of 10 MW/m2 of steady state power loading for the plasma facing components (PFCs) [19]. Therefore at least 2/3 of the power has to be dissipated in the SOL before reaching the target. This can be achieved with divertor detachment, a regime in which a large fraction of the power is transferred to and subsequently radiated away by a blanket of neutrals formed in front of the targets. Detachment is routinely achieved on many divertor tokamaks and its onset is manifested by parallel-to-B plasma pressure gradients in the SOL and a rollover of target ion flux density with increasing core density during density ramp-up discharges [24]. It is generally very difficult to diagnose the divertor region with spatially resolved measurements. To our knowledge, divertor Thomson scattering systems have been installed solely at ASDEX-U [126] and DIII-D [127]. The complicated diagnostic access to divertor plasmas in tokamaks motivates to study the effect in linear plasma devices. The Pilot-PSI linear plasma generator offers a high density ($n_e \sim 10^{21}$ m^{-3}) and low temperature ($T_e \sim 1$ eV) plasma whose parameters are similar to those expected during partially detached ITER divertor operation [54].

5.3 Experimental setup

Pilot-PSI [55] is a linear device using a high pressure cascaded arc discharge source [56]. Figure 1 gives a schematic overview of the device. A cylindrical r-ϕ-z coordinate system is used, where the z-coordinate is aligned with the magnetic field and is the axis of symmetry of the plasma beam and z=0 is situated at the exit of the source discharge channel. The cascaded arc operates in steady state and the discharge channel is fed by a constant gas flow rate typically in the range of 1.5 - 3.0 standard liters per minute (slm), resulting in a discharge channel pressure in the range 10^3 -10^4 Pa. The plasma exhausts into the vacuum vessel and is confined by an axial magnetic field that can be varied in discrete steps between 0.2 T and 1.6 T. Ionization fractions close to the source are between 5% and 10%. Typical discharge currents are 100 - 220 A. The pressure in the vessel is determined by the pumping and the inflow of the residual neutrals from the source and is typically of the order of several Pa. The plasma beam is terminated at axial position z=56 cm by a solid, actively cooled target. The key diagnostic was Thomson scattering which was performed at two axial locations (at z=4 cm and z=54 cm, referred to as "upstream" and "target" locations, respectively) and is particularly suited to measure low temperature plasmas in the range 0.07 eV to 5.0 eV [66]. A single Langmuir probe was embedded in the target with a collecting area

Table 5.1 – List of shots with the corresponding machine settings. I_{dis} is the source discharge current, Q_v is the gas inflow to the source, "Pumping" corresponds to the rotational speed of the Roots pump. The label "SP"corresponds to the case when a second, identical Roots pump was switched on to further reduce the neutral background pressure P_n.

I_{dis} (A)	Q_{V} (slm)	Pumping (rpm)	P_n (Pa)	Pumping speed (l/s)
220	2.5	1000	12.6	331
220	2.5	1500	8.6	484
220	2.5	2000	6.6	631
220	2.5	2870	5.1	817
220	2.5	SP	3.2	1302
220	1.8	1000	8.9	337
220	1.8	1500	6.1	492
220	1.8	2000	4.7	638
220	1.8	2870	3.6	833
220	1.8	SP	2.4	1250
120	2.5	1000	12.6	331
120	2.5	1500	8.6	484
120	2.5	2000	6.7	622
120	2.5	2870	5.0	833

perpendicular to the magnetic field lines. The collector was a circular copper surface of 2 mm in diameter while the rest of the target area was covered by a boron-nitride (BN) coating. The pressure at the gas inlet to the source and the background neutral pressure, which we will denote P_n, were measured by a strain gauge and a capacitance manometer, respectively. The pumping speed was regulated in order to control P_n. Investigating the effect of P_n on the Pilot-PSI plasma beam was the main focus of this experiment and was performed for a B-field of 0.2T and several values of input powers and source gas flow settings. Tab. 5.1 gives the shot numbers and the corresponding machine settings used in the experiment.

5.4 Results & Discussion

For the low field (B=0.2T) setting, P_n scans were performed by changing the pumping speed for two values of gas flow and discharge current settings (Tab. 5.1). The range of achieved P_n varies from 2.4 Pa to 12.6 Pa.

5.4.1 Effect of P_n on source operation

It is important to show that changes in P_n do not affect operation of the source. In Fig. 5.2 the dependence of the discharge channel pressure and the arc input power is plotted against the neutral pressure P_n in the vessel (the arc is current-regulated).

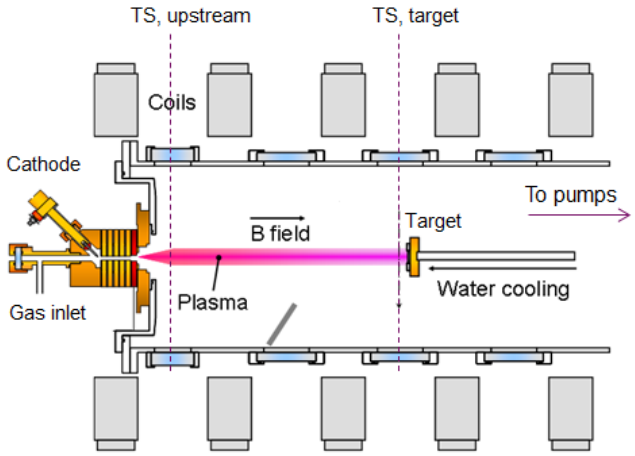

Figure 5.1 – Schematic layout of the Pilot-PSI device.

There is no significant dependence of neither of the quantities on P_n in the given range of 2.4 to 12.6 Pa. On the other hand P_n strongly depends on the inlet gas flow Q_v and the discharge current I_{dis}. We conclude in this section that by changing P_n we do not change the conditions under which the cascaded arc discharge operates.

5.4.2 Effect of P_n on upstream plasma

Fig. 5.3 shows radial plasma profiles for the case I_{dis}= 220A and Q_V=2.5 slm (Tab. 1) for the lowest and highest case of P_n, 3.2 Pa and 12.6 Pa, respectively. As can be seen from Fig. 5.3, at the upstream location, an increase in P_n leads to the decrease of T_e but at the same time also to an increase of n_e. On the other hand, we observe that the electron static pressure is approximately conserved. This indicates that no energy is lost due to changes in P_n at this location of the plasma beam. It is proposed that the electrons are cooled due to ionization of a significantly larger amount of neutrals that are present inside (or within) and in the vicinity of the plasma beam. Conversely, this additional ionization causes the observed increase in n_e. This behavior is analogous also for other cases of I_{dis} and Q_v. The plasma static pressure was calculated assuming quasi-neutrality ($n_e = n_i$) and equipartition ($T_e = T_i$) which holds given the low temperature, high density plasmas in the experiment. Additionally, recent measurements using a collective Thomson scattering (CTS) diagnostic at Pilot-PSI [124] have confirmed T_e=T_i at z =4 cm. It is also important to justify neglecting the dynamic pressure component in this comparison. It is known from earlier work using spectroscopic measurements [54, 128] that the plasma flow velocity at z=4 cm is between 2 km/s and 5 km/s for a broad range of machine settings in terms of B, I_{dis} and Q_{V}. Knowing the plasma static pressure p_{stat}, the total plasma pressure p_{tot} can be calculated in as $p_{\text{tot}} = p_{stat}(1+M^2)$, where M is the Mach number. The bracket on the RHS is a factor representing the contribution of the dynamic pressure. If we assume that the axial flow velocity in our experiment did not exceed 5 km/s, the increase of the total pressure at z=4 cm associated with the dynamic component would not exceed

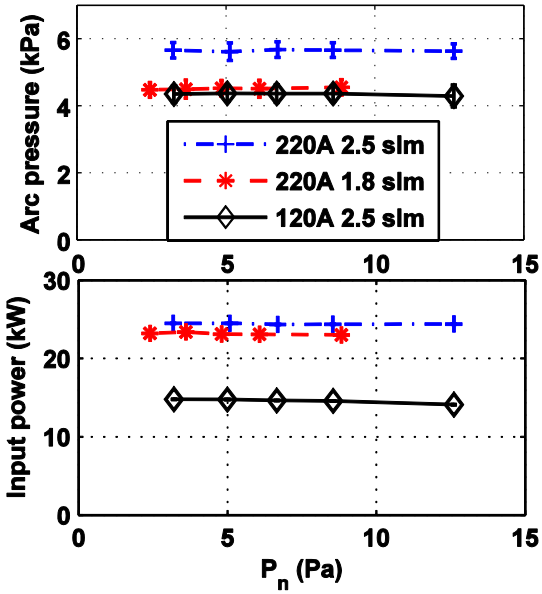

Figure 5.2 – Dependence of the pressure in the arc discharge channel and the arc input power on the neutral pressure in the vessel P_n for various source settings.

5% (center of the beam) and 12% (edge of the beam) of the static plasma pressure for the high P_n case. This is about the same order as the uncertainty associated with the reproducibility of the shots and therefore we choose to neglect the dynamic component in the upstream (z=4cm) location, $p_{\mathrm{u,tot}} \simeq p_{\mathrm{u,stat}}$. For the lower P_n cases, the same consideration leads to even smaller differences in $p_{\mathrm{u,tot}}$ and $p_{\mathrm{u,stat}}$. In this section it is concluded that the upstream pressure stays reasonably constant over the range of background pressures achieved during the experiment. This is important since our aim is to quantify how the neutral pressure affects the reduction of plasma pressure from upstream location to target location.

5.4.3 Effect of P_n on target plasma

Figure 5.4 compares upstream to target plasma parameters for the same low and high Pn cases as in the previous section. It can be seen that there is a significant Te drop from upstream to target for both Pn cases. While at the upstream position, Te $\sim$ 3 eV, at the target this is reduced to Te $\sim$ 0.2 - 0.3 eV. At such low temperatures below 1 eV volume recombination processes are expected to be important [129]. As for n_e, for the low pressure (P_n=3.2 Pa) case it is reduced from 2×10^{20} m^{-3} to $\sim 8 \times 10^{19}$ m^{-3} while for the high pressure (P_n=12.6 Pa) case the target density is reduced to 2×10^{18} m^{-3}. Such a strong drop cannot be explained by Bohm-like acceleration of the plasma flow velocity towards the neutralizing target plate since the target T_e is comparable in both P_n cases, implying comparable sound speed c_s. Again, the $T_e = T_i$. assumption was used here, since T_i was not measured at the target. In order to explain the strong reduction of density by the Bohm mechanism, T_i at the target would have to be much higher than at the source (z=4 cm) which is unrealistic.

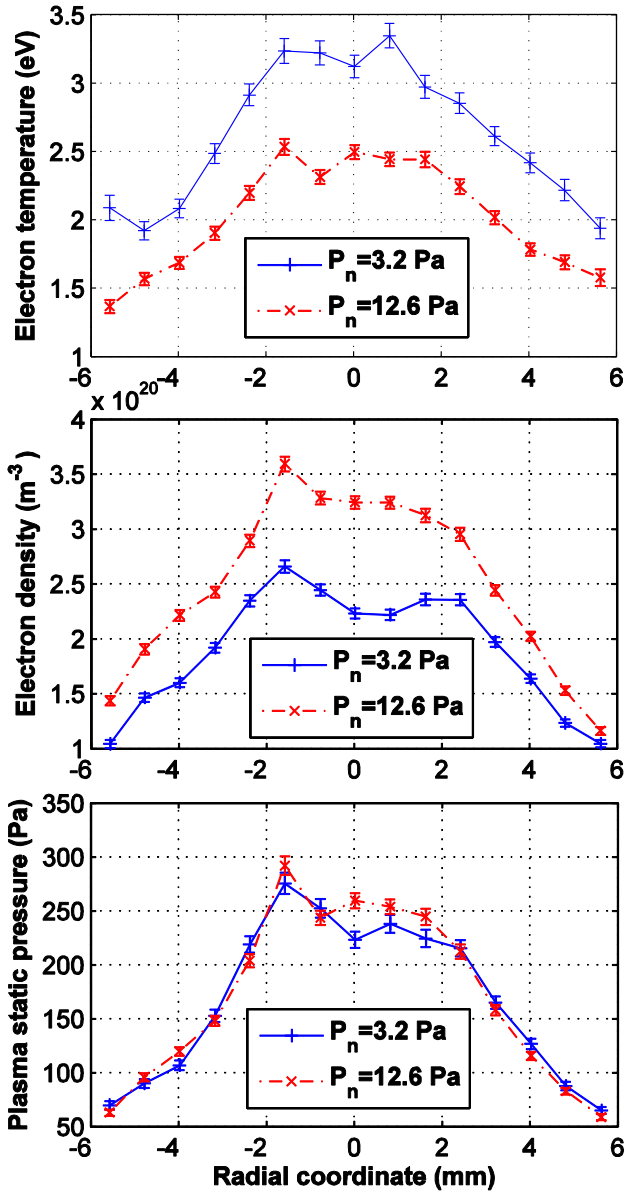

Figure 5.3 – Upstream profiles of T_e, ne and the static electron pressure for the cases of low (3.2 Pa) and high (12.6 Pa) P_n.

5.4.4 Comparison of TS and LP measurements

In order to confirm the extremely low densities measured at the target by TS they are compared to the ion flux measurements from the embedded target Langmuir probe (LP). The ion branch of the LP I-V characteristic yields the ion saturation current which was calculated by fitting the ion branch of the probe IV-characteristic by a first order polynomial and subsequently extrapolating its value at the floating potential V_f. I_{sat} can be directly related to the incoming ion flux density to the probe, $\Gamma_{\mathrm{LP}} = I_{\mathrm{sat}}/A$, where I_{sat} is the probe ion saturation current and A=πr^2 is the probe

area and r=1 mm is the probe radius. Next, the ion flux density to the target was computed from the measured profiles assuming Bohm sheath edge conditions, $\Gamma(r) = n_e(r)c_s(r) = n_e(r)\sqrt{(2k(T_e(r) + T_i(r))/m_i)}$, where k is the Boltzmann constant and mi is the hydrogen ion mass (all SI units). The obtained radial profile of the ion flux density can be fitted by a Gaussian function of the form $\Gamma(r) = \Gamma_{max}\exp(-(r/\lambda_\Gamma)^2)$, where $\Gamma_{\max}$ is the peak flux density and λ_Γ is the characteristic profile width, both obtained from the fitting procedure. The ion flux density averaged over a hypothetical probe surface at the TS position can then be evaluated as the following surface average:

$$\langle \Gamma_{TS} \rangle = \frac{\int_0^{2\pi}\int_0^R r\Gamma(r)\mathrm{d}r\mathrm{d}\phi}{\int_0^{2\pi}\int_0^R r\mathrm{d}r\mathrm{d}\phi} = \Gamma_{\max}\frac{\lambda_\Gamma^2}{R^2}\left(1 - \exp\left(-\frac{R^2}{\lambda_\Gamma^2}\right)\right) \tag{5.1}$$

Based on mechanical tolerances and precision of alignment, we assume that the center of the probe was aligned with the center of the plasma beam with a precision of 1.5 mm. Given the typical characteristic Γ profile widths λ_Γ are in all cases >10 mm, the uncertainty in $\langle \Gamma_{\mathrm{TS}} \rangle$ related to this potential misalignment is lower than the uncertainty of the n_e and T_e measurements themselves (the propagation of uncertainty for the derived quantity $\Gamma(r)$ is included via the variance formula). Figure 5(a) shows an absolute comparison of Γ_{TS} and Γ_{LP} as a function of P_n while figure 5(b) compares Γ_{TS} and Γ_{TS} directly for different arc discharge conditions given in Tab. 1. An exponential reduction of the ion flux density with P_n is found. It can be seen that the flux densities measured by the two diagnostics show agreement within 30%, with regard to the fact that measurements were performed 2 cm from each other and to the uncertainty associated especially with the analysis of the Langmuir probe IV characteristic. In this section, the extreme rarefaction of the target plasma spanning three orders of magnitude, is confirmed by comparing two independent diagnostics.

5.4.5 Plasma pressure loss

Plasma detachment in tokamaks is manifested by breaching of the plasma pressure balance on the open magnetic flux surfaces of the SOL [24]. These pressure gradients appear when the target T_e is low enough for momentum-removal processes to start occurring, typically for $T_e < 10$ eV [101]. From sections 5.4.2, 5.4.3 it can be seen that the plasma T_e produced by Pilot-PSI is about 3.5 eV or lower (depending on the cascaded arc source input settings), falling off strongly towards the target (for the case of $B = 0.2$T). In this section, the upstream pressure is compared to the target pressure via the introduction of a pressure loss factor, defined by $f_{\mathrm{loss}} = p_u/p_t$ where p_u and p_t are the upstream and target total plasma pressures (static+dynamic), respectively. Such ratios, or their inverse equivalents, are commonly introduced in two-point models of tokamak SOLs, e.g. [102, 103]. The f_{loss} was estimated in the following way. First, we have made the same ansatz as in section 5.4.4 and fitted the pressure profiles by Gaussian curves of the form $p(r) = p_{\max}\exp(-(r/\lambda_p)^2)$, similarly as the flux profiles. Then, f_{loss} is determined in two ways: 1) dividing the peak plasma pressures of upstream and target profiles (corresponding to the center of the profile, $r = 0$ and 2) dividing the mean plasma pressure of upstream and target profiles. We

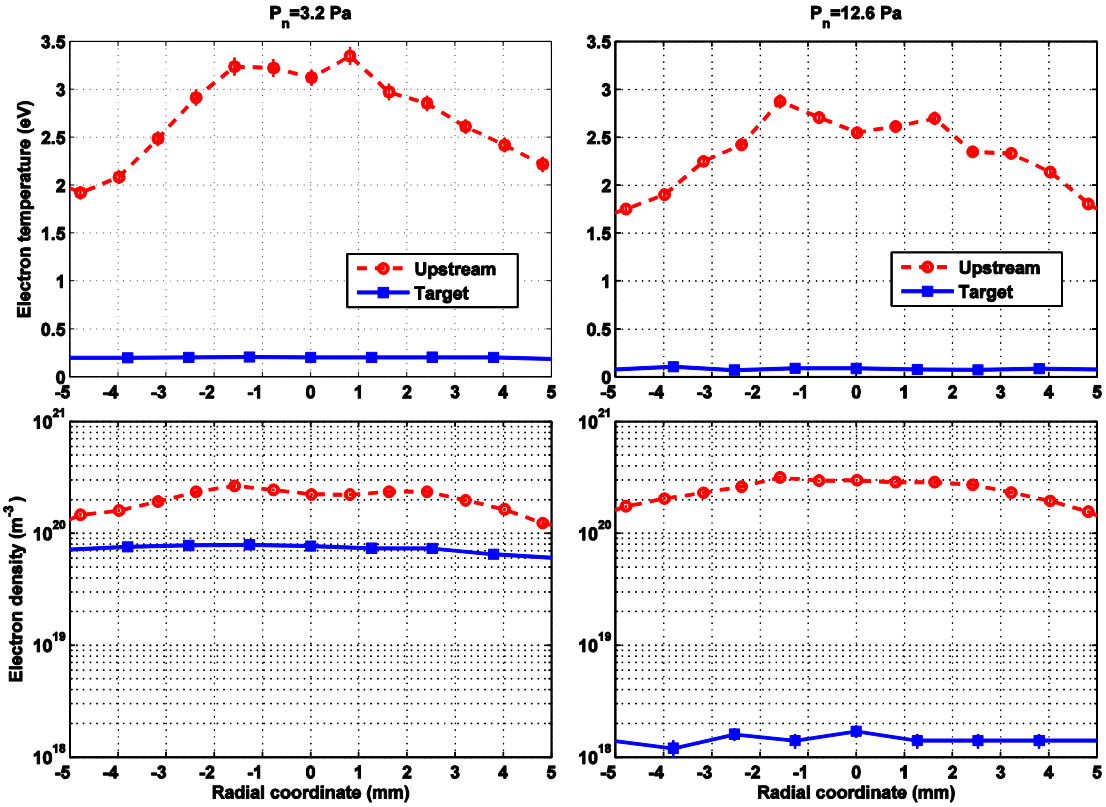

Figure 5.4 – Comparison of the upstream (red circles) and target (blue squares) T_e and ne TS radial profiles for low (3.2 Pa) and high (12.6 Pa) background neutral pressure P_n.

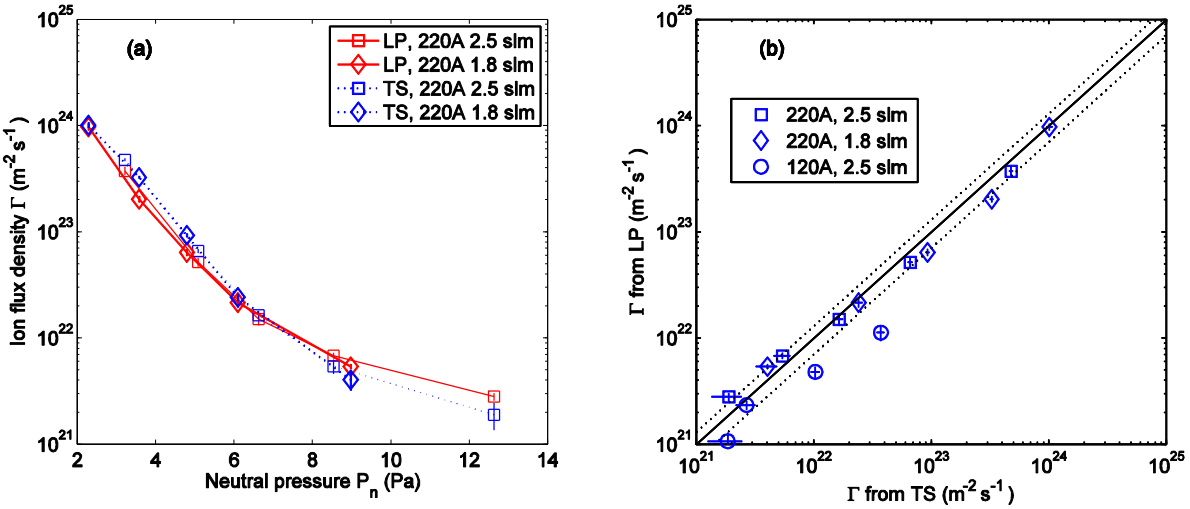

Figure 5.5 – Comparison of the ion fluxes from the LP and TS (section 5.4.4) displayed as a P_n scan (a) and as a direct comparison (b) for different source settings from Table 1. In (a), the 120A case is omitted in order to maintain clarity of the figure, nevertheless showing the same trend. In (b), the solid line indicates equality while the dashed lines represent 30% deviation from equality.

will label these loss factors $f_{\text{loss,max}}$ and $f_{\text{loss,mean}}$, respectively. Figure 5.6 summarizes the results by plotting $f_{\text{loss,max}}$ and $f_{\text{loss,mean}}$ as a function of P_n and the central T_e at the target. Similarly to the flux reduction from section 5.4.4, the reduction of pressure is strongly non-linear. For the lowest case of P_n, $f_{\text{loss,mean}} \sim 4$ while for the highest P_n, $f_{\text{loss,mean}} \sim 1000$. Globally, the pressure loss factor increases exponentially in the P_n range between 2 and 6 Pa and for higher values shows a trend to saturate, for each discharge condition. Moreover, $f_{\text{loss,max}}$ is always higher than $f_{\text{loss,mean}}$.

It is important to restate that the calculations of the loss factors assume $T_e = T_i$. If this is valid, the principal source of uncertainty in the estimation of f_{loss} originates in the determination of the total plasma pressure using expression 5.1. For the upstream location, the dynamic pressure contribution is neglected, $(1+M^2) \approx 1$. This is discussed and justified in section 5.4.2. As a result, the p_u is slightly underestimated. At the target, the Bohm sheath edge condition is used, $M = 1$. However, in reality, target TS measurements were performed ∼2 cm in front of the surface, still far from the sheath edge, meaning that $M < 1$. The M =1 assumption was used in order to provide an upper bound for p_t. Thus, p_t used for calculation of f_{loss} is overestimated, at most by a factor of 2. Both uncertainties are marginal compared to the order-of-magnitude differences between p_u and p_t and in fact, both of them go in the direction making f_{loss} even higher. If the assumption of equipartition stated above is not valid and $T_i = \alpha T_e$ at the target, pt would be by a factor $\alpha/2 + 1$ higher. This would impact f_{loss} by reducing it by the same factor.

The measurements clearly demonstrate that the f_{loss} is determined by the P_n in the vessel, indicating the importance of plasma-neutral interaction processes (including interactions with H_2 molecules). However, it is important to point out again that the build-up of P_n in the vessel is not determined by the recycling and recombining neutrals, as in a tokamak, but by the influx of residual neutrals from the source, making direct extrapolation of the results to tokamaks extremely challenging. On the other hand, this enables to decouple P_n from the target flux Γ, while in tokamaks these two quantities are interlinked in a non-trivial way. Based on the existing literature on low temperature plasmas in tokamak divertors and linear devices, the main relevant plasma momentum loss processes considered responsible for the observed floss under the present experimental conditions are suspected to be 1) ion-neutral friction, which is mediated by the resonant charge-exchange (CX) process and elastic i-n collisions, both active in plasmas with $T_e < 5$ eV [102] 2) electron-ion recombination (EIR), comprising three-body and radiative recombination, shown to be occurring in detached divertors of C-mod, JET and ASDEX-upgrade at $Te \sim 1$ eV [129–132] and 3) molecule-assisted/activated recombination (MAR), first identified in a fusion relevant environment at NAGDIS-II [40]. The latter is strongly dependent on the presence of rotationally and vibrationally excited molecules. The presence of such molecules was shown via Fulcher-band spectroscopy in Pilot-PSI [109]. Moreover, for a cascaded arc source similar to Pilot-PSI, it has been shown that the population of high-n excited states of hydrogen cannot be explained by EIR alone, suggesting MAR as a possible population process [133]. A future path to follow in order to provide even more detailed data would be to exploit the Magnum-PSI linear plasma generator which will enable to

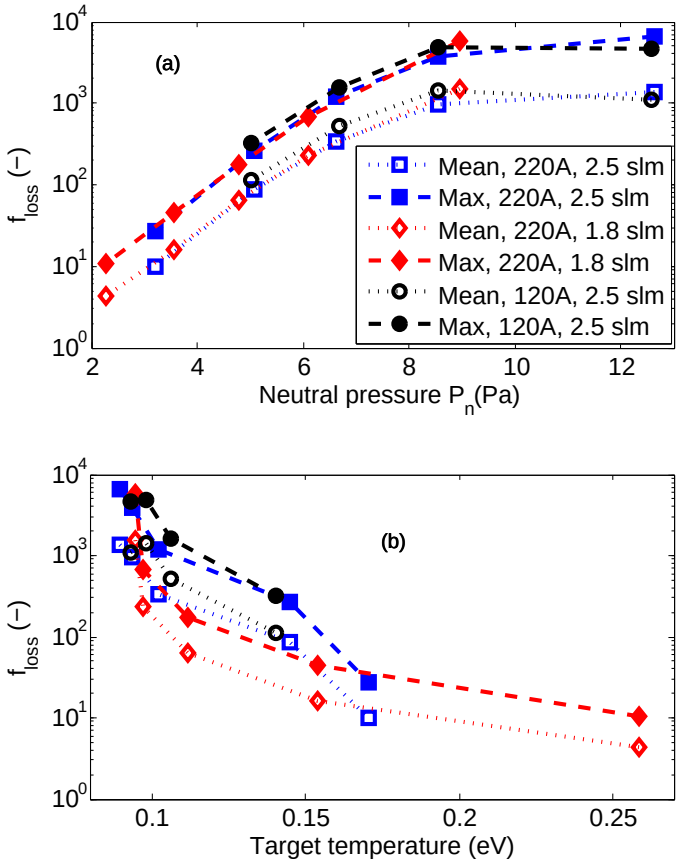

Figure 5.6 – Pressure loss factor calculated from mean plasma pressure (dotted curves) and peak values (dashed curves) as a function of P_n (a) and the target temperature (b) for the different discharge conditions.

move the plasma source in the axial direction, thus enabling axial measurements and reconstruction of 2-D maps of the plasma T_e and n_e. Moreover, it will be equipped with a collective Thomson scattering (CTS) diagnostic system to measure ion temperatures and flow velocities.

5.5 Conclusions

A set of measurements with Thomson scattering (TS) at two axial locations and a single Langmuir probe (LP) embedded in the target were performed at the Pilot-PSI linear device, mainly focusing on the influence of the background neutral pressure P_n in the vessel. T_e drops, typically from 3 eV to 0.1 eV were observed from upstream to target location, indicating the importance of both momentum loss processes and volume recombination. Moreover, extreme rarefaction of the plasma beam was found from source to target location in terms of reduction of the ion flux density and the plasma pressure. These quantities were determined using a target embedded LP and incoherent TS, respectively. By varying P_n from 2.4 Pa to only 12.6 Pa, the loss of plasma pressure changes approximately exponentially, from ∼5 up to ∼5000. The

comparison of the target TS measurements and the LP show reasonable agreement, taking into account the fact that the measurements are situated 2 cm from each other. Lastly, the results show that the performance of cascaded arc linear devices in terms of ability to deliver high plasma fluxes to a target can be significantly improved by marginal reduction of the background pressure (i.e. by applying additional pumping).

Chapter 6

Soledge2D-Eirene simulations of the Pilot-PSI linear plasma device compared to experimental data

Published as K. Jesko, Y. Marandet, H. Bufferand, J.P Gunn, H.J van der Meiden, G. Ciraolo, Soledge2D-Eirene simulations of the Pilot-PSI linear plasma device compared to experimental data, Contrib. Plasma Phys. ***58*** *(2018) 798-804.*

6.1 Abstract

Predictions for the operation of tokamak divertors are reliant on edge plasma simulations typically utilizing a fluid plasma code in combination with a Monte Carlo code for neutral species. Pilot-PSI is a linear device operating with a cascaded arc plasma source that produces plasmas comparable to those expected in the ITER divertor ($T_e \sim 1$ eV, $n_e \sim 10^{21}\mathrm{m}^{-3}$). In this study, plasma discharges in Pilot-PSI have been modelled using the Soledge2D fluid plasma code [72] coupled to the Eirene neutral Monte Carlo code. The plasma is generated using an external source of plasma density and power. These input parameters are tuned in order to match Thomson scattering (TS) measurements close to the cascaded arc source nozzle. The sensitivity of the simulations to different atomic physics models was explored. It was found that elastic collisions between ions and hydrogen molecules have a strong influence on calculated profiles. Without their inclusion, supersonic flow regimes are obtained with M ~ 2 close to the target plate. Simulation results have been compared with experimental findings using TS close to the target and in the case of Pilot-PSI, a Langmuir probe embedded in the target. Comparison between experimental trends observed in a background pressure scan [100] and the simulations show that the inclusion of the elastic collision is mandatory for the trends to be reproduced.

6.2 Introduction

The technological limit of steady-state power loading of the ITER plasma-facing components (PFCs) is 10 MW/m^2 [19]. The plasma heat flux to the PFCs is chanelled through a narrow layer given by the power flux fall-off length, λ_q. The numerical value of this parameter has been extrapolated to ITER using multi-machine scaling [18] and has a pessimistic value of $\sim$ 1 mm. Therefore, in order to avoid excessive heating of the PFCs, a large fraction of the plasma heat flux has to be dissipated before reaching the divertor targets. This can be achieved by radiation of a significant amount of power by impurity species and/or by transferring the plasma kinetic energy to neutral hydrogen particles (e.g. via excitation, charge-exchange) which are inherently present in the vicinity of the plasma-solid interface. Neither photons nor neutral particles follow magnetic field lines and can potentially spread the heat load over a larger area of the PFCs. Additionally, these processes can lead to detached divertor regimes, where significant reduction of power and particle fluxes can occur between upstream and target locations. For ITER and next step fusion facilities, predictions of heat and particle transport from upstream locations of the scrape-off layer to the PFCs rely largely on modelling using fluid/Monte Carlo code packages (i.e. SOLPS, SolEdge2D-Eirene, EDGE2D-Eirene, SOLDOR/NEUT2D). Within this work, we use the SolEdge2D-Eirene code to simulate the Pilot-PSI linear plasma device. Pilot-PSI offers a high density ($n_e \sim 10^{20} - 10^{21}$ m^{-3}), low temperature ($T_e \sim$ 0.1 - 5 eV) plasma relevant to detached divertors. The simulations are compared to experimental data published in [100]. Such an approach enables to 1) provide interpretation for the experimental results by detailed bookkeeping of individual processes within the code, 2) assess how accurately the code can reproduce experimental findings with implications for divertors and 3) point towards ways of improving the performance of linear plasma devices to deliver high power and particle fluxes for the needs of material testing.

6.3 The Pilot-PSI linear plasma generator

The Pilot-PSI [54] linear device uses a cascaded arc discharge source and is depicted in Fig. 7.1. A cylindrical r-ϕ-z coordinate system is used, where the z-coordinate is aligned with the magnetic field and is the axis of symmetry of the plasma beam and z=0 is situated at the exit of the source discharge channel. The cascaded arc operates in steady state and the discharge channel is fed by a constant gas flow rate typically in the range of 1.5 to 3.0 standard liters per minute (1 slm $\sim 4\times10^{20}$ molecules per second). The plasma leaving the arc discharge chamber is confined by an axial magnetic field that in the experiment shown here had a magnitude of 0.2T. Typical discharge currents are 100 - 220 A. The background neutral pressure in the vessel is given by the pumping and the inflow of the residual neutrals from the source and is typically of the order of several Pa. The plasma beam is terminated at axial position z=56 cm by an actively cooled solid target. The key diagnostic was Thomson scattering which was performed at two axial locations (at z=4 cm and z=54 cm, referred to as "upstream" and "target" locations, respectively) and is particularly suited to measure low temperature plasmas

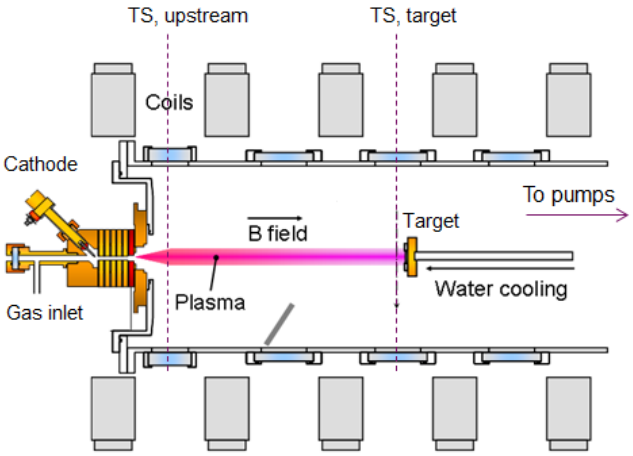

Figure 6.1 – Schematic layout of the Pilot-PSI linear plasma device, with the two positions where radial profile measurements using Thomson scattering can be performed.

in the range 0.07 eV to 5.0 eV [66]. A single Langmuir probe was embedded in the target with a collecting area perpendicular to the magnetic field lines. The current collecting surface was circular and 2 mm in diameter. The backround neutral pressure, which we will denote as P_n, was measured by a capacitance manometer.

6.4 Simulation setup

The Soledge2D transport code was designed for investigation of the transport of quasineutral plasma in the tokamak edge plasma and in the SOL [72, 134] and is coupled to the kinetic Monte-Carlo (MC) code Eirene [90]. The code assumes toroidal symmetry. The equations for density, parallel velocity and electron and ion temperature are solved. The parallel transport is solved self-consistently while the cross-field transport is imposed by ad-hoc diffusion coefficients. Kinetic corrections for cases with low collisionality are provided by the use an artificial flux limiter. Drifts, electric fields and currents are implemented in Soledge2D [135], however they were turned off in simulations presented in this contribution.

The geometry of the linear plasma device may seem very different from a tokamak, however they have common aspects, which enable to create a field-aligned grid that the code can directly use. The grid for the linear device can be regarded as a subspace of a tokamak grid. It is in fact topologically equivalent to a scrape-off layer with no toroidal field and no major radius, i.e. the plasma is simulated up to the axis of symmetry, unlike tokamaks. The axial magnetic field of the linear device corresponds to the poloidal magnetic field of a tokamak and had a constant value of 0.2 T in all simulations presented here, in line with the experiment. The grid used in the simulations is depicted in Fig. 7.2. Additionally, a variable grid density is used in order to provide high resolution in the plasma beam and close to the walls, while in areas of less interest the cells are larger, to save computational time.

The plasma wall interaction is treated using the penalization technique [86] which

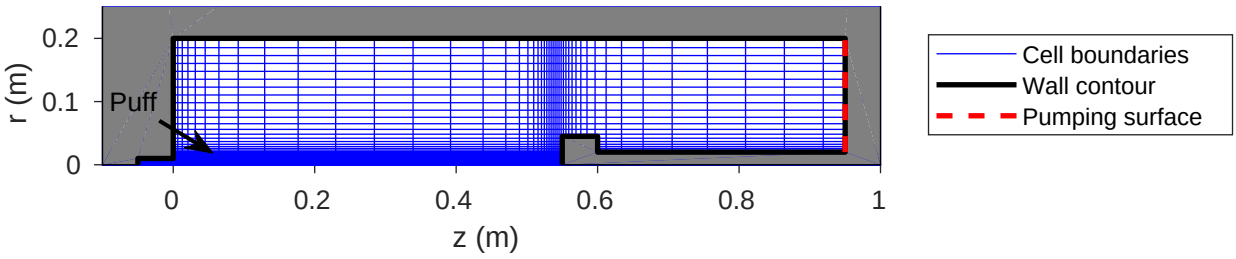

Figure 6.2 – The Pilot-PSI non-uniform grid used in the Soledge2D-Eirene simulations.

recovers standard Bohm boundary conditions and sheath heat transmission at the plasma-wall interface, i.e. $|M| \geq 1$ and $q_{t,\alpha} = \gamma_\alpha n M c_s T_\alpha$, where M is the Mach number, $q_{t,\alpha}$ is the energy flux density through the interface for species α (electrons or ions), c_s is the sound speed and γ_α are the sheath heat transmission factors for ions and electrons, set to 2.5 and 4.5 , respectively. The Soledge2D energy equations are written in terms of the total energy. However, the values of heat transmission factors reported here are for the internal energy part. We assume the ion velocity distribution function at the sheath edge to be a shifted Maxwellian with c_s normal to the wall, so the effective sheath heat transmission factor for ions is in fact 3.5 for $T_i = T_e$. This choice ensures internal consistency of the code and is related to the coupling of SolEdge2D and Eirene. On the axis of symmetry the boundary condition of vanishing perpendicular gradients is used.

Anomalous values are assigned to the radial transport coefficients. For density, a diffusion coefficient of $D_i = 0.3$ m^2/s is chosen based on an estimate obtained from the Bohm diffusion coefficient for T_e=1 eV and B =0.2 T and is found to reproduce broadening of beam profiles at least qualitatively, Fig. 6.5 (D). Simulation results were found not to be sensitive to the radial thermal conductivities in the range 0.1 - 3.0 m^2/s. In the simulations, values of $\chi_\perp^{e,i} = 0.3$ m^2/s are used.

It is beyond the scope of this contribution to model the details of the cascaded arc discharge self-consistently. This would require inclusion of the electric currents and drifts in the simulations, as well as thermionic emission from the hot cathode. However, the principal focus here lies in the interaction of the plasma beam with the surrounding neutral gas. Therefore, the plasma particle and power sources are directly prescribed as external volumetric source terms in the Soledge2D equations. The shape and magnitude of these is defined to match Thomson scattering profiles measured close to the source. For example, the external volumetric source terms for the plasma ion/electron source has the form of a Gaussian function in both r and z directions:

$$S_n^{(ext)}(r,z) = \frac{S_n^{(ext,tot)}}{C} \exp\Big(-(r-r_{src})^2/\lambda_r^2 \Big) \exp\Big(-(z-z_{src})^2/\lambda_z^2 \Big), \tag{6.1}$$

where r_{src}, z_{src} are the positions of the profile maxima, λ_r, λ_z are the profile widths, C is a normalization constant such that the volume integral over the simulation domain be equal to the total number of injected particles, i.e. $\int_V S_n^{ext} \mathrm{d}V = S_n^{ext,tot}$. The position and spatial extent of the external volumetric source terms was chosen such that it stays

well within the small area of the cascaded arc source, i.e. $r_{src} = 0$, z_{src} =-2.5 cm, $\lambda_r = 0.5$ cm, $\lambda_z = 1$ cm, Fig. 7.2.

The interaction of plasma and neutrals is handled by the Eirene Monte-Carlo code [90]. In the case of Pilot-PSI, there are three channels through which neutral particles can enter the system. 1) The constant gas flow from the cascaded arc discharge source, 2) Recycling source at the plasma wall interface and 3) Volumetric recombination. The latter two are calculated self-consistently by Eirene, while the constant gas inflow rate is simulated as a constant puff of H_2 at ambient temperature (0.03 eV) at the location depicted in Fig. 7.2. In the experiment, this is an externally controlable quantity and in the experiment [100] the value of the total source inflow was 2.5 standard liters per minute (slm) corresponding to about 10^{21} H_2/s in all experiments presented here. This value is also used in the simulations. The recycling coefficent at the plasma-wall interface is set to unity throughout all the simulations presented here. In order to achieve steady state a pumping surface must be present. This is located at the back end of the vessel, Fig. 7.2, where one can specify an absorption probability for neutral particles. The absorption probability is set to match measurements of the neutral pressure in the vacuum vessel, typically in the range of several Pa. The species considered in Eirene are hydrogen atoms H and molecules H_2 and H_2^+ molecular ions. Two different sets of atomic and molecular reactions were used in the simulations and are listed in Tab. 6.1. For the sake of clarity we label them AM1 and AM2. AM1 was the default set of reactions available in Eirene. AM2 corresponds to the model described in [92] (first used in [93]). However, in our case it is without neutral-neutral collisions and radiation opacity. Here, the main difference between the models is that the AM2 model contains two more reactions: elastic collisions between H^+ and H_2 and "ion conversion", which is a charge-exchange between H^+ and H_2. It was shown in [92] that the elastic collisions can affect the results significantly. Moreover, [80] also shows high sensitivity of JET detachment simulations to the atomic physics model. In the next section, a sensitivity study of simulation results involving both models and their refinements will be presented in order to determine the key processes at hand, i.e. the ones with significant effect on the solution.

6.5 Results & Discussion

6.5.1 Impact of atomic physics on simulation results

In order to address the sensitivity of the plasma solution to the atomic physics, four different cases (a)-(d) of atomic physics reactions were used. Case (a) is the AM1 model, Case (b) is AM2, case (c) is AM2 but with the elastic collision (6), (Tab. 6.1) and ion conversion (7) artificially turned off (this case may seem identical to case (a), however in (a), the source database for rate coefficients for some reactions is different, see caption of Tab. 6.1). Lastly, case (d) is AM2 with only the ion conversion (7) turned off. For each case (a)-(d), a converged solution was obtained for a Pilot-PSI relevant plasma, with upstream n_e and T_e values of $\sim 3{\times}10^{20}$ m^{-3} and $\sim$ 3-5 eV. Fig. 6.3 shows parallel profiles of several plasma parameters for each of these four cases. The parallel profiles

Table 6.1 – List of atomic and molecular physics processes used in Eirene, listed for both AM1 and AM2. In AM1, rate coefficients for reactions (3)-(10) originate from the HYDHEL database (the remaining ones are from AMJUEL, while in AM2 all reactions are taken from the AMJUEL database. Both databases available from www.eirene.de.

#	Reaction	AM1	AM2	Event type
(1)	$H + e \rightarrow H^+ + 2e$	yes	yes	Electron impact ionization
(2)	$H + H^+ \rightarrow H^+ + H$	yes	yes	Charge exchange
(3)	$H_2 + e \rightarrow H_2^+ + + 2e$	yes	yes	Electron impact ionization
(4)	$H_2 + e \rightarrow 2H + e$	yes	yes	Dissociation
(5)	$H_2 + e \rightarrow H + H^+ + 2e$	yes	yes	Dissociative ionization
(6)	$H_2 + H^+ \rightarrow H_2 + H^+$	**n/a**	yes	Elastic collision
(7)	$H_2 + H^+ \rightarrow H_2^+ + H$	**n/a**	yes	Ion conversion
(8)	$H_2^+ + e \rightarrow H^+ + H + 2e$	yes	yes	Dissociation
(9)	$H_2^+ + e \rightarrow H^+ + H^+ + e$	yes	yes	Dissociative ionization
(10)	$H_2^+ + e \rightarrow 2H$	yes	yes	Dissociative recombination
(11)	$H^+ + e \rightarrow H$	yes	yes	Electron-ion recombination

are taken at a radius of 1.7 mm from the axis of symmetry. It can be seen that with case (a) (AM1) the plasma enters a supersonic regime very close to the nozzle. However, in case (b) (AM2), it is found that the plasma remains subsonic. Moreover, the ion flux and plasma pressure reaching the target are also strongly reduced as opposed to case (a). The principal differences in AM1 and AM2 are the inclusion of the two processes (6), (7) in Tab. 6.1. In order to discriminate which of these two processes is responsible for the significant qualitative change in behavior, case (d) is introduced, where the ion conversion reaction (7) is turned off. In this case, the situation is very similar as in case (b), although some minor differences can be spotted, e.g. n_e and also the ion flux density is somewhat higher troughout the profile in case (b). Indeed, it is the elastic collisions (6) that are responsible for keeping the flow subsonic in case (b). To support this, in Fig. 6.4 the volumetric source terms for plasma particles, momentum and energy are plotted for the same flux tube in the same color code as Fig. 6.3. Indeed, in case (b), a strong momentum sink appears throughout the parallel profile and is also present in case (d). Although it is known [80, 92] that the elastic collision process is important in detached/low temperature plasmas, this study illustrates the important consequences that omission of this process can have on the simulation results (e.g. by using a more crude atomic physics model).

The lower density and flux density in the case (b) as opposed to case (d) can be explained by the fact that the ion conversion reaction is the first step of the "molecular assisted recombination (MAR)" reaction chain, the second step being the dissociative recombination reaction (10). Therefore, by removing the reaction (7) the MAR pathway is now effectively forbidden in the simulations. Indeed, if one zooms in on the particle source term at the inset of Fig. 6.4, one can notice that for case (b) the ionization front moves closer to the cascaded arc source and that the recombination sink is much stronger as opposed to case (d) when the MAR is deactivated. On the other hand, the magnitude of the recombination is much smaller compared to ionization in

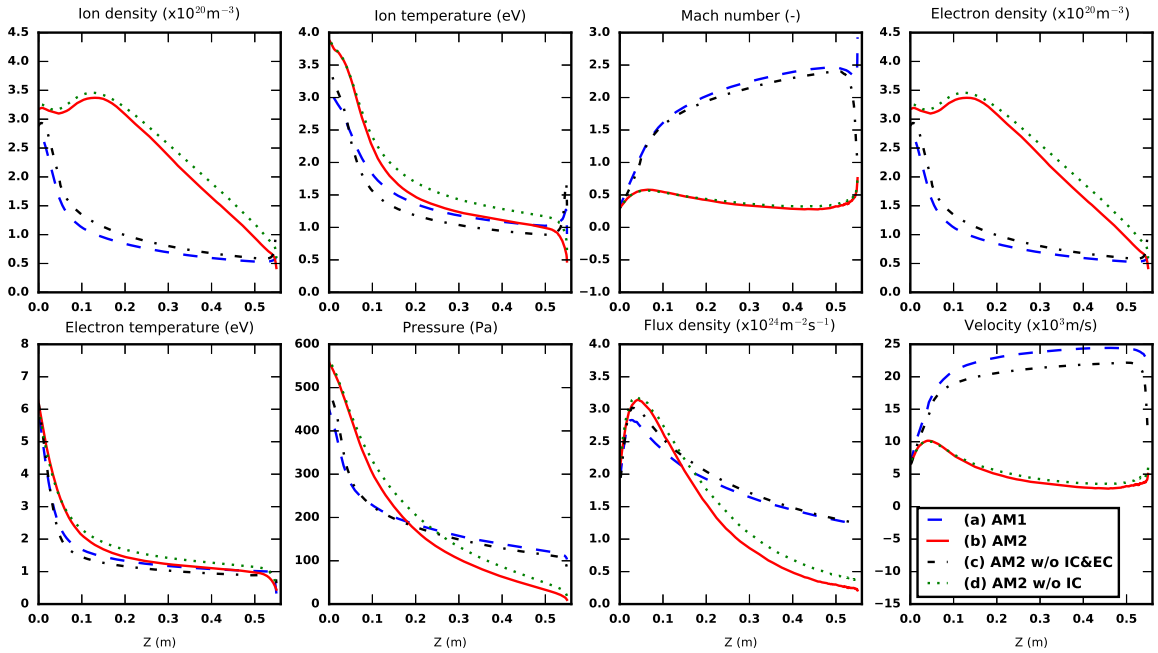

Figure 6.3 – Parallel profiles of various plasma parameters located 1.7 mm radially from the axis of symmetry, obtained by the Soledge2D-Eirene code for different versions of the atomic physics model.

both cases. It is also important to add that MAR was reported to be of large importance in linear devices [40, 136] and has triggered discussion whether it is an important recombination pathway in tokamak divertors in the past.

6.5.2 Comparison with experimental data

An experimental scan on the background pressure was performed, and is described in detail in [100]. Within the experiment, the pressure of the background neutral gas was changed between 3.2 Pa and 12.6 Pa by means of controlling the pumping speed. All the other input parameters were kept constant: The gas inflow rate to the cascaded arc source was 2.5 slm and the discharge current was 220A. Thomson scattering was performed at two locations of the plasma beam: 4 cm from the source nozzle and 2 cm in front of the target and a Langmuir probe was measuring the ion flux to the target. Experimentally, the plasma conditions at the source have been found to be insensitive to the background pressure [100]. In Fig. 6.5 (A) the ion flux density measured by the LP and recalculated from TS measurements at the target location are compared to values obtained from Soledge2D-Eirene. Strong reduction of the local ion flux is seen both by the LP and TS. In the simulations, the trend is recovered only with the full AM2 atomic physics model. However, the target ion flux density is completely insensitive to changes in the background pressure in the case where the ion conversion (IC) and elastic collision (EC) reactions are turned off. However, it was shown that the volume recombination sink is rather low in the simulations even with the IC included

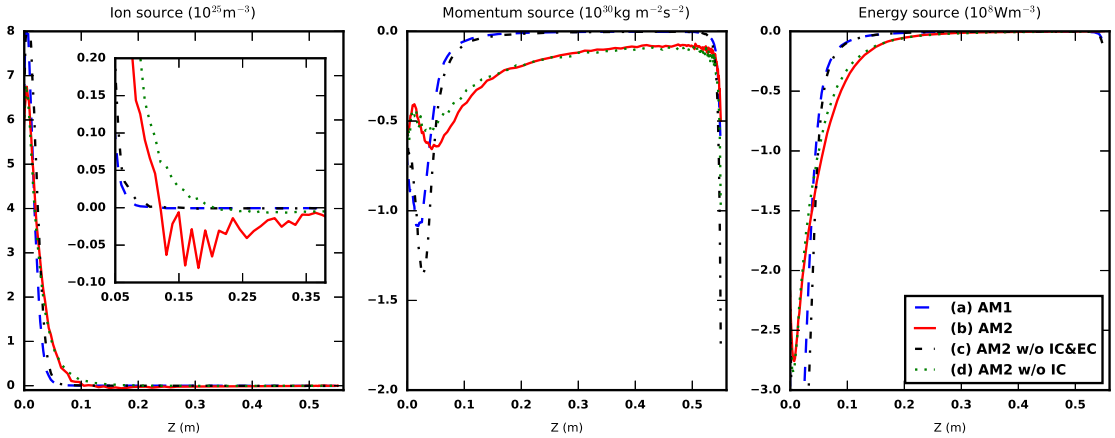

Figure 6.4 – Parallel profiles of the plasma particle, momentum and energy sources for the field line located 1.7 mm radially from the axis of symmetry. The inset figure is a zoom-in on the particle source in the range z=0.05 m to z=0.38 m.

in section 6.5.1. The reduction in ion flux density in the simulations is caused by the radial transport: The momentum sinks caused by the EC are efficient at slowing down the plasma flow (see section 6.5.1). The parallel ion transit time ($\tau_{\|} = \int_u^t v_z^{-1} \mathrm{d}z$, where v_z is the drift velocity in the z (parallel) direction) is strongly increased, as seen in Fig. 6.5 (D), giving the plasma more time for perpendicular diffusion.

In Fig. 6.5 (C) the full width half maxima of the radial ion flux profiles $\Gamma(r)$ are plotted as a function of the P_n for both experiment and simulation. In the experiment, it can be seen that at the target, the FWHM of the Γ profile is broadening with an increase in the background pressure, while at upstream it remains constant. In the simulations this trend can only be reproduced with the full AM2 model. It is to be noted that the magnitude of the broadening in the simulations is set by the perpendiclar diffusion coefficients. In the case of omission of the EC and IC processes a constant value of the broadening throughout the P_n scan is obtained.

Next, the total, radial section-integrated ion flux

$$\Gamma_{tot}(z) = \int_S r\Gamma(r,z)\mathrm{d}r\mathrm{d}\phi = 2\pi \int_0^R r\Gamma(r,z)\mathrm{d}r, \tag{6.2}$$

where S is the area of the radial section of the vessel and R is the vessel radius) is plotted for both experiments and simulations. There was no measurement available to calculate the plasma velocity upstream, however, from earlier work using spectroscopy [54, 128] it can be taken that the plasma flow velocity at z=4 cm is between 2 km/s and 5 km/s for a broad range of machine settings in terms of B-field, discharge current and flow rate. A Mach number of 0.4 was assumed for all the experimental profiles in question. This assumption may seem crude, however what we are really interested in is the *reductions* of plasma flux, rather than the absolute values. As can be seen in Fig. 6.5 (B), the total ion flux at the target is strongly reduced with the exception of the case with the lowest background pressure, for which we cannot conclude regarding this matter. For all the other P_n cases, the strong reduction of the integrated particle flux

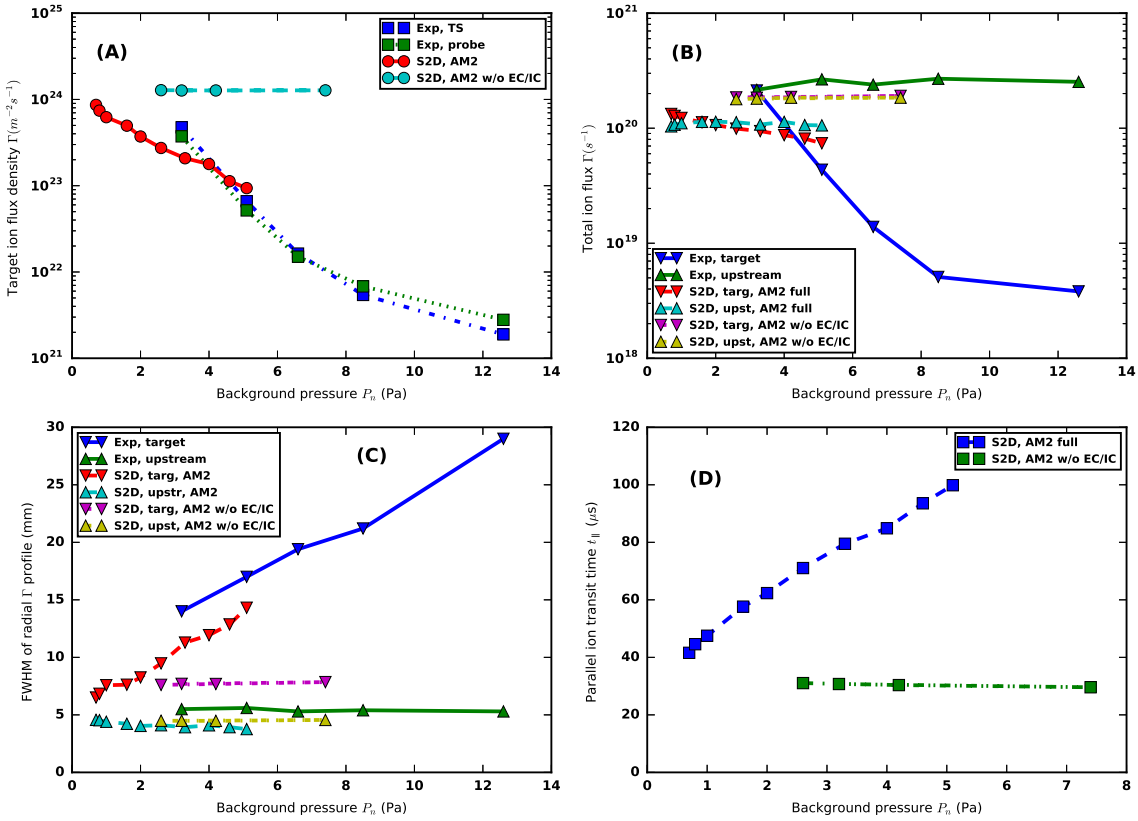

Figure 6.5 – Comparisons between measurements of various quantities with TS and a LP and Soledge2D-Eirene simulations using different versions of the atomic physics model: (A) Target ion flux density, (B) Total, section integrated ion flux upstream and at the target, (C) FWHM of the radial ion flux density profile upstream and at the target and (D) ion transit time for two cases of the atomic physics model.

$\Gamma_t ot$ translates to the fact that there has to be a net plasma sink in the volume between upstream and target. In the simulations, if the EC/IC reactions are not included, this trend is not recovered, there is no difference between the total flux at upstream and target. On the other hand, after the inclusion of these processes, a small reduction in the total ion flux is recovered in the simulations for the higher end of the P_n scan. For cases with very low background pressure, the total ion flux at the target increases compared to upstream. This means that ionization dominates over recombination in the volume between these two locations, given the higher temperature for the cases with low P_n. The low P_n cases were not accessible experimentally due to constraints of the pumping system and conversely, the high P_n cases could not be simulated due to numerical instabilities. Future work will be focused on broadening the window of overlap between measurements and simulations.

6.6 Conclusions

In this paper we report on Soledge2D-Eirene simulations of the Pilot-PSI linear plasma device with focus on using different atomic physics models and the sensitivity of the results to them. Subsequently, simulation results are compared to experimental data from Thomson scattering and a single Langmuir probe. The elastic collision between ions and hydrogen molecules is identified as a key player in the simulations, providing momentum sinks which keep the plasma flow subsonic as opposed to cases when the process is not included. The ion conversion reaction provides the pathway for the H_2^+ branch of molecule assisted recombination (MAR), which is the strongest recombination channel, however the total magnitude of recombination is small compared to the total ionization source. Comparison between experimental trends observed in a background pressure scan and the simulations show that the inclusion of the elastic collision is mandatory for the trends to be reproduced. This result demonstrates that it is important to use the atomic model introduced in [93] for detached/low temperature cases with high neutral molecule densities and that using versions without elastic collisions can lead to qualitatively different simulation results. Strong reduction of the ion flux density at the target is reproduced in the simulations, however it is mainly driven by radial transport. The total volume recombination source appears to be underestimated in the simulations. However, cases with high background pressure were not accessible so far in the simulations and are subject to further study.

Acknowledgments

This work was granted access to the HPC resources of Aix-Marseille University financed by the project Equip@Meso (ANR-10-EQPX-29-01) of the program "Investissements d'Avenir" supervised by the Agence Nationale pour la Recherche. This work was carried out with financial support from NWO and was carried out within the framework of the Erasmus Mundus International Doctoral College in Fusion Science and Engineering (FUSION-DC). This work has been carried out within the framework of the EUROfusion Consortium and has received funding from the Euratom research and training programme 2014-2018 under grant agreement No 633053. The views and opinions expressed herein do not necessarily reflect those of the European Commision.

Chapter 7

Studying divertor relevant plasmas in the Pilot-PSI linear plasma device: Experiments vs. Modelling

Published as K. Ješko, Y. Marandet, H. Bufferand, J.P Gunn, H.J van der Meiden, G. Ciraolo, Studying divertor relevant plasmas in Pilot-PSI: Experiments vs. Modelling, Plasma Physics and Controlled Fusion ***60*** *125009 (2018)*

7.1 Abstract

Predictions for the operation of tokamak divertors are reliant on edge plasma simulations typically consisting of a fluid plasma code in combination with a Monte Carlo code for neutral species. Pilot-PSI is a linear device operating with a cascaded arc plasma source that produces plasmas comparable to those expected during the inter-ELM phase in the ITER divertor ($T_e \sim 1$ eV, $n_e \sim 10^{20}\mathrm{m}^{-3}$). In this study, plasma discharges in Pilot-PSI have been modelled using the Soledge2D fluid plasma code [72] coupled to the Eirene neutral Monte Carlo code [90] in order to a) investigate which phenomena need to be included in the modeling to reproduce experimental trends and b) provide new insights to the interpretation of experiments. The simulations highlight the key role of ion/molecule elastic collisions in determining the ion flux reaching the target. Recombination is likely to play a role at high molecular background pressure. However, even with the most advanced atomic and molecular model used in this work, T_e at the target is overestimated with respect to the measurements using TS and spectroscopy. T_e in the simulations appears to saturate at 0.7 eV for a wide range of parameters, while experimentally values of 0.1-0.3 eV are found. As a consequence, in the simulations the volume recombination is underestimated, which is a strong function of T_e when it is below 1 eV. Further analysis of simulation results using a two-point formalism shows that inelastic collisions between electrons and neutral background particles remove most of the energy flux, mainly via dissociation of molecules and molecular ions. However this happens mostly in the upstream region of the beam where T_e >1 eV. For T_e <1 eV, there seems to be no significant energy removal mechanism

in the simulated cases. The results also indicate that conclusions on the importance of volume processes, e.g. recombination, cannot be solely based on T_e or the dominance of certain reaction rate coefficients over others, but rather the complete transport picture, including macroscopic flow, has to be taken into account. In the cases studied here, the plasma is typically advected to the wall too fast for recombination to remove a significant fraction of the particle flux.

7.2 Introduction

The power transported from the core plasma through the separatrix is channelled to the plasma-facing componets (PFCs) via the scrape-off layer (SOL). The thickness of the SOL mapped to the outer mid-plane is of the order of several millimeters and for ITER it has been predicted to be ~ 1 mm [18], leading to a total plasma wetted area of $\sim$2.3 m^2 [19] (this includes geometrical effects like flux expansion and inclination of divertor targets). During D-T operation, the power entering the SOL is expected to be ~ 100 MW, leading to an average heat flux density of $\sim$40 MW/m^2 in case of no mitigation. On the other hand, the technological limit for steady-state power loading of ITER plasma facing components is 10 MW/m^2 [19]). This mismatch of expected and tolerable power fluxes is a major challenge on the way to harnessing fusion energy. The excess power has to be radiated away either by neutral hydrogenic or impurity species, ultimately leading to divertor plasma detachment [20,24,25], a regime in which both particle and power fluxes to divertor targets are strongly reduced. Understanding the key processes at play in divertor detachment is mandatory in order to optimize divertor performance.

7.2.1 Linear devices as divertor simulators

Linear plasma devices have been used extensively as divertor simulators in the past. A very important aspect of linear devices is that their cost per shot is significantly lower than in standard tokamaks, due to their inherently simpler construction and staff requirements. First experiments simulating and demonstrating the feasibility of a gaseous divertor concept were performed at the QED device [28, 29], showing strong reduction of power flux to a solid target in the last chamber of the device by increasing the neutral pressure in the chamber. This reduction was attributed to ions diffusing radially due to elastic collisions with neutral molecules, which were fed into the chamber. In similar experiments at PISCES [30], strong reduction of heat flux to the target was also found with increase of target chamber gas pressure, explained by anomalous radial transport. A significant body of knowledge originates from the Nagdis linear device. In [40–42], based on spectroscopy and comparison with the CRAMD collisional radiative model [43], molecular activated recombination is identified as an important process that reduces the particle flux arriving at the target, in H/He mixture plasmas. However, the importance of radial transport is also pointed out in [44]. Additionally, the effect of transients on a detached plasma are

assessed in [45]. Other devices with divertor physics research include TPD-I, MAP-2 and GAMMA10/PDX and progress on these is reviewed in [46].

In this work, we study a divertor-relevant plasma in the Pilot-PSI device. Pilot-PSI can provide densities of $10^{20} - 10^{21}$ m^{-3}, which is about one order of magnitude higher than typical plasmas produced by the other devices mentioned before, and more relevant to the regimes expected in ITER. The typical electron temperature (T_e) close to the plasma source is 3-5 eV in a hydrogen plasma.

7.2.2 Relevance of linear devices to divertor physics

The relevance of experiments in linear devices to tokamak divertors is often discussed, e.g. in [20]. Indeed, in a tokamak SOL, T_e upstream, e.g. at the midplane separatrix, is ∼100 eV, while T_e at the divertor target can be even below 1 eV under detached conditions. Clearly, Pilot-PSI cannot access the high upstream temperatures. Therefore, Pilot-PSI can only mimic the area adjacent to the targets, where T_e is low. More subtle differences that might not be so evident are related to the physics of particle balance: under high recycling and detached conditions in tokamaks, most of the particle source is concentrated in a "recycling region", poloidally located between X-point and the target plate. The ionization is maintained by power arriving via conduction from further upstream (which is a fraction of the auxiliary heating power). In Pilot-PSI the particle source is maintained by the cascaded arc, and a part of this plasma exhausts into the target chamber. The operation of the cascaded arc is de-coupled from what is happening in the target chamber, as will be seen later. Another difference is that the neutral background pressure P_n in the vessel is set by the inflow of residual gas from the cascaded arc discharge chamber, since only about 10% of the gas fed into the discharge chamber is exhausted to the vessel in the form of plasma. In a tokamak, all neutrals in the divertor originate from plasma recombination, primarily on the solid surface. This is illustrated by the fact that the divertor neutral pressure is strongly coupled to the target particle flux, while in Pilot-PSI it is not the case. For the sake of completeness, it is important to note that for deeply detached divertors, a significant fraction of recombination can take place in the volume [129, 137].

Regarding the differences between divertors and linear plasma machines it is evident that a direct extrapolation of results from one to the other is difficult. However, it is still valuable to apply an edge transport suite to Pilot-PSI. Firstly, it can be checked how accurately the code reproduces trends observed experimentally (i.e. code-experiment benchmarking), possibly pointing at additional missing physics in the code. Secondly, the code can give good insights into which atomic/molecular (or other) processes are responsible for the reduction of power and particle fluxes to the target, i.e. do the book-keeping between the various mechanisms that drive flows in the plasma, i.e. ionisation/recombination, parallel and perpendicular transport etc.

Several linear devices have been modelled previously using different code packages. For instance, Pilot-PSI has been simulated using the B2.5-Eunomia code [47], Eunomia being a neutral Monte-Carlo (MC) code specifically developed for the geometry of linear devices. An advantage of the B2.5-Eunomia suite is a built-in collisional-radiative

model that can calculate line emission using the local T_e and also the population densities of vibrational states. Next, simulations for Magnum-PSI have been carried out by B2.5-Eirene [48]. However, these simulations were performed before the Magnum-PSI device was launched and therefore without input from experiments. In the simulations, typically higher temperatures were obtained compared to the actual operational characteristics of Magnum-PSI [49]. Moreover, the geometry of the device assumed in the simulations does not correspond to the final layout. In another instance [50], the PSI-2 linear plasma device was simulated by the B2.5-Eirene package in a non-homogeneous magnetic field. In this work, it was found that inhomogeneities in the magnetic field can drive supersonic transitions in the plasma beam and also that the choice of artificial flux limiters used in the fluid code can significantly influence results in these low temperature cases. In a more recent study [51], a new transport code LINDA for linear devices is introduced and used to assess cooling efficiencies of various noble gases in the end cell of the GAMMA-10/PDX tandem mirror, identifying xenon as the most efficient radiator. As a general feature, using transport codes in linear geometry can help to shed light on features that could remain hidden or cannot be easily interpreted due to the inherently complex geometry of tokamaks. Linear devices offer a simple, yet still physical model system on which transport codes can be tested and ultimately also compared to experiments.

7.3 Experimental setup

7.3.1 The Pilot-PSI linear device

A schematic of the Pilot-PSI linear plasma device [55] is depicted in Fig. 7.1. It employs a high pressure cascaded arc discharge source [138] for plasma generation. A steady-state gas flow is fed into the discharge channel, with typical values between 1.5 - 3.0 standard liter per minute (slm). The arc operation is sustained by a negative voltage on a hot cathode. The distance between the cathode and the grounded anode is 54 mm and the diameter of the discharge channel is 16 mm (in Figure 7.1, the cascaded arc source is not drawn to scale). Typical achievable discharge currents for steady state source operation are 100 - 200 A. The plasma then exhausts into the vessel and is transported to an actively cooled solid target, located approximately 0.56 m from the source nozzle. The plasma is confined by an axial magnetic field generated by a set of five coils. The magnetic field inside the vessel is homogeneous and can be varied in the range 0.2 - 1.6 T. In the experiments shown in this work, only the 0.2T setting was used. The low field reduces Ohmic heating effects which can cause post-heating of the plasma beam downstream from the source [54]. The pumping system is situated at the back of the vessel, the background neutral pressure in the vessel is set by the pumping rate and the inflow of the residual neutrals from the source and is typically of the order of several Pa. A cylindrical R-ϕ-Z coordinate system is used to describe the system, where the Z-coordinate is aligned with the magnetic field and is the axis of symmetry of the plasma beam and z=0 is situated at the exit of the source discharge channel and the target is located at z=56 cm.

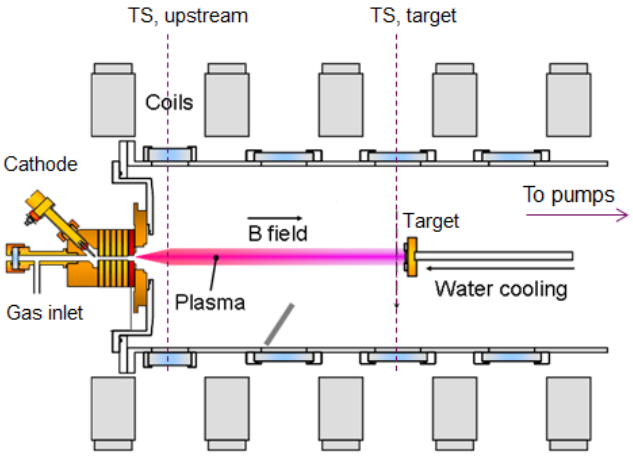

Figure 7.1 – Schematic layout of the Pilot-PSI linear plasma device, with the two positions where radial profile measurements using Thomson scattering can be performed.

7.3.2 Diagnostics

The key diagnostic was Thomson scattering which was performed at two axial locations (at z=4 cm and z=54 cm, referred to as "upstream" and "target" locations, respectively) and is particularly suited to measure low temperature plasmas in the range 0.07 eV to 35 eV [66] with a radial spatial resolution of 0.6 cm. The system uses an Nd:YAG laser operating at the second harmonic, 532 nm. The scattered light detection is performed with an image intensifier and an ICCD camera. The system is capable of measuring electron density and temperature profiles of a plasma column of 30 mm in diameter with a spatial resolution of 0.6 mm.

A single Langmuir probe was embedded in the target with a collecting area of circular shape and a diameter of 2 mm. The probe area was perpendicular to the magnetic field lines, minimising effects of the magnetic pre-sheath which tend to increase the effective collection area of the probe, especially at low grazing angles of the magnetic field [67]. As will be seen later, the probe setup used here gave good agreement with the target Thomson scattering measurements, possibly also due to the normal incidence of the B-field.

Optical emission spectroscopy was performed at the same location as target Thomson scattering, i.e. at z=54 cm, in the near UV spectral range 370 - 440 nm, using one channel of an Avantes ULS2048 spectrometer. The line of sight was perpendicular to the beam (Fig. 7.1), focused on the central part.

The background neutral pressure, which we will denote as P_n, was measured by a capacitance manometer located at a port about 20 cm radially outwards from the axis of symmetry.

7.4 Simulation setup

7.4.1 The Soledge2D fluid code

The Soledge2D transport code was designed for investigation of the transport of multi-fluid plasmas in the tokamak edge and in the SOL [72]. The equations solved by the code with the setup used in this work are the following:

$$\frac{\partial n}{\partial t} + \vec{\nabla} \cdot (n u_\parallel \vec{b}) = \vec{\nabla} \cdot (D \vec{\nabla}_\perp n) + S_n^{(N)} + S_n^{(\mathrm{ext})} \tag{7.1}$$

$$\frac{\partial n u_\parallel}{\partial t} + \vec{\nabla} \cdot (n u_\parallel^2 \vec{b}) + \nabla_\parallel \left(n k_B \frac{T_e + T_i}{m_i} \right) = \vec{\nabla} \cdot (\nu \vec{\nabla}_\perp n u_\parallel) + S_G^{(N)} \tag{7.2}$$

$$\begin{aligned} &\frac{\partial}{\partial t} \left(\frac{3}{2} k_B n T_i + \frac{1}{2} m_i u_\parallel^2 \right) + \vec{\nabla} \cdot \left(\frac{5}{2} k_B n u_\parallel T_i \vec{b} + \frac{1}{2} m_i n u_\parallel^3 \vec{b} + \kappa_i^0 T_i^{5/2} \nabla_\parallel T_i \vec{b} \right) + u_\parallel \nabla_\parallel (n k_B T_e) = \\ &\vec{\nabla} \cdot \left(\left(\frac{3}{2} k_B T_i + \frac{1}{2} m_i u_\parallel^2 \right) D \vec{\nabla}_\perp n + \frac{3}{2} k_B \chi_\alpha n \vec{\nabla}_\perp T_i + \nu n \vec{\nabla}_\perp \left(\frac{1}{2} m_i u_\parallel^2 \right) \right) + Q_{ei}^{(c)} + S_{E,i}^{(N)} + S_{E,i}^{(\mathrm{ext})} \end{aligned} \tag{7.3}$$

$$\begin{aligned} &\frac{\partial}{\partial t} \left(\frac{3}{2} k_B n T_e \right) + \vec{\nabla} \cdot \left(\frac{5}{2} k_B n u_\parallel T_e \vec{b} + \kappa_e^0 T_e^{5/2} \nabla_\parallel T_e \vec{b} \right) - u_\parallel \nabla_\parallel (n k_B T_e) = \\ &\quad + \frac{3}{2} k_B \vec{\nabla} \cdot \left(T_e D \vec{\nabla}_\perp n + \chi_\alpha n \vec{\nabla}_\perp T_e \right) - Q_{ei}^{(c)} + S_{E,e}^{(N)} + S_{E,e}^{(\mathrm{ext})} \end{aligned} \tag{7.4}$$

where n is the plasma density ($n = n_e = n_i$), T_i and T_e are the ion and electron tempertures, respectively, $\vec{b}$ is the unit vector in the direction of the magnetic field and the operators are defined in the following way: $\nabla_\parallel = \vec{b} \cdot \vec{\nabla}$ and $\vec{\nabla}_\perp = \vec{\nabla} - \vec{b} \nabla_\parallel$. The term $Q_{ei}^{(c)}$ represents the coupling between electrons and ions and has the form $Q_{ei}^{(c)} = \beta n^2 T_e^{-3/2} (T_i - T_e)$, where $\beta = \frac{\sqrt{m_e}}{m_i} 4\sqrt{\pi} e^4 Z^2 \ln\Lambda$. The anomalous perpendicular transport coefficients D, ν and χ_i, χ_e are for density, parallel momentum and ion/electron energy, respectively, and are uniform in the whole simulation domain throughout this work. The terms $S_n^{(N)}$, $S_G^{(N)}$ and $S_{E,\alpha}^{(N)}$ are sources of particles, parallel momentum and energy due to neutral particles, respectively. These source terms due to neutrals are calculated by the kinetic Monte-Carlo (MC) code Eirene [90], which will be described in section 7.4.2. The terms $S_n^{(ext)}, S_G^{(ext)}, S_{E,i}^{(ext)}, S_{E,e}^{(ext)}$ represent externally forced sources of plasma particles, momentum and energy, and are used to generate the plasma beam in this setup of the code. Their exact form is discussed in the end of this section. Drifts, electric fields and currents are implemented in Soledge2D [135] but were turned off in all simulations shown in this work since the focus was on atomic and molecular physics, i.e. the interaction of the plasma beam and the neutral background.

The geometry of the linear plasma device may seem very different from a tokamak, however they have common aspects, which enable to create a field-aligned grid that the code can directly use. The grid for the linear device can be regarded as a subspace of a tokamak grid. It is in fact topologically equivalent to a scrape-off layer with no toroidal

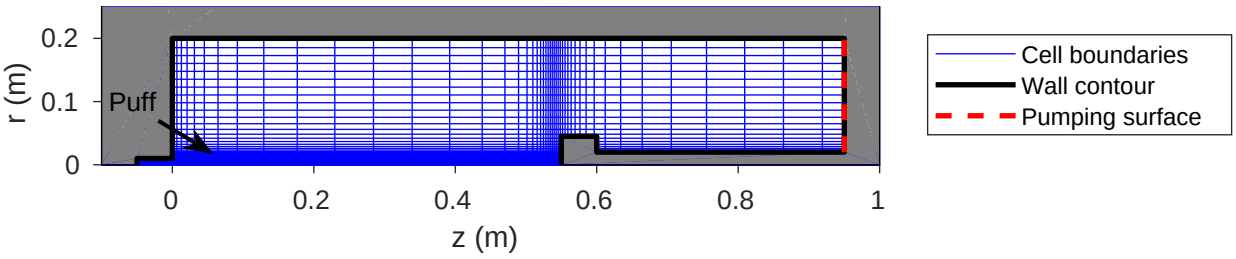

Figure 7.2 – The Pilot-PSI non-uniform grid used in the Soledge2D-Eirene simulations.. The small region demarcated by 0 cm $< R <$ 1 cm and -5 cm $< Z <$ 0 cm is a "source region", where the external volumetric source terms based on formula 8.1 are prescribed. The pumping surface is located at the back of the vessel, where an absorption probability (albedo) for impinging particles can be defined. The recycling coefficient in the "source region" is set to 0 for reasons described in the text. The remainder of the vessel walls use a recycling coefficient $R = 1$. The gas puff is located at $(R, Z) = (1.005, 0.000)$ cm.

field, i.e. the plasma is simulated up to the axis of symmetry. The axial magnetic field of the linear device corresponds to the poloidal magnetic field of a tokamak and has a constant value of 0.2 T in all simulations presented here, in line with the experiment. The grid used in the simulations is depicted in Fig. 7.2. Additionally, a variable grid density is used in order to provide high resolution in the plasma beam and close to the walls, while in areas of less interest the cells are larger, to save computational time.

The plasma wall interaction is treated using the penalization technique [86–89], a unique feature of SolEdge2D permitting simulation of the plasma up to the first wall in tokamaks. Standard Bohm boundary conditions and sheath heat transmission are imposed at the plasma-wall interface, i.e. $|M| \geq 1$ and $q_{t,e} = \gamma_e n M c_s T_e$, where M is the Mach number, $q_{t,e}$ is the energy flux density through the interface for electrons. For ions, the energy flux density is given by $q_{t,i} = nMc_s(\gamma_i T_i + 1/2M^2 c_s^2)$ since the energy of the mean flow has to be accounted for, where c_s is the sound speed and γ_α are the sheath heat transmission factors for ions and electrons, set to 2.5 and 4.5, respectively. Note that even though Soledge2D energy equations are written in terms of the total energy, the values of heat transmission factors reported here are for the internal energy part. We assume the ion velocity distribution function at the sheath edge to be a shifted Maxwellian with c_s normal to the wall, so the effective sheath heat transmission factor for ions is in fact 3.5 for $T_i = T_e$ (that is, on the high side). However, this choice ensures internal consistency of the code and is related to the coupling of Soledge2D and Eirene. On the axis of symmetry the boundary condition of vanishing perpendicular gradients is used. It should be noted that the PIC database connecting the magnetic pre-sheath entrance conditions to the ion velocity distribution at the wall available in Soledgde2D-Eirene [72] is not used here since the former is designed for grazing magnetic field incidence.

Anomalous values are assigned to the radial transport coefficients and a sensitivity study to the choice of these transport coefficients is performed in section 7.5.2.

It is beyond the scope of this contribution to model the details of the cascaded arc discharge self-consistently. This would require inclusion of the electric currents and

Table 7.1 – Values of various constants used for the external source terms (formula 8.1) for the reference case

Type	$S_i^{(\mathrm{ext,tot})}$	λ_r (mm)	λ_z (mm)	r_0 (mm)	z_0 (mm)
$S_n^{(\mathrm{ext})}$	4.1×10^{20} $\mathrm{m^{-3}s^{-1}}$	5.0	10.0	0	-25
$S_{Ee}^{(\mathrm{ext})}$	1.2×10^{3} $\mathrm{Wm^{-3}}$	3.5	7.1	0	-25
$S_{Ei}^{(\mathrm{ext})}$	0.3×10^{3} $\mathrm{Wm^{-3}}$	3.5	7.1	0	-25

drifts in the simulations, as well as thermionic emission from the hot cathode. However, the principal focus here lies in the interaction of the plasma beam with the surrounding neutral gas. Therefore, the plasma particle and power sources are directly prescribed as external volumetric source terms $S_n^{(ext)}, S_G^{(ext)}, S_{E,i}^{(ext)}, S_{E,e}^{(ext)}$ in the Soledge2D equations (1)-(3), section 7.4.1. The shape and magnitude of these is defined to match Thomson scattering profiles measured close to the source (shown in section 7.5.1). For example, the external volumetric source terms for the plasma ion/electron source has the form of a Gaussian function in both r and z directions:

$$S_n^{(ext)}(r,z) = \frac{S_n^{(ext,tot)}}{C}\exp\Big(-(r-r_0)^2/\lambda_r^2\Big)\exp\Big(-(z-z_0)^2/\lambda_z^2\Big), \tag{7.5}$$

where r_{src}, z_{src} are the positions of the profile maxima, λ_r, λ_z are the profile widths, C is a normalization constant such that the volume integral over the simulation domain be equal to the total number of injected particles, i.e. $\int_V S_n^{(ext)}\mathrm{d}V = S_n^{(ext,tot)}$. A similar external source term is also defined for the energy source on electrons and ions, $S_{Ee}^{(ext)}$ and $S_{Ei}^{(ext)}$, respectively. The position and spatial extent of the external volumetric source terms was chosen such that it stays well within the small area of the cascaded arc source. The values of the individual constants for the reference case are listed in Tab. 7.1. These are kept the same for all the other cases in this work.

7.4.2 Eirene for neutral particles

The interaction of plasma and neutrals is treated by the well-established Eirene Monte-Carlo code [90]. In Pilot-PSI, neutrals enter the system by three channels 1) the residual gas entering the vessel from the cascaded arc source 2) main ion recycling, e.g. at the target and 3) recombination in the volume. The latter two are calculated self-consistently by Eirene, while the constant gas inflow rate is simulated as a constant puff of H_2 at ambient temperature (0.03 eV) at the location depicted in Fig. 7.2. In the experiment, this is an externally controllable quantity, and the value of the total source inflow was 2.5 standard liters per minute (slm) corresponding to about 10^{21} H_2/s in all experiments presented here. This value is also used in the simulations. The recycling coefficient at the plasma-wall interface is set to unity throughout all the simulations presented here, except for two locations: The pumping surface is located at the back end of the vessel, Fig. 7.2, where one can specify an absorption probability (albedo) for neutral particles. The absorption probability is set to match measurements of the neutral pressure in the vacuum vessel, typically in the range of several Pa. The second

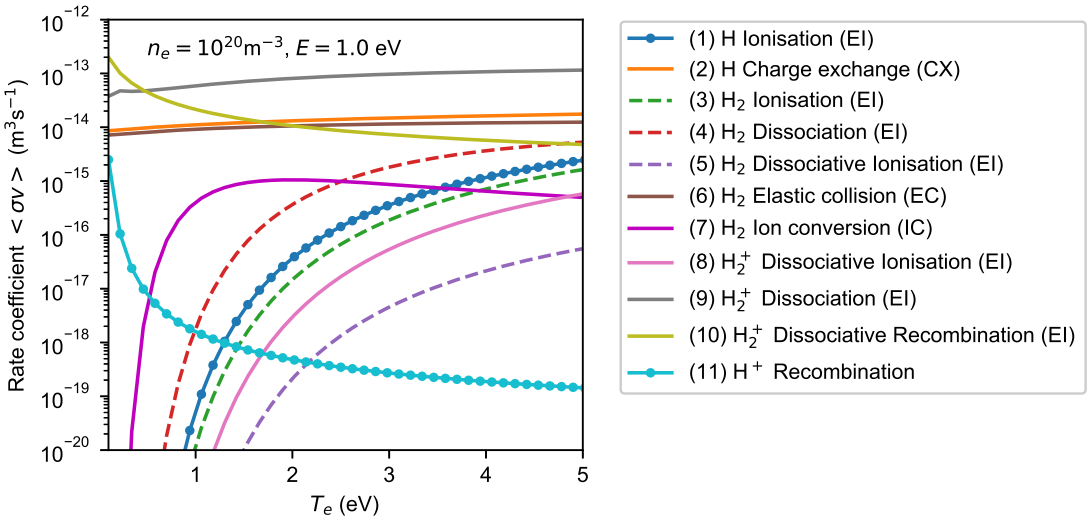

Figure 7.3 – Plots of rate coefficients for different processes used in the atomic physics model in Eirene as a function of T_e and for n_e=10^{20} m^{-3} in case of density dependent rate coefficients (processes (1), (3-5) and (8-11)) and for a relative energy of $E = 1$ eV for reactions (2) and (6)). The reaction numbering in the legend of the figure is the same as in Tab. 7.2. The rate coefficients are taken from the AMJUEL database (available from www.eirene.de) .

region where the recycling coefficient is not unity is the source region, where it is set to 0. Since the cascaded arc source is not modelled self-consistently, but rather by adding external source terms described in section 7.4.1, formula 8.1, it is of little interest to take into account recycling of ions on the walls of the source region. This would also render tweaking of the source terms for matching with upstream Thomson scattering profiles more challenging. The species considered in Eirene are hydrogen atoms H and molecules H_2 and H_2^+ molecular ions. The latter is treated in the static approximation, i.e. its motion is not followed and the next collision is supposed to happen at the location of birth - in other words, H_2^+ is treated as a short-lived species. This assumption will be checked *a posteriori* in section 7.5.3. The atomic physics model used in Eirene is depicted in Tab. 7.2. This model is the same as the model described in [92], which was used extensively in predictive simulations for ITER [93], however, in our case neutral-neutral collisions and radiation opacity were not included. Including molecular processes is critical for reproduction of basic experimental features in Pilot-PSI. A plot of selected rate coefficients for reactions in Tab. 7.2 is shown in Fig. 7.3 in order to show which processes become dominant in which temperature regions for a given density. We point out here the importance of the ion conversion process (7) that is the dominant contributor to the formation of H_2^+ molecular ions in the T_e range of interest. The molecular ion can then either dissociate into a main ion and an atom, reaction (9), or dissociatively recombine into two atoms. The latter process, including the preceding ion conversion, is termed molecular assisted recombination (MAR). The third possible reaction including H_2^+, dissociative ionisation (8) is comparatively negligible in the T_e range of interest.

Table 7.2 – List of atomic and molecular physics processes used in Eirene.

#	Reaction	Event type
(1)	$H + e \rightarrow H^+ + 2e$	Electron impact ionization
(2)	$H + H^+ \rightarrow H^+ + H$	Charge exchange
(3)	$H_2 + e \rightarrow H_2^+ + 2e$	Electron impact ionization
(4)	$H_2 + e \rightarrow 2H + e$	Dissociation
(5)	$H_2 + e \rightarrow H + H^+ + 2e$	Dissociative ionization
(6)	$H_2 + H^+ \rightarrow H_2 + H^+$	Elastic collision
(7)	$H_2 + H^+ \rightarrow H_2^+ + H$	Ion conversion
(8)	$H_2^+ + e \rightarrow H^+ + H^+ + 2e$	Dissociative ionization
(9)	$H_2^+ + e \rightarrow H^+ + H + e$	Dissociation
(10)	$H_2^+ + e \rightarrow 2H$	Dissociative recombination
(11)	$H^+ + e \rightarrow H$	Electron-ion recombination

7.5 Results & Discussion

7.5.1 Understanding basic features

Table 7.3 – Radial transport coefficients and pumping albedos used in the simulations presented.

Case	D (m^2/s)	χ_e, χ_i (m^2/s)	albedo ($\times 10^{-2}$)	P_n (Pa)	Remark
(a)	0.3	0.3	0.54	3.3	ref. case
(b)	0.3	1.0	0.54	3.4	
(c)	1.0	1.0	0.54	3.6	
(d)	0.1	0.1	0.54	3.2	
(e)	0.3	0.3	2.00	1.3	
(f)	0.3	0.3	1.20	1.9	
(g)	0.3	0.3	0.80	2.6	
(h)	0.3	0.3	0.40	4.1	
(i)	0.3	0.3	0.25	5.0	
(j)	0.3	0.3	0.17	6.0	
(k)	0.3	0.3	0.54	4.0	el. coll. off

The reference case is defined by the input parameters in Tab. 7.3 and case (a). The sensitivity of the results to the choice of the transport coefficients is discussed in the next section (cases (b) to (e)). The pumping albedo was adjusted to match a background pressure of P_n=3.2 Pa. The external source terms were adjusted manually for the reference case until satisfactory agreement with measured upstream Thomson scattering profiles was achieved. The resulting upstream (Z=4 cm) radial profiles of n_e and T_e of the reference case simulation are shown in Fig. 7.4 together with the upstream Thomson scattering measurement which were used for the matching. For all the other cases, the same parameters for the source terms were used. Next, 2-D maps of plasma parameters of the reference case (a) are shown on Fig. 7.5. As a general

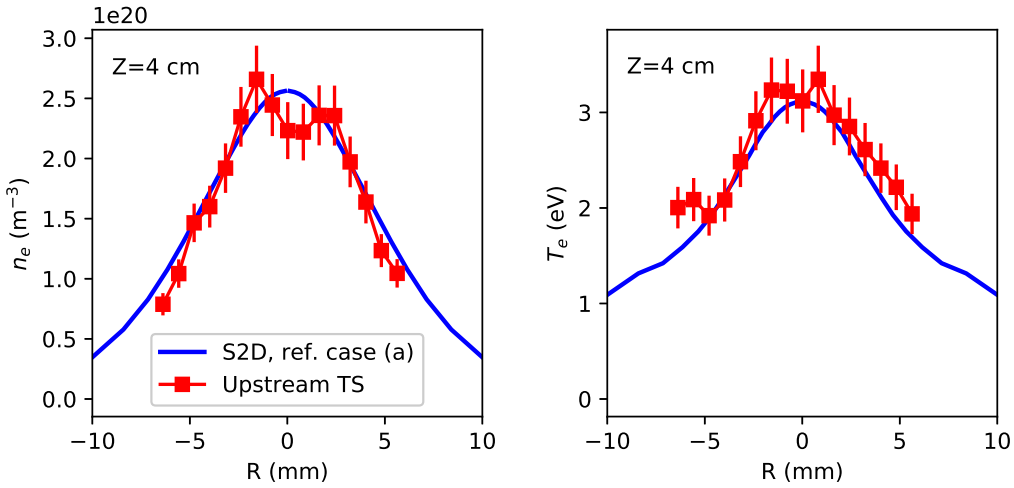

Figure 7.4 – Comparison of upstream n_e, T_e profiles measured by Thomson scattering and simulation results for the reference case (a). The match was obtained by adjusting the free parameters of the external volumetric source terms, see section 7.2.

feature, there is a strong, monotonic axial reduction of all the quantities from upstream towards the target (with the exception of the parallel velocity, which is not monotonic, but decelerates in the usptream region of the beam and then accelerating towards the target again, which is expected from the imposed boundary conditions).The total plasma pressure is the sum of the static and dynamic components, $P_{\mathrm{tot}} = P_{\mathrm{stat}} + P_{\mathrm{dyn}} = n_i k_B T_i + n_e k_B T_e + n_i c_s^2 M^2$. From the plot of the flux density Γ and total plasma pressure P_{tot}, it may misleadingly seem that the beam is not reaching the target, however, this is just a consequence of the specific geometry and the imposed radial transport. In fact, in the reference case, most of the flux from the source plasma is reaching the target. This is shown in Fig. 7.6 (A), where the axial profile of the total, cross-section integrated flux density, $\Gamma_{\mathrm{tot}} = \int_0^{2\pi} \int_0^{R_{\mathrm{vess}}} r\Gamma(r) \mathrm{d}r\mathrm{d}\phi$ is plotted (R_{vess} is the radius of the vessel). Γ_{tot} decreases only by about 20%, meaning that there are net sinks of plasma between upstream and target locations (It was shown in [139] that MAR is the most efficient recombination channel for these cases.), however most of the flux still reaches the target. Instead, the strong reduction in the parallel ion flux density observed in Fig. 7.5 is driven mainly by the radial transport, which is effectively causing broadening of the beam, from about ∼4 mm upstream to ∼ 12 mm at the target, as can be seen in Fig. 7.6.

7.5.2 Sensitivity to radial transport

The sensitivity of the results to the choice of radial transport coefficients was also examined, as these are free parameters of the model. Four different sets of transport coefficients were tested including the reference case and are listed in Tab. 7.3, cases (a)-(d). All other parameters, including the external volumetric source terms, were kept constant for these cases. From Fig. 7.6 (B), it can be seen that in case (b), where

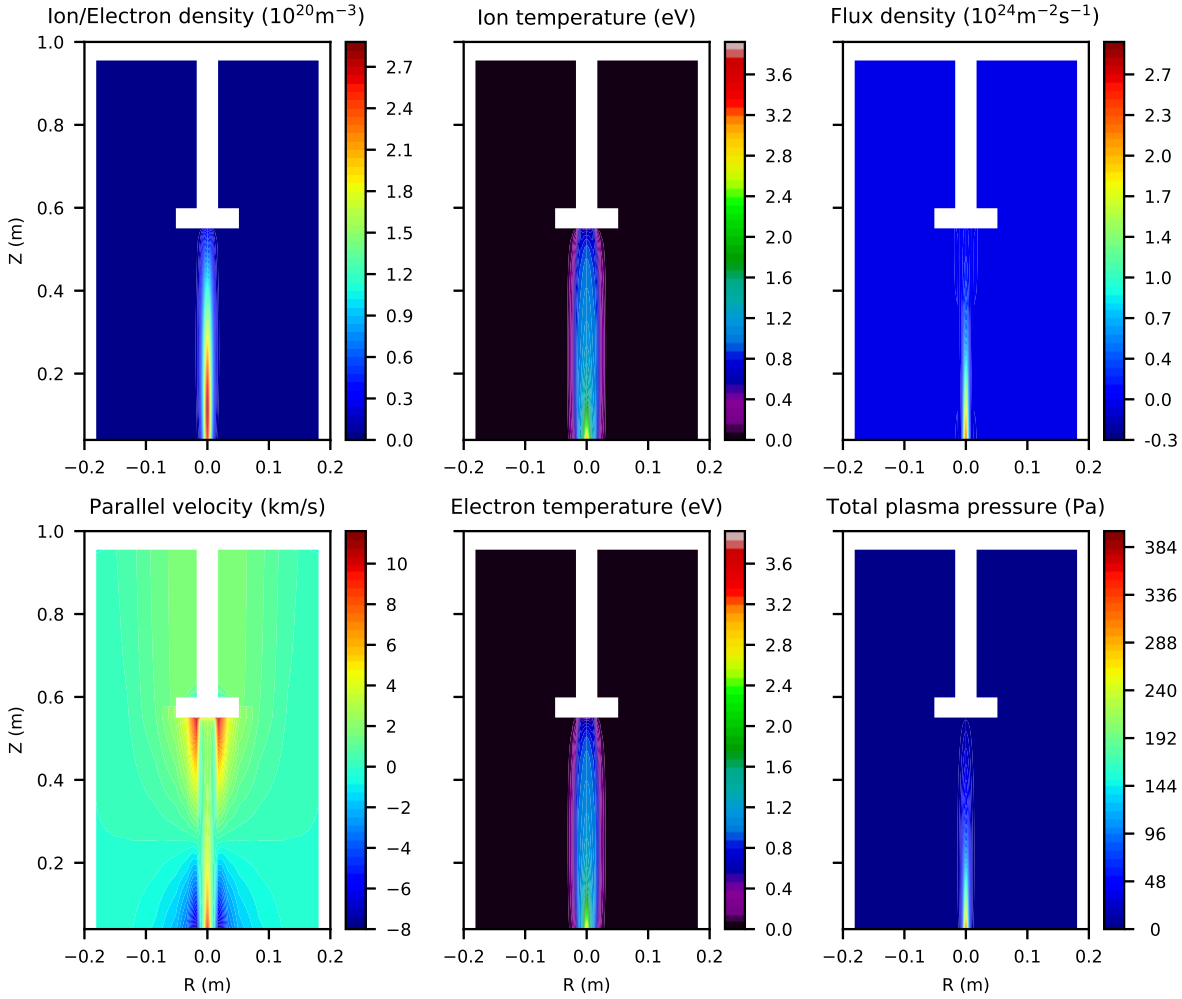

Figure 7.5 – Plots of plasma parameters for the reference case (a). The blank areas correspond to space taken up by the target and vessel walls.

only the energy transport coefficients were changed, there is no significant difference neither in the axial profiles of the total ion flux, beam width and total energy flux. However, when the particle diffusion coefficient D is changed, the beam width increases much faster for case (c), when $D = 1$ m/s^2 and slower when $D = 0.1$ m/s^2. In terms of changes of total ion flux, Fig. 7.6 (A) it decreases roughly by similar amounts, between about 15-25%. However, it is to be noted that the total initial ion fluxes (i.e. at the upstream location, Z=4 cm) are not identical. From Fig. 7.6 (C) it can be seen that most energy is reaching the target in the case (d) (excluding case (j) which belongs to a different scan), when the transport coefficients have the lowest values, and is about 60 W. However, the difference between the other cases is not substantial, the amount being 50 W, 49 W, 41 W for cases (a), (b), (c), respectively.

Parallel profiles for the flux tube at r= 1.4 mm are plotted in Fig. 7.7. The parallel profiles are more suitable for the interpretation of results compared to the 2D maps in figures 7.5 and 7.9 since they reveal also more subtle features. For the reference case

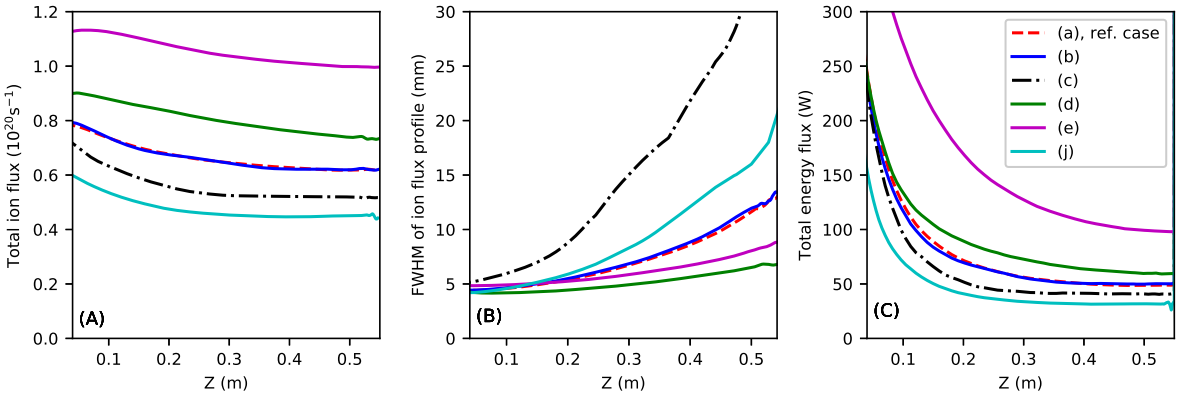

Figure 7.6 – (A) Parallel profiles of the total, section integrated flux density, (B) parallel profile of the beam width (Full width half maximum of the radial flux density $\Gamma(r)$) and (C) parallel profile of the total, section integrated energy flux, listed for a number of different cases from Tab. 7.3.

(a), we have first a small increase of density up to $Z \simeq 0.1$ m, and after that a steady reduction towards the target plate. The increase of the density in this part is driven by a reduction in the parallel flow velocity, rather than ionisation sources in the volume. Although there is a positive source of plasma in the region (Fig. 7.8), the flux density profile, Fig. 7.7, is decreasing in this region (and also throughout the whole axial profile), meaning that the $\vec{\nabla} \cdot (D\vec{\nabla}_\perp n)$ term on the R.H.S. of the continuity equation 7.1 is stronger in absolute magnitude than the contribution of neutrals to the particle source $S_n^{(\mathrm{N})}$ ($S_n^{(\mathrm{ext})}$=0 by definition here, Tab. 7.1). The $\vec{\nabla}\cdot(D\vec{\nabla}_\perp n)$ term can be looked at as a sink term arising from the presence of perpendicular transport. Since there is an axial drop in the flux density, the observed density increase must be compensated by a reduction in the parallel flow velocity, which is indeed the case. In the remaining part of the profile 0.1 m < Z < 0.55 m, we can see that the axial gradient in the parallel flow velocity is not so pronounced, and it is too weak to compete with the sinks due to radial transport and interactions with neutrals, and as a consequence, also the density decreases in this part. In fact, in this region, the plasma is recombining, $S_n^{(\mathrm{N})}$ <0, which is expected given that $T_e < 2$ eV and T_e dependencies of rate coefficients from Fig. 7.3.

In case (b), with the perpendicular energy diffusivities $\chi_e = \chi_i$ increased to 1 m/s^2, there is no significant change in the obtained profiles, indicating that the simulations are not sensitive to this parameter. However, in case (c) also the particle diffusion coefficient D was increased to the same value, 1 m/s^2. This has a very strong influence on the observed profiles, mainly reducing the density, flux density and total plasma pressure. Indeed, the ion flux density at the target is now only a small fraction of the original flux density upstream. However, it is important to point out that the T_e nor T_i do not change much by increasing D.

Conversely, in case (d), all perpendicular diffusion coefficients have been reduced to 0.1 m/s^2. As expected, with the reduced radial transport, the plasma density and flux density are much higher than in the reference case (a). Again, the T_e and T_i profiles do not show a significant response to the change of the perpendicular transport

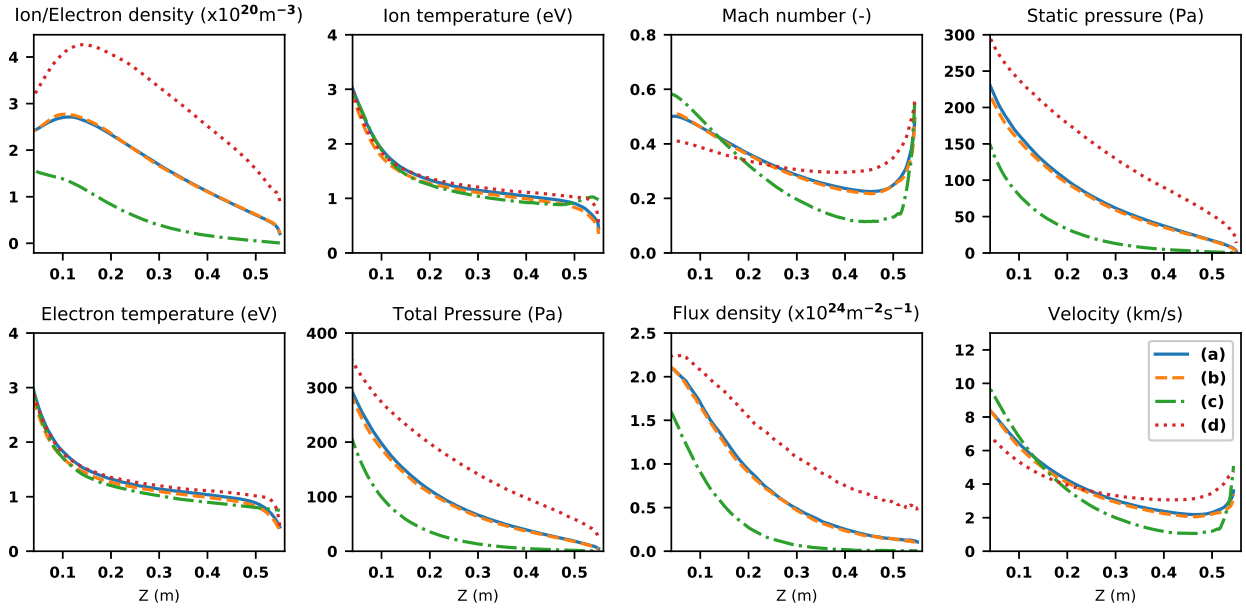

Figure 7.7 – Parallel profiles of various plasma parameters on the flux tube located 1.4 mm from the axis of symmetry (Description of cases in Tab. 7.3).

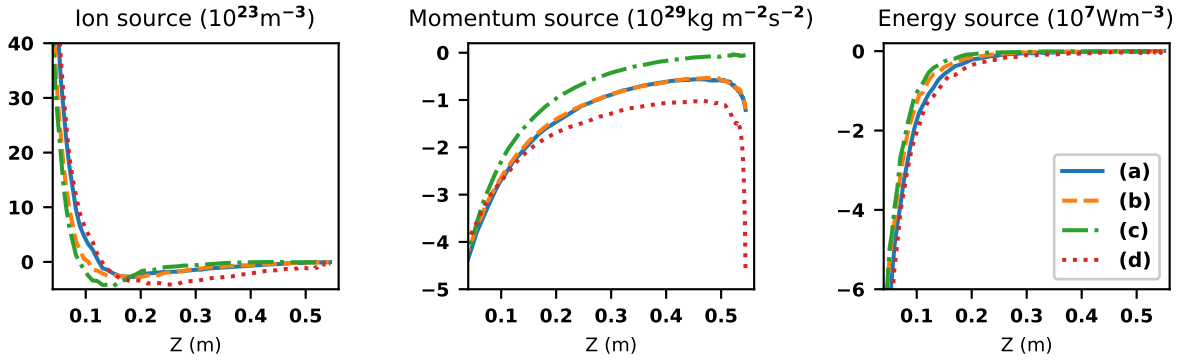

Figure 7.8 – Parallel profiles of volumetric source terms of particles, momentum, and energy (sum of electron and ion energy source terms) due to neutral particles (Description of cases in Tab. 7.3).

coefficients, although one can see that in general the temperature is slightly higher than in the reference case (a). It is to be noted that here the perpendicular transport is strong enough to suppress the slight increase in density described in the previous paragraph for cases (a) and (b).

7.5.3 Neutral inventory

2D maps of various moments of species treated by Eirene are depicted in Fig. 7.9 for the reference case (a). It can be seen that the molecular density profile is hollow, with molecules depleted in the center of the beam. The remaining molecules in the beam are heated by the plasma to typical temperatures up to 1 eV. Hollow molecular profiles

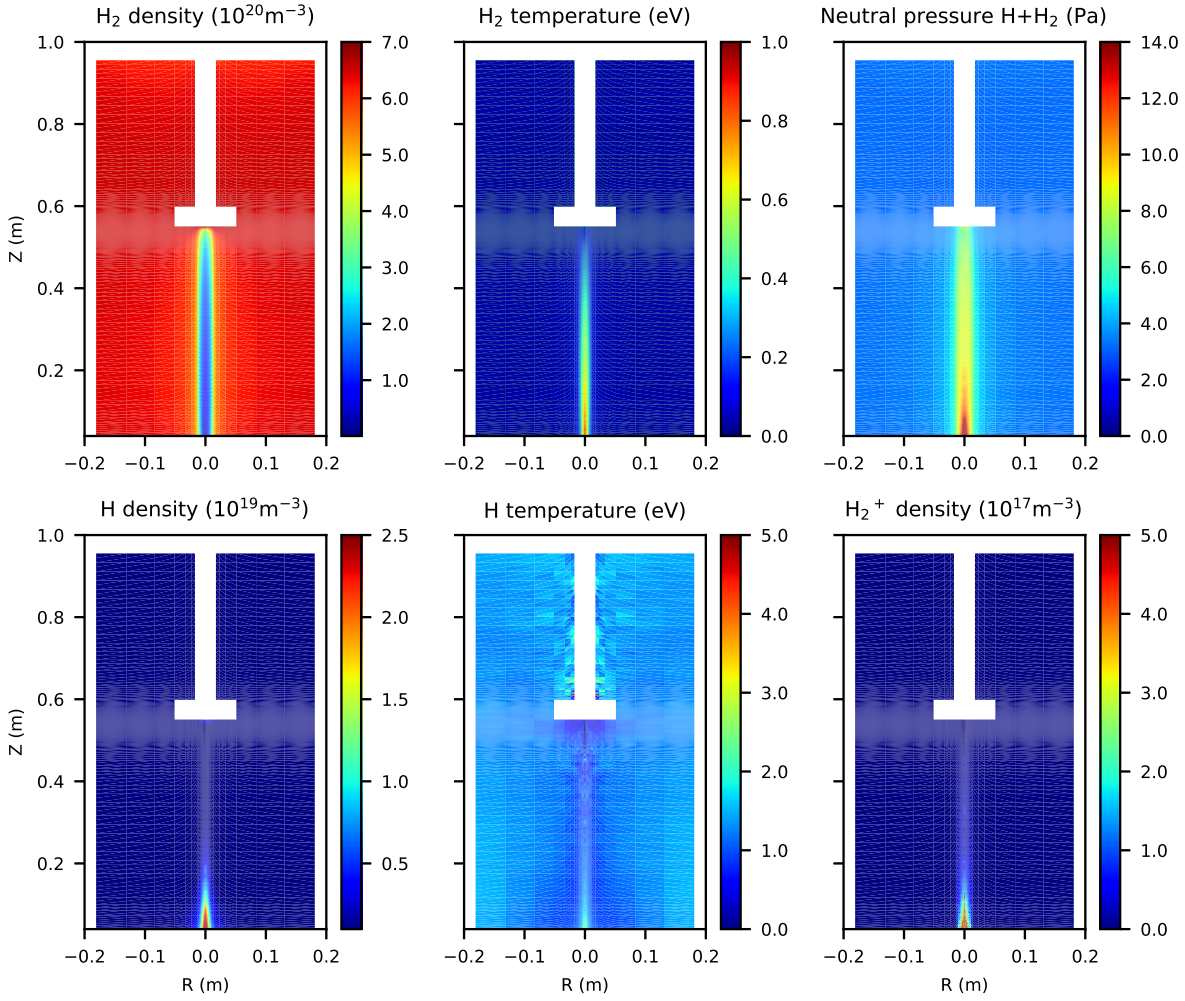

Figure 7.9 – Plots of parameters of species treated by Eirene for the reference case (a). The blank areas correspond to space taken up by the target and vessel walls. The neutral pressure is the combined static pressure of atoms and molecules, $P_n = n_{\mathrm{H}} k T_{\mathrm{H}} + n_{\mathrm{H}_2} k T_{\mathrm{H}_2}$. The trajectories of molecular ions are not followed in Eirene, they are instantaneously followed by reactions (8), (9) or (10), Tab. 7.2.

and heating of molecules was observed in Pilot-PSI in [109] and this is in line with the modelling. On the other hand, the H atoms are mainly present in the upstream area of the plasma, where the plasma is hot enough for dissociation of molecules and molecular ions to be efficient. The density of molecular ions is significantly lower than the typical plasma, molecule and atomic densities, and peak values are of the order $10^{17}\mathrm{m}^{-3}$, concentrated in upstream areas of the beam. The neutral static pressure P_n is uniform outside of the plasma beam and is elevated in the center.

As promised in section 7.4.2, the static assumption on H_2^+ molecular ions is to be tested. In Fig. 7.10 the axial profile of the mean free path for the destruction of H_2^+ (based on reactions (9) and (10), Tab. 7.2) molecular ions is plotted for the reference case (a) for two different radii. The figure shows that this mean free path is well below 1 mm throughout the profile. This is smaller compared to the cell size for most of

the length of the beam, except for a thin region close to the target plate, where the cell size becomes low. However, here also T_e becomes low, and there is not much H_2^+ formed in the first place. The T_e gradient length is in the order of 10 cm throughout most of the simulation domain. The picture does not change for other simulation cases or other radii. It is concluded that the quasi-static assumption is satisfied throughout the beam in the simulations presented here.

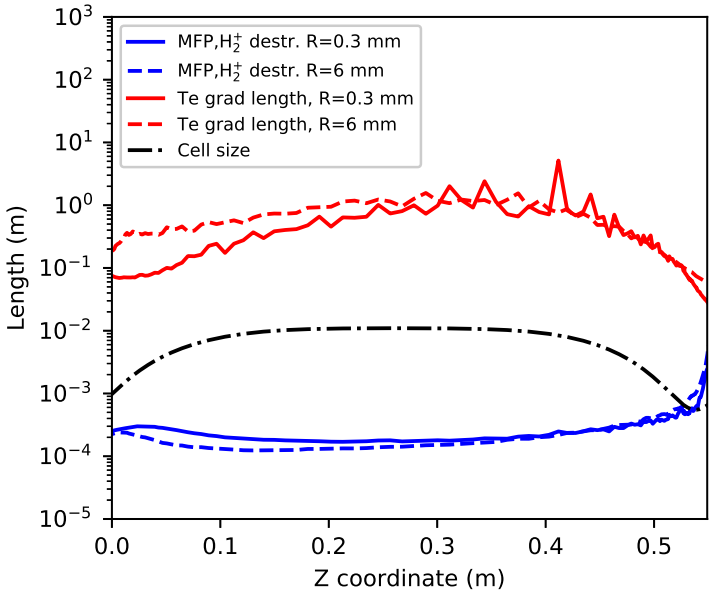

Figure 7.10 – Parallel profiles of mean free paths for the destruction of H_2^+ molecular ions compared to the cell size at that given point, and also T_e parallel gradient lengths for different radii.

7.5.4 Comparison with experiment: Scanning neutral background pressure

In order to see whether we can reproduce basic experimental trends, we simulated part of a background pressure scan experiment described in [100]. In this experiment, the effect of the background pressure in the vessel P_n on the plasma beam was investigated, by changing the pumping speed. In the simulations, P_n was changed by tweaking the albedo of the pumping surface at the back of the vessel, Fig. 7.2. The parameters used in the simulations are presented in Tab. 7.3. In the last column of the table, the background pressure is listed for each case: this is not an input parameter, but a result of the simulation. Numerical instabilities in the code related to the ion conversion reaction (7) have so far prevented us to converge cases with P_n higher than 6.0 Pa. To be more specific, it was found that by removing reaction (7), higher pressures can be reached.

The simulation results will be analyzed in more detail in the following section. Here, we focus on comparing these simulations with the background pressure scan experiment.

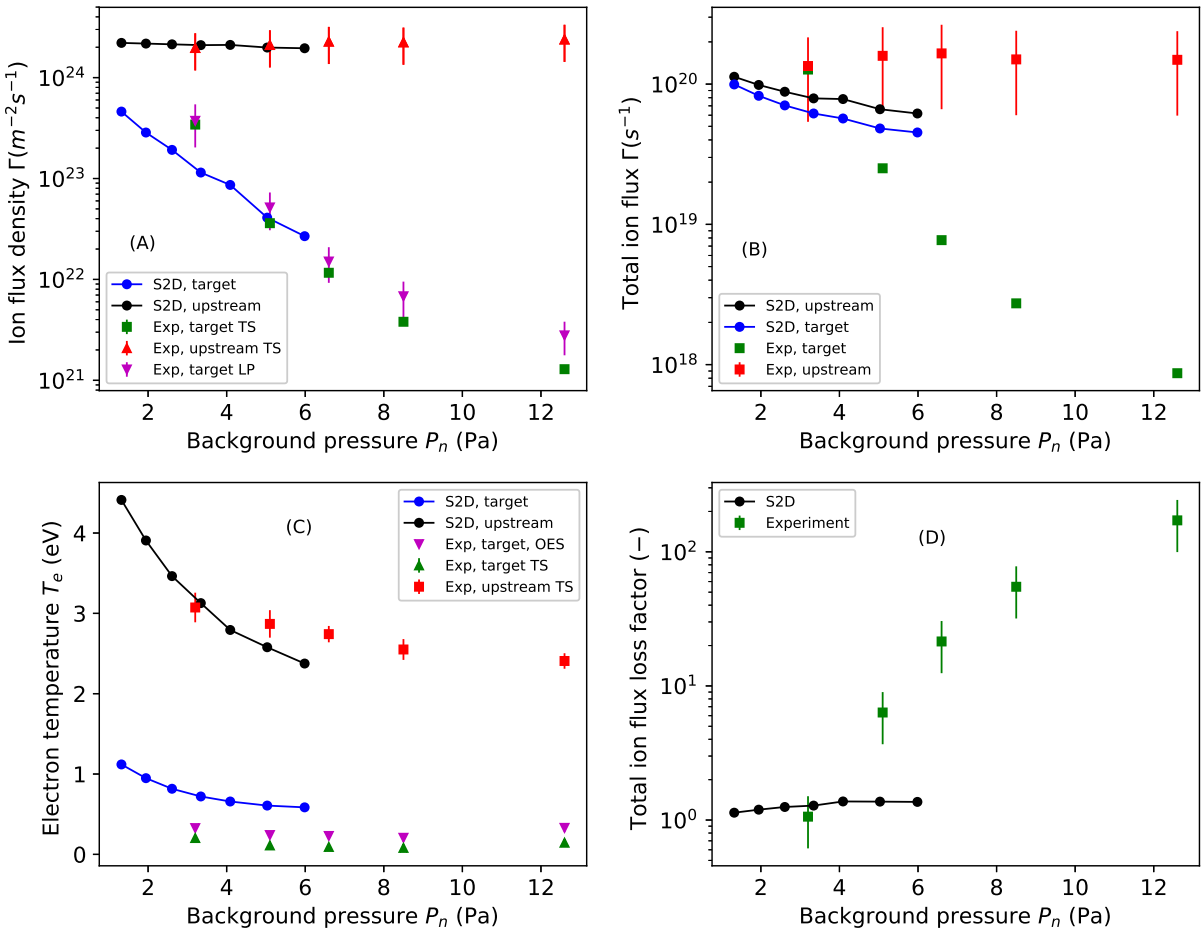

Figure 7.11 – Comparison of the peak flux density for a given field line (A), total ion flux (B) and T_e (C) between simulations and estimated from available diagnostics for the P_n scan.

The most striking finding resulting from this comparison is shown in Fig. 7.11 (C). The code is unable to reproduce the low temperatures found in the experiment (using spectroscopy and Thomson scattering), and this is even true for the reference case (the case where $P_n = 3.2$ Pa), i.e. the one used for matching the upstream profiles. The electron temperature in the simulations seems to saturate at a level of ~ 0.7 eV. This happens regardless of the assumed value of the radial transport coefficient D. We think that this affects the particle balance, leading to further discrepancies, which we address in the following.

In Fig. 7.11 (A), the flux density at the target is plotted, measured by a Langmuir probe embedded in the target and recalculated from the Thomson scattering (assuming that the density at the TS target position is equal to the density at the sheath edge). Both from the TS and LP a strong reduction of the flux density with the background pressure is found.

For completeness, the upstream flux density is also plotted, both from the code and recalculated from upstream TS. However, it is important to note that the experimental

value is just a rough estimate, assuming an upstream Mach number between 0.2 and 0.7 (these were typical values measured in Pilot-PSI in [54]). These bounds give the associated error bars shown for the upstream flux in Fig. 7.11 (A) and (B). However, even such a large uncertainty cannot prevent from concluding that the flux density is strongly reduced at the target.

The approach from the previous section, where we compare flux densities, cannot give conclusions on the global particle balance, e.g. on the importance of recombination, as a reduction of flux density can be driven also by radial transport. Therefore, in Fig. 7.11 (B), the section-integrated particle flux is plotted, again as a function of P_n, from the target and upstream TS profiles and from the simulation result. For the calculation of the fluxes from the TS profiles, the same approach as in the previous section was used. Figure 7.11 (D) shows the ratio of the upstream total ion flux to the target total ion flux for both experiment and simulation. Experimentally, the integrated fluxes are strongly reduced for cases where P_n >4.0 Pa, even given the experimental uncertainty on the upstream flux. This indicates that there is strong volume recombination occurring between the upstream and target locations for these cases. The presence of high-n Balmer line radiation also indicates a recombining regime. High-n states are dominatly populated by electron-ion recombination [129] and are considered to be a signature of this process [140]. A typical experimental spectrum is plotted in Fig. 7.12 with Balmer lines up to $n = 14$ clearly visible. Visually, the color of the plasma was blue in the near-target region, characteristic of a recombining region, instead of pink/red, which is typical for ionizing plasma. The spectroscopic investigation showed Balmer lines only, from which we infer that the impurity content in the plasma is low and that impurity radiation does not constitute an important energy loss channel in the studied plasmas.

The code, on the other hand, does not show a strong drop in the integrated particle flux at the target. The integrated upstream particle flux is also decreasing in the simulations. The strong local reduction found in Fig. 7.11 (A) and weak reduction of the total particle flux in Fig. 7.11 (B) indicate that the assumed radial transport coefficients chosen might be too high for the cases studied here. However, the sensitivity study performed in section 7.5.2 indicates that beam-width effects arising from changing the radial transport coefficient are not significant, as they tend to impact the density more than T_e, the latter being the important driver for recombination.

As rate coefficients for atomic and molecular processes, e.g. recombination, are a strong functions of T_e, we also compare the T_e from the code and the experiment. For the target location, apart from TS, T_e was also determined using optical emission spectroscopy, using a Boltzmann plot method on high-n Balmer lines. In the experiment, both upstream and target T_e are weak functions of P_n. Upstream, $T_e \sim$ 2.5 -3.0 eV, and at the target, $T_e \sim$ 0.1 -0.3 eV. In the code, the upstream T_e is more sensitive to increasing P_n, but at the target, T_e appears to decrease only slightly, and is higher by about a factor ∼3 than values measured experimentally. Typically (e.g. based on Fig. 7.3), one would expect the plasma to be strongly recombining also at sub 1 eV temperatures predicted by the simulations, but Fig. 7.11 (B) shows that this is not the case. The reason for this can be illustrated by comparing typical recombination time scales. For the electron-ion recombination process (11), Tab. 7.2, a density of $5{\times}10^{19}$

and T_e=0.7 eV, the recombination time $\tau_{\mathrm{rec}} = 7.8$ ms. The typical particle transit time, between upstream and target, calculated as $\tau_{\parallel} = \int_u^t 1/u_{\parallel} \mathrm{d}z$, where $u_{\parallel}$ is the parallel fluid velocity and z is the parallel coordinate. The parallel transit time for the highest P_n case (j) obtained in the simulations is ∼0.3 ms, and is lower for the cases with lower P_n. Therefore, the ion electron pairs simply do not get enough time to recombine via channel (11) under these conditions. If T_e were ∼0.2 eV, $\tau_{\mathrm{rec}} = 0.2$ ms, indicating that the recombination would become important. This shows that conclusions on the global importance of recombination cannot be based on arguments related to the local T_e or simply on the dominance of certain rate coefficients, but rather the whole transport picture, including the macroscopic flow has to be considered.

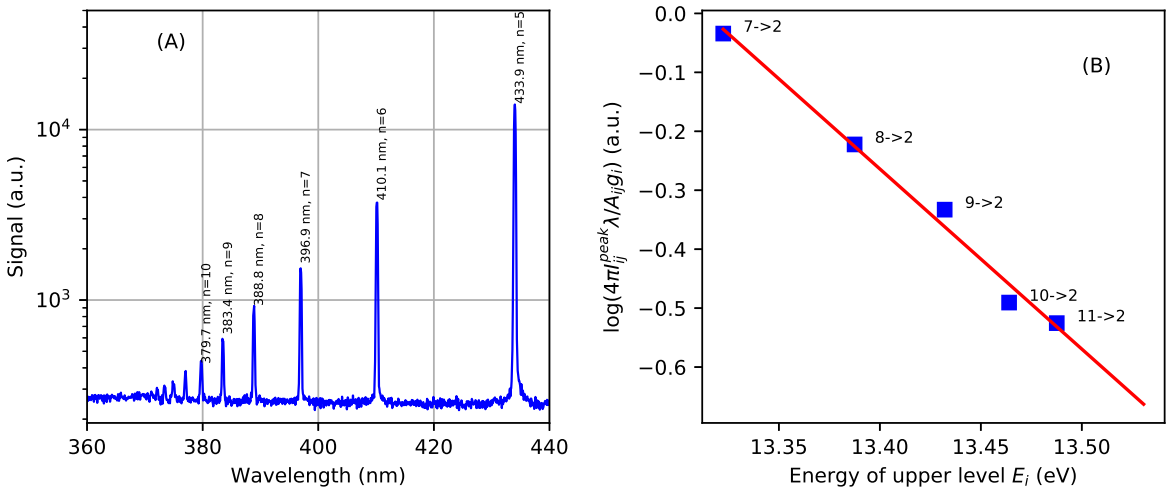

Figure 7.12 – (A) Typical experimental spectrum of the near target plasma from a visible spectrometer looking at the near-target plasma showing high-n Balmer line radiation and (B) an example of a Boltzmann plot using lines transitions 7-2 through 11-2, yielding a temperature of 0.3 eV in this particular case.

Concerning the H_2^+ branch of the MAR pathway, the situation is more complicated, since the recombination rate depends on the rate of formation of H_2^+ via ion conversion, which decreases as a function of T_e, and also on the ratio of the rates of the dissociative recombination (10) and of the competing, purely dissociative process (9), which is stronger for $T_e > 1$ eV. In any case, these processes are included in the framework of the code and they are not causing significant recombination.

7.5.5 Two-point analysis of simulation results

In order to analyse the resulting profiles more deeply, we apply a 2-point formatting analysis inspired by similar analyses performed in [114–116].The aim here is to do the "book keeping" between different processes driving the gradients in the profiles of the particle flux density $\Gamma = nv$, total plasma pressure $\Pi = nm_iv_i^2 + n_ikT_i/e + n_ekT_e/e$ and the parallel heat flux density for electrons q_e and ions q_i. To identify which terms contribute the most to the reduction of e.g. the particle flux, we integrate the continuity

equation 7.1 between an upstream position, denoted "u" and a position close to the target, denoted "t". Further on, these two positions correspond to upstream and target TS positions, i.e. Z=4 cm and 54 cm, respectively. Next, we formally look at the radial transport term $\vec{\nabla} \cdot (D\vec{\nabla}_{\perp} n)$ on the R.H.S. of the equation as an additional source term and denote it $S_n^{\perp}$. Taking into account the simple, orthogonal geometry of the linear device and assuming steady state (time dependent term vanishes, which is the case in a converged simulation), we obtain the following:

$$\Gamma_t - \Gamma_u = \int_u^t S_n^{(\perp)} \mathrm{d}z + \int_u^t S_n^{(N)} \mathrm{d}z \tag{7.6}$$

where Γ is the parallel particle flux density. The external source term $S_n^{(\mathrm{ext})}$ from equation 7.1 vanishes by definition due to the choice of the "u" and "z" positions. The same can be done with the momentum equation 7.2, in which case we multiply the equation by the ion mass m_i so that the quantity in the divergence on the L.H.S. is the total plasma pressure Π defined earlier in this section. Again, we formally rename the term associated with radial transport $\vec{\nabla} \cdot (\nu \vec{\nabla}_{\perp} n u_{\parallel})$ as $S_G^{(\perp)}$. After the integration we have:

$$\Pi_t - \Pi_u = \int_u^t m_i S_G^{(\perp)} \mathrm{d}z + \int_u^t m_i S_G^{(N)} \mathrm{d}z \tag{7.7}$$

i.e., the reduction of the total pressure between upstream and target location for a given flux tube is driven by momentum sources (sinks) due to neutrals and radial transport.

For the ion and electron energy equations 7.3 and 7.4, we move the electron pressure gradient term $u_{\parallel} \nabla_{\parallel} n k_B T_e$ to the R.H.S. of the equation. Then, we formally rename the perpendicular energy transport term (the 1st term on the R.H.S. of equations 7.3, 7.4) as $S_{E,i}^{(\perp)}$ and $S_{E,e}^{(\perp)}$, respectively. After integration, we obtain the following:

$$q_{t,\alpha} - q_{u,\alpha} = \int_u^t S_{E,\alpha}^{(\perp)} \mathrm{d}z + \int_u^t S_{E,\alpha}^{(N)} \mathrm{d}z \pm \int_u^t Q_{\alpha}^{(c)} \mathrm{d}z \mp \int_u^t u_{\parallel} \frac{\partial (n k_B T_e)}{\partial z} \mathrm{d}z \tag{7.8}$$

where q is the total heat flux density and α is a species index, i.e. ions or electron in our case. In case of the double sign ($\pm$) operator, the upper and lower sign corresponds to ion and electrons, respectively. The other symbols were defined in section 7.4.1. The obtained equation states that the reduction of the total heat flux density between upstream and target location for a given flux tube for a given species is driven by radial transport, sources/sinks due to the interaction with neutrals, sources/sinks due to temperature equilibration and a term associated with the pressure gradient, which is in fact the combined effect of the electric field force and ion-electron friction force.

For the electron energy equation, we can go one step further, and decompose the electron energy source term due to neutrals $S_{E,e}^{(N)}$ into its different contributions (remaining in the framework of the Eirene atomic & molecular physics model used in the simulations presented here)

Table 7.4 – List of potential energies (in eV) appearing in the electron energy loss terms of equation 7.9. The number in the superscript refers to the label of the reaction in Tab. 7.2 to which the potential is associated

$\chi^{(1)}_{\text{ion}}$	$\chi^{(4)}_{\text{diss}}$	$\chi^{(5)}_{\text{diss}}$	$\chi^{(3)}_{\text{ion}}$	$\chi^{(8)}_{\text{diss}}$	$\chi^{(9)}_{\text{diss}}$
13.6	10.5	28.1	15.4	10.5	25.5

$$
\begin{aligned}
S^{(N)}_{E,e} = &- \chi^{(1)}_{\text{ion}} n_e n_{\text{H}} \langle \sigma v \rangle^{(1)}_{\text{ion}} - \chi^{(4)}_{\text{diss}} n_e n_{\text{H}_2} \langle \sigma v \rangle^{(4)}_{\text{diss}} - \chi^{(5)}_{\text{diss}} n_e n_{\text{H}_2} \langle \sigma v \rangle^{(5)}_{\text{diss}} \\
&- \chi^{(3)}_{\text{ion}} n_e n_{\text{H}_2} \langle \sigma v \rangle^{(3)}_{\text{ion}} - \chi^{(8)}_{\text{diss}} n_e n_{\text{H}^+_2} \langle \sigma v \rangle^{(8)}_{\text{diss}} - \chi^{(9)}_{\text{diss}} n_e n_{\text{H}^+_2} \langle \sigma v \rangle^{(9)}_{\text{diss}} \\
&- n_e^2 \langle E \sigma v \rangle^{(11)}_{\text{rec}} - n_e n_{\text{H}} \Big(\langle E \sigma v \rangle^{(1)} - \chi^{(1)}_{\text{ion}} \langle \sigma v \rangle^{(1)}_{\text{ion}} \Big),
\end{aligned}
\tag{7.9}
$$

where n_e, n_H and n_{H_2} are the electron, neutral atom and neutral molecule densities, $\langle \sigma v \rangle^{(\text{i})}$ are rate coefficients in m^3s^{-1} and the upper index (i) denotes the process they are associated to from Tab. 7.2 and the values $\chi^{(\text{i})}$ are potential energies associated with those reactions, e.g. for the H ionisation reaction (1) this energy is equal to the ionisation potential, $\chi^{(1)}_{\text{ion}}$= 13.6 eV. The values of the other potentials are listed in Tab. 7.4.The quantities of the form $\langle E \sigma v \rangle^{(\text{i})}$ are total energy loss rate coefficients associated with a certain process or set of processes. These loss rates are obtained from collisional radiative modelling and are readily available in the AMJUEL database (www.eirene.de). In this case, we have the energy loss rate for electron-ion recombination (penultimate term in equation 7.9), and a term associated with line radiation by atomic hydrogen, which corresponds to the last term $-n_e n_{\text{H}} \Big(\langle E \sigma v \rangle^{(1)} - \chi^{(1)}_{\text{ion}} \langle \sigma v \rangle^{(1)}_{\text{ion}} \Big)$. Since the energy weighted rate coefficient $\langle E \sigma v \rangle^{(1)}$ already includes the losses due to ionisation, we have to subtract them from total energy loss since we have already included net ionisation losses in equation 7.9 (1st term). Therefore, the last term in equation 7.9 represents the net electron energy loss due to hydrogenic radiation.

In Fig. 7.13 (A), the integrated loss term for particle flux density Γ is plotted in the form of a bar chart and is split into two contributions: radial transport and sources due to neutrals, for cases (e), (f), (g), (a), (h), (i), (j), (c), (d) from Tab. 7.3. The cases are ordered by increasing background pressure. Case (k) uses the same setting as the reference case (a) with the exception that the elastic ion-molecule collision (process (6), Tab. 7.2) is switched off. The charts are for the flux tube located 1.4 mm off-axis. If the bar is positive, the contribution of the given process increases the flux density Γ; if it is negative, it decreases Γ. The sum of the two contributions is then equal to the difference in target and upstream flux, $\Gamma_t - \Gamma_u$. From the bar chart, it can clearly be seen that most of the reduction of the target flux density is driven by the radial transport, in every plotted case. For cases (e-g), with lower background pressure, the integrated source term due to neutrals is positive, meaning that ionisation dominates recombination. However, as P_n is increased, it can be seen that this contribution is reduced and that the balance flips towards negative contribution for cases (h-j), meaning that in those cases recombination dominates. Still, the source terms related to neutral interactions remain comparatively small with regard to radial transport.

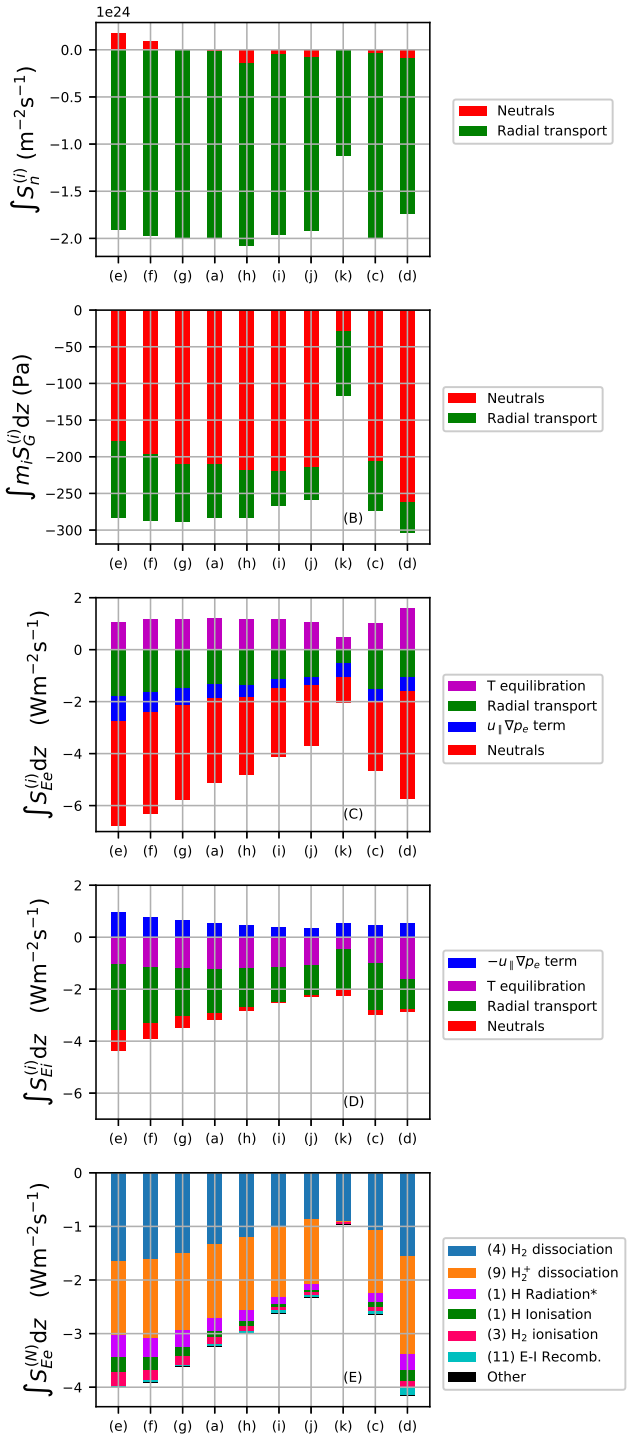

Figure 7.13 – Bar plot of the integrated source terms for particles (A), momentum (B), electron energy (C), ion energy (D) and the energy source term due to interactions with neutrals (E) broken down into its different contributions. Detailed description of the terms are provided in the text.

Case (k), where the elastic collision was switched off, is qualitatively different from the other cases. Here, the contribution of radial transport is about ~ 2 times smaller and

the contribution of neutrals is negligible.

In Fig. 7.13 (B), the integrated loss term for the total pressure Π is plotted, in a similar way as the particle flux density in the previous paragraph. In this case, the reduction of total pressure is driven mostly by interactions with neutrals, and radial transport plays a secondary role. As P_n is increased, there is also a slight increase in the momentum sinks due to neutrals, and a reduction of the momentum sinks due to radial transport. However, in case (k), when the elastic collision (6) is switched off, the momentum sink term is significantly decreased. This indicates that elastic ion-molecule collisions are dominantly responsible for reduction of the total plasma pressure Π.

In Fig. 7.13 (C) and (D) the integrated loss terms for the energy flux density of electrons and ions are plotted, respectively. As pointed out earlier in this section (equation 7.8), the reduction in energy flux density can be driven by sources/sinks due to neutrals, radial transport, electron-ion temperature equilibration and a term related to the pressure gradient. In the case of electrons, most of the energy is dissipated by neutrals, a smaller part of it by radial transport and an even smaller fraction by the pressure gradient term. In case of the electrons, there is also a positive contribution due to the temperature equilibration term. For the reduction of ion energy flux density, the channel due to neutrals is small and energy flux dissipation due to radial transport is dominant. The temperature equilibration term has the same magnitude but opposite sign, by definition. As a general feature, the ions are transfering heat to the electrons. This is consistent with the fact that the combined energy sinks due to other processes are stronger for electrons in the regimes explored here, particularly the sinks due to neutrals. Still, the temperature equilibration term is strong enough to maintain $T_e = T_i$ throughout the axial profile, as can be seen in e.g. Fig. 7.7.

It is interesting to further break down the integrated electron energy sink term due to neutrals $S_{E,e}^{(N)}$ following equation 7.9. This is plotted in Fig. 7.13 (E). It can be seen that the strongest energy neutral dissipation channels are dissociation of H_2 molecules (4) and H_2^+ molecular ions (9). Processes related to atomic hydrogen, like ionisation and line radiation, play a secondary role in energy dissipation. Moreover, even the atomic hydrogen results from the presence of molecules, as most of it is formed by dissociation of molecules or molecular ions.

Since from the previous section we found that the simulations overestimate T_e close to the target, we look more closely at the energy sink term to see the spatial distribution of electron energy sinks. Parallel profiles of the most important contributors to the electron energy source term due to neutrals ($S_{E,e}^{(N)}$) are plotted for the flux tube located 1.4 mm from the axis of symmetry. As expected from the two-point analysis described earlier, the contributions of dissociative processes (4) and (9) are the most important energy sinks, followed by radiation and ionisation of atomic hydrogen. However, these processes seem to be efficient only in the upstream region ($Z < 0.25$m), where T_e is sufficiently high. For $Z > 0.3$m, the electron energy sinks are negligible. We infer that the reason why the T_e decreases rapidly in the upstream region (Fig. 7.8) is this strong spatial localisation of the energy sinks. Conversely, T_e in the region closer to the target decreases only slightly. However, T_e measured experimentally is systematically lower than in the simulations. This indicates that there could be missing energy dissipation

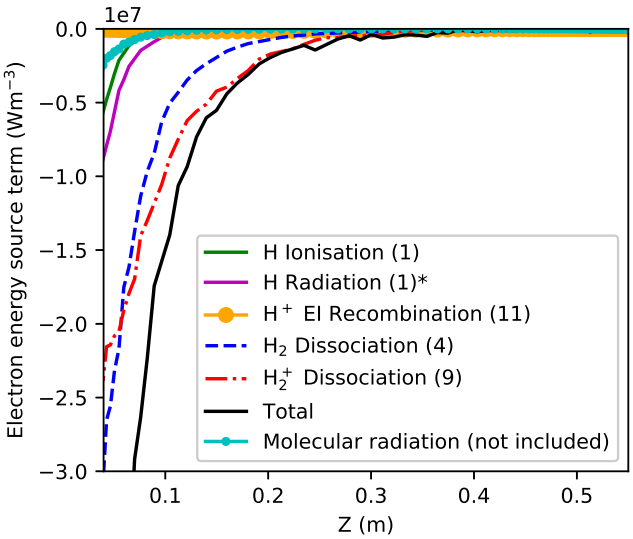

Figure 7.14 – Parallel profiles of the total electron energy sink terms due to interactions with neutrals, following equation 7.9, for the flux tube located 1.4 mm off axis. Only the most important contributions are plotted. Moreover, the sink term related to intrinsic molecular radiation is also plotted, in order to gauge its magnitude, but it is not included in the atomic physics framework of simulations presented here. The * indicates that the plotted term is net radiation, with ionisation losses subtracted.

channels in the simulations. One possibility could be the intrinsic radiation of molecules themselves (e.g. due to molecular lines/bands) which is not included in the current framework. An energy-weighted rate coefficient is available for this kind of loss process in the AMJUEL database under reference H10.2.2.h2r, obtained by collisional-radiative modelling. This term was used to simply calculate the energy loss from the resulting n_e, n_{H_2} and T_e (i.e. not in a self-consistent way) of the simulation result shown in Fig. 7.14. It turns out that this term is approximately two orders of magnitude lower compared to the sum of the other channels, and is also spatially localized at the upstream region. Therefore, it is considered unlikely that proper inclusion of intrinsic molecular radiation would alter the T_e profiles significantly. Other possible dissipation mechanisms should be considered to resolve this discrepancy. It is also important to stress here that the vibrational distribution of neutral hydrogen molecules is described in a simplified way. In particular, individual vibrationally excited species are not followed, but a vibrational distribution as a function of the local T_e is assumed based on [113], and this distribution is used when calculating rate coefficients for i.e. the ion conversion reaction (7). Therefore, the energy costs associated with vibrational excitations are also not accounted for, and it is speculated that these additional energy sinks could contribute to the reduction of T_e.

We also point out here that electric currents and drifts were not included in the simulations presented here. It is difficult to make statements about their impact without running the simulations with their inclusion. However, currents flowing through a plasma are expected to act as additional heating mechanism via Ohmic heating, espe-

cially for low temperature plasmas. Additional heating would lead to an even higher T_e at the target, not helping resolve the observed discrepancy.

7.5.6 Implications for divertors

Implications of results from linear devices for tokamak divertors have to considered carefully due to the differences in geometry and operation. However, we think that the findings presented here can still provide some useful insights. In the previous section, it has been shown that inelastic collisions of the electrons with the surrounding molecules provide a strong heat dissipation channel, accounting for >50% of the reduction of the total heat flux density (Fig. 7.13) for a given flux tube. It is important to point out that in Pilot-PSI a large part of the molecules originate from the cascaded arc source, since only a fraction (typically ∼10%) is ionised. In tokamaks this is not the case, since the neutrals in the divertor are exclusively supplied by the plasma recycling itself, i.e. via target plate neutralisation and volume recombination of ions and electrons and further recombination of the resulting atoms into molecules. In general, the molecule density is typically lower than the atomic density and it is concentrated close to the target plates, especially for open divertor configurations. However, recent modelling efforts of closed divertor geometries at DIII-D [120–122] have shown molecular densities comparable to Pilot-PSI conditions, up to 10^{20} m^{-3} and a near-target T_e ∼1 eV. Such refinements of the divertor geometry have resulted in better performance in terms of power dissipation, both from the edge transport codes and modelling and experiments. Similar results have been obtained by modelling of the super-X divertor for MAST-upgrade [123], which has a very closed divertor wall geometry and is expected to operate at high molecular pressures. It is expected that in such divertor conditions, the principle acting mechanisms in terms of atomic and molecular physics, will be the same. In our setup of the Soledge2D-Eirene transport code, comparisons with modelling and experiments show that T_e close to the target is overestimated by the code under the examined, low T_e, high n_e conditions.

7.6 Conclusion & Outlook

The Soledge2D-Eirene tokamak edge plasma transport code has been applied in the cylindrical geometry of the Pilot-PSI linear plasma device with the aim to a) assess how well the code can reproduce experimental trends and b) give new insights into the interpretation of experiments. The effect of the neutral pressure P_n on the simulation results was investigated and compared to measurements using TS, an embedded LP in the target and visible spectroscopy. It has been found that in the simulations, T_e at the target is overestimated with respect to the measurements using TS and spectroscopy. T_e in the simulations appears to saturate at 0.7 eV for a wide range of parameters (also in response to changes of the perpendicular transport coefficients, the main unknown parameter in the simulations), while experimentally values of 0.1-0.3 eV are found. It is inferred that the overestimation of T_e in the simulations is the cause for the

underestimation of volume recombination, which is a strong function of T_e for $T_e < 1$ eV.

A two-point formatting approach was used to analyse the drivers of the reduction of flux density, total plasma pressure and the heat flux density in the simulations between upstream and target locations. It was found that the strongest driver for reduction of the particle flux density on a given flux tube was radial transport. For the reduction of total plasma pressure, elastic ion-molecule collisions are the dominant mechanism. For the heat, inelastic collisions between electrons and neutral backround particles dissipate most of the heat flux. From these inelastic processes, dissociation of molecules and molecular ions were found to be the strongest contributors. However, these energy sinks are located in the upstream region, where T_e is high enough to efficiently break up molecules and molecular ions; in locations close to the target, the simulations do not predict any mechanism that could dissipate the heat flux and subsequently reduce T_e to values of 0.2 eV found in the experiment, i.e. where volume recombination could remove a significant number of plasma particles. A rudimentary estimate was made to try to account for intrinsic (line/band) radiation of molecules themselves, which was not included in the neutral physics model in Eirene in the simulations presented here, however it turned out that it is unlikely that this process could explain the discrepancy in T_e. Other mechanism will be looked into in the future, for instance energy costs due to vibrational excitations of molecules. Moreover, the convergence issues for $P_n > 6$ Pa when ion conversion is present merit further investigation.

Further possibilities to study plasmas relevant to detachment are offered by the Magnum-PSI linear plasma device, with a better diagnostic coverage. Target calorimetry and a newly installed bolometric diagnostic [71] could shed more light on studies of the power balance, while a collective Thomson scattering diagnostic [124] (under development) could give axial velocity information.

Acknowledgments

This work was granted access to the HPC resources of Aix-Marseille University financed by the project Equip@Meso (ANR-10-EQPX-29-01) of the program “Investissements d’Avenir” supervised by the Agence Nationale pour la Recherche. This work was carried out with financial support from NWO and was carried out within the framework of the Erasmus Mundus International Doctoral College in Fusion Science and Engineering (FUSION-DC). This work has been carried out within the framework of the EUROfusion Consortium and has received funding from the Euratom research and training programme 2014-2018 under grant agreement No 633053. The views and opinions expressed herein do not necessarily reflect those of the European Commision.

Chapter 8

Gas puff experiments at Magnum-PSI from the perspective of power exhaust

in preparation for submission as K. Jesko, Y. Marandet, I. Classen, H.J. van der Meiden, J.P. Gunn, J. Vernimmen, G. Akkermans, R. Perillo, T.W. Morgan and the Magnum-PSI team, Gas puff experiments at Magnum-PSI from the perspective of power exhaust

8.1 Abstract

Magnum-PSI is a linear device operating with a cascaded arc plasma source that produces plasmas comparable to those expected during the inter-ELM phase in the ITER divertor ($T_e \sim 1$ eV, $n_e \sim 10^{20}\mathrm{m}^{-3}$). In this study we determine the sheath heat transmission coefficient for a hydrogen plasma by comparing the heat flux estimated from Thomson scattering (TS) and target calorimetry. The results clearly show that the usually assumed value of the sheath heat transmission $\gamma = 7$ severely underestimates the energy flux to the target for the sub 1 eV, high density plasmas studied in these experiments. Inclusion of the 13.6 eV and 2.2 eV for surface ion and atom recombination, respecively, is needed for the heat flux estimated from TS to be consistent with calorimetry. Although the agreement is significantly improved, the values deduced from TS are still about $\sim$ 10-20% lower than calorimetry. A case study using the Soledge2D-Eirene code indicates that this could be explained by energetic neutrals depositing their energy on the target. However, in the Soledge2D-Eirene modelling, we were not able to reproduce the low T_e observed experimentally by target TS. Comparisons between the experimentally measured bolometer incident heating power and the one estimated from the code output using a synthetic diagnostic show an underestimation by the code by a factor of ~ 7 in the best case. If the effect of radiation of excited atoms created by electron-impact dissociation of molecules and molecular ions is accounted for in the synthetic diagnostic, this discrepancy can be reduced to a factor ~ 3 at best.

8.2 Introduction

In ITER, in the D-T phase at fusion gains of $Q = 10$, the steady state power crossing the last closed flux surface (LCFS) and entering the scrape-off layer (SOL) is expected to be about ∼100 MW [125]. Based on scaling laws and also theoretical work the typical power scrape-off length in the inter-ELM phase is expected to be $\lambda_q < 5$ mm . This leads to a total plasma wetted area which, accounting for flux expansion and target inclination, is estimated to be around 2.3 m^2, resulting in a power loading of ~ 40 MW/m^2 of the divertor target plates, in case of no mitigation. This is above the technological limit of 10 MW/m^2 of steady state power loading for the plasma facing components (PFCs) [19]. Therefore, a large fraction of the power has to be dissipated in the SOL before reaching the target. This can be achieved with divertor detachment, a regime in which a large fraction of the power is dissipated in the SOL/divertor region, reducing the ionisation source and lowering the near-target electron temperature to values where volume recombination becomes significant, leading to a reduction of the ion flux to the target.

Divertor detachment has been routinely achieved in many divertor tokamaks and its onset is manifested by parallel-to-B plasma pressure gradients in the SOL and a rollover of target ion flux density with increasing core density during density ramp-up discharges [24]. It is generally very difficult to diagnose the divertor region with spatially resolved measurements. The complicated diagnostic access to divertor plasmas in tokamaks motivates to study the effect in linear plasma devices. The Pilot-PSI linear plasma generator offers a high density ($n_e \sim 10^{21}$ m^{-3}) and low temperature ($T_e \sim 1$ eV) plasma whose parameters are similar to those expected during partially detached ITER divertor operation [54].

In this work, we study a divertor-relevant plasma in the Magnum-PSI device. Magnum-PSI can provide densities of $10^{20} - 10^{21}$ m^{-3}, relevant to the regimes expected in ITER. In earlier work at Pilot-PSI [112] it was found that the low T_e measured close to the target could not be reproduced in the simulations using the Soledge2D-Eirene edge transport code, indicating that the energy losses are underestimated in the framework of the code. The main aim of this work is also to address power and particle balance in Magnum-PSI experimentally and also using an edge transport code. However, here we exploit the target calorimetry diagnostic, previously unavailable at Pilot-PSI, and the newly installed resistive bolometry [71] to help shed more light on these potentially missing energy dissipation mechanisms.

8.3 Methods

8.3.1 Experimental setup

The Magnum-PSI linear plasma device [49,68,69] is based on a cascaded arc discharge source [56]. Magnum-PSI has a number of major advantages with respect to its forerunner, Pilot-PSI [54]. Firstly, it uses a superconducting magnet, which enables continuous operation at a magnetic field of up to 2.5 T. Secondly, it uses a two-stage differential

Table 8.1 – Machine setting of Magnum-PSI during the target gas puff experiment, corresponding to the magnetic field (B), discharge current of the cascaded arc source (I_{dis}), source gas flow rate $\phi_{\mathrm{H_2}}^{(\mathrm{S})}$, target gas puff rate $\phi_{\mathrm{H_2}}^{(\mathrm{T})}$ (the latter two are in standard liters per minute(slm)) and the resulting target chamber background pressure $P_{\mathrm{n}}^{(\mathrm{T})}$.

B (T)	I_{dis} (A)	$\phi_{\mathrm{H_2}}^{(\mathrm{S})}$ (slm)	$\phi_{\mathrm{H_2}}^{(\mathrm{T})}$ (slm)	$P_{\mathrm{n}}^{(\mathrm{T})}$
1.2	175	7	0 - 16	0.5 - 9.6

pumping system to minimise the leakage of residual neutrals from the cascaded arc source to the target exposure chamber [70]. Thirdly, it disposes of a target analysis chamber (TEAC), where previously exposed targets can be subjected to ion beam analysis techniques without the need to remove them from the vacuum vessel. Finally, the Magnum-PSI target station is designed to be able to move along the machine axis, and also to rotate and tilt, making possible the testing of PFC materials at grazing B-field incidences. Additionally, the position of the cascaded arc source can also be moved axially. As a result, the source and target positions cannot be used a reference point for distance. Instead, the $Z = 0$ location is defined as the axis of the vacuum port/tube used for the target chamber Thomson scattering laser beamline. The positive direction is defined as the one going towards the source. The source chamber Thomson tube is located at Z =1250 mm. The positions of the source nozzle and target surface in this work were Z =1350 mm and Z =-2 mm, respectively.

An overview of the machine settings used in the frame of the experiment is provided in Tab. 8.1.

In the frame of this work, the following diagnostics have been used. Firstly, Thomson scattering was performed in the target chamber, approximately 2 cm in front ot the target surface. A calorimetric diagnostic was available, making possible measurements of the total power absorbed by the entire target station, from the difference of the incoming and outgoing cooling water temperature and the cooling water flow rate. Additionaly, a new bolometric diagnostic was installed recently [71], based on resistive foils, to measure the radiated power close to the target.

8.3.2 Simulation setup

The Soledge2D transport code was designed for investigation of the transport of multi-fluid plasmas in the tokamak edge and in the SOL [72]. The equations solved by the code with the setup used in this work are detailed in [112].

We take advantage of the topological equivalence between the magnetic field of a tokamak scrape off layer (SOL) and a linear plasma device. The grid is depicted in Fig. 8.1. The axial magnetic field of the linear device corresponds to the poloidal magnetic field of a tokamak and has a constant value of 1.2 T in all simulations presented here, as well as in the experiments presented here. Variable grid density is used in order to provide high resolution in the plasma beam and close to the walls, while in dull areas of the device the grid is coarse.

The plasma wall interaction is treated using the penalization technique [86–89],

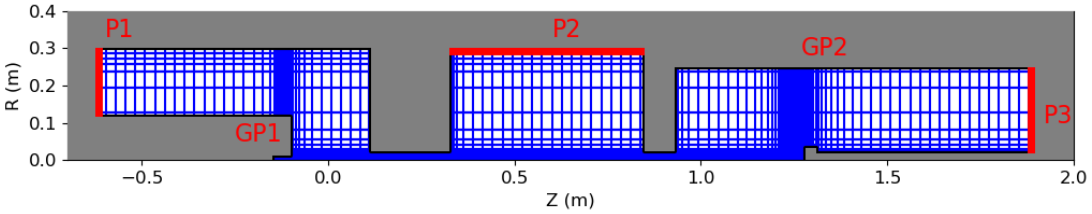

Figure 8.1 – The grid that has been used in the Magnum-PSI simulations.. The labels P1, P2 and P3 indicate the locations of pumping surfaces in the source chamber, heating chamber and target chamber, respectively. Labels GP1 and GP2 indicate the positions of the source (neutrals from cascaded arc) and target chamber gas puffing.

a unique feature of SolEdge2D permitting simulation of the plasma up to the first wall in tokamaks. Using this technique, standard Bohm boundary conditions and sheath heat transmission are recovered at the plasma-wall interface, i.e. $|M| \geq 1$ and $q_{t,e} = \gamma_e n M c_s T_e$, where M is the Mach number, $q_{t,e}$ is the energy flux density through the interface for electrons. For ions, the energy flux density is given by $q_{t,i} = nMc_s(\gamma_i T_i + 1/2M^2 c_s^2)$ since the energy of the mean flow has to be accounted for, where c_s is the sound speed and γ_α are the sheath heat transmission factors for ions and electrons, set to 2.5 and 4.5, respectively. Note that even though Soledge2D energy equations are formulated in terms of the total energy, the values of heat transmission factors shown here are for the internal energy part. The ion velocity distribution function at the sheath edge is assumed to be a shifted Maxwellian with c_s normal to the wall, so the effective sheath heat transmission factor for ions is in fact 3.5 in the case of $T_i = T_e$ (on the high side). However, this choice ensures internal consistency of the code and is related to the coupling of Soledge2D and Eirene. On the axis of symmetry the boundary condition of vanishing perpendicular gradients for all quantities is used. In this work, PIC database relating the magnetic pre-sheath entrance conditions to the ion velocity distribution at the wall available in Soledgde2D-Eirene [72] is not employed here since the former is designed for grazing magnetic field incidence. The effect of drifts and electric currents is not considerd in this phase of the work.

Anomalous values are assigned to the radial transport coefficients and have values of 0.05 m^2/s, 0.1 m^2/s and 0.1 m^2/s for the particle, electron and ion energy diffusivities, respectively.

The plasma particle and power sources are directly prescribed as external volumetric source terms $S_n^{(ext)}, S_G^{(ext)}, S_{E,i}^{(ext)}, S_{E,e}^{(ext)}$ in the Soledge2D equations. For instance, the external volumetric source terms for the plasma ion/electron source has the form of a Gaussian function in both r and z directions:

$$S_n^{(ext)}(r,z) = \frac{S_n^{(ext,tot)}}{C} \exp\Big(-(r-r_0)^2/\lambda_r^2 \Big) \exp\Big(-(z-z_0)^2/\lambda_z^2 \Big), \tag{8.1}$$

where r_{src}, z_{src} are the positions of the profile maxima, λ_r, λ_z are the profile widths, C is a normalization constant such that the volume integral over the simulation domain be equal to the total number of injected particles, i.e. $\int_V S_n^{(ext)} \mathrm{d}V = S_n^{(ext,tot)}$. A similar

external source term is also defined for the energy source on electrons and ions, $S_{Ee}^{(ext)}$ and $S_{Ei}^{(ext)}$, respectively. The position and spatial extent of the external volumetric source terms was chosen such that it stays well within the small area of the cascaded arc source. The values of the individual constants are listed in Tab. 8.3

The transport of neutrals and their interaction with the plasma is adressed by the Eirene Monte-Carlo code [90]. Hydrogenic atoms and molecules are ubiquitous in Magnum-PSI as they are fed into the cascaded arc source at a steady gas flow rate of typically 2-10 standard litres per minute (slm). Only a small fraction of these is ionised, the rest being exhausted into the vessel. This is simulated by a steady gas puff in the source region, displayed in Fig. 8.1 by label GP1. The possibility to of a gas puff in the target chamber has also been included, at the position labeled by GP2 in the same figure. The differential pumping is mimicked by defining a pumping surfaces in each chamber of the device, approximately at the location of the pumping ducts. A coefficient of absorption (albedo) is defined on this surface and its value is adjusted to recover the background pressure measured by baratron gauges in each chamber. The values of the albedos are typically < 0.1. The species considered in Eirene are hydrogen atoms H and molecules H_2 and H_2^+ molecular ions. The latter is treated in the static approximation, i.e. its motion is not followed and the next collision is supposed to happen at the location of birth. The validity of this was checked in [112].

The model for plasma-neutral interactions used in Eirene is the same as in [112] and will not be detailed here.

8.4 Results and discussion

8.4.1 Reduction of ion flux at the target

The main purpose of the experiment was to investigate the effect of neutral gas on the plasma beam in the target chamber, in with particular focus on energy dissipation. This was done by performing a scan of the target chamber background pressure by puffing aditional H_2 gas into the target chamber (the machine settings used are listed in Tab. 8.1). Fig. 8.2 (A) shows the total ion flux (i.e. integrated over the cross section) as a function of the changing background pressure P_n estimated from Thomson scattering using cylindrical integration:

$$\Gamma_{\mathrm{tot}} = \int_0^{2\pi} \int_0^{R_{\mathrm{vess}}} r\Gamma(r)\mathrm{d}r\mathrm{d}\phi \tag{8.2}$$

where the local ion flux density to the target was estimated using the Bohm criterion, assuming $T_i = T_e$, a polytropic coefficient of unity and assuming a 1/2 drop of density in the pre-sheath, i.e. $\Gamma(r) = \frac{1}{2} n_e^{(\mathrm{TS})} \sqrt{2T_e^{(\mathrm{TS})}/m_{\mathrm{i}}}$, where $n_e^{(\mathrm{TS})}$ and $T_e^{(\mathrm{TS})}$ are the measured electron density and temperature, respectively. The latter assumption (i.e. on the density drop in the pre-sheath) was verified in Pilot-PSI experiments [117]. It can be seen that the total ion flux drops from the value of about 4.6×10^{20} s^{-1} to below 5×10^{19} s^{-1}. However, all the source settings are kept the same. This indicates

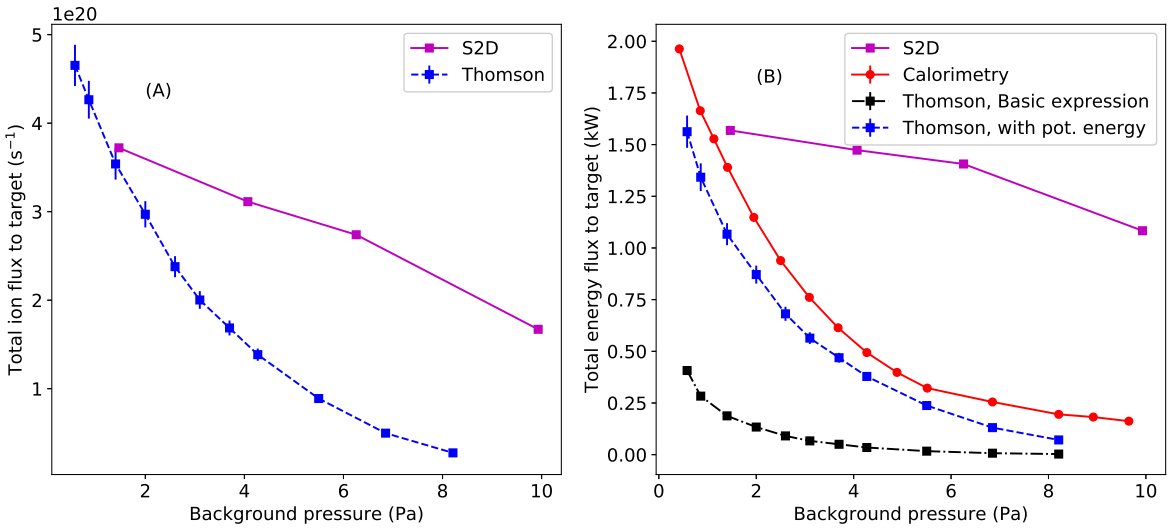

Figure 8.2 – Response of the total ion flux density to the target (A) and the total energy flux to the target (B), estimated from TS and calorimetry and recovered by modelling using Soledge2D-Eirene (labeled 'S2D' in the legend). The energy flux estimation from TS is carried out using the basic expression and the expression including potential energy terms.

Table 8.2 – Values of the individual constants used in the calculation of the sheath heat transmission coefficient, expression 8.3, in order to obtain Fig. 8.3, based on expression 8.3.

χ_i (eV)	χ_r (eV)	$R_{\mathrm{i,E}}$, $R_{\mathrm{e,E}}$, $R_{\mathrm{i,N}}$ (-)	δ (-)
13.6	2.2	0	0

that the plasma is recombining and the results is consistent with earlier experiments at both Magnum-PSI and Pilot-PSI [100].

8.4.2 Comparing energy flux to target from calorimetry and Thomson scattering

The calorimetric diagnostic gives the total energy flux absorbed by the target station. For comparison, we want to estimate this also from the TS measurements located 2 cm in front of the target. The energy flux impinging on the target is typically calculated from sheath physics and is parametrized for a given sheath edge ion flux density Γ_i and electron temperature T_e by using a dimensionless "sheath heat transmission factor"γ_{sh}, i.e. $q_{\mathrm{t}} = \gamma_{\mathrm{sh}} T_e \Gamma_i$. For $T_e = T_i$, following the analysis in [23], p. 654, the value of the sheath heat transmission factor can be written as

$$\gamma_{\mathrm{sh}} = \underbrace{(2.5 - e\frac{V_{\mathrm{sh}}}{T_e})(1 - R_{\mathrm{i,E}})}_{\text{(i)}} + \underbrace{\frac{2}{1-\delta}(1 - R_{\mathrm{e,E}})}_{\text{(ii)}} + \underbrace{\frac{\chi_i}{T_e}}_{\text{(iii)}} + \underbrace{\frac{\chi_r}{T_e}(1 - R_{\mathrm{i,N}})}_{\text{(iv)}}. \tag{8.3}$$

The first term represents the kinetic energy of the ions entering the sheath (assuming a 1D drifting Maxwellian velocity distribution) and the energy acquired in the

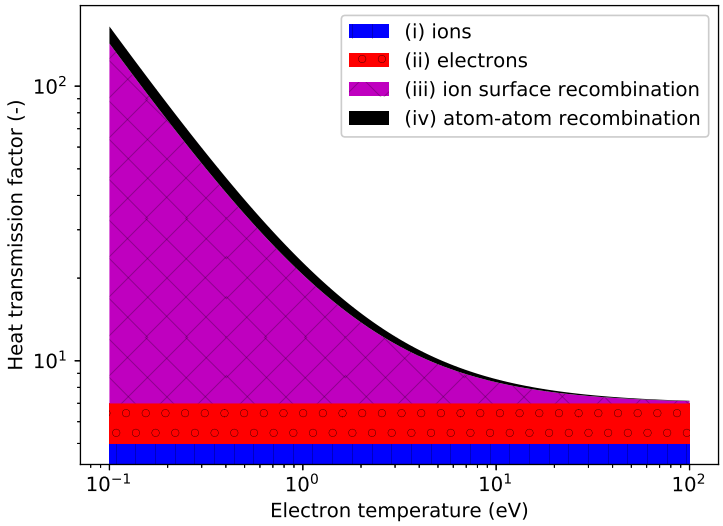

Figure 8.3 – The sheath heat transission factor broken down into its various contributions based on expression 8.3. The meanings of the various terms (i-iv) used in the expression are detailed in the text. It can be seen that for $T_e < 5$ eV, the heat transmission factor is dominated by the surface recombination channel.

sheath electric field, eV_{sh}. Reflection is allowed for, $R_{\mathrm{e,i}}$ being the ion energy reflection coefficient (accounting for ion backscatter as a neutral atom). The second term represents the energy deposited by electrons, which is increased by secondary electron emission, δ being the secondary electron emission yield, and decreased by reflection, $R_{\mathrm{e,E}}$ being the electron energy reflection coefficient. The third term represents the recombination energy of ions χ_i on the surface. Lastly, the fourth term represents the atom-atom recombination energy into molecules at the surface, with reflection allowed for by the coefficient $R_{\mathrm{i,E}}$. Usually, terms 3 and 4 are neglected (e.g. for reasons detailed in [118]), yielding the typically used value of this coefficient of around 7-8 [23] for a hydrogen plasma and a floating target. However, when T_e is lower than 10 eV, especially term (iii) and also (iv) gain significant importance. This can be seen in from Fig. 8.3, where the heat transmission factor was plotted as a function of T_e (=T_i) assuming that the individual quantities in expression 8.3 take the values from Tab. 8.2.

We calculate the total energy flux from the TS measurements by cylindrical integration of the radially resolved energy fluxes for two different cases: (a) without considering terms (iii) and (iv) in expression 8.3, i.e. using the standard value, T_e independet value of $\gamma_{sh} = 7$ and (b) with considering the (T_e dependent) terms (iii) and (iv), and using values from Tab. 8.2. We do this for each case of the background pressure/target puff scan. The comparison of these energy fluxes obtained from TS with calorimetry is shown in Fig. 8.2. The case without the inclusion of (iii) and (iv) grossly underestimates the energy absorbed by the target. On the other hand, when (iii) and (iv) are included, reasonable agreement between the calorimetry and TS estimations of the energy flux are obtained, the TS estimation being always lower

than calorimetry, by roughly 20%. One potential explanation could be related to the fact that the TS estimation inherently only includes the energy flux due to the plasma. However, neutral atoms and molecules are also present in and in the vicinity of the plasma, and undergo collisional processes with it. For instance, dissociation products, charge-exchange atoms etc. can also contribute to the heating of the target. In the following section, the Soledge2D-Eirene code will be exploited to give information on the energy fluxes due to neutrals.

Further sources for the discrepancy could be related to the fact that we assume plasma parameters equal to 0 beyond the radial extent of the TS measurements in the energy flux estimation. However, at 1.2T, the beam is narrow. By linearly extrapolating the profiles outside of the TS measurement range, the agreement can be improved, although the missing 20% cannot be acounted for. Another source of error can be caused by target radiation, as the surface temperature can rise beyond 1000 °C. However, this is relevant only for the low P_n part of the scan, and would in fact cause underestimation of the energy flux by calorimetry, thus effectively moving the two curves in Fig. 8.2 further apart.

In summary, this comparison indicates that it is mandatory to include the terms (iii) and (iv) when estimating the energy flux to the target from TS measurements in typical Magnum-PSI conditions, which are similar to those expected in the ITER divetor during detachment.

8.4.3 Comparison with modelling using Soledge2D-Eirene - energy flux absorbed by target

Initial Soledge2D-Eirene simulations were performed for two main reasons: 1) to see if the reduction of ion and energy flux to the target can be reproduced by simulation of the gas puffing scan and 2) to give an estimate of the various contributions to the target energy flux.

The Soledge2D-Eirene modelling was performed in the following way: we chose the experimental TS n_e and T_e profiles for a case with a backround pressure of 1.4 Pa as a "reference case". Next, we tried to manually adjust the free parameters of the model, i.e. the widths and magnitudes of the external volume particle and energy sources, section 8.3.2, which yielded the parameters depicted in Tab: 8.3. The comparison between the simulation results and the measured TS profiles is depicted in Fig. 8.4. Even though in the depicted case we have attempted to match the target TS profiles with the simulation, it can be seen that the match is not entirely satisfying. For n_e, the code overestimates the density in the central area of the beam ($|R| < 2$ mm), however, the profile is well matched outside of this area. In the case of T_e, the simulation overestimates it by a factor of ~ 2 throughout the profile. It has been found that the free parameters that we could vary were not very effective to control the T_e profile. However, the total ion and energy fluxes to the target could be matched, as can be seen from Fig. 8.2, by looking at the datapoint corresponding to a background pressure corresponding to 1.5 Pa (leftmost datapoint of the "S2D" dataset corresponding to the modelling). The total ion flux is matches well with the TS estimate, and the

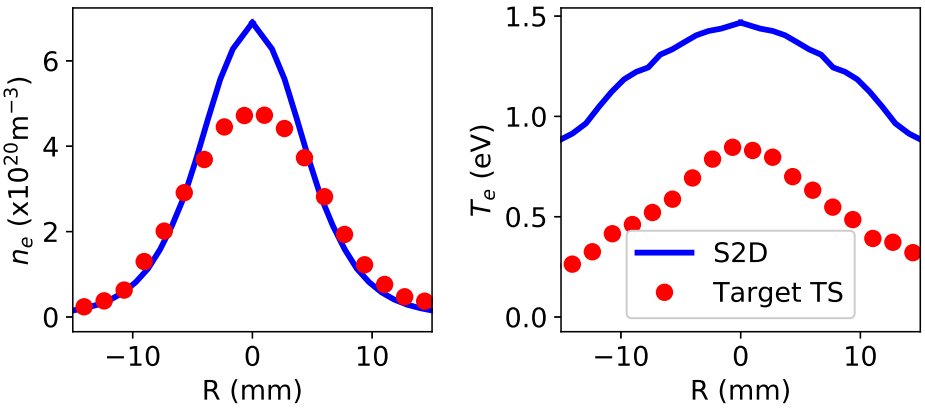

Figure 8.4 – Comparison of radial n_e and T_e profiles measured by TS 2 cm in front of the Magnum-PSI target and Soledge2D-Eirene simulation results. This is the "reference" case at $P_n = 1.5$ Pa, which was used for tuning the free parameters of the simulation from Tab. 8.3 in order to get this match. It is noted that the match is not entirely satisfactory, especially for the T_e profile, where the simulation is approximately by a factor ~ 2 higher than the TS measurement.

total energy flux from the simulation is about 15% higher with respect to the one obtained from calorimetry. Despite the factor ~ 2 mismatch between T_e determined experimentally and obtained in the modelling for the reference case, we consider that it still has value to model the background pressure scan experiment. We model this by puffing additional H_2 gas in the target chamber at the location depicted by label "GP2" in Fig. 8.1.

In the modelling, there is a slight drop in both the total ion flux and the total energy flux to the target, however, the effect is weak and does not match the experimentally observed strong reductions over the P_n scan. This result gives additional evidence that there are energy loss mechanisms missing from the code that are apparently active in the studied Magnum-PSI plasma conditions. It is speculated that the absence of these loss mechanisms is could also be responsible for the difficulty in modelling the low T_e already in the reference case, 8.4.

Additionally, in Fig. 8.5 we break down the energy flux density to the target, as calculated from Soledge2D-Eirene, into its individual contributions, for the reference case simulations (i.e. where the match with the experimental TS profiles is best). It can clearly be seen that the biggest contributor is the potential energy released during ion and atom recombination at the surface. This is consistent with our experimental finding in Fig. 8.2. The energy fluxes due to ion and electron kinetic/thermal energies (i.e. terms (i) and (ii) in eq. 8.3) are about ~ 7 times smaller. Moreover, the energy fluxes due to energetic neutrals (i.e. charge exchange atoms, dissociation products, energetic molecules, etc.) appear to be of a similar magnitude as the fluxes associated with ions and electrons. This offers one potential explanation of the still-observed underestimation of the TS estimated total energy flux w.r.t. calorimetry in Fig. 8.2, as TS does not provide any information on the neutral fluxes. On the other hand, the calorimetry does not distinguish what is the origin of the energy flux, and naturally

Table 8.3 – Values of various constants used for the external source terms (formula 8.1) for the reference case

Type	$S_i^{(\mathrm{ext,tot})}$	λ_r (mm)	λ_z (mm)	r_0 (mm)	z_0 (mm)
$S_n^{(\mathrm{ext})}$	6.0×10^{20} $\mathrm{m^{-3}s^{-1}}$	5.0	10.0	0	-125
$S_{Ee}^{(\mathrm{ext})}$	4.0×10^{3} $\mathrm{Wm^{-3}}$	3.5	7.1	0	-125
$S_{Ei}^{(\mathrm{ext})}$	0.3×10^{3} $\mathrm{Wm^{-3}}$	3.5	7.1	0	-125

also measures to contribution of the neutrals.

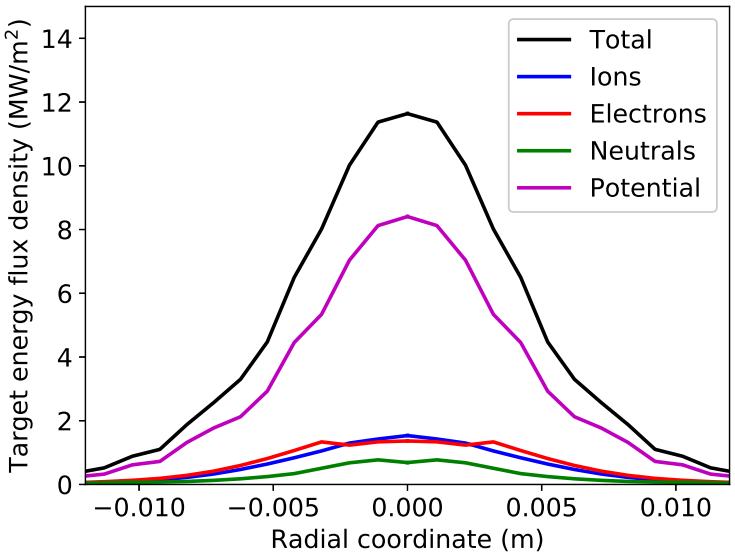

Figure 8.5 – Radial profiles of energy fluxes to the target from Soledge2D-Eirene. Breakdown of the individual contributions to the total target energy flux density profile (black curve, labeled 'Total' in legend) as calculated for the reference case. It can be seen that the energy flux due to release of potential energy at the surface (i.e. surface recombination of ions and atoms, labeled 'Potential' in legend) is the dominant contributor. The contribution of ion and electron kinetic energies is minor. The curve corresponding to legend entry 'Neutrals' is the contribution of of energetic neutrals (i.e. born from ion-molecule elastic collisions or charge-exchange) impinging on the target.

8.4.4 Radiation loss studies

In order to address the issue of potentially missing energy losses in the code, we try to exploit the newly installed four channel resistive bolometer system, recently installed at Magnum-PSI and describe in [71]. During our measurements, the system was still in a commissioning phase, resulting in only 2 channels that were available for analysis. The bolometer chords are perpendicular to the plasma beam, i.e. they provide spatially resolved information in the axial (z) direction. For a schematic drawing of the system, the reader is referred to [71]. During our measurements, we used channel 3

(ch3), looking at an area approximately 3.5 cm in front of the target. The calibrated bolometers yield the total power incident on the sensor, P_s.

In order to compare the radiation in the code with the bolometry, we have chosen the approach of applying a synthetic diagnostic to post-process the code output. In our setup of the code, two differerent sources of radiation are considered: atomic line radiation of hydrogen atoms and radiation connected to the electron-ion recombination process. These are tabulated in the form of energy loss rates in the AMJUEL database used in Eirene. The volumetric energy loss due to radiation $S_{\mathrm{e,E}}^{\mathrm{rad}}$, in W/m^3, as the sum of the two contributions, due to line radiation ($S_{\mathrm{e,E}}^{\mathrm{rad,line}}$) and electron-ion recombination ($S_{\mathrm{e,E}}^{\mathrm{rad,EIR}}$):

$$S_{\mathrm{e,E}}^{\mathrm{rad}} = S_{\mathrm{e,E}}^{\mathrm{rad,line}} + S_{\mathrm{e,E}}^{\mathrm{rad,EIR}} = \underbrace{-n_e n_{\mathrm{H}} \Big(\langle E\sigma v \rangle^{(\mathrm{ion})} - \chi^{\mathrm{ion}} \langle \sigma v \rangle^{(\mathrm{ion})} \Big)}_{1} \underbrace{-n_e^2 \langle E\sigma v \rangle^{(\mathrm{EIR})}}_{2} \quad (8.4)$$

where n_e is the electron density, n_{H} is the neutral atom density, ($\langle E\sigma v \rangle^{(\mathrm{ion})}$ is the energy loss rate[1] due the combined effects of ionisation and line radiation[2], $\langle \sigma v \rangle^{(\mathrm{ion})}$ is the effective ionisation rate coefficient[3]), χ^{ion}=13.6 eV is the hydrogen ionisation potential and $\langle E\sigma v \rangle^{(\mathrm{EIR})}$ is the radiation loss rate[4] due to electron-ion recombination.

In order to obtain the total incident power on the synthetic bolometer, we evaluate this by defining a mask function ξ in the volume, such that $\xi = 1$ in case that the bolometer "sees" the given point in the volume and $\xi = 0$ otherwise. This mask function is depends on the geometry of the bolometer aperture and the distance between the bolometer sensor foil and the aperture, described in [71]. Then, we integrate the radiant energy flux densities from points that the bolometer sees, thus we obtain the total energy flux density at the bolometer sensor, i.e.

$$q_{\mathrm{bolo}}^{(\mathrm{synth})} = \frac{1}{4\pi} \int_V \frac{\xi(\mathbf{X})}{|\mathbf{X}|^2} S_{\mathrm{e,E}}^{\mathrm{rad}}(\mathbf{X}) \frac{\mathbf{X} \cdot \mathbf{n}}{|\mathbf{X}|} \mathrm{dV} \quad (8.5)$$

where $\mathbf{X}$ is the position vector of the given volume element referenced to the bolometer sensor, $\mathbf{n}$ is the unit vector normal to the bolometer sensor surface and the integration is performed over the whole volume. The integration is performed numerically over the whole volume using the Soledge2D output radiation map $S_{\mathrm{e,E}}^{\mathrm{rad}}$.

If Fig. 8.6 (A) the bolometer incident power heating the bolometer foil is plotted for the P_n scan. This is performed for channel 4, whose line of sight intersects the beam at an axial position of approximately 4 cm in front of the Magnum-PSI target. From the scan, we can infer that there is first an increase in the plasma radiation, and a turning point at a P_n=3.5 Pa, after which the radiation starts decreasing. Additionally, the TS peak T_e and n_e profiles are plotted for the scan also in Fig. 8.6 (B) and (C),

[1] AMJUEL database entry H10.2.1.5

[2] This is the reason why in the bracket of term 1 in equation 8.4, the net energy loss related to ionisation potential has to be subtracted from the total rate, so that we are left with the net radiation loss rate.

[3] AMJUEL database entry H4.2.1.5

[4] AMJUEL database entry H10.2.1.8

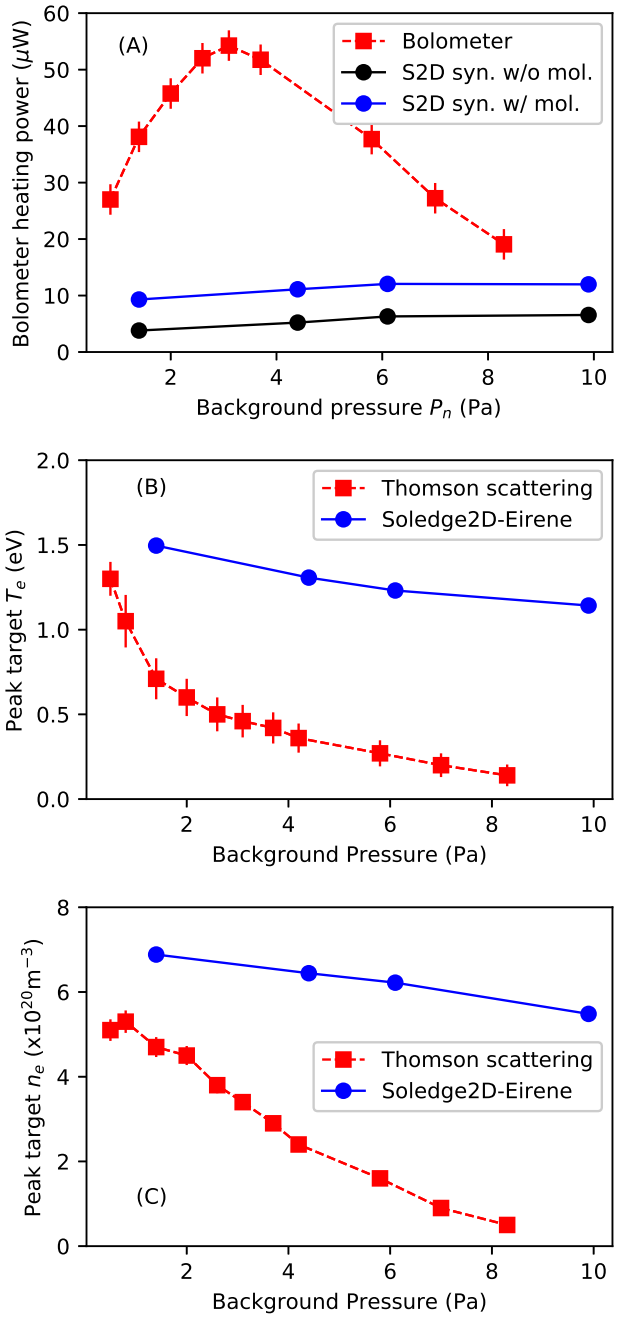

Figure 8.6 – (A) Comparison between the detector heating power measured by the bolometer (red squares) and Soledge2D-Eirene synthetic diagnostic without molecular effects (black circles) and with molecular effects (blue circles). (B) comparison between peak T_e from TS and from Soledge2D-Eirene output evaluated at the same axial location as TS. (C) comparison between peak n_e from TS and from Soledge2D-Eirene output evaluated at the same axial location as TS.

respectively. Both these quantities decrease monotonically, except for the n_e, for wich one can observe a small rollover in the very beginning of the scan. However, the increase of radiation accompanied by the simultaneous decrease of both T_e and n_e indicate a

sharp increase in the volumetric radiated power rate. This is characteristic of radiation related recombination.

Now we try to compare, at least qualitatively, and in view of the matching problems discussed earlier, the experimental bolometry with the synthetic diagnostic in the Soledge2D-Eirene simulations. In Fig. 8.6, the black datapoints represent the heating power computed from the Soledge2D-Eirene calculated volumetric cooling rate, formula 8.4, and using the synthetic diagnostic based on formula 8.5. We can see that the synthetic diagnostic underestimates the radiation measured in the experiments, even for the case where the match between n_e and T_e is the best, where the radiation predicted by the code is approximately $\sim$7 times lower. In the rest of the scan, the comparison is not very informative, as both T_e and n_e differ considerably.

However, we have made an attempt to reconcile the radiation from the code and from the experiment. Dissociative processes involving molecules and molecular ions are known to produce excited atomic hydrogen [141]. These losses are included in the Soledge2D-Eirene simulations and can be recalculated from the code using the relevant energy loss rate coefficient[5] in the AMJUEL database. The case where we included this contribution into the radiative power losses is plotted as the blue line in Fig. 8.6. As we can see, this indeed increases the radiation observed on the detector by a factor ~ 2.5. However, the code still underestimates the radiation by a factor of ~ 3 (for the lowest P_n case).

8.5 Conclusion

In this work, we have studied the ITER-relevant plasma beam at the Magnum-PSI linear plasma device from the perspective of power exhaust using Thomson scattering (TS), calorimetry and the newly installed bolometric diagnostic. We can reproduce the strong reduction of the particle and energy flux to the target during target gas puffing experiments, consistently with similar experiments performed at Pilot-PSI [139]. Comparisons between the total energy flux deposited on the target measured by calorimetry and estimated from TS clearly show that the usually assumed value of the sheath heat transmission $\gamma = 7$ is not a suitable choice for the sub 1 eV, high density plasmas studied in these experiments. It is mandatory to include also the potential energy from target ion and atom recombination in the TS estimation of the heat flux in order to get values consistent with calorimetry. Although the agreement is significantly improved, the values deduced from TS are still about $\sim$ 10-20% (case dependent) lower than calorimetry. Initial Soledge2D-Eirene modelling of the target heat flux density suggests that the contribution of energetic neutrals impinging on the target could be a potential effect explaining this discrepancy.

We have also attempted to model the Magnum-PSI plasma beam using the Soledge2D-Eirene code. We were not able to reproduce the low T_e observed experimentally by target TS. This indicates that there are missing energy losses in the code setup. This has led us to investigate the radiated power in Magnum-PSI by using the newly in-

[5]In this case, this corresponds to AMJUEL dataset entry labelledl H10.2.2.H2c

stalled resistive bolometer [71]. Comparisons between the experimentally measured bolometer incident heating power and the one estimated from the code output using a synthetic diagnostic show an underestimation by the code by a factor of ~ 7 in the best case. If the effect of radiation of excited atoms created by electron-impact dissociation of molecules and molecular ions is accounted for in the synthetic diagnostic, this discrepancy can be reduced to a factor ~ 3 at best. Even if the missing volumetric power loss remains unexplained, this result highlights the crucial role that molecules play in Magnum-PSI.

8.6 Acknowledgements

This work was granted access to the HPC resources of Aix-Marseille University financed by the project Equip@Meso (ANR-10-EQPX-29-01) of the program "Investissements d'Avenir" supervised by the Agence Nationale pour la Recherche. This work was carried out with financial support from NWO and was carried out within the framework of the Erasmus Mundus International Doctoral College in Fusion Science and Engineering (FUSION-DC). This work has been carried out within the framework of the EUROfusion Consortium and has received funding from the Euratom research and training programme 2014-2018 under grant agreement No 633053. The views and opinions expressed herein do not necessarily reflect those of the European Commision.

Bibliography

[1] "Paris Agreement," *United Nations Framework Convention on Climate Change*, 2015.

[2] "2017 Revision of World Population Prospects," *United Nations*, 2017.

[3] H. RAE, "Selecting Heavy Water Processes," *Materials Science Forum*, vol. 31, pp. 19–38, 1978.

[4] M. Kikuchi, K. Lackner, and M. Quang, *Fusion Physics*. International Atomic Energy Agency, 2012.

[5] J. D. Lawson, "Some criteria for a power producing thermonuclear reactor," *Proceedings of the Physical Society. Section B*, vol. 70, no. 1, pp. 6–10, 1957.

[6] J. D. Huba, "NRL PLASMA FORMULARY Supported by The Office of Naval Research," *Plasma Physics*, 2013.

[7] M. Wakatani, V. S. Mukhovatov, K. H. Burrell, J. W. Connor, J. G. Cordey, Y. V. Esipchuk, X. Garbet, S. V. Lebedev, M. Mori, K. Toi, S. M. Wolfe, J. G. Cordey, D. Boucher, A. N. Chudnovskii, J. W. Connor, J. C. DeBoo, W. A. Houlberg, S. M. Kaye, Y. Miura, Y. Ogawa, M. V. Osipenko, F. Ryter, T. Takizuka, G. Bateman, G. Bracco, D. J. Campbell, T. N. Carlstrom, Y. N. Dnestrovski, T. Fujita, A. Fukuyama, P. Gohil, M. J. Greenwald, T. Hoang, G. M. Hogeweij, A. E. Hubbard, O. J. Kardaun, J. E. Kinsey, J. A. Konings, M. Marinucci, Y. R. Martin, D. R. Mikkelsen, J. Ongena, T. H. Osborne, F. W. Perkins, A. R. Polevoi, M. N. Rosenbluth, D. P. Schissel, J. A. Snipes, P. M. Stubberfield, E. J. Synakowski, A. Taroni, K. Thomsen, M. F. Turner, N. A. Uckan, M. Valovic, G. Vlad, R. E. Waltz, J. Weiland, H. Zohm, F. W. Perkins, D. E. Post, N. A. Uckan, M. Azumi, D. J. Campbell, N. Ivanov, N. R. Sauthoff, M. Wakatani, W. M. Nevins, M. Shimada, and J. Van Dam, "Plasma confinement and transport," *Nuclear Fusion*, vol. 39, no. 12, pp. 2175–2249, 1999.

[8] L. Spitzer and R. Härm, "Transport phenomena in a completely ionized gas," *Physical Review*, vol. 89, no. 5, pp. 977–981, 1953.

[9] M. Keilhacker, A. Gibson, C. Gormezano, P. Lomas, P. Thomas, M. Watkins, P. Andrew, B. Balet, D. Borba, C. Challis, I. Coffey, G. Cottrell, H. D. Esch, N. Deliyanakis, A. Fasoli, C. Gowers, H. Guo, G. Huysmans, T. Jones, W. Kerner,

R. König, M. Loughlin, A. Maas, F. Marcus, M. Nave, F. Rimini, G. Sadler, S. Sharapov, G. Sips, P. Smeulders, F. Söldner, A. Taroni, B. Tubbing, M. von Hellermann, D. Ward, and J. Team, "High fusion performance from deuterium-tritium plasmas in JET," *Nuclear Fusion*, vol. 39, pp. 209–234, feb 1999.

[10] J. T. p. b. M. Watkins), "Physics of high performance JET plasmas in DT," *Nuclear Fusion*, vol. 39, pp. 1227–1244, sep 1999.

[11] J. Jacquinot, V. Bhatnagar, J. Cordey, L. Horton, D. Start, R. Barnsley, P. Breger, J. Christiansen, S. Clement, S. Davies, J. Ehrenberg, L.-G. Eriksson, G. Fishpool, M. Gadeberg, P. Harbour, H. Jäckel, K. Lawson, J. Lingertat, C. Lowry, C. Maggi, G. Matthews, R. Monk, D. O'Brien, E. Righi, G. Saibene, R. Sartori, B. Schunke, A. Sips, M. Stamp, D. Stork, J. Strachan, A. Tanga, K. Thomsen, and J. Team, "Overview of ITER physics deuterium-tritium experiments in JET," *Nuclear Fusion*, vol. 39, pp. 235–253, feb 1999.

[12] J. Gunn, S. Carpentier-Chouchana, F. Escourbiac, T. Hirai, S. Panayotis, R. Pitts, Y. Corre, R. Dejarnac, M. Firdaouss, M. Kočan, M. Komm, A. Kukushkin, P. Languille, M. Missirlian, W. Zhao, and G. Zhong, "Surface heat loads on the ITER divertor vertical targets," *Nuclear Fusion*, vol. 57, p. 046025, apr 2017.

[13] G. Fishpool, J. Canik, G. Cunningham, J. Harrison, I. Katramados, A. Kirk, M. Kovari, H. Meyer, and R. Scannell, "MAST-upgrade divertor facility and assessing performance of long-legged divertors," *Journal of Nuclear Materials*, vol. 438, pp. S356–S359, jul 2013.

[14] J. Horacek, R. A. Pitts, J. Adamek, G. Arnoux, J.-G. Bak, S. Brezinsek, M. Dimitrova, R. J. Goldston, J. P. Gunn, J. Havlicek, S.-H. Hong, F. Janky, B. LaBombard, S. Marsen, G. Maddaluno, L. Nie, V. Pericoli, T. Popov, R. Panek, D. Rudakov, J. Seidl, D. S. Seo, M. Shimada, C. Silva, P. C. Stangeby, B. Viola, P. Vondracek, H. Wang, G. S. Xu, Y. Xu, and J. Contributors, "Multi-machine scaling of the main SOL parallel heat flux width in tokamak limiter plasmas," *Plasma Physics and Controlled Fusion*, vol. 58, p. 074005, jul 2016.

[15] M. Kocan, R. Pitts, G. Arnoux, I. Balboa, P. de Vries, R. Dejarnac, I. Furno, R. Goldston, Y. Gribov, J. Horacek, M. Komm, B. Labit, B. LaBombard, C. Lasnier, R. Mitteau, F. Nespoli, D. Pace, R. Panek, P. Stangeby, J. Terry, C. Tsui, and P. Vondracek, "Impact of a narrow limiter SOL heat flux channel on the ITER first wall panel shaping," *Nuclear Fusion*, vol. 55, p. 033019, mar 2015.

[16] T. Eich, A. W. Leonard, R. A. Pitts, W. Fundamenski, R. J. Goldston, T. K. Gray, A. Herrmann, A. Kirk, A. Kallenbach, O. Kardaun, A. S. Kukushkin, B. Labombard, R. Maingi, M. A. Makowski, A. Scarabosio, B. Sieglin, J. Terry, and A. Thornton, "Scaling of the tokamak near the scrape-off layer H-mode power width and implications for ITER," *Nuclear Fusion*, vol. 53, no. 9, 2013.

[17] R. J. Goldston, "Heuristic drift-based model of the power scrape-off width in low-gas-puff H-mode tokamaks," *Nuclear Fusion*, vol. 52, no. 1, 2012.

[18] T. Eich, B. Sieglin, A. Scarabosio, W. Fundamenski, R. J. Goldston, and A. Herrmann, "Inter-ELM power decay length for JET and ASDEX Upgrade: Measurement and comparison with heuristic drift-based model," *Physical Review Letters*, vol. 107, no. 21, 2011.

[19] R. A. Pitts, A. Kukushkin, A. Loarte, A. Martin, M. Merola, C. E. Kessel, V. Komarov, and M. Shimada, "Status and physics basis of the ITER divertor," in *Physica Scripta T*, vol. T138, 2009.

[20] S. I. Krasheninnikov and A. S. Kukushkin, "Physics of ultimate detachment of a tokamak divertor plasma," *Journal of Plasma Physics*, vol. 83, no. 05, p. 155830501, 2017.

[21] W. Engelhardt, G. Becker, K. Behringer, D. Campbell, A. Eberhagen, G. Fussmann, O. Gehre, G. V. Gierke, E. Glock, G. Haas, M. Huang, F. Karger, M. Keilhacker, O. KlÜber, M. Kornherr, G. Lisitano, H. M. Mayer, D. Meisel, E. R. Müller, H. Murmann, H. Niedermeyer, W. Poschenrieder, H. Rapp, F. Schneider, G. Siller, K. H. Steuer, G. Venus, H. Vernickel, and F. Wagner, "Divertor efficiency in ASDEX," *Journal of Nuclear Materials*, vol. 111-112, no. C, pp. 337–342, 1982.

[22] M. Keilhacker, "The asdex divertor tokamak," *Nuclear Fusion*, vol. 25, no. 9, pp. 1045–1054, 1985.

[23] P. C. Stangeby, *The plasma boundary of magnetic fusion devices*. Institute of Physics Pub, 2000.

[24] G. F. Matthews, "Plasma detachment from divertor targets and limiters," *Journal of Nuclear Materials*, vol. 220-222, pp. 104–116, apr 1995.

[25] S. I. Krasheninnikov, A. S. Kukushkin, and A. A. Pshenov, "Divertor plasma detachment," *Physics of Plasmas*, vol. 23, no. 5, 2016.

[26] A. Pshenov, A. Kukushkin, and S. Krasheninnikov, "Energy balance in plasma detachment," *Nuclear Materials and Energy*, vol. 12, pp. 948–952, aug 2017.

[27] K. Verhaegh, B. Lipschultz, B. Duval, J. Harrison, H. Reimerdes, C. Theiler, B. Labit, R. Maurizio, C. Marini, F. Nespoli, U. Sheikh, C. Tsui, N. Vianello, and W. Vijvers, "Spectroscopic investigations of divertor detachment in TCV," *Nuclear Materials and Energy*, vol. 12, pp. 1112–1117, aug 2017.

[28] W. L. Hsu, M. Yamada, and F. H. Tenney, "Neutral gas blanket effects in a gaseous divertor," *Journal of Nuclear Materials*, vol. 111-112, no. C, pp. 311–316, 1982.

[29] W. L. Hsu, M. Yamada, and P. J. Barrett, "Experimental simulation of the gaseous tokamak divertor," *Physical Review Letters*, vol. 49, no. 14, pp. 1001–1004, 1982.

[30] L. Schmitz, R. Lehmer, G. Chevalier, G. Tynan, P. Chia, R. Doerner, and R. W. Conn, "Experimental simulation of the gaseous divertor concept in PISCES-A," *Journal of Nuclear Materials*, vol. 176-177, no. C, pp. 522–527, 1990.

[31] M. J. de Graaf, R. Severens, R. P. Dahiya, M. C. M. van de Sanden, and D. C. Schram, "Anomalous fast recombination in hydrogen plasmas involving rovibrational excitation," *Physical Review E*, vol. 48, pp. 2098–2102, sep 1993.

[32] R. F. G. Meulenbroeks, D. C. Schram, M. C. M. van de Sanden, and J. A. M. van der Mullen, "Wall Association and Recirculation in Expanding Thermal Arc Plasmas," *Physical Review Letters*, vol. 76, pp. 1840–1843, mar 1996.

[33] R. Meulenbroeks, R. Engeln, M. Beurskens, C. Box, van de M.C.M. Sanden, van der J.J.A.M. Mullen, and D. Schram, "Recirculation and arc effects in argon-hydrogen expanding cascaded arc plasmas," 1994.

[34] R. F. G. Meulenbroeks, M. F. M. Steenbakkers, Z. Qing, M. C. M. van de Sanden, and D. C. Schram, "Four ways to determine the electron density in low-temperature plasmas," *Physical Review E*, vol. 49, pp. 2272–2275, mar 1994.

[35] R. F. G. Meulenbroeks, A. J. van Beek, A. J. G. van Helvoort, M. C. M. van de Sanden, and D. C. Schram, "Argon-hydrogen plasma jet investigated by active and passive spectroscopic means," *Physical Review E*, vol. 49, pp. 4397–4406, may 1994.

[36] R. Meulenbroeks, R. Engeln, M. Beurskens, C. Box, van de M.C.M. Sanden, van der J.J.A.M. Mullen, and D. Schram, "Recirculation and arc effects in argon-hydrogen expanding cascaded arc plasmas," 1994.

[37] Z. Qing, M. J. de Graaf, M. C. M. van de Sanden, D. K. Otorbaev, and D. C. Schram, "Experimental characterization of a hydrogen/argon cascaded arc plasma source," *Review of Scientific Instruments*, vol. 65, pp. 1469–1471, apr 1994.

[38] Z. Qing, D. K. Otorbaev, G. J. H. Brussaard, M. C. M. van de Sanden, and D. C. Schram, "Diagnostics of the magnetized low-pressure hydrogen plasma jet: Molecular regime," *Journal of Applied Physics*, vol. 80, p. 1312, aug 1998.

[39] M. C. M. van de Sanden, G. M. Janssen, J. M. de Regt, D. C. Schram, J. A. M. van der Mullen, and B. van der Sijde, "A combined Thomson–Rayleigh scattering diagnostic using an intensified photodiode array," *Review of Scientific Instruments*, vol. 63, pp. 3369–3377, jun 1992.

[40] N. Ohno, N. Ezumi, S. Takamura, S. I. Krasheninnikov, and A. Y. Pigarov, "Experimental evidence of molecular activated recombination in detached recombining plasmas," *Physical Review Letters*, vol. 81, no. 4, pp. 818–821, 1998.

[41] N. Ezumi, D. Nishijima, H. Kojima, N. Ohno, S. Takamura, S. I. Krasheninnikov, and A. Y. Pigarov, "Contribution of molecular activated recombination to hydrogen plasma detachment in the divertor plasma simulator NAGDIS-II," *Journal of Nuclear Materials*, vol. 266, pp. 337–342, 1999.

[42] D. Nishijima, U. Wenzel, K. Ohsumi, N. Ohno, Y. Uesugi, and S. Takamura, "Characteristics of detached plasmas associated with electron-ion and molecular assisted recombinations in NAGDIS-II," *Plasma Physics and Controlled Fusion*, vol. 44, no. 5, pp. 597–610, 2002.

[43] A. Y. Pigarov and S. I. Krasheninnikov, "Application of the collisional-radiative, atomic-molecular model to the recombining divertor plasma," *Physics Letters, Section A: General, Atomic and Solid State Physics*, vol. 222, no. 4, pp. 251–257, 1996.

[44] E. M. Hollmann, D. G. Whyte, D. Nishijima, N. Ohno, Y. Uesugi, and N. Ezumi, "Evidence for the importance of radial transport in plasma detachment in the Nagoya University Divertor Simulator (NAGDIS-II)," *Physics of Plasmas*, vol. 8, no. 7, pp. 3314–3320, 2001.

[45] N. Ohno, D. Nishijima, S. Takamura, Y. Uesugi, M. Motoyama, N. Hattori, H. Arakawa, N. Ezumi, S. Krasheninnikov, A. Pigarov, and U. Wenzel, "Static and dynamic behaviour of plasma detachment in the divertor simulator experiment NAGDIS-II," *Nuclear Fusion*, vol. 41, no. 8, pp. 1055–1065, 2001.

[46] N. Ohno, "Plasma detachment in linear devices," *Plasma Physics and Controlled Fusion*, vol. 59, no. 3, 2017.

[47] R. C. Wieggers, D. P. Coster, P. W. C. Groen, H. J. De Blank, and W. J. Goedheer, "B2.5-Eunomia simulations of Pilot-PSI plasmas," *Journal of Nuclear Materials*, vol. 438, no. SUPPL, 2013.

[48] M. Baeva, W. J. Goedheer, N. J. Lopes Cardozo, and D. Reiter, "B2-EIRENE simulation of plasma and neutrals in MAGNUM-PSI," *Journal of Nuclear Materials*, vol. 363-365, no. 1-3, pp. 330–334, 2007.

[49] H. J. Van Eck, T. Abrams, M. A. Van Den Berg, S. Brons, G. G. Van Eden, M. A. Jaworski, R. Kaita, H. J. Van Der Meiden, T. W. Morgan, M. J. Van De Pol, J. Scholten, P. H. Smeets, G. De Temmerman, P. C. De Vries, and P. A. Zeijlmans Van Emmichoven, "Operational characteristics of the high flux plasma generator Magnum-PSI," *Fusion Engineering and Design*, vol. 89, no. 9-10, pp. 2150–2154, 2014.

[50] H. Kastelewicz and G. Fussmann, "Plasma modelling for the PSI linear plasma device," *Contributions to Plasma Physics*, vol. 44, no. 4, pp. 352–360, 2004.

[51] M. S. Islam, Y. Nakashima, and A. Hatayama, "Investigation of plasma behavior during noble gas injection in the end-cell of GAMMA 10/PDX by using the multi-fluid code 'LINDA'," *Plasma Physics and Controlled Fusion*, vol. 59, no. 12, 2017.

[52] A. Kukushkin, H. Pacher, G. Janeschitz, A. Loarte, D. Coster, G. Matthews, D. Reiter, R. Schneider, and V. Zhogolev, "Basic divertor operation in ITER-FEAT," *Nuclear Fusion*, vol. 42, pp. 187–191, feb 2002.

[53] A. Kukushkin, H. Pacher, V. Kotov, G. Pacher, and D. Reiter, "Finalizing the ITER divertor design: The key role of SOLPS modeling," *Fusion Engineering and Design*, vol. 86, pp. 2865–2873, dec 2011.

[54] G. J. Van Rooij, V. P. Veremiyenko, W. J. Goedheer, B. De Groot, A. W. Kleyn, P. H. Smeets, T. W. Versloot, D. G. Whyte, R. Engeln, D. C. Schram, and N. J. Cardozo, "Extreme hydrogen plasma densities achieved in a linear plasma generator," *Applied Physics Letters*, vol. 90, no. 12, 2007.

[55] B. de Groot, R. S. Al, R. Engeln, W. J. Goedheer, O. G. Kruijt, H. J. Meiden, P. R. Prins, D. C. Schram, P. H. Smeets, V. P. Veremiyenko, W. A. Vijvers, J. Westerhout, A. W. Kleyn, N. J. Cardozo, and G. J. van Rooij, "Extreme hydrogen plasma fluxes at Pilot-PSI enter the ITER divertor regime," *Fusion Engineering and Design*, vol. 82, no. 15-24, pp. 1861–1865, 2007.

[56] G. M. W. Kroesen, D. C. Schram, and J. C. M. de Haas, "Description of a flowing cascade arc plasma," *Plasma Chemistry and Plasma Processing*, vol. 10, pp. 531–551, dec 1990.

[57] J. J. Beulens, D. Milojevic, D. C. Schram, and P. M. Vallinga, "A two-dimensional nonequilibrium model of cascaded arc plasma flows," *Physics of Fluids B: Plasma Physics*, vol. 3, pp. 2548–2557, sep 1991.

[58] Vijvers W, *A high-flux cascaded arc hydrogen plasma source (PhD thesis)*. PhD thesis, 2011.

[59] S. E. Selezneva, M. I. Boulos, K. G. Y. Letourneur, M. F. A. M. van Hest, M. C. M. van de Sanden, and D. C. Schram, "Supersonically expanding cascaded arc plasma properties: comparison of Ne, Ar and Xe," *Plasma Sources Science and Technology*, vol. 12, pp. 107–118, feb 2003.

[60] M. van de Sanden, G. Brussaard, W. Kessels, A. de Graaf, M. van Hest, K. Letourneur, and D. Schram, "Diagnostics on the cascaded arc generated downstream plasma," *LRP / Ecole Polytechnique Fédérale de Lausanne*, vol. 629/99, 1999.

[61] M. Zibrov, M. Balden, T. Morgan, and M. Mayer, "Deuterium trapping and surface modification of polycrystalline tungsten exposed to a high-flux plasma at high fluences," *Nuclear Fusion*, vol. 57, p. 046004, apr 2017.

[62] G. De Temmerman, J. Zielinski, S. van Diepen, L. Marot, and M. Price, "ELM simulation experiments on Pilot-PSI using simultaneous high flux plasma and transient heat/particle source," *Nuclear Fusion*, vol. 51, p. 073008, jul 2011.

[63] J. Zielinski, R. Al, H. van der Meiden, W. Melissen, J. Rapp, and G. De Temmerman, "Production and characterization of transient heat and particle pulses in Pilot-PSI," *Journal of Nuclear Materials*, vol. 415, pp. S70–S73, aug 2011.

[64] J. J. Zielinski, H. J. van der Meiden, T. W. Morgan, D. C. Schram, and G. D. Temmerman, "Characterization of a high-power/current pulsed magnetized arc discharge," *Plasma Sources Science and Technology*, vol. 21, p. 065003, dec 2012.

[65] T. W. Morgan, T. M. de Kruif, H. J. van der Meiden, M. A. van den Berg, J. Scholten, W. Melissen, B. J. M. Krijger, S. Bardin, and G. De Temmerman, "A high-repetition rate edge localised mode replication system for the Magnum-PSI and Pilot-PSI linear devices," *Plasma Physics and Controlled Fusion*, vol. 56, p. 095004, sep 2014.

[66] H. J. Van Der Meiden, A. R. Lof, M. A. Van Den Berg, S. Brons, A. J. Donné, H. J. Van Eck, P. M. Koelman, W. R. Koppers, O. G. Kruijt, N. N. Naumenko, T. Oyevaar, P. R. Prins, J. Rapp, J. Scholten, D. C. Schram, P. H. Smeets, G. Van Der Star, S. N. Tugarinov, and P. A. Van Emmichoven, "Advanced Thomson scattering system for high-flux linear plasma generator," *Review of Scientific Instruments*, vol. 83, no. 12, 2012.

[67] J. P. Gunn, "The influence of magnetization strength on the sheath: Implications for flush-mounted probes," *Physics of Plasmas*, vol. 4, no. 12, pp. 4435–4446, 1997.

[68] H. J. N. van Eck, A. W. Kleyn, A. Lof, H. J. van der Meiden, G. J. van Rooij, J. Scholten, and P. A. Zeijlmans van Emmichoven, "Divertor conditions relevant for fusion reactors achieved with linear plasma generator," *Applied Physics Letters*, vol. 101, p. 224107, nov 2012.

[69] J. Scholten, P. Zeijlmans van Emmichoven, H. van Eck, P. Smeets, G. De Temmerman, S. Brons, M. van den Berg, H. van der Meiden, M. van de Pol, M. Graswinckel, P. Groen, A. Poelman, and J. Genuit, "Operational status of the Magnum-PSI linear plasma device," *Fusion Engineering and Design*, vol. 88, pp. 1785–1788, oct 2013.

[70] H. J. N. van Eck, W. R. Koppers, G. J. van Rooij, W. J. Goedheer, R. Engeln, D. C. Schram, N. J. L. Cardozo, and A. W. Kleyn, "Modeling and experiments on differential pumping in linear plasma generators operating at high gas flows," *Journal of Applied Physics*, vol. 105, p. 063307, mar 2009.

[71] G. van Eden, M. Reinke, S. Brons, G. van der Bijl, B. Krijger, R. Lavrijsen, S. Huber, R. Perillo, M. van de Sanden, and T. Morgan, "Plasma radiation studies in Magnum-PSI using resistive bolometry," *Nuclear Fusion*, vol. 58, p. 106006, oct 2018.

[72] H. Bufferand, G. Ciraolo, Y. Marandet, J. Bucalossi, P. Ghendrih, J. Gunn, N. Mellet, P. Tamain, R. Leybros, N. Fedorczak, F. Schwander, and E. Serre, "Numerical modelling for divertor design of the WEST device with a focus on plasma-wall interactions," *Nuclear Fusion*, vol. 55, no. 5, 2015.

[73] J. Bohdansky, "Important sputtering yield data for tokamaks: A comparison of measurements and estimates," *Journal of Nuclear Materials*, vol. 93-94, pp. 44–60, 1980.

[74] W. Eckstein, J. Bohdansky, and J. Roth, "Physical sputtering," *Nuclear Fusion*, no. Suppl, 1991.

[75] N. Mellet, J. P. Gunn, B. Pégourié, A. Hakola, M. Airila, Y. Marandet, and P. Roubin, "Influence of the magnetised sheath on the redeposition location of sputtered tungsten and its effect on the net erosion," *Nuclear Materials and Energy*, vol. 12, pp. 488–493, aug 2017.

[76] J. P. Biersack and W. Eckstein, "Sputtering studies with the Monte Carlo Program TRIM.SP," *Applied Physics A Solids and Surfaces*, vol. 34, no. 2, pp. 73–94, 1984.

[77] J. Denis, B. Pégourié, J. Bucalossi, H. Bufferand, G. Ciraolo, J. L. Gardarein, J. Gaspar, C. Grisolia, E. Hodille, M. Missirlian, E. Serre, and P. Tamain, "Wall surface temperature calculation in the SolEdge2D-EIRENE transport code," in *Physica Scripta*, vol. 2016, 2016.

[78] E. A. Hodille, A. Založnik, S. Markelj, T. Schwarz-Selinger, C. S. Becquart, R. Bisson, and C. Grisolia, "Simulations of atomic deuterium exposure in self-damaged tungsten," *Nuclear Fusion*, vol. 57, no. 5, 2017.

[79] F. Reimold, M. Wischmeier, M. Bernert, S. Potzel, A. Kallenbach, H. W. Müller, B. Sieglin, and U. Stroth, "Divertor studies in nitrogen induced completely detached H-modes in full tungsten ASDEX Upgrade," *Nuclear Fusion*, vol. 55, no. 3, 2015.

[80] C. Guillemaut, R. A. Pitts, A. S. Kukushkin, J. P. Gunn, J. Bucalossi, G. Arnoux, P. Belo, S. Brezinsek, M. Brix, G. Corrigan, S. Devaux, J. Flanagan, M. Groth, D. Harting, A. Huber, S. Jachmich, U. Kruezi, M. Lehnen, C. Marchetto, S. Marsen, A. G. Meigs, O. Meyer, M. Stamp, J. D. Strachan, S. Wiesen, and M. Wischmeier, "Influence of atomic physics on EDGE2D-EIRENE simulations of JET divertor detachment with carbon and beryllium/tungsten plasma-facing components," *Nuclear Fusion*, vol. 54, no. 9, 2014.

[81] M. Wischmeier, M. Groth, A. Kallenbach, A. V. Chankin, D. P. Coster, R. Dux, A. Herrmann, H. W. Müller, R. Pugno, D. Reiter, A. Scarabosio, and J. G. Watkins, "Current understanding of divertor detachment: Experiments and modelling," *Journal of Nuclear Materials*, vol. 390-391, no. 1, pp. 250–254, 2009.

[82] P. Tamain, H. Bufferand, G. Ciraolo, C. Colin, P. Ghendrih, F. Schwander, and E. Serre, "3D Properties of Edge Turbulent Transport in Full-Torus Simulations and their Impact on Poloidal Asymmetries," *Contributions to Plasma Physics*, vol. 54, pp. 555–559, jun 2014.

[83] P. Tamain, H. Bufferand, G. Ciraolo, C. Colin, D. Galassi, P. Ghendrih, F. Schwander, and E. Serre, "The TOKAM3X code for edge turbulence fluid simulations of tokamak plasmas in versatile magnetic geometries," *Journal of Computational Physics*, vol. 321, pp. 606–623, sep 2016.

[84] J. Bucalossi, M. Missirlian, P. Moreau, F. Samaille, E. Tsitrone, D. van Houtte, T. Batal, C. Bourdelle, M. Chantant, Y. Corre, X. Courtois, L. Delpech, L. Doceul, D. Douai, H. Dougnac, F. Faïsse, C. Fenzi, F. Ferlay, M. Firdaouss, L. Gargiulo, P. Garin, C. Gil, A. Grosman, D. Guilhem, J. Gunn, C. Hernandez, D. Keller, S. Larroque, F. Leroux, M. Lipa, P. Lotte, A. Martinez, O. Meyer, F. Micolon, P. Mollard, E. Nardon, R. Nouailletas, A. Pilia, M. Richou, S. Salasca, and J.-M. Travère, "The WEST project: Testing ITER divertor high heat flux component technology in a steady state tokamak environment," *Fusion Engineering and Design*, vol. 89, pp. 907–912, oct 2014.

[85] C. Bourdelle, J. Artaud, V. Basiuk, M. Bécoulet, S. Brémond, J. Bucalossi, H. Bufferand, G. Ciraolo, L. Colas, Y. Corre, X. Courtois, J. Decker, L. Delpech, P. Devynck, G. Dif-Pradalier, R. Doerner, D. Douai, R. Dumont, A. Ekedahl, N. Fedorczak, C. Fenzi, M. Firdaouss, J. Garcia, P. Ghendrih, C. Gil, G. Giruzzi, M. Goniche, C. Grisolia, A. Grosman, D. Guilhem, R. Guirlet, J. Gunn, P. Hennequin, J. Hillairet, T. Hoang, F. Imbeaux, I. Ivanova-Stanik, E. Joffrin, A. Kallenbach, J. Linke, T. Loarer, P. Lotte, P. Maget, Y. Marandet, M. Mayoral, O. Meyer, M. Missirlian, P. Mollard, P. Monier-Garbet, P. Moreau, E. Nardon, B. Pégourié, Y. Peysson, R. Sabot, F. Saint-Laurent, M. Schneider, J. Travère, E. Tsitrone, S. Vartanian, L. Vermare, M. Yoshida, R. Zagorski, and J. Contributors, "WEST Physics Basis," *Nuclear Fusion*, vol. 55, p. 063017, jun 2015.

[86] H. Bufferand, B. Bensiali, J. Bucalossi, G. Ciraolo, P. Genesio, P. Ghendrih, Y. Marandet, A. Paredes, F. Schwander, E. Serre, and P. Tamain, "Near wall plasma simulation using penalization technique with the transport code SOLEDGE2D-EIRENE," *Journal of Nuclear Materials*, vol. 438, no. SUPPL, 2013.

[87] L. Isoardi, G. Chiavassa, G. Ciraolo, P. Haldenwang, E. Serre, P. Ghendrih, Y. Sarazin, F. Schwander, and P. Tamain, "Penalization modeling of a limiter in the Tokamak edge plasma," *Journal of Computational Physics*, vol. 229, no. 6, pp. 2220–2235, 2010.

[88] A. Paredes, H. Bufferand, G. Ciraolo, F. Schwander, E. Serre, P. Ghendrih, and P. Tamain, "A penalization technique to model plasma facing components in a tokamak with temperature variations," *Journal of Computational Physics*, vol. 274, pp. 283–298, 2014.

[89] B. Bensiali, G. Chiavassa, and J. Liandrat, "Penalization of Robin boundary conditions," *Applied Numerical Mathematics*, vol. 96, pp. 134–152, 2015.

[90] D. Reiter, M. Baelmans, and P. Börner, "The eirene and B2-eirene codes," *Fusion Science and Technology*, vol. 47, no. 2, pp. 172–186, 2005.

[91] A. Pigarov, S. Krasheninnikov, W. West, T. Rognlien, J. Boedo, D. Whyte, C. Lasnier, T. Petrie, M. Schaffer, and J. Watkins, "DIII-D edge plasma simulations with UEDGE code including non-diffusive anomalous cross-field transport," *Journal of Nuclear Materials*, vol. 313-316, pp. 1076–1080, mar 2003.

[92] V. Kotov, D. Reiter, R. A. Pitts, S. Jachmich, A. Huber, and D. P. Coster, "Numerical modelling of high density JET divertor plasma with the SOLPS4.2 (B2-EIRENE) code," *Plasma Physics and Controlled Fusion*, vol. 50, no. 10, 2008.

[93] A. S. Kukushkin, H. D. Pacher, V. Kotov, D. Reiter, D. Coster, and G. W. Pacher, "Effect of neutral transport on ITER divertor performance," *Nuclear Fusion*, vol. 45, no. 7, pp. 608–616, 2005.

[94] R. Schneider, D. Reiter, H. P. Zehrfeld, B. Braams, M. Baelmans, J. Geiger, H. Kastelewicz, J. Neuhauser, and R. Wunderlich, "B2-EIRENE simulation of ASDEX and ASDEX-Upgrade scrape-off layer plasmas," *Journal of Nuclear Materials*, vol. 196-198, no. C, pp. 810–815, 1992.

[95] Y. Marandet, H. Bufferand, G. Ciraolo, P. Genesio, P. Meliga, J. Rosato, E. Serre, and P. Tamain, "Effect of Statistical Noise on Simulation Results with a Plasma Fluid Code Coupled to a Monte Carlo Kinetic Neutral Code," *Contributions to Plasma Physics*, vol. 56, no. 6-8, pp. 604–609, 2016.

[96] D. Coster, "Characterization of oscillations observed in reduced physics SOLPS simulations," *Contributions to Plasma Physics*, apr 2018.

[97] R. D. Smirnov, A. S. Kukushkin, S. I. Krasheninnikov, A. Y. Pigarov, and T. D. Rognlien, "Impurity-induced divertor plasma oscillations," *Physics of Plasmas*, vol. 23, p. 012503, jan 2016.

[98] S. Krasheninnikov, A. Kukushkin, V. Pistunovich, and V. Pozharov, "Self-sustained oscillations in the divertor plasma," *Nuclear Fusion*, vol. 27, pp. 1805–1816, nov 1987.

[99] G. Janssen, "Design of a general plasma simulation model : fundamental aspects and applications," *PhD thesis, TU Eindhoven*, 2000.

[100] K. Ješko, H. J. van der Meiden, J. P. Gunn, J. W. Vernimmen, and G. De Temmerman, "Plasma pressure and particle loss studies in the Pilot-PSI high flux linear plasma generator," *Nuclear Materials and Energy*, vol. 12, pp. 1088–1093, aug 2017.

[101] B. Lipschultz, B. LaBombard, J. L. Terry, C. Boswell, and I. H. Hutchinson, "Divertor Physics Research on Alcator C-Mod," *Fusion Science and Technology*, vol. 51, pp. 369–389, apr 2007.

[102] P. Stangeby, "Can detached divertor plasmas be explained as self-sustained gas targets?," *Nuclear Fusion*, vol. 33, pp. 1695–1705, nov 1993.

[103] K. Borrass, D. Coster, D. Reiter, and R. Schneider, "Study of recombining gas targets," *Journal of Nuclear Materials*, vol. 241-243, pp. 250–254, feb 1997.

[104] D. A. D'Ippolito, J. R. Myra, and S. J. Zweben, "Convective transport by intermittent blob-filaments: Comparison of theory and experiment," *Physics of Plasmas*, vol. 18, p. 060501, jun 2011.

[105] N. OHNO, K. FURUTA, and S. TAKAMURA, "Visualization of Intermittent Blobby Plasma Transport in Attached and Detached Plasmas of the NAGDIS-II," *Journal of Plasma and Fusion Research*, vol. 80, no. 4, pp. 275–276, 2004.

[106] M. Hubeny, B. Schweer, D. Luggenhölscher, U. Czarnetzki, and B. Unterberg, "Thomson scattering of plasma turbulence on PSI-2," *Nuclear Materials and Energy*, vol. 12, pp. 1253–1258, aug 2017.

[107] S. H. Müller, C. Theiler, A. Fasoli, I. Furno, B. Labit, G. R. Tynan, M. Xu, Z. Yan, and J. H. Yu, "Studies of blob formation, propagation and transport mechanisms in basic experimental plasmas (TORPEX and CSDX)," *Plasma Physics and Controlled Fusion*, vol. 51, p. 055020, may 2009.

[108] Y. Hayashi, K. Ješko, H. J. Van Der Meiden, J. W. Vernimmen, T. W. Morgan, N. Ohno, S. Kajita, M. Yoshikawa, and S. Masuzaki, "Plasma detachment study of high density helium plasmas in the Pilot-PSI device," *Nuclear Fusion*, vol. 56, no. 12, 2016.

[109] N. Den Harder, D. C. Schram, W. J. Goedheer, H. J. De Blank, M. C. Van De Sanden, and G. J. Van Rooij, "Residual gas entering high density hydrogen plasma: Rarefaction due to rapid heating," *Plasma Sources Science and Technology*, vol. 24, no. 2, 2015.

[110] A. E. Shumack, D. C. Schram, J. Biesheuvel, W. J. Goedheer, and G. J. van Rooij, "Diagnosing ions and neutrals via n = 2 excited hydrogen atoms in plasmas with high electron density and low electron temperature," *Physical Review E*, vol. 83, p. 036402, mar 2011.

[111] W. Eckstein, *Computer Simulation of Ion-Solid Interactions*. Springer-Verlag, 1991.

[112] K. Jesko, Y. Marandet, H. Bufferand, H. J. van der Meiden, J. Gunn, and G. Ciraolo, "Studying divertor relevant plasmas in the Pilot-PSI linear plasma device: Experiments vs. modelling," *Accepted in Plasma Physics and Controlled fusion*, 2018.

[113] T. Greenland and D. Reiter, "The Role of Molecular Hydrogen in Plasma Recombination," *Report*, vol. JUEL-3258, no. FZ-Juelich, 1996.

[114] C. Sang, H. Y. Guo, P. C. Stangeby, L. L. Lao, and T. S. Taylor, "SOLPS analysis of neutral baffling for the design of a new diverter in DIII-D," *Nuclear Fusion*, vol. 57, no. 5, 2017.

[115] V. Kotov and D. Reiter, "Two-point analysis of the numerical modelling of detached divertor plasmas," *Plasma Physics and Controlled Fusion*, vol. 51, no. 11, 2009.

[116] P. C. Stangeby and C. Sang, "Strong correlation between D 2 density and electron temperature at the target of divertors found in SOLPS analysis," *Nuclear Fusion*, vol. 57, no. 5, 2017.

[117] J. Westerhout, *Carbon chemical erosion in high flux and low temperature hydrogen plasma*. PhD thesis, 2010.

[118] J. Marki, R. A. Pitts, T. Eich, A. Herrmann, J. Horacek, F. Sanchez, and G. Veres, "Sheath heat transmission factors on TCV," *Journal of Nuclear Materials*, vol. 363-365, no. 1-3, pp. 382–388, 2007.

[119] U. Fantz, D. Reiter, B. Heger, and D. Coster, "Hydrogen molecules in the divertor of ASDEX Upgrade," *Journal of Nuclear Materials*, vol. 290-293, pp. 367–373, mar 2001.

[120] C. F. Sang, P. C. Stangeby, H. Y. Guo, A. W. Leonard, B. Covele, L. L. Lao, A. L. Moser, and D. M. Thomas, "SOLPS modeling of the effect on plasma detachment of closing the lower divertor in DIII-D," *Plasma Physics and Controlled Fusion*, vol. 59, no. 2, 2017.

[121] C. Sang, H. Y. Guo, P. C. Stangeby, L. L. Lao, and T. S. Taylor, "SOLPS analysis of neutral baffling for the design of a new diverter in DIII-D," *Nuclear Fusion*, vol. 57, no. 5, 2017.

[122] L. Casali, C. Sang, A. Moser, B. Covele, H. Guo, and C. Samuell, "Modelling the effect of divertor closure on detachment onset in DIII-D with the SOLPS code," *Contributions to Plasma Physics*, vol. 58, pp. 725–731, jul 2018.

[123] E. Havlickova, M. Wischmeier, and G. Fishpool, "Modelling the Effect of the Super-X Divertor in MAST Upgrade on Transition to Detachment and Distribution of Volumetric Power Losses," *Contributions to Plasma Physics*, vol. 54, no. 4-6, pp. 448–453, 2014.

[124] H. J. Van der Meiden, J. W. Vernimmen, K. Bystrov, K. Jesko, M. Y. Kantor, G. De Temmerman, and T. W. Morgan, "Collective Thomson scattering system for determination of ion properties in a high flux plasma beam," *Applied Physics Letters*, vol. 109, no. 26, 2016.

[125] A. Loarte, B. Lipschultz, A. S. Kukushkin, G. F. Matthews, P. C. Stangeby, N. Asakura, G. F. Counsell, G. Federici, A. Kallenbach, K. Krieger, A. Mahdavi, V. Philipps, D. Reiter, J. Roth, J. Strachan, D. Whyte, R. Doerner, T. Eich, W. Fundamenski, A. Herrmann, M. Fenstermacher, P. Ghendrih, M. Groth, A. Kirschner, S. Konoshima, B. Labombard, P. Lang, A. W. Leonard, P. Monier-Garbet, R. Neu, H. Pacher, B. Pegourie, R. A. Pitts, S. Takamura, J. Terry, and E. Tsitrone, "Chapter 4: Power and particle control," *Nuclear Fusion*, vol. 47, no. 6, 2007.

[126] H. Murmann, S. Götsch, H. Röhr, H. Salzmann, and K. H. Steuer, "The Thomson scattering systems of the ASDEX upgrade tokamak," *Review of Scientific Instruments*, vol. 63, pp. 4941–4943, oct 1992.

[127] D. G. Nilson, T. N. Carlstrom, D. N. Hill, C. L. Hsieh, G. D. Porter, R. E. Stockdale, and J. C. Evans, "Divertor Thomson scattering on DIII-D," *Fusion Engineering and Design*, vol. 34-35, pp. 609–612, 1997.

[128] V. P. Veremiyenko, "An ITER-relevant magnetized hydrogen plasma jet," phd, Eindhoven University of Technology, Eindhoven, Netherlands, 2006.

[129] D. Lumma, J. L. Terry, and B. Lipschultz, "Radiative and three-body recombination in the Alcator C-Mod divertor," *Physics of Plasmas*, vol. 4, no. 7, pp. 2555–2566, 1997.

[130] G. McCracken, M. Stamp, R. Monk, A. Meigs, J. Lingertat, R. Prentice, A. Starling, R. Smith, and A. Tabasso, "Evidence for volume recombination in JET detached divertor plasmas," *Nuclear Fusion*, vol. 38, pp. 619–629, apr 1998.

[131] R. Monk, A. Meigs, L. Horton, L. Ingesson, J. Lingertat, G. Matthews, M. O'Mullane, R. Prentice, M. Stamp, G. McCracken, and P. Stangeby, "Volume recombination and detachment in JET divertor plasmas," *Journal of Nuclear Materials*, vol. 266-269, pp. 37–43, mar 1999.

[132] U. Wenzel, K. Behringer, A. Carlson, J. Gafert, B. Napiontek, and A. Thoma, "Volume recombination in divertor I of ASDEX Upgrade," *Nuclear Fusion*, vol. 39, pp. 873–882, jul 1999.

[133] W. E. N. van Harskamp, C. M. Brouwer, D. C. Schram, M. C. M. van de Sanden, and R. Engeln, "Population inversion in a magnetized hydrogen plasma expansion as a consequence of the molecular mutual neutralization process," *Physical Review E*, vol. 83, p. 036412, mar 2011.

[134] L. Isoardi, G. Chiavassa, G. Ciraolo, P. Haldenwang, E. Serre, P. Ghendrih, Y. Sarazin, F. Schwander, and P. Tamain, "Penalization modeling of a limiter in the Tokamak edge plasma," *Journal of Computational Physics*, vol. 229, no. 6, pp. 2220–2235, 2010.

[135] H. Bufferand, C. Baudoin, J. Bucalossi, G. Ciraolo, J. Denis, N. Fedorczak, D. Galassi, P. Ghendrih, R. Leybros, Y. Marandet, N. Mellet, J. Morales, N. Nace, E. Serre, P. Tamain, and M. Valentinuzzi, "Implementation of drift velocities and currents in SOLEDGE2D–EIRENE," *Nuclear Materials and Energy*, vol. 12, pp. 852–857, 2017.

[136] S. I. Krasheninnikov, A. Y. Pigarov, and D. J. Sigmar, "Plasma Recombination and Divertor Detachment," *Contributions to Plasma Physics*, vol. 36, no. 2-3, pp. 314–318, 1996.

[137] J. L. Terry, B. Lipschultz, A. Y. Pigarov, S. I. Krasheninnikov, B. LaBombard, D. Lumma, H. Ohkawa, D. Pappas, and M. Umansky, "Volume recombination and opacity in Alcator C-Mod divertor plasmas," *Physics of Plasmas*, vol. 5, no. 5, pp. 1759–1766, 1998.

[138] W. A. Vijvers, C. A. Van Gils, W. J. Goedheer, H. J. Van Der Meiden, D. C. Schram, V. P. Veremiyenko, J. Westerhout, N. J. Lopes Cardozo, and G. J. Van Rooij, "Optimization of the output and efficiency of a high power cascaded arc hydrogen plasma source," *Physics of Plasmas*, vol. 15, no. 9, 2008.

[139] K. Jesko, Y. Marandet, H. Bufferand, J. Gunn, H. van der Meiden, and G. Ciraolo, "Soledge2D-Eirene simulations of the Pilot-PSI linear plasma device compared to experimental data," *Contributions to Plasma Physics*, vol. 58, pp. 798–804, jul 2018.

[140] R. C. Isler, G. R. McKee, N. H. Brooks, W. P. West, M. E. Fenstermacher, and R. D. Wood, "Signatures of deuterium recombination in the DIII-D divertor," *Physics of Plasmas*, vol. 4, no. 8, pp. 2989–2996, 1997.

[141] R. K. Janev, W. D. Langer, J. Post, Douglas E., and J. Evans, Kenneth, "Elementary processes in hydrogen-helium plasmas: Cross sections and reaction rate coefficients," *Research supported by DOE,. Berlin and New York, Springer-Verlag (Springer Series on Atoms and Plasmas. Volume 4), 1987, 335 p.*, vol. 4, 1987.

Summary

Nuclear fusion has the potential to become the ultimate energy source of the future, due to the fact that it is clean, stable, safe and inexhaustible. It does not have the intermittency issues of renewable energy sources, and therefore eliminates the need for energy storage solutions. The baseline approach for achieving fusion is by heating up the fuel, deuterium and tritium, to temperatures high enough to overcome the repulsive electrostatic forces between the nuclei. At such temperatures, the fuel is completely stripped from its electrons. In other words, it is in the plasma state. Currently, the most promising candidate of a fusion reactor is the tokamak, a device where the hot, thermonuclear plasma is confined by magnetic fields. However, the progress in making fusion a viable energy source is slow as new hurdles are discovered each time the machines are scaled further up towards more reactor-relevant sizes.

Currently, one of the biggest hurdles in delivering a viable fusion reactor is the problem of power exhaust. The International Thermonuclear Experimental Reactor, ITER, now under construction at the Cadarache site in France, is a joint scientific venture of the European Union, India, Japan, China, Russia, South Korea, and the United States. This will be the largest tokamak ever built, with the aim of producing 500 MW of fusion power. A significant amount of this power will be channeled to solid, plasma facing components (PFCs) through a narrow slice of the plasma called the scrape-off layer. The plasma-surface interaction is localized in the *divertor*, designed to prevent impurities from the wall to penetrate into the core plasma. The PFCs in the divertor have been chosen to be actively cooled tungsten monoblocks, which can safely operate up to an energy flux density of 10 MW/m^2. Unmitigated, steady state energy flux densities coming through the scrape-off layer to the divertor can exceed 100 MW/m^2. Therefore, mitigation is needed to reduce this energy flux to tolerable values. This is done by injecting impurities that radiate a significant amount of the energy coming from the scrape-off layer in the divertor, thereby also lowering the electron temperature to below 10 eV in the divertor, as opposed to the keV values in the reactor core. If the temperature is lowered even further, the near-surface plasma can start recombining, thereby reducing also the particle flux to the targets. This is typically called a detached divertor plasma. The typical plasma temperature and density during plasma detachment will be of the order of ~ 1 eV and $\sim 10^{20}$ m^{-3}, respectively. Such plasma conditions are readily achievable in the linear plasma devices of the Dutch Institute for Energy Research (DIFFER), Magnum-PSI and Pilot-PSI, as they were designed to produce ITER divertor relevant plasmas for the needs of PFC material related testing.

A set of measurements with Thomson scattering (TS) at two axial locations and a single Langmuir probe (LP) embedded in the target were performed at the Pilot-PSI linear device, mainly focusing on the influence of the background neutral pressure in the vessel. Extreme rarefaction of the plasma beam was found from source to target location in terms of reduction of the ion flux density and the plasma pressure. By varying background neutral pressure from 2.4 Pa to only 12.6 Pa in the vessel, the loss of plasma pressure changes approximately exponentially, from $\sim$5 up to $\sim$5000. These findings confirm that a low temperature plasma can be effectively extinguished by a blanket of neutrals gas, confirming earlier results obtained at similar linear plasma devices, although in our case at a higher density. In our case, the loss of plasma flux is attributed to volume recombination. Moreover, the results show that the performance of cascaded arc linear devices in terms of ability to deliver high plasma fluxes to a target can be significantly improved by marginal reduction of the background pressure (i.e. by applying additional pumping), which was used in the design uf the Upgraded Pilot-PSI (UPP) facility.

Predictions for the operation of tokamak divertors (especially ITER and beyond) rely heavily on edge plasma simulations using so-called *edge transport codes*, consisting of a fluid plasma code coupled to a Monte-Carlo code for neutral species. It is important to compare code results to experiments if this is to be a valid approach. Linear devices offer a good testbed for code-experiment comparison, since they remove uncertainties related to complex magnetic geometry in a tokamaks, and they also offer a much more simple diagnostic access. Given the good quality set of data obtained at Pilot-PSI, we have decided to model Pilot-PSI (and later also Magnum-PSI) using the Soledge2D-Eirene package, Soledge2D being the plasma fluid code developed at the Institute for Magnetic Fusion Research at CEA Cadarache and Eirene being the neutral Monte-Carlo code developed at Forschungszentrum Jülich. On the other hand, the code can give good insights for into which atomic/molecular (or other) processes are responsible for the reduction of power and particle fluxes to the target, i.e. do the book-keeping between the various mechanisms that drive flows in the plasma, i.e. ionisation/recombination, parallel and perpendicular transport, and so forth.

As a result of the code-experiment comparison, it has been found that in the simulations, the electron temperature T_e close to the target (of both Pilot-PSI and Magnum-PSI) is systematically higher in comparison to the measurements using TS and spectroscopy. In the simulations, T_e in the simulations appears to saturate at 0.7 eV for a wide range of parameters, while experimentally values of 0.1 - 0.3 eV are found. This was also tested in response to changes of the perpendicular transport coefficients, which are the main free parameter in the simulations, however the result showed was not sensitive to this choice.

We have looked in more detail what process dissipates most of the energy in the simulations. Inelastic collisions between electrons and neutral backround molecules are the largest energy loss mechanism. From these inelastic processes, dissociation of molecules and molecular ions were found to be dominant. However, these energy sinks are active in the upstream region of the plasma beam, where T_e is high enough ($\sim$ 1 eV) to efficiently break up molecules and molecular ions; in locations close to

the target, the simulations do not predict any mechanism that could dissipate the heat flux and subsequently reduce T_e to values of 0.2 eV found in the experiment, i.e. where volume recombination could remove a significant number of plasma particles. As a consequence, the simulations also cannot reproduce the strong volume recombination observed experimentally. The comparatively high T_e values indicate that there are missing energy dissipation channels in the simulations. The intrinsic radiation of molecules themselves (e.g. due to molecular lines/bands) was considered, but initial estimates showed that the power dissipated by this channel is negligible, especially at low T_e. The possibility of further energy dissipation by vibrational excitation (the energy costs associated with these excitations not being included in the code setup used in the thesis) of the molecules is suggested as a possible explanation.

There is a long standing discussion whether molecular activated recombination (MAR), an alternative recombination pathway mediated by vibrationally excited molulces, is an important recombination pathway in fusion relevant plasmas. Evidence that MAR is occurring is indeed ubiquitous from linear plasma devices, usually from detailed analysis of excited state populations. From the simulations, it has been concluded that the total, volume integrated recombination sink due to MAR is up to 25% of the total particle flux, for all simulation cases. The amount of particles that MAR can remove is limited by a competing, purely dissociative process. This confirms earlier results by *Fantz et al., Journal of Nuclear Materials, 2001*, from ASDEX-Upgrade.

The final part of the work was focussed on studying the energy balance of the plasma in Magnum-PSI mainly using calorimetry and Thosmon scattering. The main result of this part is that the usually assumed value of the sheath heat transmission factor $\gamma = 7$ is not a suitable choice for the sub 1 eV, high density plasmas studied in these experiments. It is mandatory to include also the potential energy from target ion and atom recombination in the estimation of the heat flux from Thomson scattering in order to get values consistent with calorimetry. Although it is known that the potential energy of recombination is deposited at the solid surface, we are not aware of such clear experimental evidence showing the contribution to the target energy flux in the literature.

Implications of results from linear devices for tokamak divertors have to considered with care due to the differences in geometry and operation. However, we think that the findings presented here can still provide some useful insights. It has been shown that inelastic collisions of the electrons with the surrounding molecules provide a strong heat dissipation channel. It is important to point out that in Pilot-PSI and Magnum-PSI the molecule density is high, due the cascaded arc source and the dominance of wall association of neutral atoms, which is often not the case for tokamaks. However, recent modelling efforts of planned, more closed divertor geometries at DIII-D and MAST-Upgrade have shown molecular densities comparable to our conditions, up to 10^{20} m^{-3} and a near-target T_e $\sim$1 eV. Such refinements of the divertor geometry have resulted in better performance in terms of power dissipation, both from the edge transport code modelling and experiments. It is expected that in such divertor conditions, the principle acting mechanisms in terms of atomic and molecular physics will be the same as in the two linear devices studied in this work. The results presented in this thesis

are believed to have contributed to the understanding of the low temperature, high density buffer plasmas relevant to tokamak divertors.

Résumé

La fusion nucléaire pourrait devenir la source d'énergie ultime du futur, du fait qu'elle est propre, stable, sûre et quasi-inépuisable. De plus elle ne présente pas les problèmes d'intermittence des sources d'énergie renouvelables et élimine donc le besoin de solutions de stockage d'énergie. La méthode de base pour réaliser la fusion consiste à chauffer le combustible, un mélange de deutérium et de tritium, à des températures suffisamment élevées pour vaincre les forces électrostatiques répulsives exercées entre les noyaux. A de telles températures, le carburant est complètement débarrassé de ses électrons. En d'autres termes, il est à l'état de plasma. Actuellement, le candidat le plus prometteur pour un réacteur à fusion par confinement magnétique est le tokamak. Cependant, les progrès réalisés pour faire de la fusion une source d'énergie viable sont lents, de nouveaux obstacles étant découverts chaque fois que les machines sont redimensionnées pour atteindre des tailles plus proches que celle que devra avoir un réacteur.

Actuellement, le principal obstacle à la mise en place d'un réacteur à fusion viable est le problème de l'extraction de puissance. Le réacteur thermonucléaire expérimental international ITER, actuellement en construction sur le site de Cadarache en France, est une entreprise scientifique commune à l'Union européenne, aux Etats-Unis, l'Inde, le Japon, la Chine et la Russie. Ce sera le plus grand tokamak jamais construit, dans le but de produire 500 MW d'énergie de fusion. Une fraction substantielle de cette puissance sera acheminée vers des éléments de paroi, les composants face au plasma (PFC), via une couche limite étroite (SOL) à la surface du plasma confiné. L'interaction plasma-surface est localisée dans le divertor, conçu pour empêcher les impuretés de la paroi de pénétrer dans le plasma central. Les PFC du divertor seront des monoblocs en tungstène activement refroidis, pouvant fonctionner en toute sécurité jusqu'à une densité de flux énergétique de 10 MW/m^2. Les densités de flux d'énergie traversant la couche-limite jusqu'au divertor peuvent dépasser 100 MW/m^2 en régime permanent en l'absence d'atténuation par étalement sur une surface plus importante, ce qui nécessite de prendre des mesures spécifiques. Pour ce faire, on injecte des impuretés pouvant rayonner une quantité importante d'énergie dans la SOL et le divertor, ce qui abaisse également la température des électrons à moins de 10 eV dans le divertor, par opposition aux valeurs de l'ordre du keV dans le coeur du réacteur. Si la température est encore abaissée, le plasma proche de la surface peut commencer à se recombiner, réduisant ainsi le flux de particules vers les cibles. Ceci est généralement appelé le *détachement* du plasma. La température et la densité de plasma typiques pendant le détachement seront respectivement de l'ordre de ~ 1 eV et $\sim 10^{20}$ m^{-3}. Ces conditions de plasma,

nécessaires au fonctionnement d'un réacteur, sont facilement réalisables dans les machines à plasma linéaires de l'Institut DIFFER au Pays-Bas, Magnum-PSI et Pilot-PSI, qui ont été conçus pour produire des plasmas pertinents pour les tests de PFC du divertor d'ITER.

Un ensemble de mesures avec diffusion Thomson (DT) à deux emplacements axiaux et une sonde de Langmuir (SL) intégrée dans la cible ont été effectuées sur la machine linéaire Pilot-PSI, en se concentrant principalement sur l'influence de la pression de gaz neutre ambiante dans le chambre à vide. Une extrême raréfaction du faisceau de plasma a été constatée de la source à la cible, se manifestant par une réduction de la densité de flux ionique et de la pression de plasma. En faisant varier la pression du gaz neutre de seulement 2.4 Pa à 12.6 Pa dans la chambre, la pression plasma baisse de manière exponentielle, passant d'un facteur 5 à 5 000. Ces découvertes confirment qu'un plasma basse température peut être efficacement éteint par une couche de gaz neutre, confirmant ainsi les résultats antérieurs obtenus avec des machines à plasma linéaire similaires, bien que, dans notre cas, la densité soit plus élevée. Dans notre cas, la perte de flux de plasma est attribuée à la recombinaison volumique. De plus, les résultats montrent que la capacité des machines linéaires à arc en cascade à délivrer des flux de plasma élevés à une cible peuvent être considérablement améliorées par une réduction marginale de la pression ambiante de gaz neutre (par exemple, en appliquant un pompage supplémentaire), qui a été utilisée dans la conception d'une l'installation améliorée, le "Upgraded Pilot-PSI" (UPP).

Les prédictions concernant le fonctionnement des divertors de tokamak (en particulier ITER et au-delà) reposent largement sur des simulations de plasma de bord utilisant ce que l'on appelle des "codes de transport de bord", constitués d'un code de plasma fluide couplé à un code Monte-Carlo pour les espèces neutres. Il est important de comparer les résultats du code aux expériences pour que cette approche soit valable. Les machines linéaires constituent un bon banc d'essai pour la comparaison code-expérience, car ils suppriment les incertitudes liées à la géométrie magnétique complexe dans un tokamak et offrent un accès de diagnostic beaucoup plus simple. Compte tenu de la qualité des données obtenues sur Pilot-PSI, nous avons décidé de modéliser Pilot-PSI (puis Magnum-PSI) à l'aide du code de transport de bord Soledge2D-Eirene, Soledge2D étant le code de fluide plasma développé à l'Institut de recherche sur la fusion par confinement magnétique rattaché au CEA Cadarache et Eirene étant le code Monte-Carlo neutre développé au Forschungszentrum Jülich. Par ailleurs, le code peut donner une idée fiable des processus atomiques/moléculaires contrôlant la réduction de puissance et du flux de particules vers la cible, en tenant une comptabilité détaillée des divers mécanismes qui régissent les flux dans le plasma, comme l'ionisation/recombinaison, le transport parallèle et perpendiculaire, etc.

A la suite de la comparaison code-expérience, il a été constaté que dans les simulations, la température des électrons T_e proche de la cible (à la fois pour Pilot-PSI et Magnum-PSI) est systématiquement supérieure à celle mesurée avec TS et spectroscopie. Dans les simulations, T_e semble saturer à 0.7 eV pour une large gamme de paramètres, tandis que des valeurs expérimentales de 0.1 à 0.3 eV sont mesurées. Les résultats des simulations pour cette tempértaure ne sont pas sensibles aux modifica-

tions des coefficients de transport perpendiculaires, qui sont le paramètre libre principal dans les simulations.

Nous avons examiné plus en détail le processus qui dissipe le plus d'énergie du plasma dans les simulations. Les collisions inélastiques entre les électrons et les molécules du gaz neutre ambiant constituent le mécanisme de perte d'énergie le plus important. En dehors de ces processus inélastiques, la dissociation des molécules et des ions moléculaires s'est révélée être dominante. Cependant, ces puits d'énergie sont actifs dans la région en amont du faisceau de plasma, où T_e est suffisamment élevé ($\sim$ 1 eV) pour rompre efficacement les molécules et les ions moléculaires ; Dans les endroits proches de la cible, les simulations ne prédisent aucun mécanisme qui pourrait dissiper le flux de chaleur et ramener par la suite T_e aux valeurs de 0.2 eV trouvées dans l'expérience, c'est-à-dire où la recombinaison en volume pourrait éliminer un nombre important de particules chargées. En conséquence, les simulations ne peuvent pas non plus reproduire la forte recombinaison volumique observée expérimentalement. Les valeurs relativement élevées de T_e indiquent qu'il manque des canaux de dissipation d'énergie dans les simulations. Le rayonnement intrinsèque des molécules elles-mêmes (par exemple en raison de lignes/bandes moléculaires) a été pris en compte, mais les estimations initiales ont montré que la puissance dissipée par ce canal est négligeable, en particulier à faible T_e. La possibilité d'une dissipation d'énergie supplémentaire par excitation vibrationnelle (les coûts énergétiques associés à ces excitations n'étant pas pris en compte dans la version du code utilisé dans la thèse) des molécules est suggérée comme une explication possible.

On s'interroge depuis longtemps sur le fait de savoir si la recombinaison activée par molécules (RAM), une voie de recombinaison alternative où des molecules excitées par vibration jouent un rôle, est une voie de recombinaison potentiellement importante dans les plasmas pertinents pour la fusion. La preuve de la présence de RAM est en effet omniprésente dans les dispositifs à plasma linéaires, généralement à partir d'une analyse détaillée des populations d'états excités. D'après les simulations, il a été conclu que le puits de recombinaison intégré sur le volume total dû à la RAM atteignait 25% du flux total de particules, pour tous les cas de simulation. La quantité de particules chargées que la RAM peut éliminer est limitée par un processus concurrent purement dissociatif. Ceci confirme les résultats antérieurs de *Fantz et al., Journal of Nuclear Materials, 2001*, sur ASDEX-Upgrade.

La dernière partie du travail a été consacrée à l'étude du bilan énergétique du plasma dans Magnum-PSI, principalement par calorimétrie et diffusion Thomson. Le résultat principal de cette partie est que la valeur généralement utilisée pour le facteur de transmission de la chaleur de la gaine $\gamma = 7$ n'est pas un choix approprié pour les plasmas de haute densité inférieurs à 1 eV étudiés dans ces expériences. Il est indispensable d'inclure également l'énergie potentielle provenant de la recombinaison ionique et atomique cible dans l'estimation du flux thermique de la diffusion de Thomson afin d'obtenir des valeurs compatibles avec la calorimétrie. Bien que l'on sache que l'énergie potentielle de la recombinaison se dépose à la surface du solide, à notre connaissance il n'y avait jusqu'ici dans la littérature pas de mise en évidence expérimentale aussi claire de cette contribution au flux d'énergie sur la cible.

Les implications des résultats des machines linéaires pour les divertors de tokamaks doivent être considérées avec soin en raison des différences de géométrie et de fonctionnement. Cependant, nous pensons que les résultats présentés ici apportent des informations utiles. Il a été démontré que les collisions inélastiques des électrons avec les molécules environnantes constituent un canal puissant de dissipation de la chaleur. Il est important de souligner que dans Pilot-PSI et Magnum-PSI, la densité moléculaire est élevée, en raison de la source d'arc en cascade et de la dominance de l'association des atomes neutres dans la paroi, ce qui n'est souvent pas le cas pour les tokamaks. Cependant, les efforts récents de modélisation des géométries de futurs divertor fermées à DIII-D et à MAST-Upgrade ont montré des densités moléculaires comparables à nos conditions, jusqu'à 10^{20} m $^{-3}$ et une valeur proche de cible $T_e \sim 1$ eV. Ces raffinements de la géométrie du divertor ont entraîné de meilleures performances en termes de dissipation de puissance, à la fois de la modélisation du code de transport de bord et des expériences. On s'attend à ce que, dans de telles conditions de plasma, les principaux mécanismes d'action en physique atomique et moléculaire soient les mêmes que dans les deux dispositifs linéaires étudiés dans ce travail. Nous pensons par conséquent que les résultats présentés dans cette thèse ont contribué à la compréhension des plasmas de haute densité et basse température pertinents pour les divertors détachés des tokamaks.

Curriculum vitae

Karol Ješko was born on the 23rd of September 1989 in Košice, which was part of Czechoslovakia at the time. After finishing high school in 2009 at Gymnázium Šrobárova 1 in Košice, he studied Theory and Technology of Nuclear Fusion at the Czech Technical University in Prague, Czech Republic. In 2014 he graduated with honours on the subject of *Model of the electron velocity distribution function of JET divertor target plasmas*. From October 2014 he started a joint PhD project in the framework of the Erasmus Mundus Fusion Doctoral College program. He spent half of the time at the Institute for Magnetic Fusion Research at the CEA Cadarache nuclear research centre in France and the other half at the Dutch Institute for Fundamental Energy research in Nieuwegein and later in Eindhoven, Netherlands, under the umbrellas of Aix-Marseille university and TU Eindhoven. The results of this work are presented in this dissertation.

List of publications

This thesis is based on the following publications:

- **Plasma pressure and particle loss studies in the Pilot-PSI linear plasma generator**
  K. Ješko, H. J. van der Meiden, J. Gunn, J. Vernimmen, and G. De Temmerman *Nuclear Materials and Energy* (2017) 1088-1093.

- **Soledge2D-Eirene simulations of the Pilot-PSI linear plasma device compared to experimental data**
  K. Ješko, Y. Marandet, H. Bufferand, J.P Gunn, H.J van der Meiden, G. Ciraolo *Contributions to Plasma Physics* **58** (2018) 798-804.

- **Studying divertor relevant plasmas in the Pilot-PSI linear plasma device: experiments versus modelling**
  K. Ješko, Y. Marandet, H. Bufferand, J.P Gunn, H.J van der Meiden, G. Ciraolo *Plasma Physics and Controlled Fusion* **60** (2018) 125009.

The author of this thesis was also co-author of the following publications:

- **Assessment of the effect of parallel temperature gradients in the JET SOL on Te measured by divertor target Langmuir probes**
  I.Ďuran, K.Ješko, V.Fuchs, M.Groth, C.Guillemaut, J.P.Gunn, J.Horacek, R.A.Pitts, D.Tskhakaya and the JET-EFDA Contributors *Journal of Nuclear Materials* **463** (2015) 432-435.

- **Plasma detachment study of high density helium plasmas in the Pilot-PSI device**
  Y. Hayashi, K. Ješko, H.J. van der Meiden, J.W.M. Vernimmen, T.W. Morgan, N. Ohno1, S. Kajita, M. Yoshikawa and S. Masuzaki *Nuclear Fusion* **56** (2016) 126006.

- **Collective Thomson scattering system for determination of ion properties in a high flux plasma beam**
  H.J. van der Meiden, J.W.M. Vernimmen, K.E. Bystrov, K. Jesko, M.Y. Kantor, G. De Temmerman, T.W. Morgan *Applied Physics Letters* **109** (2017) 261102.

- **Experimental evidence of enhanced recombination of a hydrogen plasma induced by nitrogen seeding in linear device Magnum-PSI**
  R. Perillo, G.R.A. Akkermans, I.G.J. Classen, W. A. J. Vijvers, R. Chandra, K. Jesko, J.W.M. Vernimmen, M.R. de Baar and the MAGNUM-PSI team, *Submitted to Nuclear Materials and Energy*, 2018.

Acknowledgements

I was particularly looking forward to writing this part of the thesis, as I truly feel the need to express my gratitude to a large number of people without whom this thesis would be less than a shadow of itself. I will attempt to thank as many people as I possibly can, and would like to apologize if I forgot someone. I spent my first few weeks at IRFM, CEA Cadarache in France, then almost a year at DIFFER in Nieuwegein, then two years at CEA Cadarache in France and the final year at DIFFER again, so I was in contact and working with a fairly large number of people, to whom I dedicate the following paragraphs.

First, I would like to thank my thesis director at CEA Cadarache, Jamie Gunn, for guiding me throughout my thesis. Jamie, I specifically want to thank you for the fact that you had enough confidence in me to give me the freedom to choose and define my own research. By this approach, you have changed me from a person that was "awaiting orders" into someone who now has the inner motivation to find and work on topics of interest. I also want to thank you for your patience and solution-oriented approach to the university-related bureaucracy we had because of the co-tutelle. Finally, I also enjoyed all the pleasant non-work related times, and thanks also for sharing your interesting and humorous reflections on the local reality and life style in the south of France. Jamie, thank you for being not only a thesis director but also a coach and friend at the same time.

Next, I would like to thank my promoter/thesis director at DIFFER, Richard van de Sanden, for providing guidance and support especially in the final stages of my thesis. Richard, we didn't meet very often, but when we did you have always given me a lot of feedback that made me look at my results in a different way. You have brought your own perspective, and I am grateful that you have pointed me towards relevant research that I had not known from within the fusion community.

I would like to thank Hennie van der Meiden, for being my day-to-day supervisor at DIFFER. Hennie, I was fascinated by your dedication towards plasma diagnostics, and your high level of expertise in it. Thanks to you and your skills, I was able to obtain high-quality data in the first year of my thesis, during the difficult times when only the Pilot-PSI experiment was running at the old location of the institute in Nieuwegein. You were confident enough in me to let me find my own way in research, and provided support to all of my ideas and experimental proposals at DIFFER. You were the first person to read my manuscript and I wish to thank you for all the thorough comments. I have also strongly enjoyed your company as a person, during lunches, experiments and the PFC meeting in Ljubljana.

I want to thank Yannick Marandet from PIIM/CNRS in Marseille, for greatly advancing my PhD work, by showing me with a lot of patience how to use an edge transport code, and for his insights on the physics of neutrals, but also physics in general. Yannick, your responsiveness to my requests and questions had a massive impact on this thesis, and you were heavily involved in a large part of the work. Thanks to your approachability, we have had a lot of discussions at the CEA about my work and you pointed me in the right directions and gave me the right tools to pursue them. Yannick, I truly enjoyed working with you and I want to thank you for all the time and dedication you provided.

Next, I wish to thank Hugo Bufferand, for setting up the first ever linear device case in the Soledge2D-Eirene code framework. Hugo, I was amazed at your coding skills when you literally translated my words into a working simulation in the matter of hours, and I thank you for solving all my follow-up issues with the code setup. I want to thank Guido Ciraolo, our group leader at the CEA, for supporting the Soledge2D-Eirene work on Pilot-PSI, and for maintaining a good atmosphere around the corridors of the institute. I also wish to thank Jean-Yves Pascal, for sending the power supply and probe measurement circuit to DIFFER, and for the splendid trip to the Alps; Pascale Monier-Garbet, for helping me in the first weeks after my arrival at the CEA; Nicolas Fedorczak and Patrick Tamain, for your input and discussions during our regular group meetings.

I also want to thank fellow PhD students of the divertor group at the CEA: Matteo Valentinuzzi, for discussions and troubleshooting of Soledge2D-Eirene, the mini-basketball tournaments and gym climbing sessions; Alberto Gallo, for his extroversion that "kept the blood flowing" in the group, and for showing me how a good presentation is made; Julien Denis, for his insights on desorption and for providing a quality alternative to the usual coffee machine; post-doctoral researcher Owen Jones for his great tips on things to do in Provence. I also want to thank fellow PhD students from other groups, for pleasant times during lunches and coffee breaks: Iaroslav Morgal, Georgiy Zadvitsky, Yan Sun, Nicolas Nace, Cristian Sommariva, Camille Baudoin, Arvydas Sepetys, Serafina Baschetti, Anastasia Dvornova, Olivier Février, Etienne Hodille and Adrien Autrique.

I will now come back to my first year at the DIFFER institute. Here, I am very grateful to Kirill Bystrov. Kirill, you were a very experienced operator and physicist with amazing problem solving skills. I thank you for your input during my experiments, and also for giving me the training to become operator of the Pilot-PSI linear plasma device. Your friendship makes me look back at the time I spent in Utrecht with a feeling of nostalgia. Richard Al, thank you for helping me with the installation of my probe systems, and for always being in a good mood despite the frequent machine failures. We have had so many great laughs during mounting and soldering. I thank Damien Aussems, for staying to perform experiments on the weekend and in the night. Those were very dynamic times, and I hope we will never have to repeat them again :-). I also wish to thank Mikhail Zibrov, for our frequent discussions about any topic, and for the resistors you obtained and Branka Vanovac, for the nice company at the DIFFER guesthouse and social dinners during those cold winter nights. For keeping a pleasant

atmosphere at the institute, I also wish to thank fellow PhD students and post-docs Irem Tanyeli, Sébastien Bardin, Vladimir Kvon, Long Cheng, Fabien Jaulmes and Wei Lu.

The second time I came to DIFFER it was a changed institute, in a different building in a different city. The Magnum-PSI device was back online and experiments were running again, and I wish to thank the Magnum-PSI team for making this possible: Hans van Eck, John Scholten, Jordy Vernimmen, Santi Alonso van de Westen, Erik Vos, Mark van de Pol and Serge Brons. I have to thank Jordy specifically also for the hard work at Pilot-PSI in the old days, on the diagnostics and day-to-day operations.

I was extremely happy to see that when I arrived for the second time at DIFFER there was already a whole new community of edge plasma physicists and diagnosticians working there, and I wish to thank you all for your contributions and for all the nice discussions we had. In particular, Renato Perillo, thanks for all the insights on plasma chemistry and on the positive boost in energy I felt when talking to you, and for being one of my paranimfen; Gijs Akkermans, for the time you spent in the control room during my experiments and the diagnostic expertise you provided; Ray Chandra, for the illumating discussions about edge modelling; Ivo Classen, for being critical towards my thesis manuscript and Jonathan van den Berg, for being one of my paranimfen and the nice chats about near surface plasma physics. I also want to thank Timo Ravensbergen, Wouter Vijvers and Artur Perek for the pleasant times at the coffee machine. I wish you all the best in the exciting research you are doing! I also thank Egbert Westerhof for reading my manuscript and providing feedback and Hugo de Blank and Jonathan Citrin for all the good questions during the edge modelling meetings.

I wish to thank Tom Morgan, my group leader at DIFFER, for supporting my stay at DIFFER and experimental proposals and for flexibility in the experimental planning. Tom, I think you have made the group thrive and I felt really good there. I also wish to thank fellow students in our group, Yu Li, Wei Ou, Chidozie Onwudinanti, Shih-Chi Wang, Mozhgan Laki and Peter Rindt for the illuminating discussions about materials for fusion and your interesting talks at the PMI meetings. Special thanks go to Stein van Eden, for working hard to make the new bolometer work, which I used in one of my key experiments. In the end, it worked pretty well!

I would like to thank Greg de Temmerman, for writing down the initial proposal for my PhD project, and for giving his approval to hire me. Greg, I wish we could have worked more together, as you have great knowledge on the physics of plasma-surface interactions. I also enjoyed talking to you at conferences, and listening to your numerous talks, and I admire your sportive endeavours!

I also want to thank Han Genuit and Alex Poelman for programming the software that made my life significantly easier, Gerben Land at the electronics department for making the circuits I had requested, the crew at the mechanical workshop, led by Peter Wortman, for their professionalism in manufacturing the parts I needed, Bram Lamers for all the CAD drawings and Jan-Willem Wahlbrinck for the IT support. The institute would never work were it only staffed by physicists :-).

I am also grateful to have had very good office mates: Jun Wang and Jorge Rosas Saad. I think we managed to keep our spirits high, even at times when there was a lot

of work.

I wish to thank Conrad Becker and Michele Francia at the doctoral school at Aix-Marseille university for their patience with complicated administrative processes, and Clazien Saris for doing the administration on the TU Eindhoven side. I admit that I was a complicated case in this regard.

I also want to thank Roger Jaspers, Niek Lopes Cardozo and Richard Engeln for their help in setting up the co-tutelle agreement. I have to express my praise for the Erasmus Mundus Fusion-DC team: Kathleen van Oost, Frank Janssens, Jean-Marie Noterdaeme and Guido van Oost. Thank you for your effort in making this funding scheme available to students from all over the world.

I feel it is also important to thank my alma mater, the Faculty of Nuclear Sciences and Physical Engineerg of the Czech Technical University in Prague. I think the university has prepared me very well for the PhD journey. I wish to thank specifically Jan Mlynář and Petr Kulhánek for their great teaching of fusion and plasma physics, and Ivan Ďuran from IPP Prague for being a brilliant supervisor of my master thesis.

Last but not least, I want to thank the people who stand closest to me on a personal level. I wish to thank my girlfriend Zora for putting up with all the relocation issues associated with my PhD work. Zora, you are an amazing person in your ability to adapt to new situations in different countries, and I have huge respect for you. I think we managed to have a great time during our stay in Aix-en-Provence! I also want to thank my parents and brother, who were fully in support of my PhD journey even if this meant that we did not see each other much during the past four years. I hope that the notion that I had completed this journey can compensate for that.